Atomic ensembles in a microcavity : from cavity protection to single atom control

Pierre-Antoine Bourdel

SORBONNE UNIVERSITÉ

THÈSE DE DOCTORAT
DE SORBONNE UNIVERSITÉ

Spécialité : Physique

École doctorale nº564: Physique en Île-de-France

réalisée sous la direction de Jakob REICHEL

au Laboratoire Kastler Brossel

Laboratoire Kastler Brossel
Physique quantique et applications

présentée par

Pierre-Antoine BOURDEL

Sujet de la thèse :

Atomic ensembles in a microcavity: from cavity protection to single atom control

soutenue le 5 décembre 2022

devant le jury composé de :

M.	Whitlock Shannon,	Prof.,	Univ. Strasbourg,	Rapp. - Prés. jury
M.	Brantut Jean-Philippe,	Prof. assist.,	EPFL,	Rapporteur
Mme	Diamanti Eleni,	Dir. de rech.,	Sorbonne Univ.,	Examinatrice
Mme	Hilico Adèle,	Maît. de conf.,	Univ. Bordeaux,	Examinatrice
M.	Volz Jürgen,	Prof.,	Humboldt-Univ. Berlin,	Examinateur
M.	Reichel Jakob,	Prof.,	Sorbonne Univ.,	Directeur de thèse
M.	Long Romain,	Maît. de conf.,	Sorbonne Univ.,	Encadrant de thèse

Contents

Introduction

In the development of physics, experiments and theories are intertwined such that experimental results can remodel our understanding of physics phenomena and give birth to new fields. The 2022 Nobel Prize in physics illustrates this point, by awarding Alain Aspect, John F. Clauser and Anton Zeilinger for ground-breaking experiments establishing that nonlocality and entanglement are realities. It was also recognised that such experiments "pioneered " quantum information science. In quantum physics, experimental breakthroughs have also stemmed from techniques enabling individual control of elementary systems and of their interactions. Earlier Nobel Prizes acknowledged for such developments, when awarding Hans G. Dehmelt and Wolfgang Paul "for the development of the ion trap technique" (1989) or Serge Haroche and David J. Wineland "for ground-breaking experimental methods that enable measuring and manipulation of individual quantum system" (2012). The latter recognised the breakthroughs of the team of Serge Haroche in the field of Cavity Quantum ElectroDynamics (CQED). This field studies one of the simplest interactions one could think of: that of a single atom with a single mode of the electromagnetic field.

In a sense, CQED was born with Purcell's observation of the atoms' spontaneous emission enhancement when interacting with a resonator [1]. This result demonstrates that spontaneous emission is not a property of the atoms alone but a property of the coupling between atoms and the modes of the electromagnetic field, the density of which a resonator modifies. When decreasing the volume of the mode sustained by the resonator, the energy density of the corresponding electromagnetic field increases, and so does the strength of its interaction with an atom in the resonator. If the interaction strength is larger than the decay rates from both the atom (spontaneous emission) and the resonator (photon scattering, leakage), new physics phenomena are possible, beyond the Purcell effect. In this so-called "strong coupling regime", a single quantum of energy can be coherently exchanged between the atom and the resonator (or cavity) field many times before being lost through the previously mentioned decay processes. Such exchange corresponds to Rabi oscillations at the level of a single quantum. Their spectral counterpart is the normal mode splitting: because of the strong coupling between the atom and the cavity, even if the cavity is tuned to resonance with the atom, the resonances of the interacting system (atom plus cavity) are split apart, far from the non-interacting resonances. Though this effect can be explained by classical physics [2], it remains striking that the presence of a single atom can shift the cavity completely out of resonance.

Experimentally, it has been quite a challenge to isolate from their environment both the atom and the resonator, and reduce the complex possibilities of interactions to the sole coherent exchange between the effective two-level systems. Pioneering CQED experiments

were performed with Rydberg atoms flying through high-finesse superconducting microwave resonators [3–6]. It then developed in the field of optics, mainly with neutral atoms flying through optical Fabry Perot cavities [7, 8], and later by placing inside a cavity a single ion trapped in electric fields [9]. More recently the strong coupling regime was demonstrated for artificially engineered quantum systems: superconducting qubits in the microwave domain [10] and quantum dots in the optical domain [11, 12].

By bringing answers to questions that previously could only be stated in terms of famous thought experiments by the founders of quantum mechanics, CQED shows that striking experimental results model our understanding of physics. The collapse and revival of Rabi oscillations in the one-atom maser [6] illustrate the quantum statistical and discrete nature of the cavity field. The famous collapse of the wavefunction was observed for the cavity field [13]. Interestingly in this case, it appeared as a progressive mechanism happening upon repeating Quantum Non Demolition (QND) measurement of the number of photons of the field. Reciprocally in optical CQED, the state of a single atomic qubit could be QND-measured with no exchange of energy [14][1]. The progressive loss of coherence of a non-classical superposed (Schrödinger cat) state of the cavity fields was observed with repeated measurements [15].

The achievements of CQED are not restricted to these fascinating fundamental aspects. Cavities have been used to improve the collection efficiency of single photons emitted by a single atom [16] or a single ion [17]. A single emitter strongly coupled to an optical cavity has been proposed to be a node in a quantum network [18, 19], *i.e.* an infrastructure able to initialise, process and propagate quantum information among its different nodes. In this proposal, the single atom in the cavity serves as a "stationary qubit", and the photon is the "flying qubit", as it is able to propagate in fibres quickly and with reasonably low loss.

For example, some experiments in the group of Gerhard Rempe follow this line. A single atom strongly coupled to a cavity has been used to generate a single photon in a state entangled to that of the atom [20]. If the photon is sent through a fiber to another cavity where its state is transferred to a second atom, the two atoms in distant cavities end up entangled [21], realising a minimalistic quantum network. Then, following the proposals of references [22, 23] that rely on the full reflection of a single photon at the input of a cavity strongly coupled to an atom, a controlled-NOT (CNOT) gate was operated between the cavity atom and a single photon [24]. Later a non-destructive Bell-state measurement of two atoms in distant cavities was demonstrated [25]. It generates a maximally entangled state between the two nodes.

As compared to the first CQED demonstrations operating with hot atomic beams, these experiments benefited from the higher degree of control of cold atoms [26–29], superbly illustred by the cooling down of a single atom to the motional ground state of a dipole trap, inside a strong coupling cavity [30]. Some of these later strong coupling experiments worked with more than a single atom. In the groups of Gerhard Rempe and Dieter Meschede, several experiments have involved two individual atoms inserted in the cavity with a one-dimensional optical lattice perpendicular to the cavity [31, 32]. It permitted the demonstration of two-

[1] These two similar results illustrate an interesting complementary of Rydberg-micro-wave and optical CQED. In the first case, the Rydberg atom is the means to acquire information about the micro-wave cavity field, and effort is done to generate non-classical states of this field. In the second case, the cavity mode is probed optically to acquire information about the atoms, and effort is made to generate non-classical states of atoms.

atom entanglement [32] and of an atom-atom CNOT gate [33]. In the group of Tilman Esslinger, the feedback of atoms on the cavity field - an essential feature of strong coupling - is used to couple the cavity to the collective density excitation of a Bose Einstein condensate, used as a mechanical oscillator [34, 35]. Later experiments involved another specificity of CQED: the cavity photon-mediated interactions between atoms [36, 37]. Quantum Non Demoltion measurement is a third essential feature of CQED. The back action it generates can be used to squeeze the spin distribution of an atomic ensemble [38, 39], generating *probabilistically* a spin-squeezed entangled state, of metrological interest [40], from an initially separable state. Combined with One-Axis Twisting [41], QND measurement can produce spin-squeezed states *deterministically* [42, 43]. Up to 20 dB of metrological gain was achieved with this combination [44]. Together with qubit rotations, QND has been used in our group to generate entanglement among tens of atoms, probabilistically [45], then deterministically, in a quantum Zeno dynamics scheme [46].

Similarly, the first half of this manuscript decribes experiments with an indiscernible ensemble of cold atoms in a strong coupling cavity. In CQED with ensembles, the homogeneity of atom-cavity interaction is a core issue. In our experimental setup, the trap is engineered for maximal and homogeneous coupling. However, its lightshift induces a distribution of atomic frequencies. The situation of a resonator coupled to N emitters with different frequencies is quite common. It was shown theoretically that a coherent cavity-emitters interaction is still possible if the collective coupling is sufficiently large [47–49]. This effect, called "cavity protection", has been demonstrated in three solid-states experiments [50–52] with at least millions of emitters. We report here cavity protection with only two hundred atoms, thanks to our strong single-atom coupling [53]. Taking advantage of the narrow resonances in the cavity-protected regime we engineer frequency-modulated polaritons. We also exhibit the increase in photonic weight of the dark states as the collective coupling decreases, observing a transition from a polaritonic regime to a disordered regime, with no protection. Very interesting parallel can be drawn with the recent similar study of this transition [54]. The tunability of both cold-atom setups allows to vary the amount of inhomogeneity, by tuning the trap power. This is an asset for studying the cavity protection effect. While keeping the trapping effect, we can also get rid of the inhomogeneity, for the experiments with an homogeneous frequency, in the second half of the manuscript.

In this second part, we describe the design and first results of a setup that will allow trapping and manipulating many *individual* atoms strongly coupled to a cavity. This is quite demanding in the small mode volume of such a cavity, which is why most experiments have involved one or two atoms, or an indiscernible atomic ensemble. Fortunately, it was shown over the last decade that ensembles of many individually-resolved atoms can been obtained with optical tweezers. The team of Philippe Grangier found that these tightly focused optical dipole microtraps could be loaded with single atoms [55, 56]. Spatial light modulators or acousto-optical deflectors (AOD) can generate arrays of up to hundreds of tweezers in almost arbitrary and reconfigurable patterns [57–60]. As single atoms in tweezers are obtained probabilistically, they are usually rearranged with extra moving tweezers so as to form defect-free structures. Combined with Rydberg interactions, tweezers arrays have proved to be an excellent platform for quantum simulation [61] with hundreds of atoms [60, 62], in a regime where classical computation becomes unfeasible.

Such tweezers arrays are excellent for scaling up the number of individual atoms in small

cavities. Their combination with strong coupling is very promising, as it enables *single* atom control, detection and addressability as well as the *collective* operations we have mentioned: QND measurement of, entanglement generation among, or cavity-mediated infinite-range interactions between the atoms. This combination has been only recently achieved in a few experiments.

Two atoms in optical tweezers have been strongly coupled to the evanescent field of a photonic crystal cavity [63] and later entangled by QND probing of the cavity [64]. Then, two experiments have implemented a one-dimensional tweezer array in a strong-coupling Fabry Perot cavity. In reference [65] the precise positioning of a single tweezer atom has been used as a microscopic superresolved probe of the standing waves sustained by the cavity. Then, with a chain of two atoms perpendicular to the cavity, a minimalist "mid-circuit" measurement was operated, by showing that the cavity measurement of one atom does not alter the hyperfine coherence of the second atom [66]. With a chain of tweezers along the cavity axis, a variable (probabilistic) number of up to eight atoms has been strongly coupled to a cavity [67].

The experimental platform we have been building for a few years is part of this new generation. It combines 1) a cavity engineered for strong and equal coupling of many single atoms and 2) tweezers generated from two separate AODs to produce a reconfigurable array of single atoms, and couple to the cavity an arbitrary subset of the array. Our resonator is a fiber Fabry-Perot cavity, with a high finesse at both 780 nm and at $1559 \approx 2 \times 780$ nm. The first is the CQED probe, resonant with the D_2 line of ^{87}Rb. The latter is a trapping lattice, commensurate with the probe standing wave, in such a way that atoms trapped in the lattice are equally and strongly coupled to the cavity probe field. We use a high-numerical aperture lens to generate optical tweezers in and out of the cavity mode. For atoms not interacting with the cavity, we setup a one-dimensional static tweezer array far from the cavity: the “qubit storage register”. A two-dimensional AOD is used to move one or multiple atoms from the cavity to the "storage register" and reversely.

With this unique combination of two AODs and the strong coupling microcavity, our experiment should allow to perform 1) quantum simulations of all-to-all coupled spin ensembles, with single-spin resolved detection and controllable disorder, 2) "mid-circuit" measurements of an arbitrary subset of our single atom array, of interest for quantum error correction, and 3) to generate and use *spatially distributed* entanglement for multiparameter quantum metrology.

Thesis outline

Chapter I introduces the general lines of our experimental platform. We present the basic theoretical framework for CQED, as well as the entanglement generation and QND atomic state measurement enabled in the single atom strong coupling regime. We then explain the dual-AOD-cavity architecture of our setup, after reviewing the few other experiments where several individual atoms have been strongly coupled to a resonator. Finally we present the key qualitative elements of the theory of cavity protection, as well as previous experimental

demonstrations of this effect.

Chapter II describes the main building blocks of our cold atom–CQED setup. We show how the cavity has been designed to achieve strong and homogeneous coupling along its entire length. We describe the different steps to prepare a polarised cold atomic ensemble in the micro-cavity and we demonstrate its strong collective coupling.

Chapter III describes the cavity protection effect observed in our experiment, and how we frequency-modulated cavity-atoms hybrid states in the protected regime. We first present experimental characterisation of the atomic frequency distribution induced by the trap lattice. Then, we measure polaritons much narrower than the distribution, a signature of cavity protection. Finally, in the protected regime, thanks to the sensitivity of the atomic frequency to the lattice trap, we engineer frequency-modulated polaritons.

In chapter IV we study the transition between the cavity-protected regime and the disordered regime, by decreasing the ratio between the collective coupling and the disorder strength. We observe the corresponding decrease of the protection effect, which manifests by an increasing coupling between the cavity and the "dark" states. We account for the variation of the coupling to the cavity both in the experiments and in the simulations.

Chapter V is devoted to describing the setup required to generate multiple tweezers inside the microcavity. The high numerical aperture lens under vacuum - previously aligned with the micrometric cavity mode - focuses the tweezers from two AODs close to diffraction limit. The AODs are fed with phase and amplitude-optimised multi-frequency radio-frequency signals to generate up to one hundred tweezers per AOD.

Chapter VI describes the characterisation of a single atom trapped in a single tweezer and its strong coupling to the cavity. First, we test the ability of the cavity to detect a single atom, in the intra-cavity lattice. This detection is indeed at the core of all subsequent results with tweezers. A molasses aligned to the cavity mode allows achieving the collisional blockade regime where at most one atom is loaded in the tweezer. We then characterise its temperature and the trap frequencies, which provide an in-situ verification of the waist size of the tweezer. To optimise the coupling of the single atom to the cavity, we add to the tweezer trap the intra-cavity lattice trap, specially designed for maximising coupling. In this double trap, we further optimise the coupling by mapping the cavity mode with the single trapped atom, to find the optimal position for the tweezer. We demonstrate the strong coupling of the atom to the cavity by measuring the transmission spectrum. Finally, using both AODs and setting up our qubit storage register, we start operating up to nine tweezers, which we load probabilistically with single atoms.

To conclude, we summarise the main results of the thesis and discuss the next steps and perspectives of our new experimental platform.

Chapter I

Cavity Quantum ElectroDynamics with an array of tweezers single atoms

I.1 CQED basics and capabilities

I.1.1 A single atom coupled to a single cavity mode

The Jaynes-Cummings Hamiltonian [68] is paradigmatic in the field of CQED: it is suited to describe the dipole interaction between a single atom modeled as a two-level system and the electric field sustained by the cavity, under the rotating-wave approximation. Once added the non-interacting Hamiltonian of the single-mode cavity and the atom, the full Hamiltonian writes:

$$H_{JC} = \hbar g\Big(\sigma^+ a + \sigma^- a^\dagger\Big) + \hbar\omega_a \sigma^+\sigma^- + \hbar\omega_c a^\dagger a, \tag{I.1}$$

where ω_c is the frequency of the cavity mode closest to resonance with the atomic frequency ω_a, a and $a^\dagger$ are the annihilation and creation operators for this cavity mode, $\sigma^+ = |e\rangle\langle g|$ and $\sigma^- = |g\rangle\langle e|$ are the atomic two-level system raising and lowering operators, with ground and excited states $|g\rangle$ and $|e\rangle$, and g is the coupling strength of the atom to a single photon:

$$g = \frac{-\boldsymbol{d}.\boldsymbol{\mathcal{E}}}{\hbar}, \tag{I.2}$$

where $\boldsymbol{d}$ is the dipole strength, and $\boldsymbol{\mathcal{E}}$ is the single photon electric field of the cavity mode. g depends on the position of the atom with respect to the cavity mode, and the maximal value g_{max} is obtained at the position of the maximal single photon electric field:

$$g_{max} = \sqrt{\frac{d^2\omega_c}{2\hbar\varepsilon_0 V}} = \sqrt{\frac{3\lambda^2 c\gamma}{4\pi V}}, \tag{I.3}$$

where γ is the atomic transition Half-Width at Half Maximum (HWHM) and V is the cavity mode volume.

The Jaynes-Cummings Hamiltonian describes the coherent energy exchange between the atom and the cavity mode. It couples the non-interacting eigenstates $|e, n-1\rangle$ and $|g, n\rangle$, with

a coupling strength $g\sqrt{n}$, where n is the number of energy quanta. The Jaynes-Cummings Hamiltonian can be diagonalized. Within a subspace of a given n, the eigenfrequencies are:

$$\omega_{\pm}^{(n)} = n\omega_c + \frac{1}{2}\Big(\Delta_{ac} \pm \sqrt{\Delta_{ac}^2 + 4g^2 n}\Big), \tag{I.4}$$

where $\Delta_{ac} = \omega_c - \omega_a$ is the atom-cavity detuning. Picture a. of figure I.1 shows the eigenfrequencies $\omega_{\pm}^{(n)}$ (x axis) for variable Δ_{ac} and n = 1,2,3. The atomic and cavity frequencies are plotted as plain lines and cross at $\Delta_{ac} = 0$. The interaction lifts the degeneracy of the non-interacting eigenstates $|e, n-1\rangle$ and $|g, n\rangle$ and produces an avoided crossing close to $\Delta_{ac} = 0$. When the cavity and the atom are exactly on resonance ($\Delta_{ac} = 0$), the separation between the two is $2g\sqrt{n}$. In the case of a single energy quantum, we get the so-called vacuum-field Rabi splitting $2g$ [69].

I.1.2 Opening the coupled system

The Jaynes-Cummings Hamiltonian corresponds to an isolated system. For a more complete description we have to include atomic spontaneous emission, cavity losses and pumping from a probe field, which make the atom-cavity system open. Thus we use a master equation formalism, where the evolution of the system is described by:

$$\frac{d\rho}{dt} = \frac{1}{i\hbar}\Big[H, \rho\Big] + \mathcal{L}_a\rho + \mathcal{L}_c\rho, \tag{I.5}$$

where ρ is the density matrix, $\mathcal{L}_c$ and $\mathcal{L}_a$ are Linbald operators for cavity losses and spontaneous emission respectively:

$$\mathcal{L}_a\rho = \gamma(2\sigma^-\rho\sigma^+ - \rho\sigma^+\sigma^- - \sigma^+\sigma^-\rho) \tag{I.6}$$

$$\mathcal{L}_c\rho = \kappa(2a\rho a^\dagger - \rho a^\dagger a - a^\dagger a\rho)\,, \tag{I.7}$$

where we assume that the cavity induces a negligible change of the decay rate in free space, which applies in our case, because the solid angle subtended by the cavity is small.

Replacing H by the Jaynes-Cummings Hamiltonian H_{JC} in equation I.5, the steady state solution corresponds to $|g, 0\rangle$, with no excitation. To recover excitation in the steady state, we consider pumping the coupled system with a probe at frequency ω_p, which is described by the following semiclassical phenomenological Hamiltonian:

$$H_p = -i\hbar\eta(ae^{i\omega_p t} - a^\dagger e^{-i\omega_p t}), \tag{I.8}$$

where η is the effective amplitude of the pumping field. Thus the total Hamiltonian writes, in the probe-frequency rotating frame:

$$H = H_{JC} + H_p = \hbar g\Big(\sigma^+ a + \sigma^- a^\dagger\Big) - \hbar g\Delta_{pa}\sigma^+\sigma^- - \hbar g\Delta_{pc}a^\dagger a - i\hbar\eta(a - a^\dagger), \tag{I.9}$$

where $\Delta_{pa} = \omega_p - \omega_a$ and $\Delta_{pc} = \omega_p - \omega_c$.

In the experiments described later, we acquire information by pumping the cavity mode with a probe, and collecting the light transmitted through the cavity. In the limit of weak

excitation, the transmission in intensity can be computed analytically from solving the master equation I.5, in the restricted subspace spanned by states $|g,0\rangle$, $|g,1\rangle$ and $|e,0\rangle$. In [70] this approach is used to compute the population of the excited state p_e and the average cavity photon number n_{cav}, from which we can deduce the transmission in intensity T:

$$p_e = \langle \sigma^+ \sigma^- \rangle = \frac{\eta^2 g^2}{|g^2 - (\Delta_{pa} + i\gamma)(\Delta_{pc} + i\kappa)|^2} \tag{I.10}$$

$$T = \kappa n_{cav} = \kappa \langle a^\dagger a \rangle = \frac{\kappa \eta^2 |\Delta_{pa} + i\gamma|^2}{|g^2 - (\Delta_{pa} + i\gamma)(\Delta_{pc} + i\kappa)|^2} \tag{I.11}$$

$$= \frac{\eta^2/\kappa}{\left(1 + 2C\frac{1}{1+\Delta_{pa}^2/\gamma^2}\right)^2 + \left(\frac{\Delta_{pc}}{\kappa} - 2C\frac{\Delta_{pa}/\gamma}{1+\Delta_{pa}^2/\gamma^2}\right)^2}, \tag{I.12}$$

These formula assume the low-excitation limit, $n_{cav} \ll 1$, which in practice, requires the probe intensity to be small enough. In these expressions, where we have introduced the cooperativity $C = g^2/(2\kappa\gamma)$, the figure of merit of CQED that compares the rate of coherent energy exchange between the field and the atom, g, with the rates of the two lossy incoherent processes, κ and γ. Strong coupling is the regime where the coupling g is high enough for the atom and the cavity field to exchange the energy quantum several times before loosing it through cavity decay or spontaneous emission. It is often defined by $g > \kappa, \gamma$ or $C \geq 1$, a non-equivalent condition. Picture b. of figure I.1 illustrates the transmission spectrum for several values of the cooperativity.

In figure I.1, picture a. shows a 2D plot of T, versus $\omega_p - \omega_c$ and $\Delta_{ca} = \omega_c - \omega_a$, together with the eigenfrequencies of the isolated system (equation I.4). One can see that the transmission peaks are, in good approximation, located at the position of the isolated system eigenfrequencies (this approximation is valid in the strong coupling regime).

The transmission spectrum contains more information. For $\Delta_{ca} = 0$, the spectrum obtained by scanning the probe frequency is shown in picture b: it exhibits two peaks with equal amplitude, which reflects that the eigenstates are equal superposition of $|g,1\rangle$ and $|e,0\rangle$. Picture a. shows that for $\Delta_{ca} \neq 0$, the peak closest to the cavity frequency has a higher transmission. As $|\Delta_{ca}|$ increases, the eigenstates converge towards the non-interacting states $|g,1\rangle$ and $|e,0\rangle$ and the one converging towards $|e,0\rangle$ becomes "dark".

The width of the peaks exhibits a similar behavior. In our case, the linewidth of the cavity is larger than that of the atom: $\kappa/2\pi = 14.2$ MHz and $\gamma/2\pi = 3.0$ MHz. For $\Delta_{ca} = 0$ both peaks have equal width $(\kappa+\gamma)/2$. For $\Delta_{ca} \neq 0$, the peak of the eigenstate with higher probability of cavity excitation is larger than the other peak. For large $|\Delta_{ca}|$, the widths of the peaks converge towards κ or γ, depending on the non-interacting eigenstates it is closest to.

Last but not least, while an avoided crossing occurs for all coupling values g from the perspective of the isolated system eigenfrequencies, the open system analysis reveals a stricter condition to distinguish the two corresponding peaks in the transmission spectrum $T(\Delta_{pc})$. For instance, for $\Delta_{ca} = 0$, g should be significantly larger than the width of the peaks $(\kappa + \gamma)/2$ for the peaks to be well separated. Picture b. shows transmission spectra with variable values for g, and thus variable values for the cooperativity. The red line corresponds

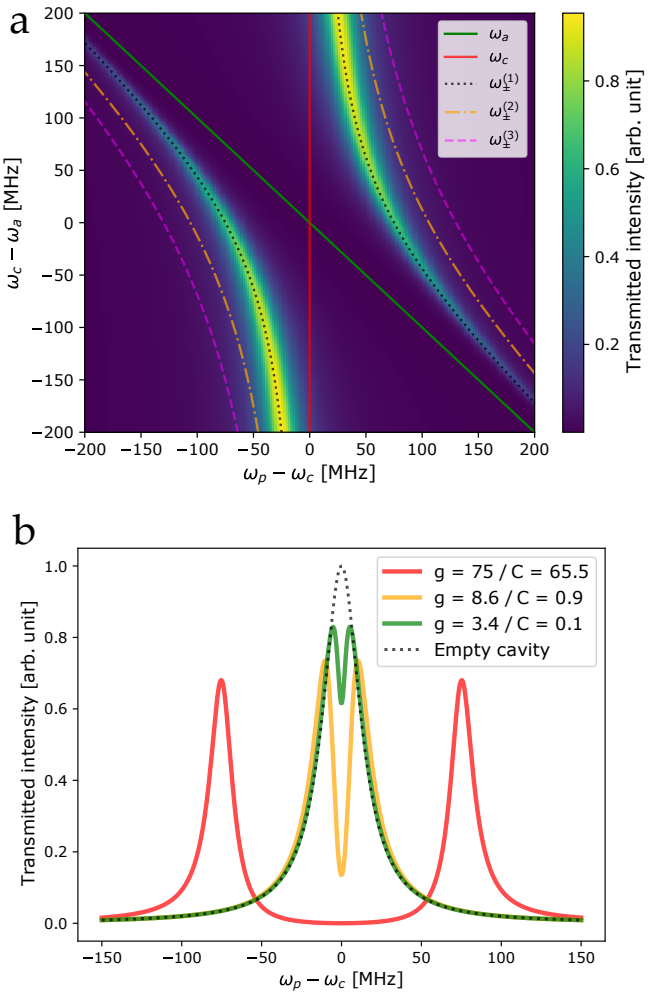

Fig. I.1 *Picture a: Cavity-atom transmission versus probe-to-cavity and cavity-to-atom detunings, superposed with the eigenfrequencies $\omega_\pm^{(n)}$ of the Jaynes-Cummings Hamiltonian (equation I.4) for n = 1,2,3 excitations. The straight lines correspond to cavity and atomic frequencies. Picture b: Transmission spectrum of the atom-cavity coupled system for different values of the coupling strength g, and the corresponding cooperativity C. The cavity is on resonance with the atom. Otherwise mentioned, all plots are done with the parameters of our cavity: $(g_{max}, \kappa, \gamma) = 2\pi \times (75, 14.2, 3.0)$ MHz.*

to the parameters of our cavity, presented in section II.2.1. It exhibits a vacuum Rabi splitting, and the cooperativity is $C \approx 65$, deep in the strong coupling. The other curves correspond to smaller values of g (κ and γ being fixed): the yellow (respectively green) curve corresponds to coupling strength $g = (\kappa + \gamma)/2$ (respectively $g = (\kappa + \gamma)/5$), and cooperativity $C \approx 1$ (respectively $C \approx 0.1$). In the limit $g \to 0$, on retrieves the empty cavity lorentzian transmission, which is the standard profile of the Fabry-Perot resonator.

I.1.3 N atoms coupled to the cavity mode

In this section, we will generalise the discussion of sections I.1.1 and I.1.2 to the case of N atoms, with the same frequency ω_a and the same individual coupling strength g to the cavity mode. As we will see, since all atoms are identically coupled to the field, it is appropriate to describe the multi-atom-cavity system using Dicke states [71]. First, we introduce the pseudo-spin 1/2 operator of the atom k: $\vec{J}_k$, such that $J_{z,k} = \sigma_k^+\sigma_k^- - 1/2$. The total pseudo spin of the N-atoms system is $\vec{J} = \sum_{k=1}^N \vec{J}_k$. We can then work with the basis $|J, J_z\rangle$, eigenstates of both $J^2 = J_x^2 + J_y^2 + J_z^2$ and $J_z = \sum_{k=1}^N J_{z,k}$, where $J \in [0, N/2]$ and $J_z \in [-J, J]$. Since the N atoms are identically coupled to the cavity mode, it is particularly suited to consider the symmetric subspace, defined by $J = N/2$, which is spanned by the Dicke states $|n_N\rangle = |J = N/2, J_z = -N/2 + n\rangle$, with $n \in 0,1,2, ..., N$. These states are invariant under exchange of any two atoms, meaning that the excitation is delocalised symmetrically over all atoms. As an example, the Dicke state corresponding to $n = 1$, also called the W state, writes:

$$|W\rangle = |1_N\rangle = |J = N/2, J_z = -N/2 + 1\rangle = \frac{1}{\sqrt{N}} \sum_{k=1}^{N} |0\rangle_{(1)} \otimes |0\rangle_{(2)} \otimes ... \otimes |1\rangle_{(k)} \otimes ... \otimes |0\rangle_{(N)} \tag{I.13}$$

Now we consider N atoms coupled to the cavity mode with equal coupling g and frequency ω_a. This system is described by the Tavis-Cummings Hamiltonian H_{TC} [72], which generalises the Jaynes-Cummings Hamiltonian:

$$H_{TC} = \hbar g\Big(J^- a^\dagger + J^+ a\Big) + \hbar\omega_c a^\dagger a + \hbar\omega_a (J_z + N/2), \tag{I.14}$$

where $J^\pm = \sum_{k=1}^N \sigma_k^\pm$ adds/removes a single excitation in the atomic ensemble, symmetrically. If the initial quantum state is within the symmetric subspace, it will remain in this subspace while evolving under the Hamiltonian H_{TC}. In the particular case where at most one excitation is present in the system, the evolution is restricted to the subspace spanned by states $|0_N, 0_c\rangle, |0_N, 1_c\rangle$ and $|1_N, 0_c\rangle$, which are tensor products of the cavity states $|0_c\rangle, |1_c\rangle$ and of the two first Dicke states $|0_N\rangle$, $|1_N\rangle$. Thus, similarly to the Jaynes-Cummings Hamiltonian, the Tavis-Cummings Hamiltonian can be diagonalised within this further restricted space. The eigenfrequencies are similar to that of equation I.4, except that g has to be replaced by the collective coupling $\Omega = g\sqrt{N}$. Simingly, the open-system derivation of the transmission in intensity T in the low-excitation limit can be done with N atoms, substituting Ω for g in equation I.11, or equally $C_N = N \times C$ for C. In both cases, the ensemble of N atoms behave as one "super-atom" with a coupling strength Ω enhanced by a factor $\sqrt{N}$, as compared to a single atom.

I.1.4 Quantum non-demolition measurement of atomic state

By strongly coupling a single atom to a cavity, it is possible to realise a quantum non-demolition (QND) measurement of the internal state of the atom. Here we describe the scheme to perform such QND measurement, which has been implemented in previous experiments of our group [14, 73]. The measurement distinguishes between the two hyperfine levels

of the ground state of ^{87}Rb, denoted $|0\rangle$ and $|1\rangle$. They are separated by $\omega_{HF}/2\pi \approx 6.8$ GHz. We tune the cavity on resonance with the transition from $|1\rangle$ to an optically excited state $|e\rangle$. The cavity linewidth being $\kappa \approx 14$ MHz, the transition $|0\rangle \rightarrow |e\rangle$ can be neglected, and the atom in state $|0\rangle$ only induces a dispersive shift of the cavity resonance, which is negligible compared to the cavity linewidth. We measure the transmission T in presence of the atom for which we want to determine the hyperfine state, with a weak probe on resonance with both the cavity and the atom ($\Delta_{pc} = \Delta_{pa} = 0$). From equation I.11, we can derive the transmission values T_1 and T_0 for an atom in the strongly coupled $|1\rangle$ and uncoupled $|0\rangle$ states respectively. The ratio of these transmission values writes:

$$\frac{T_1}{T_0} = \frac{1}{(1+2C)^2} \tag{I.15}$$

A single atom strongly coupled to the cavity reduces the transmission by a factor $(1+2C)^2$, compared to the empty cavity, or an atom in the uncoupled state. The higher the cooperativity, the lower the intensity ratio T_1/T_0 and the faster it is possible to collect enough transmitted photons to differentiate $|0\rangle$ and $|1\rangle$, given the experimental uncertainties on T_0 and T_1, which ultimately are limited by the photon shot noise. This noise scales as the $\sqrt{T_{0,1}}$, where T_0 (respectively T_1) denotes the mean value of the Poisson random variable describing the number of transmission photons collected for an empty cavity (respectively a cavity with a single atom). From propagating the uncertainty, we can compute that the noise of the ratio T_1/T_0 scales as:

$$\sqrt{\frac{1}{(1+2C)^2}\Big(1+\frac{1}{(1+2C)^2}\Big).\frac{1}{T_0}} \tag{I.16}$$

This noise should be as small as possible to have a high fidelity in the single atom detection. This requires a large cooperativity C and/or a large T_0 value. T_0 is proportional to both the probe intensity and the probe duration. On the one hand, the probe intensity cannot be made arbitrarily large since this would break the low excitation limit for which expressions I.11 and I.15 are valid. On the other hand, the experimentalists benefit from having a probe duration as small as possible for the detection to be fast. Therefore, it is beneficial to have the largest cooperativity possible, to increase the signal-to-noise ratio of T_1/T_0.

Figure I.2 shows how T_1/T_0 varies with g and C, given our values of κ and γ. In the former CQED experiment of our group, the fiber microcavity was designed such as to reach a very high single atom cooperativity $C = 145$. Thanks to this exceptional value, a fast (100 µs) and high fidelity ($> 99.9\,\%$) QND measurement of the hyperfine state was demonstrated in reference [74].

The transmission measurement constitutes an ideal projective measurement of the atom in the basis $|0\rangle$, $|1\rangle$. For N atoms identically coupled to the field, measuring transmission projects in the basis $|0_N\rangle$, $|0_N\rangle^{\perp}$, where $|0_N\rangle^{\perp}$ is the subspace orthogonal to Dicke state $|0_N\rangle$. It was shown in [14] that this is a quantum non-demolition measurement, meaning that the only backaction of the measurement on the atom is the reduction of coherence inherent to quantum projection. This strongly contrasts with free-space fluorescence measurement of the atomic internal state, where the spontaneous emission associated to the measurement generates an extra backaction on the external degree of freedom of the atom, which forbids

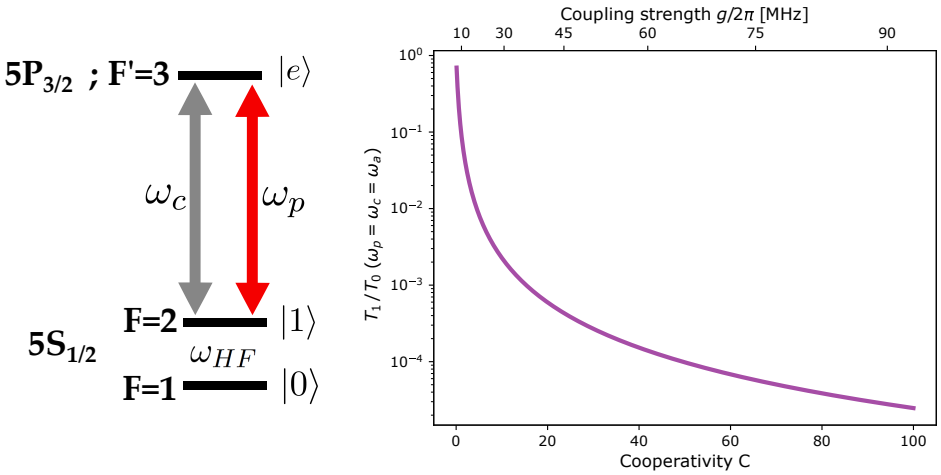

Fig. I.2 *Left: Diagram with the levels of the D_2 line of ^{87}Rb ($5_{1/2} \leftrightarrow 5P_{3/2}$) involved in the QND detection of the hyperfine state. The cavity and the probe are tuned on resonance with the transition from hyperfine state $F = 2$ (denoted $|1\rangle$) to $F' = 3$. The state $|0\rangle$, 6.8 GHz-apart ($\omega_{HF}/2\pi$) is uncoupled to the cavity. Right: Ratio of transmission, T_1/T_0 for a variable coupling strength g (κ and γ are fixed), and a probe on resonance with the atom and the cavity. The other parameters are that of our cavity: $(\kappa, \gamma)/2\pi = (14.2, 3.0)$ MHz. The lower T_1/T_0, the faster one can differentiate the two hyperfines states $|0\rangle$ and $|1\rangle$.*

from repeating indefinitely the measurement. For an atom in state $|1\rangle$ in the cavity, the rate of spontaneous emission is reduced by a factor $1/C$, and thus strong coupling reduces significantly the associated backaction. For an atom in state $|0_N\rangle$, it is far from resonance with the cavity and thus the spontaneous emission as well as its associated backaction are negligible. In the previous CQED experiment of our group[14], the non-demolition measurement of the state of a single atom was set such that, in average, less than 0.2 photons are scattered.

I.1.5 Cavity-based entanglement generation

Such non-demolition projective measurement of the internal state of an atomic ensemble has been central in the schemes implemented in our team to generate multi-atom entangled states: the Dicke state $|W\rangle = |1_N\rangle$ was produced probabilistically by state-projection heralded by cavity transmission [45] as well as with a quantum-Zeno dynamics scheme [46]. In both cases, the Husimi Q distribution, that fully characterises states within the symmetric subspace, was measured with a combination of micro-wave pulses on the transition $|0\rangle \leftrightarrow |1\rangle$ and transmission measurements. Such distribution allowed to certify the entanglement of ~ 10 atoms among ~ 40.

QND measurements of the population imbalance $N_1 - N_0$ in a ensemble of N qubits (where the qubit levels are $|0\rangle$ and $|1\rangle$, as shown in figure I.2) can also be used to generate spin squeezed states. Starting with an uncorrelated "coherent" spin state, prepared on the equator of the generalised Bloch sphere, a measurement of J_z (proportional to the population imbalance) will exert a backaction that reduces (squeezes) the spin noise distribution along the z axis. To implement a measurement sensitive to the population imbalance, the probe

is tuned on the *side* of a resonance: either the cavity peak [75] if the cavity is far from resonance with both transitions $|0\rangle \rightarrow |e\rangle$ and $|1\rangle \rightarrow |e\rangle$, or one of the Rabi peaks [38] if the cavity is close to resonance with one of these transitions. Following the first (respectively the second) option, experiment of reference [75] (respectively [39]) demonstrated spin squeezing providing about 3 dB (respectively 10 dB) reduction of the uncertainty of the quantum phase being measured, as compared to the standard quantum limit achieved with an uncorrelated coherent spin state.

While this QND-measurement protocol generates a spin squeezed state *probabilistically*, one can achieve *unconditional* generation of such a state with a cavity-feedback protocol [42] combining One-Axis Twisting [41] and QND measurement. Such combination was implemented in reference [43]. A few years later, the same combined technique lead to an impressive squeezing of 20 dB, in reference [44].

I.2 Towards optical CQED with multiple strongly coupled atoms

In the previous section, we have introduced the basic theoretical framework for Cavity Quantum ElectroDynamics (CQED) and presented its specific capabilities in the strong coupling regime. Historically in the field of optical CQED, most experiments have worked either with one or two individual atoms, or with indiscernible ensembles of atoms. In this section, we present the architecture of our current CQED experiment, which aims at *scaling up* the number of controllable individual atoms strongly coupled to the cavity (I.2.2). Before that we will present the few experiments that have already worked with several discernible single neutral atoms and individual strong coupling to an optical resonator (I.2.1).

I.2.1 Review of optical CQED with several strongly coupled atoms

I.2.1.1 Single atoms in a conveyor belt

We will start with the two oldest experiments, where one or two single atoms are trapped in separate sites of a red-detuned optical lattice perpendicular to the cavity axis. This lattice is also used to transfer single atoms from the magneto-optical trap to the cavity, according to the single atom "conveyor belt" design proposed in reference [76].

In a former experiment of the group of Dieter Meschede (described in [77]), a cavity with an impressively high finesse (see section I.2.1.3 for a table with characteristics of the experiments presented) is strongly coupled to one or two atom(s) trapped in the conveyor belt. This allows to count how many among the two atoms are in the hyperfine state strongly coupled to the cavity. Based on a Bayesian analysis of the cavity transmission [31] and feedback in the form of hyperfine pump and repump pulses, the two-atom system is stabilised to the mixed state where only one atom is strongly coupled to the cavity [78].

In the “Quantum Information Processing” experiment of the group of Gerhard Rempe, a very high finesse cavity is strongly coupled to one or two atoms trapped in a conveyor belt. With two atoms, the four two-qubit entangled Bell states have been probabilistically prepared with cavity carving [32]. Later, a photon-mediated CNOT gate was operated in the Bell state basis [33]. Both operations rely on the strong reflection of a cavity-resonant single photon at the entrance of the cavity, when at least one atom is in the strongly coupled qubit state.

The results obtained on both setups over the years are truly impressive. However, the conveyor belt optical lattice cannot be loaded from the MOT at predetermined antinodes (which can be achieved by rearranging the atoms in the conveyor belt with another optical lattice, as proposed in reference [79]). This is a limitation for having single atoms at determined positions and thus determined coupling strengths. This strongly contrast with single atoms in individual optical tweezers, which are a convenient means to obtaining single atoms at determined positions.

I.2.1.2 Two atoms in individual tweezers

Here we present two experiments where up to two single atoms manipulated in tweezers are strongly coupled to the cavity.

The earliest reported is the nanophotonic experiment of the group of Mikhail Lukin, where atoms are coupled to the evanescent field of a photonic crystal cavity [80]. They are trapped close to the surface of the resonator, in the lattice formed by a tweezers retro-reflected on this surface. Up to two atoms are strongly coupled to the resonator, thanks to two tweezers, the position of which is tuned with separate galvanometer mirrors. In reference [63], the single atom strong coupling was demonstrated by measuring reflection spectra in both the regimes where the cavity is resonant with and detuned from the atoms. This work illustrates the ability to tune independently the position (and thus the coupling strength) and the transition frequencies (through tweezers lightshift) of each atom. In reference [64], the authors demonstrate the preservation of the single-atom hyperfine coherence and two-atom entanglement correlations upon displacing the tweezers atoms 1 µm away from the resonator. With a resonator enabling strong coupling over a larger distance (currently limited to about 3 µm, changing the galvanometer mirrors for acousto-optics deflectors (AODs) seems the natural next step of the setup, as AOD multi-tweezers operation has been pioneered in this group. It would enable more precise positioning, faster transport of single atoms over longer distances, allowing to combine the nanophotonic cavity with Rydberg operations, far from the dielectric material.

The recent experiment of Dan Stamper Kurn [81] implements of a chain of tweezer single atoms within a more standard Fabry-Perot linear optical cavity. Similarly to the two experiments resorting to a conveyor belt (section I.2.1.1), the chain of atoms is perpendicular to the cavity axis. The tweezers are generated with a 1D AOD, which should allow to obtain deterministically a chain of single atoms, after rearranging the tweezers successfully loaded with single atoms, as in reference [58]. Though it was not implemented yet, such setup can be operated with several atoms simultaneously in the cavity mode, with tunable coupling strengths depending on the tweezers positions. Nevertheless, in both papers relative to this experiment, the ease to steer the tweezers position has been used:

a) A single atom in a tweezers has been used as a probe to map the intra-cavity gaussian standing waves (at 1560 and 781 nm), in reference [65]. The distance to the cavity axis (respectively along the cavity axis) is tuned with the tweezers (respectively a galvanometer mirror). A fluorescence spectroscopy measurement allows to map the light-shift induced by the intra-cavity field in a superresolved manner.

b) Two tweezer atoms are successively moved in and out of the cavity mode for individual

hyperfine state measurement. It is shown in reference [66] that the measurement of one atom does not perturb the hyperfine state coherence of the second atom, in the context of "mid-circuit" measurements.

This platform should allow to couple several atoms to the cavity, while keeping others uncoupled, and tune individual coupling strengths to a certain extent.

However, both experiments have limitations that prevent from scaling up the number of simultanously strongly coupled atoms. In the Lukin experiment, the coupling varies very significantly along the cavity axis, and is sufficiently high over a range of typically 3 µm. It seems hard to fit a third tweezer within such a small range, and the coupling of all three atoms would not be homogeneous. In the Stamper-Kurn experiment, similar difficulties come from having the tweezer array perpendicular to the cavity. The maximal number of single atoms that can be strongly coupled is limited by the waist size of the cavity mode, which has been made small to reach strong coupling[1].

I.2.1.3 Strong and homogeneous coupling of more than two single atoms

To strongly and homogeneously couple many atoms in a linear Fabry-Perot cavity, one solution is to have an array of single atoms along the cavity axis, trapped at the antinodes of the probe standing wave. To our knowledge, the experiment of the group of Tiancai Zhang is the first to have achieved this goal, a few months ago [67]. A 1D AOD generates 11 tweezers in which up to 8 atoms are loaded and equally and maximally coupled to cavity. The vacuum Rabi splitting 2Ω is measured for all atom numbers up to $N = 8$, exhibiting the expected collective enhancement of the coupling $\Omega = g\sqrt{N}$. To help localising the thermal atom trapped in a tweezers close to an antinode of the intracavity probe standing wave (852 nm), a blue detuned intra-cavity lattice trap (820.9 nm) is added to the tweezers trap. As both standing waves are not commensurate, their beating pattern leads the maximal-coupling lattice sites to be separated by ≈ 11 µm. The 11 tweezers span a distance of ≈ 110 µm. The length of the cavity (≈ 1.3 mm) is not the main limitation to producing more tweezers, and we would guess that the field of view of the high numerical aperture lens would be the first to limit the authors to achieving more tweezers, if not the range of tweezers positions accessible in the focal plane of the objective, which depends on the exact optical layout between the AOD and the high-NA lens.

To finish and supplement this review, the table below gives a few caracteristics of the aforementioned CQED experiments. F, w_{cav}, C_{max}, L, N_{max} stand respectively for the finesse, the cavity mode waist, the maximal cooperativity, the cavity length and the maximal number of atoms involved in the experiments reported. $\perp$ (respectively $\parallel$) refers to chain of atoms (eventually only two atoms) perpendicular (respectively parallel) to the cavity axis. "Twz. arr." stands for tweezer array. The last line corresponds to our experiment. Our cavity will be presented in chapter II. Our N_{max} value corresponds to the preliminary results of section VI.7. As we will see, $N_{max} = 20$ is a very reasonable estimate of what we could

[1] For instance, if we require the coupling of all atoms to be $\geq 90\,\%$ of the on-axis maximal value, we find that the tweezers should be at a distance ≤ 8 µm from the cavity axis, given the cavity waist $w_{cav} = 24$ µm. For a standard $2.5 - 3$ µm distance between adjacent tweezers, at most 7 single atoms could be fitted.

achieve, with the already available setup.

Group	Cavity				Atom		
	F	w_{cav}	C_{max}	L	Species	Trap	N_{max}
		µm		µm			
Meschede	10^6	23	$30-80$	159	^{133}Cs	Lattice ($\perp$)	2
Rempe	6×10^5	29	4.1	485	^{87}Rb	Lattice ($\perp$)	2
Lukin	Info. unavailable		67	3	^{87}Rb	2 tweez. ($\parallel$)	2
Stamper-Kurn	1.5×10^4	24	2.3	9400	^{87}Rb	Twz. arr. ($\perp$)	2
Zhang	5.7×10^4	46	1.9	1270	^{133}Cs	Twz. arr. ($\parallel$)	8-9
Long (our exp.)	3.6×10^4	5.7	75	145	^{87}Rb	Twz. arr. ($\parallel$)	4-5

I.2.2 Our way to strongly coupling many single atoms to an optical cavity

We will now present our current CQED experiment, which has been designed to achieve strong and homogeneous coupling along the entire length of the cavity mode. For this purpose, we use an intra-cavity lattice trap commensurate with the probe trap. More specifically, we probe our ^{87}Rb atoms on the $D2$ line at $\lambda_1 = 780$ nm and we choose the lattice trap wavelength λ_2 to be twice that of the probe ($\lambda_2 \approx 2\lambda_1 = 1560$ nm). The same wavelength configuration has been used in other ^{87}Rb CQED experiments [65, 82–84] with macroscopic cavities. However none have reached the regime with several *individual* atoms in separate lattice sites. Together with engineering of the relative phase between the two lattices (explained in section II.2.1), this commensurability ($\lambda_2 \approx 2\lambda_1$) results in having each trapping site centered on a probe antinode, where the coupling is maximal. Thus atoms trapped along the entire length of the cavity are maximally *and* homogenously coupled to the probe field, as illustrated on picture a. of figure I.3. As compared to the non-commensurate standing-wave combination of the Zhang experiment, our configuration allows to trap one atom every 2 probe antinodes, instead of 26 in reference [67], a significant density improvement that should allow to couple a hundred of single atoms to the cavity, for a fully loaded intra-cavity lattice (which requires loading the lattice with a tweezer array in several steps). We combine this cavity design with tweezer arrays generated by two acousto-optic deflectors systems:

1) A 1D AOD is used to generate a 1D tweezer array along the z axis, parallel to the cavity axis, at a distance such that single atoms in this array do not couple to the cavity fields (see pictures b,c and d of figure I.3). This array is meant to store single atom qubits, while operations are done with other qubits, inside the cavity. This is why we call it the qubit "storage register".

2) A 2D AOD can generate 2D tweezer array in the x,z plane, inside the cavity mode as well as far away (picture b.). It can be used to transfer one (picture c) or several (picture d) qubits from the storage register to the cavity, and reciprocally.

This cavity-tweezers design allows for:

a) collective and symmetric multi-qubit operations, thanks to the commensurability of the intra-cavity fields: QND state measurement (see section I.1.4), cavity-mediated

interactions and entanglement generation (see section I.1.5). The resulting (possibly entangled) states will be *spatially distributed* over the entire cavity length, which is a major asset.

b) single atom resolution addressing and detection (either with single atom resolved fluorescence, or with the cavity).

The tweezers will allow to 1) selectively couple atoms to the cavity, 2) tune their position and thus their coupling strength, and 3) control their qubit frequency through tweezers lightshifts, so as to tune the atoms in and out of resonance with the cavity or with qubit-rotation microwave pulses. We emphasize that with this *dual*-AOD setup we will be able to perform cavity collective or single operations selectively on any subpart of the array of qubits. Thus, non-symmetric multiparticle entangled states can be produced. Together with the ability to generate spatially distributed *and* single-particle-addressable entangled states, our platform opens new perspectives in the field of multiparameter quantum metrology and quantum simulation (see section VII.2).

I.3 Cavity protected coherence for a collectively strong coupled atomic ensemble

In the previous section, we have described the line along which our new experimental setup has been designed. As few other CQED experiments of this new generation, it combines the abilities of strong coupling CQED with the exquisite individual atom control of tweezer arrays. On the path towards this objective, a first step has consisted in verifying the ability to strongly couple an *ensemble* of atoms to the cavity mode, which has been done by measuring the collective vacuum Rabi splitting of the ensemble. Such measurement, performed by weakly probing the coupled system, accounts for the coherent exchange of a single energy quantum between the atomic ensemble and the cavity field. Due to a large differential lightshift, the intra-cavity lattice used to trap the atomic ensemble induces a very large inhomogeneity in atomic frequency in the thermal ensemble, that exceeds by more than an order of magnitude the spectral widths of the cavity and of a single atom. However, in spite of this inhomogeneity, the atomic ensemble interacts coherently with the cavity field. In the spectral domain, this results in polaritonic resonances much narrower than the width of the distribution. This effect, theoretically predicted in [47–49], has been called "cavity protection" in reference [49], and we will use this denomination as well.

Cavity protection is the effect by which an ensemble of emitters inhomogeneous in frequency can interact coherently with a cavity field, if its collective coupling to the cavity is strong enough and under certain conditions on the shape of the frequency distribution. This section is devoted to introducing cavity protection. First we treat the case of N emitters with equal frequency (I.3.1). Then we switch to the case of N emitters with an inhomogeneous frequency distribution I.3.2, introducing the key concepts of the cavity protection effect. Finally, we present the previous experimental demonstrations of the cavity protection I.3.3).

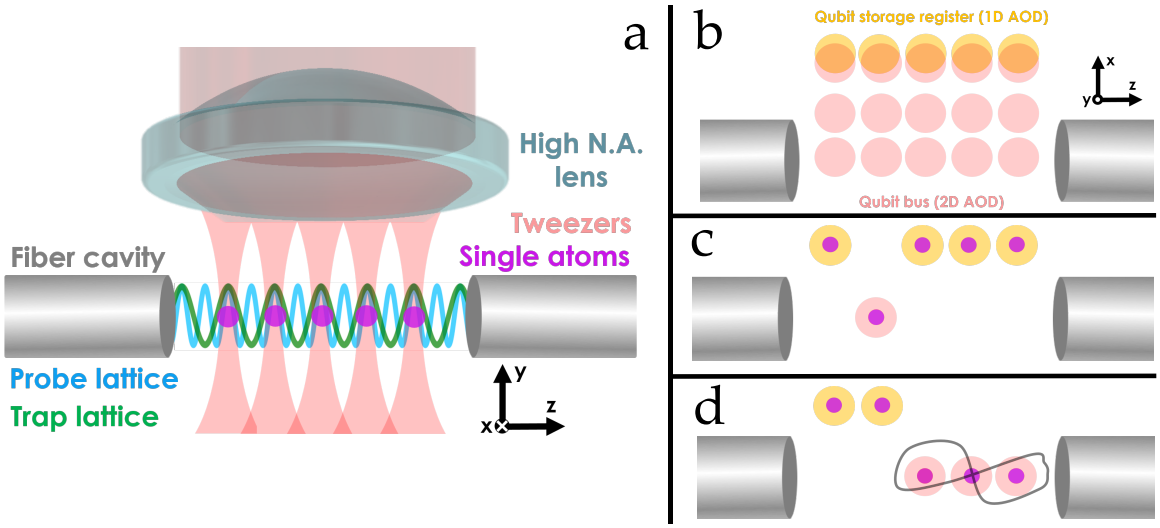

Fig. I.3 *Schematics of our optical CQED setup (not at scale). Picture a: the fiber-cavity sustains two commensurate intra-cavity lattices: the probe lattice at* 780 nm *and the trap lattice at* $\approx$ 1560 nm*. The intensity of both fields is plotted in between the two fibers. Thanks to the commensurability,* ^{87}Rb *atoms trapped at antinodes of the red-detuned trap lattice (in green) are located at antinodes of the probing field (in blue). Thus atoms trapped along the entire length of the cavity are equally and maximally coupled to the probe. Picture b, c and d show the abilities of our dual-AOD system (please notice the different reference frame). A 1D AOD is used to generate a static tweezer array (light orange), far from the cavity mode. In this "qubit storage register", atoms are stored and uncoupled to the cavity. Meanwhile, the cavity can be used to perform operations on other qubits, held in the tweezers generated from a separate 2D AOD (light red): for instance single qubit state detection (picture c) or entanglement generation among several chosen qubits (picture d). The 2D AOD or "qubit bus", allows to move one or multiple atom qubit(s) from the storage register to the cavity and vice versa.*

I.3.1 Frequency-homogeneous emitters

We start by describing the homogeneous case, where all atoms have the same frequency. For a cavity mode resonant with the atomic line in the strong coupling regime, the spectrum exhibits the well-known vacuum Rabi splitting (see figure I.1) featuring two peaks $2g\sqrt{N}$ apart in frequency, where N is the atom number, and their width is given by $(\kappa+\gamma)/2$ [85]. They correspond to the eigenstates of the coupled system with highest and lowest frequency, the polaritons:

$$|P_\pm\rangle = \frac{1}{\sqrt{2}}\left(|1,G\rangle \pm |0,W\rangle\right), \tag{I.17}$$

where $|1,G\rangle$ is the state with one photon in the cavity mode and all atoms in the ground state and $|0,W\rangle$ is a state with no photon in the cavity mode and one excitation symmetrically shared between the atoms: $|W\rangle = 1/\sqrt{N}.\left(\sum_{k=1}^{N}\sigma_k^+\right)|G\rangle$, σ_k^+ being the raising operator for atom k. The $N-1$ remaining states are degenerate and do not couple to the

cavity light field. This is reflected in the photonic weight (PW), which is defined by the overlap of the eigenstates of the coupled system $|\psi_\alpha\rangle$ with $|1,G\rangle$, $PW = |\langle G,1|\psi_\alpha\rangle|^2$ [86], and is zero for all eigenstates except $|P_\pm\rangle$. Thus these $N-1$ eigenstates are called the *dark* states.

The case of N atoms with different coupling strengths g_k does not change the previous result, except that:

1) the splitting is now given by 2Ω, where $\Omega = \sqrt{\sum_{k=1}^{N} g_k^2}$ is the collective coupling

2) $|W\rangle$ is redefined as $|W\rangle = \left(\sum_{k=1}^{N} \frac{g_k}{\Omega}\sigma_k^+\right)|G\rangle$

I.3.2 Cavity protection with frequency-inhomogeneous emitters

Now we consider the case of an ensemble of N emitters with an inhomogeneous frequency distribution, coupled to a cavity mode. Reference [47] was the first to study the coherence in such interacting system, reflected by the features of the Rabi splitting in the absorption spectrum, corresponding to Rabi oscillations in the temporal domain. There are two main conclusions to this work:

1) For a gaussian distribution of emitter frequency, the coherence is preserved and a Rabi splitting is visible if the collective coupling $\Omega = \sqrt{\sum_{k=0}^{k=N} g_k^2}$ (g_k is the coupling strength of emitter k) is large enough compared to the width Δ of the frequency distribution. For $\Omega \gg \Delta$, the width of the Rabi peaks is $(\kappa+\gamma)/2$, the same value as for a frequency-homogeneous system. This means that the coherence of the frequency-inhomogeneous system is the same as for an homogenous system, which is the essence of cavity protection. Temporally, the system exhibits Rabi oscillations, that decays with the same rate as in the homogeneous system.

2) When the collective coupling is strong enough for the system to exhibit a Rabi splitting, the splitting is in good approximation 2Ω and does not depend on the type of frequency broadening: it is the same for homogeneous or inhomogenous broadenings. This reflects that, for an inhomogeneous distribution much larger than the cavity linewidth, not only the emitters close to resonance with the cavity interact with the cavity mode. Instead, all emitters collectively interact with the cavity.

Fifteen years later, references [48, 49] extended the formalism and exhibited a supplementary requirement for the coherence of such coupled system to be preserved. In the case of an unbounded continuous distribution of frequency, the corresponding density $\rho(\omega)$ should decay asymptotically faster than $1/\omega^2$. If this condition is satisfied, then the coherence is preserved when the collective coupling is strong enough.

Figure 2 in reference [49] shows the transmission of the coupled system, for a lorentzian, a gaussian and a rectangular distribution of emitter frequency (left, middle and right plot respectively). In all 3 cases, when the collective coupling Ω is large enough compared to the width of the distribution Δ, the spectrum exhibits a Rabi splitting that, to first order in Δ/Ω, is equal to 2Ω and does not depend on the size Δ of the distribution, nor on its shape. However, the width of the transmission peaks, which reflects the coherence of the interaction, depends on the particular shape of the frequency distribution. For a gaussian distribution,

that decays faster than $1/\omega^2$ (such that cavity protection *may* take place), the width of the peaks decreases as Ω/Δ increases and converges towards $(\kappa+\gamma)/2$, the homogeneous-case value. The inhomogeneous system is cavity-protected and behaves as an homogeneous system when the collective coupling is sufficiently large. For a lorentzian distribution, which decays exactly as $1/\omega^2$, there is no cavity protection effect. In the coupling regime where the Rabi splitting exists, the width of the peaks is constant and equal to Δ. So the coherent interaction is always limited by the width of the distribution, unlike the gaussian case.

The square distribution illustrates the case of a bounded distribution. As $\rho(\omega)=0$ outside of the distribution support, a bounded distribution always exhibits cavity protection for sufficiently strong coupling. Compared to the unbounded gaussian case, one small difference is that the degree of coherence of the homogeneous case is reached for finite value of Ω, rather than asymptotically. This is clearly visible on the picture c. (Figure 2 in reference [49]), where the width of the peaks is small very soon after the onset of Rabi splitting. This contrasts with picture b. (gaussian distribution) where the peaks get thiner as the coupling increases.

Figure 4 in reference [49] illustrates the coherence achieved with these 3 distributions in the temporal domain. It shows the probability, for a coupled system initially in the upper polariton $|P_+\rangle$ (see section I.3.1), that the system is in state $|P_+\rangle$ as a function of time. In the frequency-homogeneous case, this probability would be constantly equal to 1, as $|P_+\rangle$ is an eigenstate of the frequency-homogeneous hamiltonian. In the frequency-inhomogeneous case, this is no longer exactly true: all eigenstates of the frequency-inhomogeneous hamiltonian may have a small component of $|P_+\rangle$, and thus of cavity excitation $|1,G\rangle$. Because of this component, all eigenstates may couple to the cavity and thus the excitation may decay in the subspace of the $N-1$ remaining states. This contamination vanishes as Ω/Δ increase, and, in the limit of $\Omega \gg \Delta$, the upper and lower eigenstates of the frequency-inhomogeneous hamiltonian converge towards the polaritons $|P_\pm\rangle$. As the $N-1$ other eigenstates do not couple to the cavity for infinite coupling, we will call them *dark states* in this manuscript.

For the gaussian distribution (middle plot), with a strong collective coupling $\Omega = 4\Delta$ (blue solid line), the system exhibits cavity protection, and this probability remains close to 1. It means that Rabi oscillations are not limited by the inhomogeneous frequency distribution, and that the coherence time is that of the homogeneous system. Conversely, with a moderate collective coupling $\Omega = \Delta$ (red dashed line), this probability decreases, which reflects the limited coherence in the cavity-*unprotected* regime and the corresponding decay of the excitation in the dark states. For a lorentzian distribution (left plot), where cavity protection never takes place, the excitation decays in such states, no matter the relative strength of the collective coupling, Ω/Δ.

I.3.3 Previous experimental demonstrations of cavity protection

After being theoretically predicted in references [47–49], cavity protection has been experimentally demonstrated in several solid state experiments [50–52], prior to our work. We briefly present these experiments in this section.

In reference [50] nitrogen-vacancy centers are coupled to a superconducting waveguide resonator, cooled down to 25 mK. It operates in the micro-wave regime, at a frequency of

$\approx$ 2.7 GHz, thus allowing for a temporal analysis of the dynamics of the coupled system. From the response of this system to a weak and long microwave-pulse, both the collective coupling Ω and total decay rate Γ are measured (Figure 2.b. in [50]). Figure 3 in [50] displays Γ against Ω. The black squares, corresponding to the experimental values, are plotted together with the results of several calculations. This graph shows that:

a) In the regime of low collective coupling, Γ increases as a function of Ω, which can be understood as a Purcell effect induced by the increasing coupling of the cavity to the ensemble of emitters.

b) For a sufficiently high collective coupling, Γ starts decreasing, due to the cavity protection effect. Indeed, the distribution of emitter frequency follows a q-Gaussian distribution (a combination of Gaussian and Lorentzian) that decays faster than $1/\omega^2$, and is thus eligible for cavity protection.

The green line shows the prediction for a fictitious Lorentzian distribution, where cavity protection does not occur. In this case, Γ has a constant value dictated by the width of the distribution, which contrasts with the experimental results. However, one can notice that the minimal value experimentally achieved for Γ is rather high ($\Gamma/2\pi = 3$ MHz), compared to the theoretical minimum achievable value $\Gamma/2\pi = \kappa/2 \approx 0.4$ MHz, which would require a stronger collective coupling Ω, as the calculations show.

In reference [52] pentacene molecules are coupled at room temperature to a strontium titanate dielectric resonator, operating in the micro-wave domain as well, at a frequency of $\approx$ 1.5 GHz. A population inversion of the corresponding transition in the molecules is obtained by photo-excitation at 592 nm. Figure 2.a in reference [52] shows the micro-wave response after a nanosecond light pulse, and Figure 2.c the corresponding spectrum. Similarly to the previous experiment, Ω and Γ are extracted from such measurements and plotted on picture e. The curve exhibits the same behavior as in [50]. As it extends further in the strong collective coupling regime, it allows to see the convergence of Γ towards half the width of the cavity, $\kappa_c/2$ (the single molecule homogeneous linewidth contribution to Γ, $\gamma/2$, is here negligible). This illustrates that the width of the inhomogeneous distribution (κ_s) does not contribute to the polaritons, in the cavity-protected regime. Unfortunately here κ_c/ and κ_s have the same order of magnitude, so cavity-protection brings little improvement compared to a cavity-unprotected Lorentzian distribution of same witdh (upper horizontal line on picture e).

In reference [51], an ensemble of rare-earth ions (neodymium) in a crystal is coupled to a nanophotonic resonator, cooled down to 3.6 K. Unlike the two other experiments, here the emitter-cavity interaction is in the optical domain, and is thus analysed through cavity transmission spectra such as shown on Figure 2.e in reference [51]. A slightly different protocol is followed: rather than varying the collective coupling, the authors measure spectra for variable cavity-emitter detuning (Figure 2.d in reference [51]). From individual spectra, Γ is extracted, and plotted against the detuning, in Figure 2.f of reference [51]. For a cavity on resonance with the ions, the width of the peak is that of the homogeneous system, $(\kappa+\gamma_h)/2$ (where γ_h denotes the homogeneous width of a single ion), 40,% lower the width expected for a cavity-unprotected Lorentzian distribution, $(\kappa + \gamma_h)/2 + \Delta$ (green line).

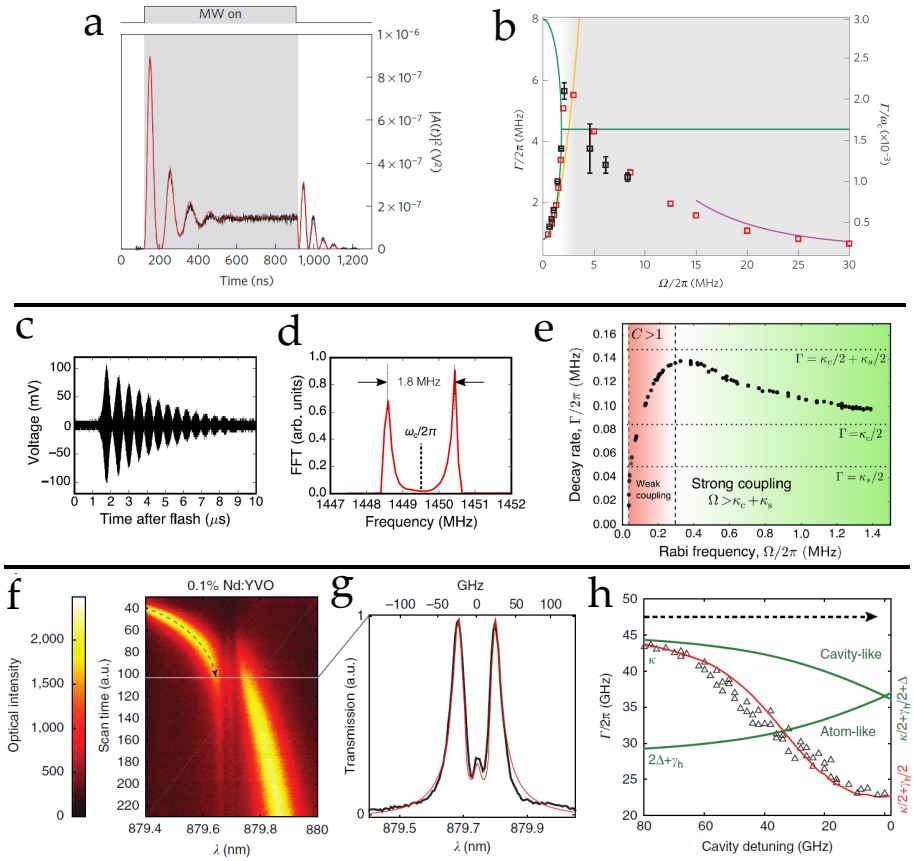

Fig. I.4 *Previous experimental demonstrations of the cavity protection effect in both the temporal domain, with microwave resonators in references [50] (pictures a. and b.) and [52] (pictures c, d and e) and in the spectral domain, with an optical resonator in reference [51]. In all 3 experiments (pictures b, e and g) it is shown that when the collective coupling to the cavity is high enough, the width of the polaritons is independent of the width of the inhomogeneous distribution of emitter frequency, enabling coherent exchange of energy between the cavity and the inhomogeneous ensemble.*

I.3.4 Our specificities regarding cavity protection

Now that we have presented earlier experimental demonstrations of the cavity protection effect, we would like to highlight the differences of our experimental setup regarding this effect, to emphasize the interest of our study:

1) In our optical micro-cavity, the single atom cooperativity is orders of magnitude higher than in the experiments reported hereinabove. Because of that, we will see later that we observe cavity protection for as few as 200 emitters, orders of magnitude lower than for the previous experiments (III.2). Due to this number downscaling, our spectra are sensitive to the discrete sampling of our inhomogeneous frequency distribution (IV.1), which is not the case in the previous experiments. Thus, we do not describe our coupled-system transmission spectra in terms of a continuous distribution, which

contrasts with all the previous experiments. This fundamental discretness of our emitter ensemble will lead us to propose new quantities to account for the emergence of coherence (IV.2 and IV.3), as Ω/Δ increases.

2) The high degree of control of our cold-atom setup allows to tune very conveniently the parameter Ω/Δ, which determines the degree of coherence of the coupled system. Ω, which scales as $\sqrt{N}$, can be tuned by varying the number of atoms N trapped in the cavity. This contrasts with the complex procedures used in references [50–52] to effectively couple a variable fraction of the fixed number of emitters in the solid state devices. Another major difference of our setup is the ability to tune the width Δ of the frequency distribution, by simply varying the intensity of the intra-cavity trap lattice, which induces the inhomogeneity (III.1.1).

3) In our experiment, the width Δ of the frequency distribution is about 10 times larger than the homogeneous-polariton width $(\kappa+\gamma)/2$. Thus, compared to the Lorentzian unprotected width $(\kappa+\gamma+\Delta)/2)$, we should expect cavity-protected polaritonic width roughly 10 times smaller. This theoretical maximal reduction is more favorable than in references [51, 52], and similar to that of reference [50]. It should be much easier for our cold-atom setup to tune the collective coupling Ω so as to go further in the cavity protected regime, compared to [50].

Simultaneously to our investigation of cavity protection, another cold-atom experiment reported a study of similar effects [54], with a complementary perspective. The authors of [54] benefited similarly from the advantages mentioned above, inherent to cold-atom setups. As we will show in chapter IV, both experiments bring new insight in the progressive emergence of cavity protection, as the collective coupling becomes larger than the frequency disorder.

I.4 Conclusion

Cavity Quantum Electrodynamics is the field that studies the coherent interaction between a mode of the electromagnetic field (isolated by means of a resonator) and one or multiple atoms. In the strong coupling regime, this interaction is faster than the loss processes. This has many powerful pratical applications, such as fast and high fidelity Quantum Non Demolition measurement of the atomic state and generation of entangled states.

Tweezer arrays are convenient to obtain and manipulate individual atoms. Our experiment is part of this new generation of CQED experiments where strong coupling capabilities are combined with the high degree of single atom control of tweezer arrays.

In our experiment, the strong coupling microcavity has a trapping lattice commensurate to the probing lattice, so that atoms trapped in the lattice are both strongly and homogeneously coupled to the probe field. We combine the cavity with two acousto-optic deflectors so as to perform CQED operations on any subpart of a1D array of single qubits. Meanwhile remaining qubits are held in a storage register, far from the cavity mode. This opens new perspectives in generating non-symmetric entangled states, spatially-distributed and locally-addressable/detectable entanglement for multiparameter quantum metrology and quantum simulation in all-to-all coupled spin ensembles (more details will be given in the outlook,

VII.2). In particular, we would like to simulate coherent energy transport in these spin ensembles, in presence of a controllable disorder. It is predicted that dark states play a role in enhancing transport efficiency, which exhibits surprising features. Interestingly, dark states are also at the core of the dynamics of cavity protection, which we study in the first part of this manuscript, thanks to the controllable inhomogeneity of our atomic ensemble.

Chapter II

A setup for cavity quantum eletrodynamics with an array of single atoms

This chapter describes the status of our experimental apparatus during the first half of my PhD, with which we obtained the results presented in chapters III and IV. The core of our setup is a high-finesse fiber-based Fabry Perot microcavity, micro-machined with a technique developed in our team in the years 2005-2015. It enables strong coupling regime at the single atom level, together with homogeneity of this coupling along the cavity axis. Its design, fabrication and stabilisation are described in section II.2. It operates with cold ^{87}Rb atoms. The generation of the cold sample of atoms in a magneto-optical-trap and its transport into the microcavity are discussed in section II.1. Finally, in section II.3 we present the ajustment of the polarisations of the cavity fields, the preparation of the atomic ensemble in a specific Zeeman sublevel and the measurement of the transmission spectrum of the cavity-atoms coupled system, which prooves that we operate in the strong coupling regime. Most of this setup has been built by previous PhD students: Sébastien Garcia, Claire Lebouteiller, Francesco Ferri and Mohamed Baghdad. Thus more technical details can be found in their thesis manuscripts [87–90].

II.1 Cooling and transporting a cloud of atoms into the microcavity

II.1.1 Cooling laser system

The first step of our experiment cycle is the preparation of a sample of cold ^{87}Rb atoms, using a magneto-optical trap (MOT) on the D_2 line ($5^2S_{1/2} \leftrightarrow 5^2P3/2$, see the level diagramm in appendix **??**). Starting with a 2D MOT, we produce a beam of cold atoms, with which we load a 3D MOT.

Figure II.1 shows a schematic of the laser system that we use for these operations. The first laser is a 1560 nm external-cavity laser with a linewidth below 10 kHz. It is frequency doubled in a periodically-poled lithium niobate (PPLN) crystal. The resulting 780 nm light injects a slave laser diode. Part of the slave light is sent in a Rubidium cell, where we imple-

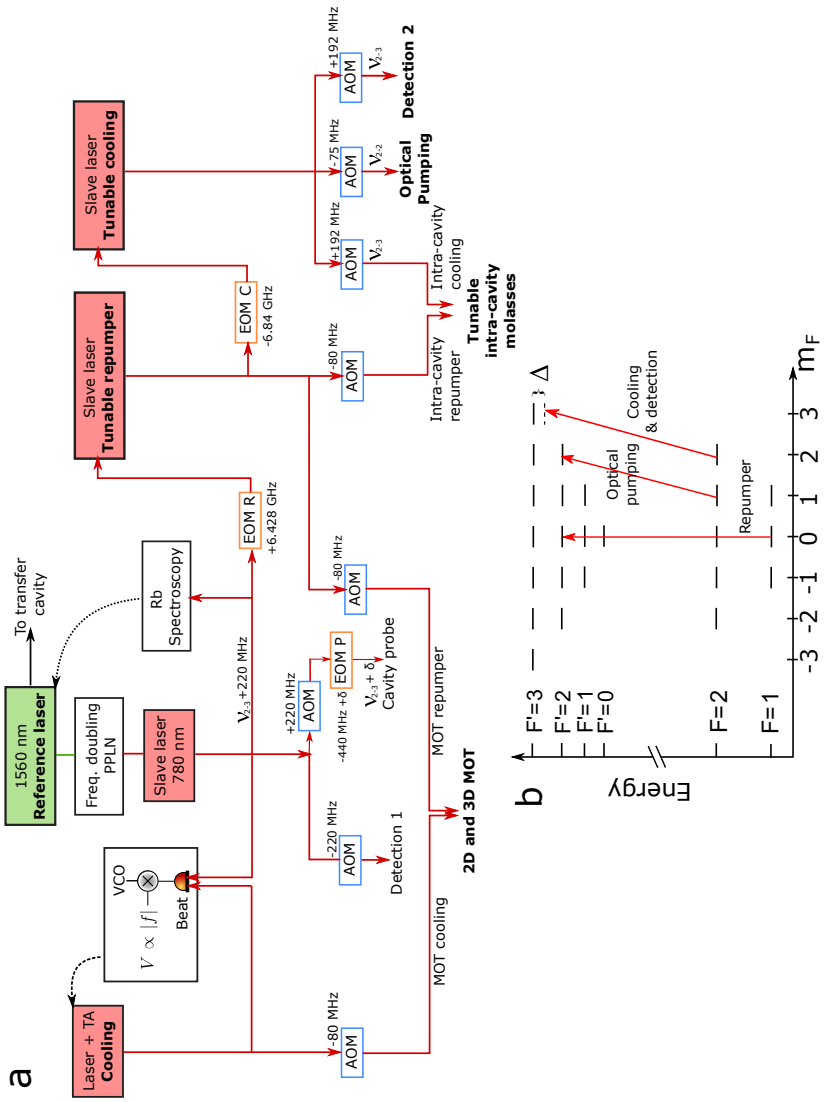

Fig. II.1 *Picture a: Schematic of the laser system used for cooling, repumping, pumping and absorption imaging of the atoms. Picture b: level diagramm of the D_2 line of ^{87}Rb, with the useful transitions. Figure adapted from Francesco Ferri PhD thesis [89].*

ment a modulation transfer spectroscopy scheme [91, 92]. The resulting error signal is used as a feedback on the 1560 nm reference laser current. The 780 nm slave light, frequency-stabilised close to the σ_+ cycling transition ($F = 2, m_F = 2 \leftrightarrow F' = 3, m'_F = 3$) is split and used for 4 purposes: frequency-locking the cooling laser of the MOTs, injecting the repumper slave laser, absorption imaging (along "Detection 1" path - see figure II.4) and probing of the cavity.

For the cooling light of the 2D and 3D MOTs we need intensities on the order of the saturation intensity ($I_{sat} = 1.6$ mW/cm^2 for the σ_+ cycling transition) with centimetric beams. Thus we seed a 1W tapered amplifier (TA) with an external-cavity laser (at 780 nm). The seeding laser is frequency-locked to the reference, by measuring the beatnote of the superposition of both lasers. The beatnote is mixed with the output of a voltage-controlled oscillator (VCO), such that the MOT cooling laser can be frequency-stabilised over a range of ≈ 100 MHz, depending on the VCO frequency. Thus we can shift the laser from the MOT to the molasses detuning ($-\Gamma$ to $-10\,\Gamma$ typically), in a few ms.

For the repumper light ($F = 1 \rightarrow F' = 2$) of the 2D and 3D MOTs, we use ≈ 10 times less power, so a laser diode alone is enough. We inject this slave laser with the 780 nm reference laser, frequency-modulated by an electro-optic modulator (EOM R on figureII.1) at 6.428 GHz. We tune the slave laser current and temperature to inject it on the +1 sideband, which is close to the repumping transition. This particular way of generating the repumping light allows quick tuning of its frequency over a range of 1.5 GHz. This choice was done to repump atoms not only in the MOTs, but also in the intracavity lattice at 1559 nm. Indeed this lattice induce significant differential lightshifts of the D_2 transitions (typically several hundreds of MHz - see section III.1.1), which we wanted to compensate.

For the same reason, the intracavity cooling light was also designed to be frequency-tunable over a similar range. We use a fraction of the repumper light to inject another slave laser, after being frequency-modulated by EOM C (see figure II.1) at 6.840 GHz. The -1 sideband sets the slave frequency close to the cooling transition. Apart from intracavity cooling, this light is used for optical pumping to the Zeeman sublevel $F = 2, m_F = 2$ and (tunable) detection of the atoms with absorption imaging (detection beams 2 and 3, see figure II.4).

II.1.2 Vacuum chamber geometry

Using these lasers, we cool the ^{87}Rb atoms with the combination of a 2D and a 3D MOT. Our vacuum apparatus consists of two glass cells, one for each MOT:

1) The lower glass cell contains a dispenser that emits ^{87}Rb atoms continuously. The atoms are cooled in the horizontal plane by the 2D MOT. It consists of a single laser beam, folded and reflected such as to provide the two horizontal contrapropagating beam couples (see figure II.2) and a magnetic field gradient of 15 G/cm. The cooling beam is elliptical along the vertical axis, it has 70 mW power, ≈ 18 mW/cm^2 intensity, and is detuned by $-2.5\,\Gamma$ with respect to the cooling transition. Before elliptical beam shaping, a 5 mW of this light is sent towards a 45° at the bottom of the glass cell, which reflects it upwards towards the upper glass cell. This beam pushes the atoms from the 2D MOT to the upper

glass cell, through a hole with a 1.5 mm diameter.

2) The upper glass cell (also called science chamber) contains the fiber cavity, in the focal plane of a high numerical aperture lens. In this glass cell, we operate a 3D MOT, the geometry of which is shown in figure II.3. Its beams have a waist of 7 mm and an intensity of 2 mW/cm^2. We use 3 pairs of coils in Helmoltz configuration to apply a compensating/bias magnetic field and a pair coils in anti-Helmoltz configuration to apply a gradient of 15 G/cm (along the z direction - see figure II.3). Please note that our 3D MOT is not inside the microcavity, because large beams required for an efficient loading of the MOT would not fit in the cavity, which has a length of $L = 145$ µm. Thus the 3D MOT is located 12 mm below the fiber-cavity, and the atoms are transported from the MOT to the cavity with a dipole trap, as explained in section II.1.4.

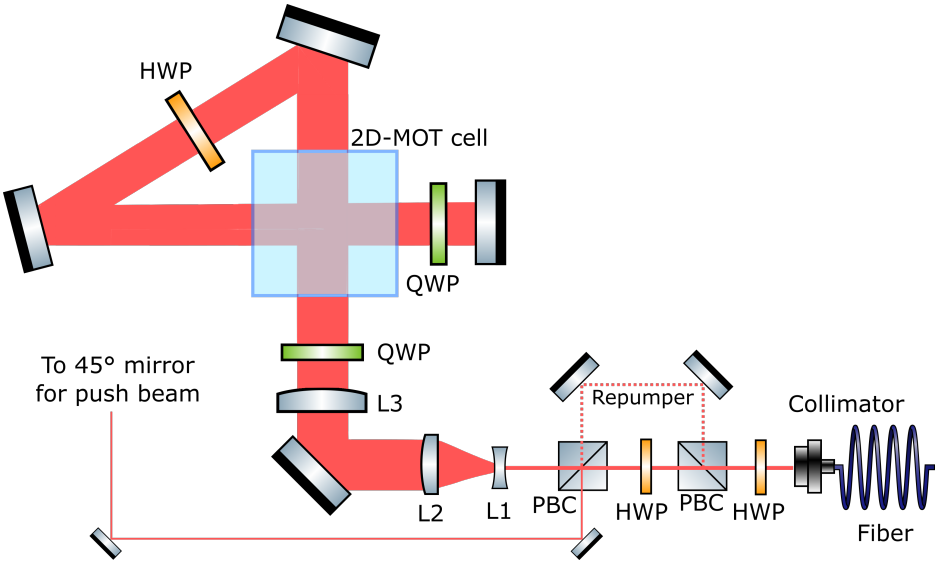

Fig. II.2 *Optical layout for the 2D MOT and the push beam. The blue square represents the lower glass-cell, where the 2D MOT atomic beam is produced. The "push beam" pushes the atomic beam upwards, towards the upper glass-cell (science chamber), where the 3D MOT is operated. Figure from Francesco Ferri PhD thesis [89].*

II.1.3 Absorption imaging detection

To detect clouds of atoms, we have 3 paths for absorption imaging (see figure II.4): "Detection 1" is at the height of the 3D MOT. It has a rather low magnification. "Detection 2" and "Detection 3" are used for imaging inside the cavity mode, 12 mm above the 3D MOT. Their magnification is higher, because the intracavity cloud is much smaller than the MOT. We use absorption imaging a) to check the required beam/cloud superposition of consecutive steps in our experimental sequence (which we describe in section II.1.4) and b) to measure temperature with the time-of-flight technique.

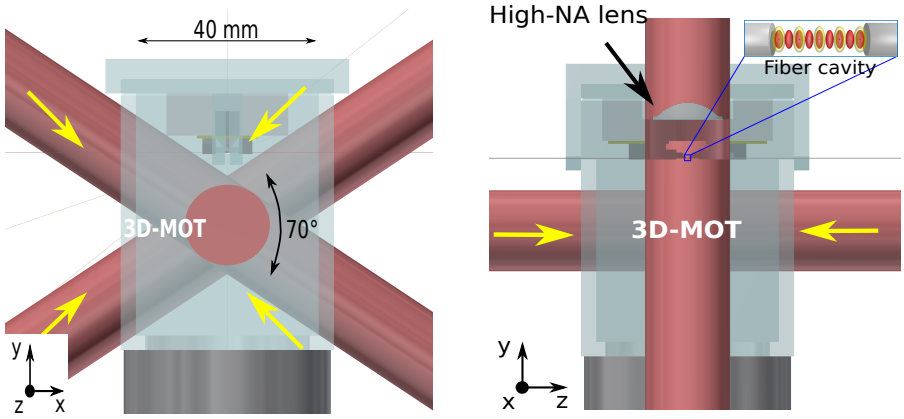

Fig. II.3 *Schematic of the science chamber. A Macor bridge holds the fiber-cavity and the high NA lens. 3D MOT beams cross* 12 mm *below the cavity. Figure from Francesco Ferri PhD thesis [89].*

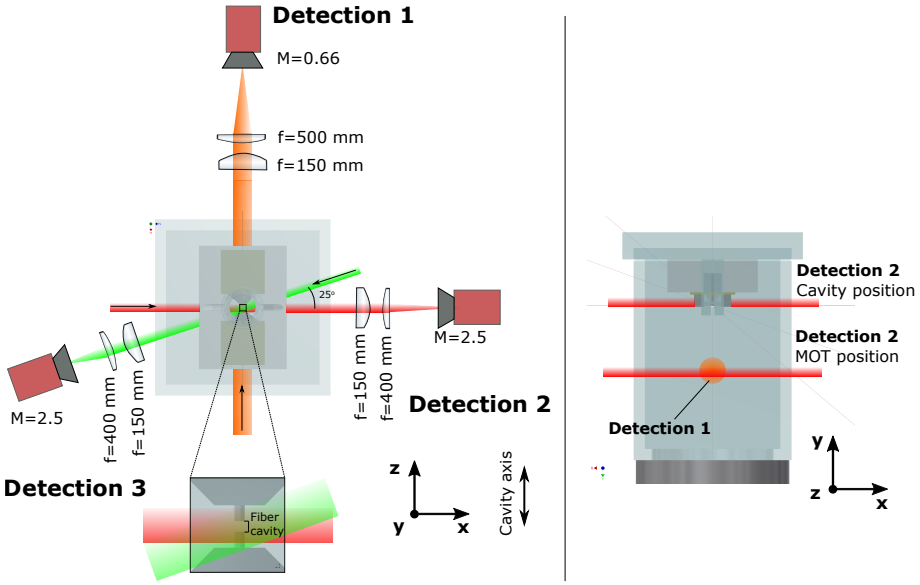

Fig. II.4 *Detection beam paths. Figure from Francesco Ferri PhD thesis [89].*

II.1.4 Transport into the microcavity

To transport atoms from the position of the MOT to the fiber cavity, located 12 mm above, we use a dipole trap at 1070 nm, far red-detuned from the D_1 and D_2 lines, to limit spontaneous emission. A collimated beam of this laser is diffracted by an acousto-optic deflector (AOD) located at the object focal point of an achromat (see figure II.5). Thus steering the AOD driving RF frequency translates vertically the horizontal beam after the achromat. A direct digital synthesizer drives the AOD [89]. The transport beam has a waist of 50 µm. Its power is 6 W at the position of the MOT, and decreased to 1 W when approaching the

cavity, to limit the heating of the fiber cavity dielectric coatings (which happens though the beam is precisely aligned with the cavity center). After observing that sloshing of the trapped cloud along the beam axis limited the loading of the atoms in the intracavity trap lattic, we added a vertical dipole beam, which we focus in the fiber cavity through the high NA lens (see figure II.5). This "guide beam" has a waist of $w_0 = 50$ µm inside the cavity, 80 µm at the position of the MOT. It reduces the sloshing amplitude from 0.5 mm to a few tens of micrometers, which is small compared to the longitudinal size of the atomic cloud. Consequently both efficiency and reproducibility of the cavity trap lattice loading are improved.

This system allows to transport 10^6 atoms over 12 mm in 100 ms with:

a) high precision of the final vertical position: standard deviation of 0.6 µm, much smaller than the waist $w_0 = 8.2$ µm of the intracavity trap lattice.

b) high efficiency: 95%.

c) low heating: 25 µK at the end of the transport, compared to 20 µK at the beginning of the transport.

For more details, please refer to the corresponding published article [93].

To finish with, here is the full sequence for the generation of a cloud of cold atoms and its loading into the transport trap:

1. Optical beams and gradients for the 2D and 3D MOTs are switched on simulateneously. After 2s of loading, 2×10^7 atoms are trapped in a ≈ 2 mm size 3D MOT, with a temperature ≈ 120 µK.

2. The transport and guide beams are switched on. Simultaneously :

   a. The detuning of the 3D MOT cooling beams is increased from $-2.5\ \Gamma$ to $-7\ \Gamma$

   b. The power of the MOT beams is reduced by $\approx 50\%$

   c. The magnetic gradient is increased from 15 to 30 G/cm, for a compressed MOT phase.

3. After 50 ms of compressed MOT, the gradient is switched off, the power of the cooling beams is further reduced and their detuning increased ($-11\ \Gamma$) for an optical molasses phase of ≈ 4 ms. The atoms are cooled down to 10 µK.

4. At the end of the molasses, cooling and repumping beams are switched off and there is a waiting delay of 30 ms before the beginning of the transport, for the atoms to thermalize in the crossed dipole trap. We end up with 10^6 atoms in trap depth 500 µK, at a temperature of 20 µK.

II.2 Cavity design and stabilisation

II.2.1 Design for strong and homogeneous coupling of an array of single atoms

Our experiment aims at reaching the strong coupling regime of CQED for every single atom of a 1D array inside the cavity (reference to the motivationnal section of chapter 1). Single

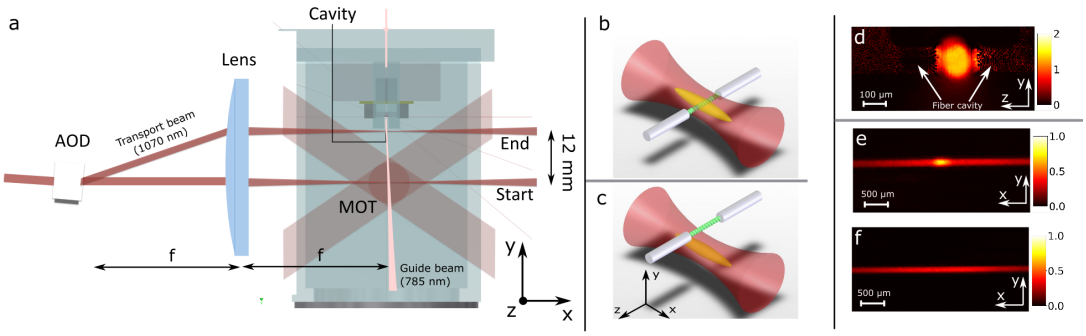

Fig. II.5 *The atoms are transported from the MOT to the cavity (12* mm *above) using a dipole trap ("Transport beam" in Picture a) perpendicular to the cavity axis. Pictures b and c show the cigar-shapped cloud of atoms (orange) trapped in the transport beam (red). The green bubbles represent the intracavity trap lattice to which the atoms are transferred, at the end of the transport (more detail in section II.3.1). Pictures e (respectively f) are absorption images showing the cloud of atoms in the transport trap at the position of the MOT, with (respectively without) the additionnal "Guide beam". The guide beam increases locally the number of atoms and the confinement along the x axis, thus reducing the sloshing of the cloud along this weak axis of the transport beam. Picture d is an absorption image taken along the axis of the transport beam: it shows the cloud of atoms at the end of the transport, inside the fiber cavity. Figures adapted from [93].*

atom strong coupling is achieved when the rate of energy coherent exchange between the atom and the cavity field (coupling rate g) is larger than the rates of the loss processes: spontenaeous emission for the atom (rate γ) and loss of the cavity photon (rate κ): $g > \kappa, \gamma$. γ and κ are Half-Widths at Half Maximum (HWHM) of the atomic and cavity resonances respectively.

A figure of merit for CQED, that we want to maximize, is the single atom cooperativity:

$$C = \frac{g^2}{2\kappa\gamma} \tag{II.1}$$

It can be expressed in terms of cavity parameters:

$$C = \frac{3\lambda^2 F}{\pi^3 w_0^2}, \tag{II.2}$$

where λ is the wavelength, F the finesse of the cavity and w_0 the waist of the cavity mode. Thus strong coupling requires:

1) A small waist, which can be achieved by having simulatenously a small radius of curvature R for the mirrors and a small cavity length L. However L needs to be large enough to fit several tens of single atoms in the intracavity lattice. The lattice has a wavelength of $\approx$ 1560 nm, so the trapping sites are separated by $\approx$ 0.78 µm. $L \approx$ 145 µm gives $\approx$ 180 lattice trapping sites, thus 90 single atoms considering a 50% loading probability

of the collisionnal blockade mechanism (see section VI.2.2). L being fixed, R is chosen as a compromise between having a high cooperativity (obtained with small R which implies small w_0) and a rather uniform cooperativity along the cavity axis (obtained with high R). We chose $R \approx 300$ µm, which provides a maximal cooperativity of $C(z = 0) = 65$, at the center of the cavity, while the cooperativity close to the mirror is still high: $C(z = L/2) = 50$.

2) A high finesse, which Fiber Fabry-Perot microcavities are very good at reaching simultaneously with small radii of curvature. They are engineered in our group by micro-machining the tip of an optical fiber with CO_2 laser ablation [94]. This technique allows to produce surfaces with controlled ellipticity [87, 89, 95–97] and very low roughness, which induces low scattering loss such that the micro-machined fiber tips are compatible with high-finesse mirrors. For our cavity, spherical mirrors have been engineered during the PhD of Sebastien Garcia [87] so that the two eigenmodes of the cavity are degenerate. Thus the cavity mode supports σ_+ photons, which allow to probe the closed (and strongest) transition $F = 2, m_F = 2 \leftrightarrow F' = 3, m'_F = 3$ of the atoms in the cavity.

We have seen how the length and mirror radii of curvature of the cavity were chosen to ensure high and rather homogeneous intensity of the probing field $\lambda_1 = 780$ nm along the cavity axis. More precisely, given the standing wave structure of this field, it is the maximal intensity at its antinodes which is homogeneous along the cavity axis. The intra-cavity lattice wavelength has also been chosen so as to achieve maximal and homogeneous coupling of the trapped atoms to the probing standing wave. For this, its wavelength λ_2 has to be a integer multiple of λ_1, so that each trapping site (corresponding to an antinode of the red-detuned trapping lattice) is at a position of maximal intensity of the probing lattice (meaning an antinode). We choose $\lambda_2 \approx 2\lambda_1$. In fact, the optimal choice is not $\lambda_2 = 2\lambda_1$ because of the Gouy effect. Taking this effect into account, the optimal value is $\lambda_2 = 1559.0$ nm. Finally, the exact overlapping of the two lattices requires a particular value for the relative phases shift at reflection, which was provided to the compagny that fabricated the dieletric Bragg reflectors on the end facet of the cavity fibers.

Once the cavity assembled, the overlapping of the two intracavity standing waves was measured with sub-wavelength precision [89]. A tapered optical fiber with an apex radius of 50 nm was inserted in the cavity as shown in the left picture of figure II.6. We will call it SNOM tip as this kind of fiber serves for "Scanning optical near-field microscopy" (SNOM). The SNOM tip is used as a pointing probe that perturbs the intracavity field and reduces the cavity transmission proportionally to the field intensity at the tip. The SNOM tip was displaced along the cavity axis, and the transmission was measured for each position of the tip. The results are shown in the right plot of figure II.6: the antinodes of the two standing waves overlapp as desired.

Finally, we will discuss the type of fibers used for our cavity. The input fiber is single-mode photonic crystal fiber, which allows propagating a single mode over a large range of wavelengths, including 780 nm and 1559 nm. Its larger mode allows a higher coupling from the fiber to the cavity, compared to a regular single-mode fiber. The output fiber of the cavity is a graded-index multi-mode fiber that allows collecting 100% of the light transmitted, at both 780 nm and 1559 nm.

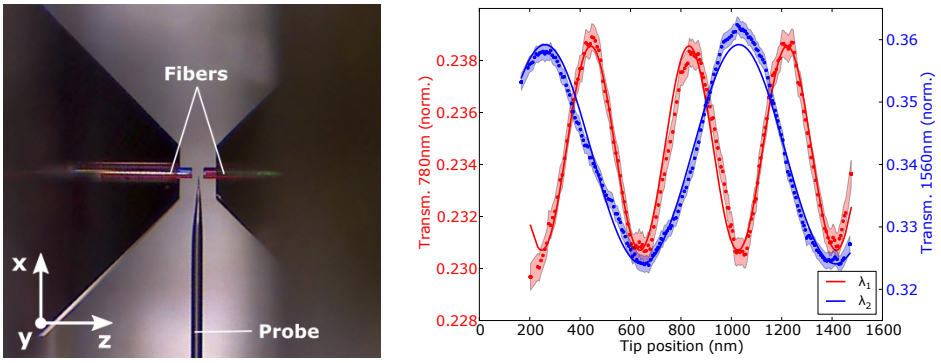

Fig. II.6 *Left: SNOM tip ("Probe") inserted in the fiber cavity induces transmission loss proportionnal to the field intensity at the position of the tip. Right: Measurement of the transmission as a function of the tip position along the z cavity axis. A low transmission corresponds to an antinode of the corresponding standing wave, meaning a high field intensity. One can see that the antinodes of the trapping field (λ_2, blue) corresponds to antinodes of the probing field (λ_1, red) with a residual distance (from fits) better than the precision of the measurement. Figures from Francesco Ferri PhD thesis [89].*

To conclude about the design of the fiber cavity, here is a summary of its parameters:

Cavity parameters	780 nm	1559 nm
Fiber models	Input: NKT LMA-10 (PCF). Output: IVG Cu50 (MMF)	
Length L	145 µm	
Radius of curvature R	309 µm	326 µm
Cavity mode waist w_0	5.7 µm	8.2 µm
Free spectral range	1.03 THz	
Half Width at Half Maximum	14.2 MHz	17.4 MHz
Finesse F	3.6×10^4	3.0×10^4
On resonance transmission	3.1%	2.1%
Coupling $g_{max}/2\pi$	75.0 MHz	
Cooperativity C_{max}	65	

II.2.2 Cavity frequency-locking and lattice intensity stabilization

We have described the full design of the fiber-cavity used in our experimental setup. We will discuss here the different locks relative to the cavity: 1) the essential lock of the cavity length/frequency, 2) a lock of the intracavity lattice intensity, and 3) a subsidiary lock of to compensate the effect of residual amplitude modulation on the cavity frequency.

We have seen in section II.2.1 that because of the Gouy effect, the optimal wavelength for the trapping lattice is 1559 nm. We use this laser to lock the frequency of the fiber cavity. The full schematic of the cavity locking is shown in figure II.7. As the 1560 nm reference laser of our setup is locked to an atomic transition (see section II.1.1), we lock the 1559 nm laser to the reference laser through a transfer cavity [98]: first the transfer cavity is locked

to the 1560 nm laser. Then we lock the 1559 nm laser to the transfer cavity. Both locks rely on the standard Pound-Drever Hall (PDH) method [99, 100].

The frequency-locked 1559 nm laser is amplified and modulated by two successive electro-optic modulators (EOM): EOM1 can be tuned over 20 GHz and serves to tune the absolute frequency of cavity while EOM2 provides a 1.47 GHz fixed modulation, for the PDH lock of the fiber cavity. Finally, a fiber acousto-optic modulator AOM L is used to tune the intensity of the 1559 nm intracavity lattice. On a parallel path, the probing 780 nm laser goes through AOM P (which we use as a fast switch) and EOM P. A side-band of the EOM modulation is used as a frequency-tunable probe for the fiber cavity. Probing and trapping lasers are combined on a dichroic and injected in the fiber cavity.

At the other end of the cavity, transmitted light is collected and the 1559 nm and 780 nm intensities are measured separately: the 1559 nm transmission is used to lock the trapping intracavity intensity, using a commercial lockbox and feedback on the output power of AOM L. The 780 nm transmission is sent either to a Single-Photon Counting Module (SPCM) (for CQED experiments, for which the probe intensity is very low to remain in the low excitation limit, see section I.1.2) or to a standard photodiode (when used with higher probe intensities, for calibration purposes).

Finally, residual amplitude modulation (RAM) occurs in EOMs 1 and 2. It induces fluctuations of the offset of the fiber cavity frequency lock error signal, and thus fluctuations of the frequency to which the cavity is locked. An extra lock was set to partially compensate the RAM [1]. It reduces the fiber cavity frequency fluctuations σ by a factor or ≈ 3, from $\sigma \approx 0.16 \times \kappa$ to $\sigma \approx 0.05 \times \kappa$, where κ is the HWHM at 1559 nm.

II.3 Preparing an ensemble of atoms in the microcavity

II.3.1 Loading the intracavity lattice

At the end of the transport, the atoms are adiabatically transferred from the crossed dipole trap (transport trap + guide trap) to the intracavity lattice, as shown in figure II.8. At the end of the transfer, we get typically 2000-2500 atoms at a temperature of 50 µK, in a lattice trap depth of 300 µK. This is the depth at which we perform the Zeeman state preparation described in section II.3.3. Afterwards, the trap depth can be increased up to 1500 µK, depending on the measurements we want to perform.

Figure II.9 shows a typical cloud of atoms trapped in the intracavity lattice, with $N \approx$ 1500 atoms. The density distribution is well described by a gaussian with standard deviation $\sigma \approx 30$ µm.

II.3.2 Adjustment of the lattice polarisation

For alkali atoms, the dipole trapping potential U_{dipole} of the ground state $^2S_{1/2}$, for a red-detuned dipole trap, is dominated by the contributions of the two first transitions: the D_1 and D_2 lines. Assuming the dipole trap detuning to these lines is much larger than there

[1] For a more detailed analysis of the sources and description of the lock, please refer to the manuscript of Mohamed Baghdad [90].

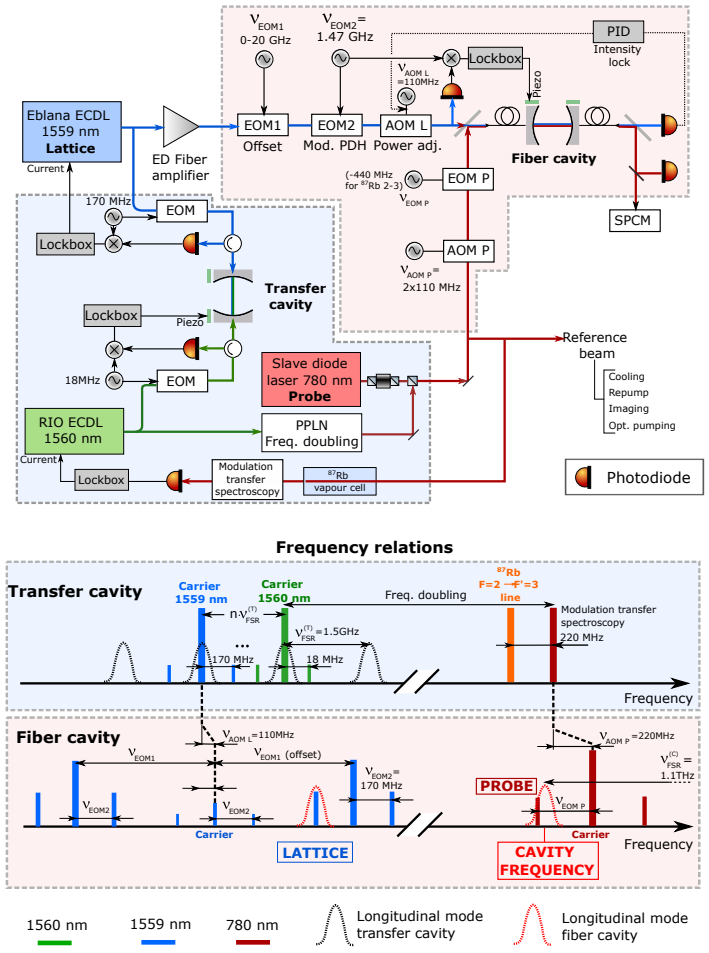

Fig. II.7 *Schematics for frequency locking in our setup. The fiber cavity is locked on the* 1559 nm *laser (in blue). The* 1559 nm *laser is locked to the transfer cavity. The transfer cavity is locked to the* 1560 nm *reference laser, which is locked itself to a* ^{87}*Rb transition, through the slave at* 780 nm *(as explained in section II.1.1). The relations between the different frequencies involved in this scheme are shown below the optical layout. Figure adapted from Francesco Ferri PhD thesis [89].*

hyperfine splittings, U_{dipole} takes the following expression, including the effect of the dipole light polarisation [101]:

$$U_{dipole}(\vec{r}) = \frac{\hbar\Gamma^2}{24}\frac{I(\vec{r})}{I_{sat}}\left(\frac{1 - Pg_F m_F}{\omega_{dip} - \omega_{D_1}} + \frac{2 + Pg_F m_F}{\omega_{dip} - \omega_{D_2}}\right), \tag{II.3}$$

where Γ is the decay rate of the excited state, $I(\vec{r})$ the local intensity of the dipole beam, I_{sat} the saturation intensity, $\omega_{dip} - \omega_{D_{1,2}}$ the detuning of the dipole laser with respect to the D_1 and D_2 lines, g_F is the Landé factor and m_F the Zeeman sublevel quantum number. Finally $P = 0$ (respectively ± 1) for a linear (respectively $\sigma_\pm$) polarised dipole trap.

According to equation II.3, any elliptic component of this polarisation lifts the degeneracy of the Zeeman states and acts as a "fictitious magnetic field" [102]. Thus, the polarisation

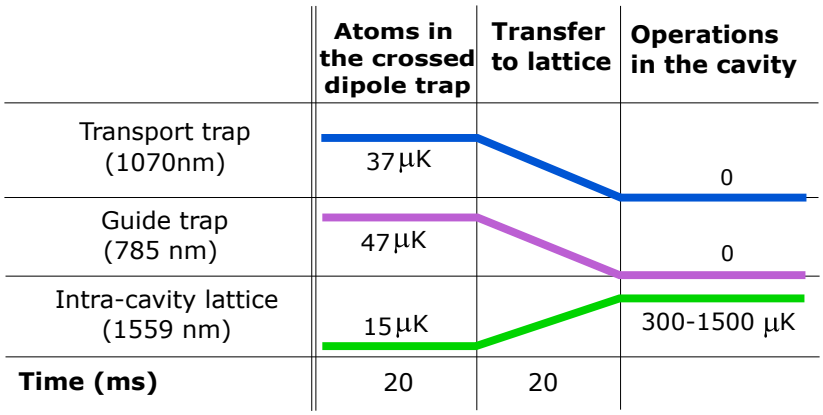

Fig. II.8 *The initial lattice trap depth is non-zero (*15 μK*) because the* 1559 nm *light is used to lock the cavity frequency (as explained in section II.2.2). This lower limit of* 15 μK *is set by the transport: even though it is carrefully aligned at the center of the cavity, the transport beam induces a thermal shock when it arrives in the cavity. This shock is visible on the piezo voltages of the cavity. We need* 15 μK *of locking light for the PDH error signal to be large enough so that the cavity lock resists to this shock. There has been quite some work with the frequency and intensity locks (ref to Francesco and Mohamed thesis) so that both work with intracavity trap depths in the range* $[15 - 1500]$ μK*. Figure from Francesco thesis.*

of the 1559 nm intracavity trap was set to be linear inside the cavity. Since the PCF input fiber does not maintain polarisation, the black box approach of [103] was used to set the polarisation of the light inside the cavity: when the polarisation of the light reflected from the cavity is the same that for the incoming light, the polarisation inside the cavity should be linear. However, this is true under the assumption that no there is no loss depending on the polarisation of light. For a finer adjustment beyond this assumption, a quantitative measurement of the fictitious magnetic field was performed with Zeeman micro-wave spectroscopy. The input intracavity polarisation was tuned to cancel them [90] (see figure II.10).

II.3.3 Zeeman state preparation for optimal coupling to the cavity

Preparing the atoms in the Zeeman sublevel $F = 2, m_F = 2$ is an important step before any CQED experiment, since this level is involved in one of the closed transitions of the D_2 line ($F = 2, m_F = 2 \leftrightarrow F = 3, m'_F = 3$), which allows to work with an effective two level system. Moreover this transition has the strongest dipole moment of all transitions in the line (ref to Steck), leading to the highest value for the coupling g.

The first step of the preparation is optical pumping [104] to $F = 2, m_F = 2$. For this we use a beam perpendicular to the cavity axis , that has the same path as detection 2 (see figure II.4). It has a waist $w_0 \approx 1.2$ mm (such that its intensity is uniform across the 145 μm length of the cavity) and polarisation σ_+, thanks to a 3 G magnetic field along the beam axis. Its intensity is $0.5\, I_{sat}$ and duration 0.5 ms. Atoms accumulate in the sublevel $F = 2, m_F = 2$, which is only dark sublevel with respect to the pumping light. Simulateneously we shine

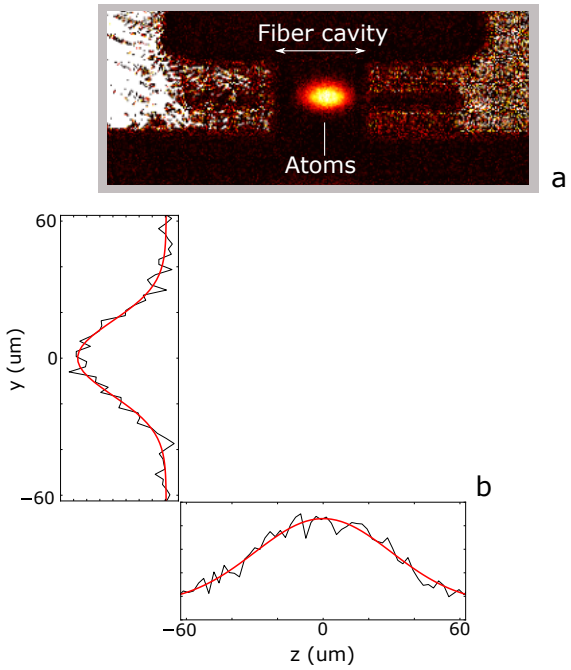

Fig. II.9 *Absorption image of a cloud of atoms trapped in the intracavity* 1559 nm *lattice, with a filling of about 140 lattice sites. Picture a. shows the fiber cavity as well. Picture b: Zoom on the atomic cloud. The two plots show density profiles integrated along the two axes, with gaussian fits. The image is an average of 10 shots, taken after a time-of-flight* 100 µs*, for which the expansion of the cloud is negligible. The trap depth is* 1 mK*. Figure from Francesco Ferri PhD thesis [89].*

repumping light [2] to repump atoms that end in $F = 1$.

We estimate that 85% of the atoms are pumped in $F = 2, m_F = 2$. To improve the fraction of atoms in $F = 2, m_F = 2$, we implement a purification scheme:

1) With a microwave adiabatic transfer in presence of a magnetic field of 3 G along the cavity axis, we transfer more than 98% of the $F = 2, m_F = 2$ atoms in $F = 1, m_F = 1$.

2) We push out of the lattice trap the atoms remaining in $F = 2, m_F = -2, -1,0,1$ with a blast beam. It is on resonance with the cycling transition, with an intensity of several I_{sat} and a duration of 0.5 ms, chosen not too long such as to push the atoms away without depumping them in $F = 1$

3) With a reversed microwave adiabatic passage we transfer the atoms back from $F = 1, m_F = 1$ to $F = 2, m_F = 2$.

The combination of the optical pumping and this purification results in 80% of the atoms in $F = 2, m_F = 2$ and no atom in the other $F = 2$ sublevels (up to measurement precision).

[2] More details about the beam geometry in section VI.2.1.

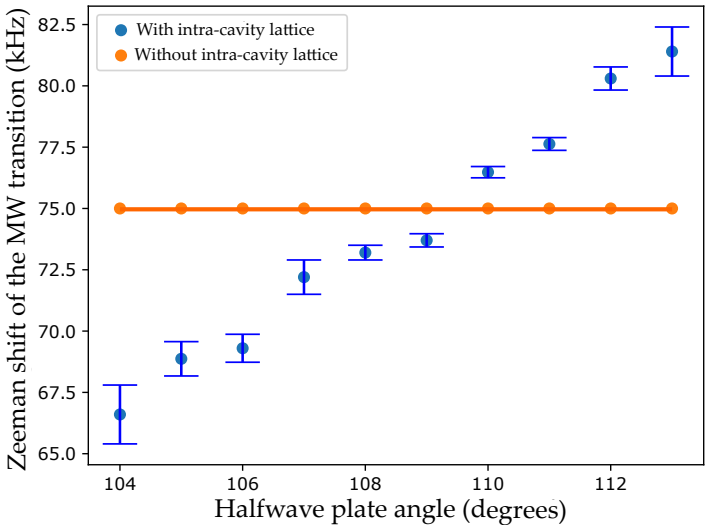

Fig. II.10 *Cancellation of the fictitious magnetic fields due to ellipticity of the intracavity lattice trap. As we rotate the angle of the half-wave plate before the fiber-cavity in-coupler, the intracavity lattice polarisation rotates as well and this induces a linear shift of frequency of the micro-wave transition* $F = 1, m_F = 0 \rightarrow F = 2, m_F = 1$ *(blue data points), accordingly to equation II.3. We also measure the frequency of the micro-wave transition in absence of lattice light (orange data points). Linear polarisation is achieved where both lines cross, at* $\approx 109.5°$*. The* 75 kHz *shift of the transition (even without lattice) is due to a* 1 G *magnetic field, used to lift the degeneracy between Zeeman levels and to monitor only one micro-wave transition. Figure adapted from Mohamed Baghdad PhD thesis [90].*

As we explain in section III.1.1, the 1559 nm trapping lattice induces large differential lightshifts as well as mixing of the F, m_F sublevels of the excited manifold ($5^2P_{3/2}$). This mixing is such that together with optical pumping ($F = 2 \rightarrow F' = 2$) or blast ($F = 2 \rightarrow F' = 3$) light, the lattice light can induce depumping from $F = 2$ to $F = 1$. This is especially problematic for the blast, where one wants to push the $F = 2$ atoms out, without depumping them in $F = 1$, where we have a reservoir of atoms of interest in $m_F = 1$. Thus we implement the chopping of the trapping lattice [105, 106], the optical pumping and blast light, using a pulse generator at 2.8 MHz. A delay generator is used to intertwine the optical pumping and blast chopped pulses with the lattice pulses, with no temporal overlapping. The chopping frequency is much higher than the trapping frequencies (for which the maximal values are ≈ 340 kHz along the cavity axis and ≈ 15 kHz perpendicularly to the cavity axis, for a trap depth of 1500 µK) such that the atoms trapping and external motion are not affected.

Finally, the lifetime of the atoms was measured at the end of the preparation in Zeeman level $F = 2, m_F = 2$, for the our standard trap depth of $U = 300$ µK. The time evolution of the number of atoms is well fitted by the sum of two exponential decays: $N(t) = N_1 e^{-t/\tau_1} + N_2 e^{-t/\tau_2}$. First a fast decay occurs ($\tau_1 \approx 50$ ms) due to atom collisions. Then a slower decay occurs, with $\tau_2 \approx 900$ ms.

II.3.4 Transmission spectrum measurement

Now that we have seen how we can prepare an ensemble of atoms in the microcavity, in the Zeeman sublevel $F = 2, m_F = 2$, we will describe how we measure the transmission spectrum of the atomic ensemble coupled to the cavity, and the calibrations required for this measurement. While all the work done in the previous sections of this chapter was done by my predecessors, I was in charge, at the beginning of my PhD, of the setup and the analyses required to calibrate the frequency axis of the transmission spectrum. This is necessary to determine precisely the collective coupling of the atomic ensemble, which was crucial for the measurements and results presented in chapters III and IV.

Considering an ensemble of $N = 1500$ atoms, with a mean coupling rate $g_{eff} = 60$ MHz (ref to the part where we explain thermal averaging), the Rabi splitting separation (ref to chap. 1) is typically $2g_{eff}\sqrt{N} \approx 4.5$ GHz. Thus we measure Rabi splittings by probing the cavity-atoms coupled system with a dedicated tunable laser diode, able to perform frequency ramps of tens of GHz without mode jump.

We typically scan a range of 8 GHz in 8 ms, while collecting the probe light transmitted through the cavity with the SPCM (see figure II.7). A typical spectrum is shown in figure II.11. It is strongly discretised, because the probe power is low so as to stay in the low excitation limit $n_{cav} \ll 1$ (reference to chap 1) where the system can be simulated more easily. In all this manuscript, probing of atomic ensembles was done with a probe intensity corresponding to $n_{cav} = 0.14$, which is still high enough so as to be able to identify the Rabi peaks.

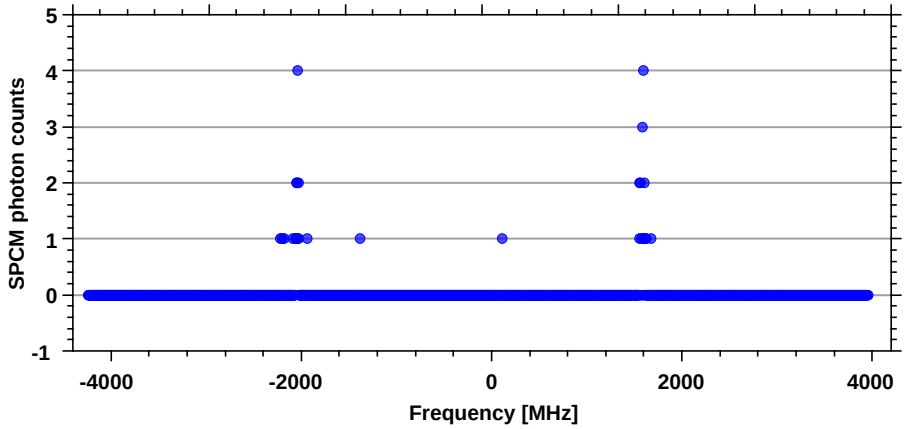

Fig. II.11 *Transmission spectrum of the cavity, coupled to an ensemble of $N \approx 900$ atoms in $F = 2, m_F = 2$. The intra-cavity lattice trap depth is 310 μK, the temperature is 50 μK and the cavity is tuned on resonance with the average atomic frequency, lightshifted by the lattice trap (as explained in sections III.1.1 and III.1.1). The frequency is referenced to the bare atoms cycling transition $5^2S_{1/2}, F = 2, m_F = 2 \leftrightarrow 5^2P_{3/2}, F' = 3, m'_F = 3$. We observe a Rabi splitting, which is the signature of collective strong coupling. The separation between the two peaks is 2Ω, where $\Omega = 2g_{eff}\sqrt{N} \approx 2\pi \times 1800$ MHz, with $g_{eff} = 60$ MHz. This corresponds to an effective cooperativity $C_{eff} = g_{eff}^2/(2\kappa\gamma) \approx 42$.*

To calibrate the frequency axis of the spectrum at each measurement, we record simultaneously:

1) The transmission signal of a standard macroscopic cavity (see figure II.12.b), that provides a frequency ruler allowing us to compensate the slight non-linearity of the frequency sweep. Indeed the sweep of the tunable laser relies on the motion of a piezo. This piezo is driven by a triangular signal and exhibit a non-linear response, close to the turning-points, such that a single sweep is better fitted by a 2^{nd} polynomial (see figure II.12.c). The macroscopic cavity has a length of $L \approx 10$ cm. The distance between successive peaks is given by the Free Spectral Range, FSR $= \frac{c}{4L} \approx 750$ MHz.

2) A saturated absorption signal of the probe laser that provides an absolute frequency reference (see figure II.12.a).

Both the FSR of the macroscopic cavity and the frequency uncertainty δf of this frequency calibration procedure were measured using the transmission spectrum of an empty cavity, with a 800 MHz frequency modulated probe, that provides another frequency ruler. We estimate the 1-standard deviation uncertainty of the frequency of the probe laser to be $\delta f = \pm 8$ MHz, much smaller than the Rabi splittings obtained with our cloud of atoms (in the range $[200 - 4000]$ MHz). Thus we can measure collective couplings (half of the Rabi splitting) with a satisfying relative uncertainty in the range $[0.4 - 8]\%$.

The polarisation of the probe has to be σ_+ to get the highest coupling rate g to the atom prepared in Zeeman state $F = 2, m_F = 2$, and to cycle in the effective two level system provided by the closed transition $F = 2, m_F = 2 \leftrightarrow F' = 3, m_F = 3$. Probing the $F = 2, m_F = 2$ atom with a σ_- photon leads to a smaller Rabi separation. Thus, for an elliptical probe polarisation, the spectrum exhibits two well separated Rabi doublets corresponding to the σ_+ and σ_- components of the probe. The ellipticity of the probe was tuned so as to eliminate the smaller Rabi doublet and the residual σ_- contribution was estimated to 2%.

II.4 Conclusion

In this chapter we have reviewed the fundamental bricks of our CQED-cold atom experiment. Two vacuum chambers are used to operate a 2D and a 3D MOT to cool down ^{87}Rb atoms. A dipole trap translated by a acousto-optic-deflector is used to transport efficiently atoms towards the cavity, with a sub-micrometer accuracy, compatible with the small waist of the cavity mode. The microcavity is a fiber-based Fabry Perot resonator produced with a laser micro-machining technique pioneered by our group. With this technique we achieve small radii of curvature (thus small cavity mode waist) and smooth surfaces (thus high finesse), such that the strong coupling regime is reached for a single atom, with a maximal cooperativity of 65. The cavity sustains two standing waves: one at 780 nm, to probe the D_2 line of ^{87}Rb and the second at 1559 nm, a far-off resonant trap lattice. The commensurability of the two standing waves and precise engineering of their phase at reflection ensures that atoms trapped in the lattice are strongly and homogeneously coupled to the probe field, over the entire 145 µm length of the cavity. The birefringence of the cavity is minimized such as to

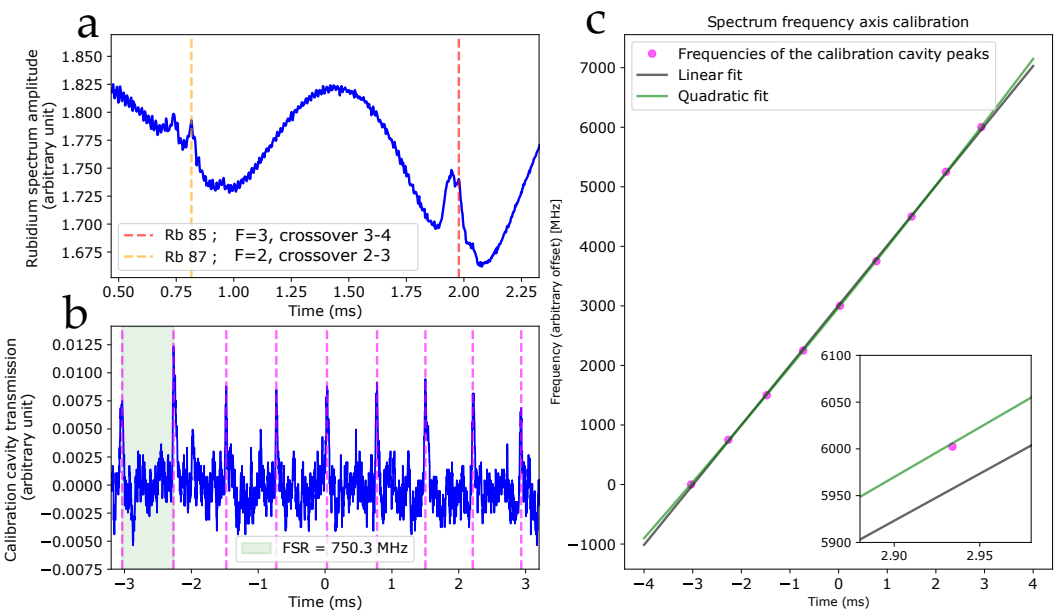

Fig. II.12 *Calibration of the frequency axis of a transmission spectrum. Initially the x axis is time. Graph a: Saturated absorption spectroscopic measurement of* ^{85}Rb *and* ^{87}Rb*, providing an absolute frequency reference. We point two peaks of the spectrum to double-check the result from the non-linearity characterisation (b and c). Graph b: Transmission signal of the macroscopic cavity, that provides a frequency ruler. Graph c:* 2^{nd} *degree polynomial fit of the times at which the probe scans the macroscopic cavity peaks, to evaluate the non-linearity in the frequency sweep. Combined with the spectroscopic absolute frequency, it provides a time-to-frequency conversion for the x axis of the transmission spectrum. The inset shows a zoom at about* -3 GHz *from the center of the scan, to exhibit the error made with a linear fit close to extremal points of the scan:* ≈ 50 MHz*. This error is compensated by the calibration, and afterwards the remaining error is much lower:* $\delta f = \pm 8$ MHz*.*

probe the cavity with σ_+ photons and drive a closed-transition of the D_2 line. By probing the vacuum Rabi splitting of an ensemble of polarised atoms and measuring the atom number with absorption imaging, we verify that we operate deep in the single atom strong coupling regime, with an effective cooperativity of 42.

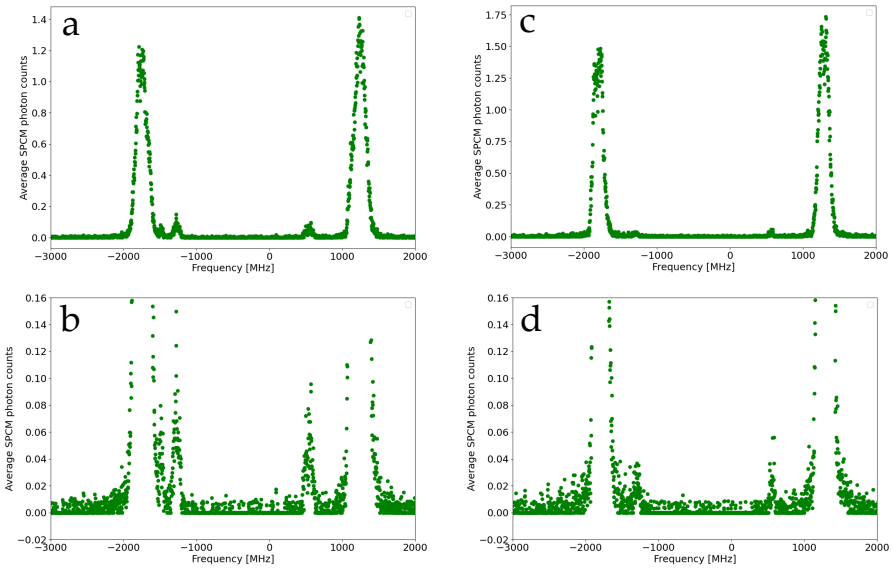

Fig. II.13 *Calibration of the polarisation of the probe. All graphs are transmission spectra averaged over* ≈ 110 *single shots. This averaging is necessary to resolve the smaller Rabi splitting corresponding to the* σ_- *component of the probe, which is not resolved in single shots such as figure II.11. Upper plots show full-scale transmission spectra, whereas lower plots are zooms in the low-transmission region, to exhibit the* σ_- *Rabi splitting, which has a rather small amplitude in all graphs because the probe is initially quite close to* σ_+*. Graphs a and b correspond to the initial setting, where the* σ_- *contribution is* $\approx 10\%$*. Graphs c and d correspond to the final setting, where this contribution has been reduced to* $\approx 2\%$*. The ratio between the two Rabi splittings is* ≈ 1.7 *theoretically, which we measure indeed in our spectra.*

Chapter III

Frequency modulation of cavity-protected polaritons

Chapters III and IV were adapted from the article "Spectral Engineering of Cavity-Protected Polaritons in an Atomic Ensemble with Controlled Disorder" [53], co-authored by Mohamed Baghdad, Pierre-Antoine Bourdel, Sylvain Schwartz, Francesco Ferri, Jakob Reichel and Romain Long. Mohamed Baghdad, Pierre-Antoine Bourdel and Sylvain Schwartz contributed equally to this work. The material related to this topic has also been presented in the PhD manuscript of Mohamed Baghdad [90], major exceptions being the theoretical model for multi-frequency polariton (appendix **??**) and the photonic weight simulation (section IV.2), which sheds a new light on understanding the transition from the disordered cavity-unprotected to the polaritonic cavity-protected regimes.

In this chapter we first characterise the inhomogeneity induced by our trapping lattice, through simulation and measurements (section III.1). Then we demonstrate the cavity protection effect (section III.2) that preserves the coherence of an inhomogeneous ensemble of a few hundreds of emitters. Finally, leveraging the narrow resonances of the protected regime, we produce polaritons featuring a comb-like frequency spectrum by modulating the light-shifted frequency of the atoms on a very fast time scale (section III.3).

III.1 Characterising the inhomogeneous frequency distributions

We have introduced the key concepts of cavity protection and the previous experimental observations of this effect. In this section we discuss, measure and simulate the inhomogoneities of our coupled system. In our cold atom experiment, two types of inhomogeneities are present. Both are due to the finite atomic temperature which implies a thermal distribution of atomic position in the intra-cavity lattice trap. This distribution converts to distributions of the coupling strength to the cavity and the atomic transition frequency, because of the significant lightshift induced by the intra-cavity lattice light. The distribution in coupling strength has small consequences, mentioned in section I.3.1. The distribution of atomic frequency leads to more profound modifications, as we have seen when introducting the cavity protection effect (I.3).

In this section, we first detail the inhomogeneity induced by the intra-cavity lattice trap

(III.1.1). Then we present the experimental measurements (III.1.3) and the simulations (III.1.2) of the coupling-weighted atomic frequency distributions, which encompasses both types of inhomogeneities.

III.1.1 Effect of the 1559 nm light on the excited state manifold

Due to a nearby resonance (the $5P_{3/2} \leftrightarrow 4D$ transition at 1529 nm - see figure III.2.b, the trapping light induces a light-shift of the excited state of the D_2 line which is $\simeq 50$ times larger than the ground state light-shift [107]. This enables a fast and accurate control of the frequency of the $|g\rangle \leftrightarrow |e\rangle$ transition. However, this also leads to broadening of the frequency distribution of the probing transition, due to finite temperature of the trapped atoms and level mixing of the $5P_{3/2}$ manifold induced by two-photon coupling [108, 109].

Following [108, 109], we describe the combined effects of light-shifts and level mixing within the $5P_{3/2}$ manifold induced by the 1559 nm light by a Stark operator $\hat{V}$, whose matrix elements in the $|F,m_F\rangle$ basis are given by:

$$\langle F',m'_F|\hat{V}|F,m_F\rangle = \sum_{|k\rangle} \frac{\langle F',m'_F|\hat{\mathbf{d}}\cdot\mathbf{E}|k\rangle\langle k|\hat{\mathbf{d}}\cdot\mathbf{E}|F,m_F\rangle}{-\hbar\Delta_k} \tag{III.1}$$

where Δ_k is defined as:

$$\frac{1}{\Delta_k} = \frac{1}{(\omega_k - \omega_{5P_{3/2}}) - \omega} + \frac{1}{(\omega_k - \omega_{5P_{3/2}}) + \omega} ,$$

all relevant states $|k\rangle$ being much farther in energy than the hyperfine splitting. In our case, given the value of the reduced matrix element and the detuning from the 1559 nnm light of each atomic line [108], we expect most ($> 99\%$) of the contribution in the sum of equation (III.1) to result from $4D_{5/2}$, $4D_{3/2}$, $6S_{1/2}$ and $5S_{1/2}$, so we keep only these lines in the simulations.

To compute the matrix elements $\langle F',m'_F|\hat{\mathbf{d}}\cdot\mathbf{E}|F,m_F\rangle$ for a given atomic line and quantization axis $\mathbf{e}_z$, we express the electric field of the 1559 nm trapping light $\mathbf{E} = (E_x,E_y,E_z)$ in the spherical basis:

$$\mathbf{E} = \sum_{q=-1,0,1} E_q \mathbf{e}_q , \tag{III.2}$$

where the $\mathbf{e}_q$ are unitary vectors and the E_q are the "pi" and "sigma" components of $\mathbf{E}$ related to $E_{x,y,z}$ by:

$$E_0 = E_z \quad \text{and} \quad E_{\pm1} = (\pm E_x + iE_y)/\sqrt{2} .$$

The dipole matrix elements of $\hat{d}_q = \hat{\mathbf{d}}\cdot\mathbf{e}_q$ are then computed using the Wigner-Eckart theorem, and reduced matrix elements taken from reference [108]. In our typical experimental situation, the magnetic field is along the cavity axis z, and the polarization of the trapping light is linear along the x direction, corresponding to $E_0/|\mathbf{E}| = 0$, $E_1/|\mathbf{E}| = 1/\sqrt{2}$ and $E_{-1}/|\mathbf{E}| = -1/\sqrt{2}$.

III.1.2 Simulation of frequency distributions

To simulate the inhomogeneous atomic frequency distribution induced by the intra-cavity trapping 1559 nm light, we assume that the atoms are in thermal equilibrium at each site of the optical lattice, described by an harmonic trap with radial frequencies $\omega_x = \omega_y$ and longitudinal frequency ω_z. Typical values for these frequencies are $\omega_{x,y}/2\pi = 14.5\,\mathrm{kHz}$, and $\omega_z/2\pi = 330\,\mathrm{kHz}$, for a trap depth of $U_0 = 1400\,\mu\mathrm{K}$,. For each atom of a given sample, we first draw x, y and z from a normal distribution with standard deviation $\sigma_{x,y,z} = \sqrt{k_B T/m\omega^2_{x,y,z}}$. Then we deduce the values of the coupling $g(x,y,z)$ (based on the cavity parameters) and of the intra-cavity lattice trap intensity $I_{dip}(x,y,z)$ (based on the maximum value at the bottom of the trap, which is estimated from light-shift measurements - see appendix **??** and corroborated by a direct transmission measurement). The intensity $I_{dip}(x,y,z)$ seen by each atom is used to construct a 16×16 matrix representing the Stark operator in the $|F,m_F\rangle$ basis of the $5P_{3/2}$ manifold, to which we subtract a constant energy term corresponding to the ground state light-shift. The output of the procedure for N atoms is a collection of $16\times N$ eigenvalues $\hbar\omega_{k,j}$ and eigenvectors $|\psi_{k,j}\rangle$, where $1 \leq j \leq 16$ and $1 \leq k \leq N$. The cavity is probed with σ_+ polarised light which couples the ground state $|5S_{1/2}, F = 2, m_F = 2\rangle$ of atom number k (denoted $|k : 2,2\rangle$) with state $|5P_{3/2}, F' = 3, m_F = 3\rangle$ (denoted $|k : 3,3\rangle$). Thus the coupling $g_{k,j}$ of the eigenstate $|\psi_{k,j}\rangle$ to the σ_+ cavity field is $g_{k,j} = g_k|\langle\psi_{k,j}|k : 3,3\rangle|$, where g_k depends on the position of the atom k in the 780 nm probe standing wave.

From that we can reconstruct the spectral distribution of the couplings to the σ_+ cavity mode:

$$\rho(\omega) = \sum_{k=1}^{N}\sum_{j=1}^{16} g^2_{k,j}\delta(\omega - \omega_{k,j}), \tag{III.3}$$

by drawing $N = 100\,000$ random atomic positions and computing the associated $(\omega_{k,j}\,;\, g_{k,j})$. We then sort the transition frequencies $\omega_{k,j}$ in equal-width bins, weighted by their coupling strength $|g_{k,j}|^2$. The calculated distributions are shown infigure III.1 for various values of the trap depth U_0. The distributions are noticeably asymmetrical and have a bounded support: the maximal (respectively minimal) atomic frequency corresponds to the minimal (respectively maximal) trap lattice intensity, and corresponds to an atom at the node (respectively the antinode) of the lattice. Thus, similarly to the simulation with a theoretical rectangular distribution (discussed in section I.3.2), we expect cavity protection to take place in our inhomogeneous system, for sufficiently large collective coupling. The rectangular distribution, though theorician-beloved, is a rather specific example for a bounded distribution, as it is not continuous at its boundaries, and symmetric. Our experimental distributions are much smoother close to their boundaries and asymmetric. This leads to specific features for the dynamics of the coupled system, which we will present in section IV.4.

III.1.3 Measurement of the frequency distributions

The strong frequency broadening in our experiment results from the combination of finite atomic temperature, light-shifts and level mixing effects described in the two previous sections. We characterize the subsequent frequency distribution experimentally by illuminating the trapped atoms with a transverse beam, perpendicular to the cavity, and measuring the relative atomic losses as a function of the beam frequency, for various trap depths. The atom ensemble is prepared in the $F = 2$ hyperfine ground state. The transverse beam has an

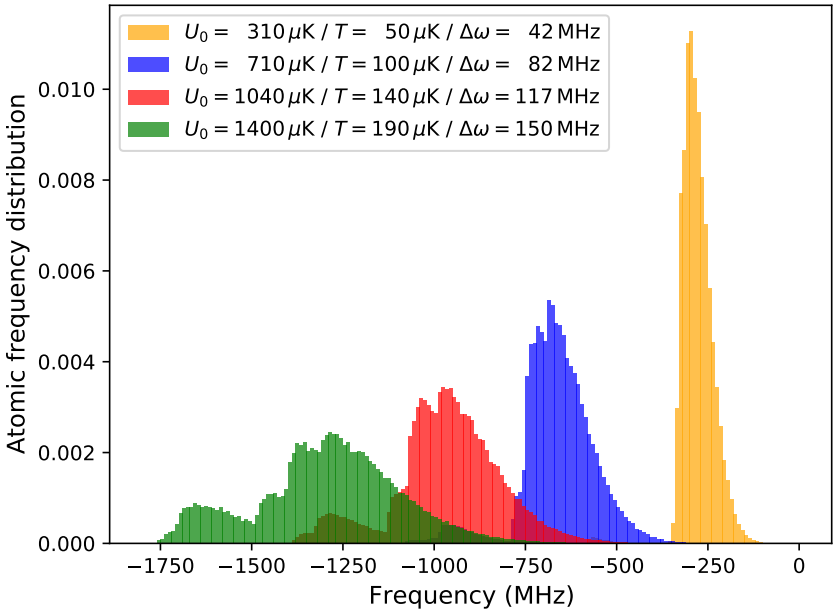

Fig. III.1 *Simulated atomic frequency distribution $\rho(\omega)$ for different trap depths. For each trap depth U_0, the temperature T used in the simulation corresponds to the typical experimental value based on time-of-flight measurements. When U_0 increases, the mean frequency of the distribution decreases linearly – as expected with red-detuned off-resonant light – and the width $\Delta\omega$ of the distribution increases. At low trap depth $U_0 = 310 \pm 10\,\mu K$ the distribution has mainly one lobe, corresponding to the $|F = 2\rangle \rightarrow |F' = 3\rangle$ transition. For larger trap depths, two-photon couplings at 1559nm mix the excited state hyperfine levels and two extra lobes appear in the distributions, at lower frequencies, corresponding roughly to transitions $|F = 2\rangle \rightarrow |F' = 2\rangle$ and $|F = 2\rangle \rightarrow |F' = 1\rangle$. This illustrates the tunability of the inhomogeneous distribution with the intensity of the trapping field.*

intensity of $I = 0.2\, I_{sat}$ and is switched on for 0.5 ms at a given frequency. Then the relative loss is measured from the vacuum Rabi splitting of the cavity transmission spectrum, which allows to obtain reliable atom number measurements down to low atom numbers.

The results are shown infigure III.2.c (dots). Because the atoms are excited with uncontrolled phases and amplitudes by this transverse beam, we expect (and observe) negligible coupling between the latter and the bright states of the coupled atom-cavity system even though the resonance condition is fulfilled. This is necessary to measure losses over the entire range of frequencies of the distribution, rather than only at the frequencies of the bright states. The measured frequency distributions show the broadening (up to 1 GHz) and shift due to the 1559 nm trapping light. The frequency ranges of the measured distributions are similar to that of the corresponding distributions of couplings $\rho(\omega)$ (see Fig.III.1). However, the measured distributions are slightly different because the transverse beam does not couple to the atoms in the same way than the σ_+ cavity-mode probe for which $\rho(\omega)$ is computed.

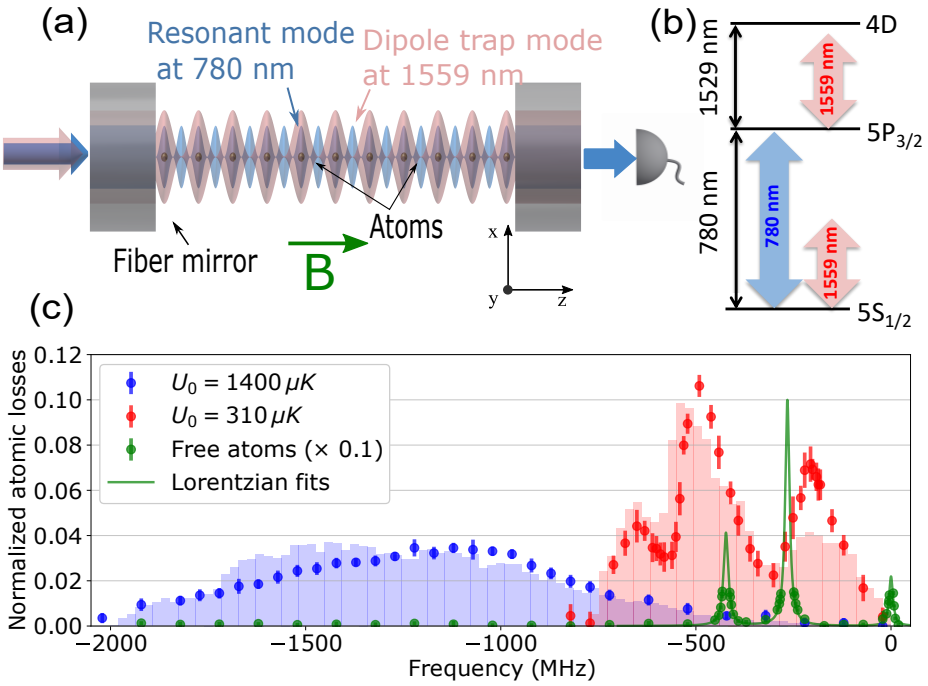

Fig. III.2 *Experimental setup of the cold atom cavity interface with tunable inhomogeneous frequency distribution. (a) Sketch of the setup. Atoms are trapped in a one-dimensional optical lattice (red) which is commensurate with the main cavity mode (blue). The latter is on resonance with the* $|g\rangle \leftrightarrow |e\rangle$ *atomic transition. (b) Simplified level diagram illustrating the proximity of the* 1559 nm *trapping light with the* $5P_{3/2} \leftrightarrow 4D$ *line. (c) Atomic frequency distribution measured by loss spectroscopy of the trapped atoms for various trap depths (Green: no trap. Red:* $U = 310\,\mu K$*. Blue:* $U = 1400\,\mu K$*). The horizontal axis corresponds to the frequency of the transverse probe beam inducing the losses, referenced to the bare* $\left|5S_{1/2}, F = 2, m_F = 2\right\rangle \leftrightarrow \left|5P_{3/2}, F' = 3, m_{F'} = 3\right\rangle$ *transition. Circles: experimentally measured losses (error bars correspond to* 1σ *spread of the data), normalized to the maximum value of the* $F' = 2$ *peak of the free atoms. Histograms: result of Monte Carlo simulations of the frequency distributions.*

The transverse beam as a circular polarisation, and its propagation axis is perpendicular to the quantization magnetic field, along the cavity axis. So its electric field has both "sigma" and "pi" components, and all the Zeeman sublevels of the $F = 2$ hyperfine ground state may play a role in the dynamics.

Thus we adapt the Monte Carlo simulation, and assume that the initial atomic population is equally distributed between these sublevels. For each atom (labelled by the index k), we use the previous procedure (section III.1.2) to compute the 5×16 transition frequencies $\omega_{k,j}(m_F)$ between the 5 ground states $|F = 2, m_F\rangle$ and the 16 excited states $|\psi_{k,j}\rangle$. Each

frequency $\omega_{k,j}(m_F)$ is associated to a coupling strength $c_{k,j}(m_F)$, defined as:

$$c_{k,j}(m_F) = \left| \left\langle \psi_{k,j} \left| \sum_{q=-1}^{1} \hat{d}_q E_q^t \right| F = 2, m_F \right\rangle \right|^2 , \tag{III.4}$$

where E_q^t are the components of the electric field of the probe beam $\mathbf{E}^t$, expressed in the spherical basis and $\hat{d}_q$ are the dipole matrix elements (see section III.1.1). For the transverse beam, we have $E_0^t/|\mathbf{E}^t| = 1/\sqrt{2}$ and $E_{\pm 1}^t/|\mathbf{E}^t| = \pm 1/2$. The simulated frequency distributions shown infigure III.2.c (histograms) are then obtained by sorting the transition frequencies $\omega_{k,j}(m_F)$ in equal-width bins, weighted by their coupling strength $c_{k,j}(m_F)$. For a given trap depth, we use an effective temperature T to match the positions of the simulated and experimental curves. The effective temperatures are 2 to 3 times the initial experimental temperatures. Interestingly, there is a relatively good qualitative agreement between the simulated frequency distributions and the loss measurements on figure III.2, even though the latter involve several complex mecanisms that are not included in the simulations, such as heating, population redistribution between the Zeeman sublevels of the $F = 2$ hyperfine ground state and depumping into the $F = 1$ undetected hyperfine ground state. The higher effective temperature could stem from these effects.

III.2 Cavity-protected polaritons in the strong collective coupling regime

To investigate the coherence properties of this inhomogeneous system, we consider the transmission spectrum of the cavity in the low excitation limit, in which we perform our experiments.

III.2.1 Model for transmission spectrum in the low-excitation

The cavity is probed with a weak pulse of σ_+ polarized light which couples the ground state $|k : 2,2\rangle$ of atom number k to $|k : 3,3\rangle$, the $|5P_{3/2}, F' = 3, m_{F'} = 3\rangle$ Zeeman sublevel of this atom. The coherent evolution of the coupled atom-cavity system is described by a multilevel version of the standard Tavis-Cummings Hamiltonian (with $\hbar \equiv 1$):

$$H = H_{\text{cav}} + H_{\text{at}} + H_{\text{int}}, \tag{III.5}$$

where:

- $H_{\text{cav}} = \omega_c a^\dagger a$ is the Hamiltonian of the cavity mode;
- $H_{\text{at}} = \sum_k \sum_j \omega_{k,j} \sigma_{k,j}^+ \sigma_{k,j}^-$ is the Hamiltonian of the multilevel atomic ensemble dressed by the 1559 nm light; the operator $\sigma_{k,j}^+$ is by definition equal to $|\psi_{k,j}\rangle\langle k : 2,2|$ and $\sigma_{k,j}^- = \left(\sigma_{k,j}^+\right)^\dagger$;
- $H_{\text{int}} = \sum_k g_k \left(\sigma_k^- a^\dagger + \sigma_k^+ a\right)$ describes the interaction between the atoms and the cavity mode in the rotating wave approximation, where:

$g_k = g(x_k,y_k,z_k)$ is the coupling constant of the atom k, at the position (x_k,y_k,z_k), and $\sigma_k^+ = |k:3,3\rangle\langle k:2,2|$. We can express H_{int} in the following form :

$$H_{\text{int}} = \sum_k \sum_j \left(g_{k,j}\sigma_{k,j}^+ a + g_{k,j}\sigma_{k,j}^- a^\dagger \right)$$

with $g_{k,j} = g_k\langle\psi_{k,j}|k:3,3\rangle$.

In the low excitation limit, where the average photon number inside the cavity is much smaller than unity, the Hilbert space can be reduced to the subspace with one excitation: $\{|1,G\rangle, |0,W\rangle\}$. $|1,G\rangle$ corresponds to the state with one photon in the cavity mode and all atoms in the ground state $|G\rangle = |1:2,2,\ldots,N:2,2\rangle$. $|0,W\rangle$ is the state with zero photon in the cavity mode and one atomic excitation $|W\rangle = \left(\sum_{k=1}^N \frac{g_k}{\Omega}\sigma_k^+\right)|G\rangle$. The (complex) transmission of the cavity as a function of the probe frequency ω taking into account photon losses κ and atomic decay γ then takes the following simple analytical form, that was derived in [49] using the input-output formalism:

$$t(\omega) = \frac{-\kappa/(2i)}{\omega_c - i\kappa/2 - \omega - \sum_{k,j} \frac{(g_{k,j})^2}{\omega_{k,j} - i\gamma/2 - \omega}}. \tag{III.6}$$

III.2.2 Experimental observation of the cavity protection effect

To exhibit the cavity protection effect, we measure the cavity transmission spectrum with a trap depth $U_0 = 1400 \pm 30\,\mu$K and a temperature $T = 190 \pm 20\,\mu$K. For these parameters the thermal-averaged single-atom coupling is $g/2\pi = 60$ MHz (see appendix **??**), thus strong coupling is reached at the level of each individual atom. Following the method presented in section III.1.2, we compute the spectral distribution of couplings $\rho(\omega)$ for these parameters. The distribution is shown in figure III.3. It has an asymmetrical shape and features a bounded support 1750 MHz wide, which corresponds to the highest possible value of the light-shift for this trap depth. The frequency ω_c of the cavity mode is tuned to resonance with the mean value of the frequency distribution. Following the procedure described in (ref to section 2.3.3) we first prepare ≈ 800 atoms in the $|F = 2,m_F = 2\rangle$ Zeeman sublevel. We then probe the cavity-atoms coupled system and measure the transmission spectrum, as described in (ref section 2.3.4).

As the single-shot spectra are strongly discretised (see figure IV.2), we average such spectra to obtain the experimental data shown infigure III.3. Because experimental fluctuations of N result into fluctuations of the collective coupling, we group and average the spectra according to their collective coupling Ω to avoid excessive broadening due to averaging. We use a 40 MHz bin centerered on $\Omega/2\pi = 1670$ MHz, where the number of spectra in the bin is maximal: ≈ 200.

Despite the broad atomic frequency distribution, the resulting averaged spectrum features only two peaks corresponding to the polaritons. To first order in $\Delta\omega/\Omega$ with $\Delta\omega$ the width of the frequency distribution, they are split by twice the collective coupling $\Omega/2\pi \simeq 1670$ MHz, which corresponds to $N \approx 770$ atoms trapped in the cavity mode. In this regime, we fully benefit from the cavity protection effect: as the two polaritons lie far from the frequency

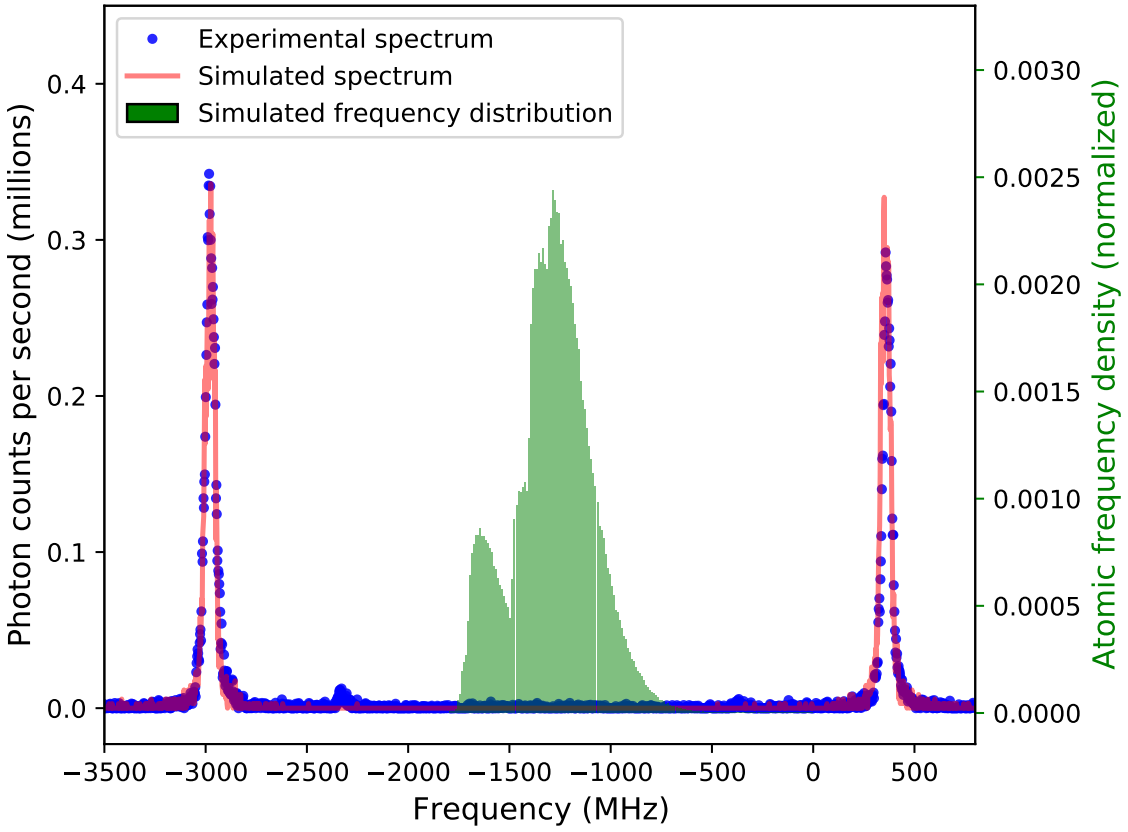

Fig. III.3 *Cavity protection effect. Blue dots represent the experimental on-resonance transmission spectrum in the regime where the collective coupling is much larger than the atomic frequency distribution. The two polariton modes appear as two narrow transmission peaks, in good agreement with the numerical simulation (red line). Green bars show the simulated atomic frequency distribution, which is much broader than the transmission peaks.*

distribution, they are decoupled from the dark states and the coherence of the system is preserved. As a consequence, the transmission spectrum resembles that of a frequency-homogeneous system (see section I.3) in spite of the strong atomic frequency inhomogeneity.

To be more quantitative about the gain in coherence obtained with the cavity protection effect, we fit independently the high and low frequency peaks of the averaged spectrum with a Voigt profile to extract the half-width at half-maximum (HWHM) of the peaks. We obtain a HWHM width ($\delta\omega_-/2\pi = 28 \pm 2\,\mathrm{MHz}$) of the low frequency peaks slightly larger than the one of the high frequency peak ($\delta\omega_+/2\pi = 24 \pm 2\,\mathrm{MHz}$), probably due to the presence of atom losses during the measurement. Indeed atom losses lead the low frequency peak to move in the same direction than the increasing frequency probe (thus the enlargment) and lead the high frequency peak to move in the opposite direction than the probe (thus the narrowing). The quoted uncertainty for $\delta\omega_\pm$ is the standard deviation of the different HWHM values obtained

for averaged spectra from non-overlapping 40 MHz bins in the $\Omega/2\pi$ interval $[1500 - 1700]$ MHz, which is deep in the cavity-protected regime, where the width does not depend on Ω. We note that the measured widths $\delta\omega_\pm$ are larger than in the homogeneous limit of $(\kappa+\gamma)/2 \simeq 2\pi \times 9\,\text{MHz}$, mainly because of the non negligible size of the collective coupling bin: 40 MHz. Indeed, the convolution of a Lorentzian with HWHM 9 MHz with a square function of size 40 MHz gives a peak of HWHM ≈ 22 MHz, close to the experimental values. The residual difference is due to 1) the finite-size of the collective coupling sample within the bin, which is not exactly uniformly distributed and 2) the uncertainty in determining the collective coupling as the distance between the peaks in a single-shot spectrum, due to its strong discretisation (see figure IV.2).

For the following, we will consider the average width $\delta\omega/2\pi = \frac{\delta\omega_+ + \delta\omega_-}{2}/2\pi = 26 \pm 2$ MHz. It is much lower than the HWHM width $\Delta\omega/2\pi \approx 150 \pm 10\,\text{MHz}$ of the frequency distribution. The ratio $\frac{\Delta\omega/2}{\delta\omega}$ can be used to define a figure of merit of the cavity protection. It compares the measured polaritonic peak width $\delta\omega$ and the width $\Delta\omega/2$ that would be obtained for a Lorentzian frequency distribution inhibiting the protection effect [47–49] This ratio is about 3 for our experiment, showing that the coherence of the polaritons is preserved[1].

Finally, we simulate the average spectrum of figure III.3 by computing many transmission spectra with a trap depth $U_0 = 1400\,\mu\text{K}$ and a temperature $T = 190\,\mu\text{K}$. The intensity transmission spectrum (relevant for a comparison with the experimental spectra) is computed as $|t(\omega)|^2$, where $t(\omega)$ is the complex transmission, given in equation III.6. We draw randomly the number of atoms N, to account for experimental fluctuations. We average single spectra (≈ 350) featuring a collective coupling within the bin $1670 \pm 28\,\text{MHz}$. This corresponds to the bin chosen for the experimental spectra, enlarged by $\pm 8\,\text{MHz}$ to account for the 1-standard deviation uncertainty on frequencies of the spectrum (ref to section 2.3.4). As can be seen on figure III.3, the simulated spectra including atom number fluctuations are in excellent agreement with the experimental data: the fitted width of the simulated spectra are $\delta\omega_+/2\pi = 27 \pm 2$ MHz and $\delta\omega_-/2\pi = 28 \pm 1$ MHz, close to the experimental values.

III.3 Polariton frequency-modulation engineering

III.3.1 Frequency modulation of polaritons in the protected regime

The coherence of the polaritons being preserved by the cavity protection, we can then harness the large sensitivity of the light-shifted atomic frequency to the trapping power to efficiently modulate the polaritonic frequencies. Frequency modulation of polaritons has been first demonstrated in reference [110], though in a different parameter regime, as explained later.

The intracavity lattice power is modulated by coupling two different frequencies of the lattice light into the cavity. To achieve this, we combine the RF signal at frequency ν_{EOM1} to an extra RF signal at frequency ν_{EOM3} and send the resulting signal to first EOM modulating the intracavity lattice light, $EOM1$ (see figure II.7). Together with the modulation at frequency ν_{EOM2} produced by the second EOM ($EOM2$), we obtain $3^3 = 27$ optical frequency components, among which: the usual one, at frequency $-\nu_{EOM1} + \nu_{EOM2}$, to which

[1] For curiosity, if we correct for the bin convolution effect, we find that, in the worse case corresponding to $\delta\omega_-/2\pi = 28$ MHz, this can be account for the convolution of a Lorentzian with HWHM 20 MHz with a bin of width 40 MHz. For such reduced with the ratio is 3.75, only slightly higher than the non-corrected value.

the cavity is locked, and an other one, at frequency $-\nu_{EOM1}+\nu_{EOM3}$, that can be tuned to be ω_m-apart from the cavity frequency, if $|\nu_{EOM2}-\nu_{EOM3}|=\omega_m/2\pi$.

As $\omega_m/2\pi = 120\,\mathrm{MHz}$ is not too large compared to the cavity linewidth $\kappa = 14.2$ MHz, both frequency components enter the cavity. The resulting beating at a frequency $\omega_m/2\pi$ leads to a temporal modulation of the lattice potential and thus of the average light-shifted frequency of the atoms $\overline{\omega_A}(t) = \overline{\omega_A^0} + \beta_o\omega_m\cos(\omega_m t)$, where β_o is the modulation index and $\overline{\omega_A^0}$ the average atomic frequency without modulation. The modulation frequency $\omega_m/2\pi = 120\,\mathrm{MHz}$ is set to be larger than the width of the polaritons $\delta\omega$ but smaller than the collective coupling $\Omega \approx 1600$ MHz. The trap depth is $1400\,\mu$K and the temperature is $190\,\mu$K, similar to the data of figure III.3. We record the transmission spectrum and average about 200 spectra.

The results are presented in Fig. III.4. Instead of the usual polariton doublet, the spectrum features two combs each consisting of several peaks. The frequency splitting between the centers of the two combs is given by the collective coupling $\Omega/2\pi$ whereas the comb teeth are separated by the modulation frequency $\omega_m/2\pi$. In contrast to the experiment of reference [110] where $\omega_m \gg \Omega$, the transmission spectrum does not result from the coupling between the cavity field and a single-frequency atomic excitation given by one sideband of the modulated atomic transition. In our case, the photonic excitation couples to a multi-frequency atomic excitation, yielding polaritons featuring multiple frequencies in their spectrum.

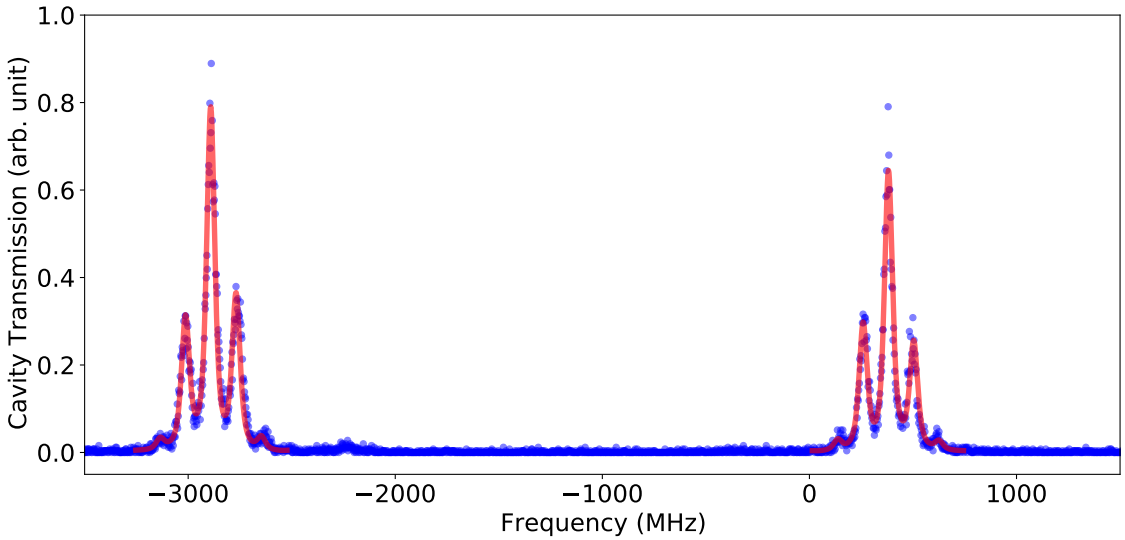

Fig. III.4 *Modulation of the polariton eigenfrequencies. Blue points: experimental data with* $\Omega/2\pi = 1630 \pm 20\,MHz$, $\omega_m/2\pi = 120\,MHz$, $\beta_o = 2.17 \pm 0.04$. *Red line: simulated spectrum obtained by numerically integrating the master equation.*

For $\omega_m \ll \Omega$, we show in section **??** that the theoretical cavity spectrum is well approximated by:

$$S(\omega) \propto \sum_n \frac{J_n^2(\beta_o/2)}{(\omega-\omega_0-n\omega_m+\Omega)^2+\gamma_s^2} + \frac{J_n^2(\beta_o/2)}{(\omega-\omega_0-n\omega_m-\Omega)^2+\gamma_s^2}, \tag{III.7}$$

where $\omega_0 = \omega_c = \overline{\omega_A^0}$ and $\gamma_s = \frac{\kappa+\gamma}{2}$. The cavity spectrum features two combs of peaks centered at $\pm\Omega$. The separation between two consecutive peaks is given by the modulation frequency ω_m. The amplitude of each peak is given by $J_n^2(\beta_o/2)$ and so we define a modulation index for the polaritons given by $\beta_p = \beta_o/2$. This linear relation is checked in section III.3.2. The spectrum of the polaritons can thus be directly controlled by tuning the modulation index and/or the modulation frequency of the trapping light. This is possible thanks to the large sensitivity of the excited state to the trapping power. An important remark is that the width of each peak in the multi-frequency polaritons is similar to the ones obtained in the non-modulated homogeneous case and is much narrower than the atomic frequency distribution as we operate in the cavity-protected regime. We would like to emphasize that we fully benefit from cavity protection here. Indeed, resolving the spectral modulation of the polaritons requires $\delta\omega < \omega_m$. Also, the modulation frequency $\omega_m/2\pi$ cannot be made arbitrarily large compared to the cavity linewidth $\kappa/2\pi = 14.2$ MHz, as it requires coupling two optical frequency, ω_m-apart, in the cavity. Thus, for satisfying $\delta\omega < \omega_m$, we benefit from having a cavity-protected small width $\delta\omega$, in particular much smaller than the width of the frequency distribution.

Let us now discuss a few technical details about spectrum averaging and fitting. From shot to shot, the number of atoms inside the cavity mode fluctuates. Thus, before averaging, we use two techniques to compensate these fluctuations:

1) we select spectra with similar atom number N, by measuring the dispersive shift $\delta\omega_c$ of the cavity frequency when the atoms are in the state $|F = 1, m_F = 1\rangle$, which is given by:

$$\delta\omega_c = \frac{-N g^2_{|2,2\rangle\to|3,3\rangle}}{2(\omega_{|1,1\rangle\to|2,2\rangle} - \omega_c)} \tag{III.8}$$

For the experimental data of figure III.4, we used a dispersive shift bin $\delta\omega_c/2\pi = -258 \pm 5$ MHz, corresponding to $N = 1130 \pm 25$ or to collective coupling $\Omega/2\pi = 2020 \pm 20$ MHz.

2) within this ± 25 atom bin, the remaining atom number fluctuations still widen the transmission peaks. Thus, before averaging spectra, we frequency-shift each spectrum so that the multipeaks centers of all spectra are aligned. Compared to a raw averaging, this technique improves the accuracy of the relative amplitudes of the different peaks in the average spectrum to which the value of β_p is very sensitive.

In spite of these two techniques, residual fluctuations remain, and the frequency values of our spectrum have an uncertainty of ± 8 MHz (see section II.3.4). Thus, the average spectrum is best-fitted when replacing the Lorentzians in equation III.7 by Voigt functions, which are convolutions of the Lorentzian lineshape with gaussian fluctuations:

$$\sum_n J_n^2(\beta_p)\,\mathrm{Voigt}(\omega - \omega_0 - n\omega_m \pm \Omega, \gamma_s, \sigma) \tag{III.9}$$

where $\mathrm{Voigt}((\omega, \gamma_s, \sigma) = \frac{1}{\sqrt{2\pi}\sigma}\Re(\mathrm{wofz}(\frac{\omega+i\gamma_s}{\sqrt{2}\sigma}))$ with wofz the Faddeeva function. This function provides a very good fit of the experimental data, except for the slight asymmetric shape (relative variation of $\pm 7\,\%$) between the right and left part of each comb, clearly visible on figure III.4.

This asymmetry stems from the coupling between the two polaritons induced by the modulation. This coupling has been neglected in equation III.7. To account for this coupling and compute a better approximation of the spectrum, we numerically integrating the master equation, using QutiP [111], for an emitter-cavity system probed by a laser swept in frequency at the same rate as in the experiment (1 GHz/ms), and with the same power. We calculate the population of the state $|1, G\rangle$ after binning the simulated results to match the experimental spectral resolution of 2.5 MHz. By using the parameters given by the experimental fit (equation III.9), we obtain a very good agreement between the experimental data and the master equation simulated spectra, even for the asymmetrical shape of the comb.

III.3.2 Modulation transfer

We now verify the expected linear transfer of the frequency modulation from the atoms to the polaritons, which expresses as $\beta_p \propto \beta_0$, that appears in equations III.9 and III.7. To this purpose, we measure β_p for different values of β_o. We reduce the frequency range of the probe laser scan by a factor of 4, zooming on the high frequency comb, to increase the frequency resolution. For each value of β_0, we measure and average ≈ 100 spectra, with the techniques explained previously in section III.3.1. We then fit the cavity spectrum with the function of equation III.9 to extract the value of β_p.

Since β_p is the result of a non-linear fit, we resort to a nonparametric bootstrap method to determine its uncertainty. For each averaged spectrum (and thus each value of β_p), we generate 500 synthetic spectra A_k ($1 \leq k \leq 500$). Then, each synthetic spectrum A_k is fitted with the formula III.9, providing a fitted parameter $\beta_{p,k}$. The errorbar for β_p is defined as the ± 1 standard deviation of the set $\{\beta_{p,k}\ ;\ 1 \leq k \leq 500\}$. To obtain the value of β_0, we measure the intensities of the different frequency components of the trapping light, using the transmission spectrum of the frequency-scanned cavity. Starting from $\overline{\delta\omega_a(t)} = \overline{\omega_A}(t) - \overline{\omega_A^0} = \beta_0\omega_m\cos(\omega_m t)$, we get:

$$\beta_0 = \frac{\delta\omega_a^{max}}{\omega_m} = \frac{|\overline{\omega_A^0}|}{\omega_m}\frac{\delta\omega_a^{max}}{|\overline{\omega_A^0}|} = \frac{|\overline{\omega_A^0}|}{\omega_m}\frac{\delta I_D^{max}}{I_D^0} \tag{III.10}$$

where $\overline{\omega_A^0}/2\pi = -1320$ MHz is the average atomic light-shift, $\omega_m/2\pi = 130$ MHz is the modulation frequency (this value is slightly different than the 120 MHz of figure III.4, for technical reasons), and I_D^0 and δI_D^{max} are, respectively, the constant and ω_m frequency-dependent components of the intensity of the trapping light. Uncertainties on β_0 are propagated from the experimental uncertainties of ω_a^0, I_D^0 and δI_D^{max}.

The results are shown in figure III.5. The linear transfert is confirmed, and the fitted slope is compatible, within its $\pm\sigma$ error bar, with the expected value 1/2.

III.4 Conclusion

The case of a single mode of the electromagnetic field coupled to N emitters with different frequencies is a situation of interest for different physics communities. It has been well known in solid state physics that achieving strong collective coupling of the emitter ensemble to

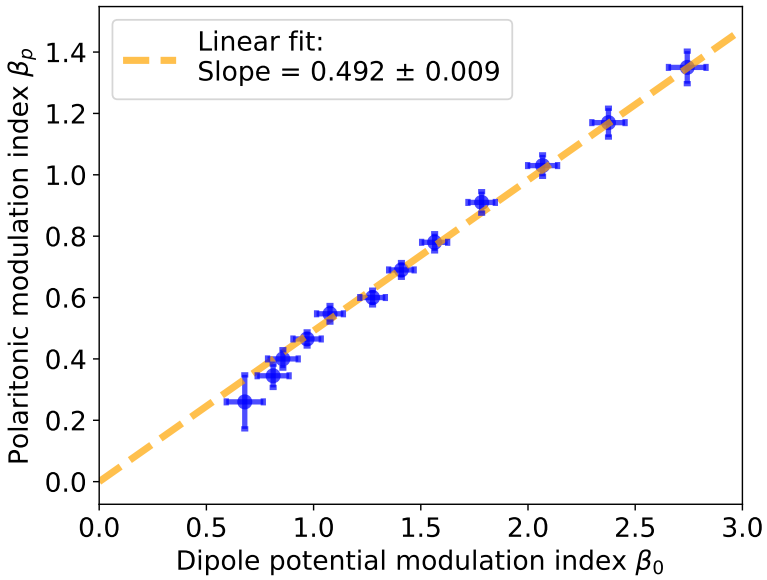

Fig. III.5 *Modulation transfer function. Blue points: experimental data of the modulation index of the polaritons β_p for different values of the modulation index β_o of the atomic frequency. Orange dashed line: linear fit of data points gives a slope of* 0.492 ± 0.009*, compatible with the theoretical slope of 0.5.*

the cavity could allow a coherent interaction between the field and emitters. As theoretical studies of this "cavity protection" effect pointed out, the coherent interaction is possible only if 1) the collective coupling Ω is large enough compared to the width $\Delta\omega$ of the inhomogeneities and 2) the inhomogeneous frequency distribution decays faster than a Lorentzian one. Several solid-states experiment have demonstrated cavity protection and exhibited the narrowing the polaritons as Ω/Δ increases. In our experimental setup, the intra-cavity lattice at 1559 nm induces a very significant differential lightshift, typically one to two orders of magnitude larger than the widths of the cavity and the atom. Together with the thermal distribution of atomic positions in the lattice, it leads to a wide but tunable distribution of atomic frequencies, which we measure with the spectrum of losses induced by a beam transverse to the cavity. As the distribution is bounded, it is eligible for cavity protection. Thanks to our single emitter strong coupling, we observe a cavity protection effect with less than 800 atoms. The polaritons peaks are much narrower than the distribution, a signature that the coherence is preserved by the strong collective coupling.

In this cavity-protected regime, we make use of the large sensitivity of the atomic frequency to the intra-cavity lattice trap power. A temporal modulation of this power induces a frequency modulation of the atomic transition, which transfers to a frequency modulation of the polaritons. We develop a model for the frequency modulated hamiltonian, that accounts very well for the experimental spectrum, including a small amplitude asymmetry between the modulation side peaks, that stems from the coupling between the two polaritons. Finally, we verify the linear transfer of the frequency modulation predicted by this model.

Chapter IV

Transition from the polaritonic regime to the disordered regime

In chapter III, we have demonstrated that cavity protection maintains the coherence of an ensemble of hundreds of emitters, in spite of their inhomogeneity in frequency. Such number is orders of magnitude lower than for previous solid-state demonstrations of cavity-protection [50–52], because our setup achieves strong coupling at the single emitter level.

Another specificity of our controllable cold-atom experiment is the ability to tune easily both the collective coupling Ω and the amount of frequency inhomogeneity $\Delta\omega$. As the cavity protection effect depends precisely on the ratio $\Omega/\Delta\omega$ we are able to observe directly the growing coherence of the coupled system, as $\Omega/\Delta\omega$ increases. In this chapter we experimentally show the transition from a "polaritonic" regime (cavity-protected) where only two polaritonic resonances are present despite an inhomogeneous frequency distribution that is much larger than the polariton resonances, to a "disordered" regime (or cavity-unprotected) where the amplitude of the polaritons decreases and many additional, randomly distributed resonances appear. In addition, as our system operates in the strong coupling regime at the single atom level, we are able to study this transition for a few tens of atoms only, highlighting the contribution of a finite number of dark states.

I mentioned earlier that most of the material of chapters III and IV were the results of an indubitable team work that lead the article [53]. My more personal contributions consisted in 1) developing the methods to calibrate the frequency axis of the transmission spectrum (see section II.3.4), which has been crucial for resolving spectrally the transition from the disordered regime to the polaritonic regime and 2) based on the intuitions illustrated in section IV.1, establishing the individual-spectrum analysis of the transition presented in section IV.4.

This chapter is organised as follows: section IV.1 proposes a visual introduction to the transition from the polaritonic to the disordered regime, based on simulated transmission spectra. One can see the increasing number of resonances, corresponding to the increasing coupling of the dark states to the cavity, which reduces the coherence of the coupled system. Then we exhibit two quantities that account for the degree of coherence of the system. In IV.2, we introduce the photonic weight of the dark states, that accounts for their coupling to

the cavity, which determines the coherence of the coupled system. Such photonic weight can be computed from numerical simulation of our few-emitter system. As we cannot directly measure the photonic weight in our discretised experimental spectra, we propose a robust experimental proxy for the photonic weight, based on the number of photon counts outside the two narrow polariton peaks, in IV.3. Finally, with these simulation and experimental tools, we exhibit the role of dark states across the transition, in IV.4, and compare our results to that of the similar simulatenous study, reported in [54].

As mentioned earlier, we go from the polaritonic regime to the disordered regime by varying the ratio $\Omega/\Delta\omega$, where $\Omega = g\sqrt{N}$ is the collective coupling and $\Delta\omega$ the width of the inhomogeneous frequency distribution. Here, $\Delta\omega$ is fixed (as we work at a given intra-cavity trap depth U_0) and we vary Ω. The thermal-averaged single atom coupling g being fixed by the trap depth U_0 (see appendix **??**), we vary Ω through the number N of atoms loaded in the intra-cavity lattice, which we tune by varying the number of atoms loaded in the 3D-MOT.

IV.1 Visual introduction to cavity protection in our discrete system

Figure IV.1 illustrates the effect of decreasing the ratio $\Omega/\Delta\omega$ with simulated transmission spectra (equation III.6). The trap depth is $U_0 = 1040$ µK, the temperature is $T = 140$ µK, the thermal-averaged coupling strength is $g/2\pi \approx 60$ MHz and the cavity is tuned on resonance with the average frequency $\overline{\omega_a}$ of the coupling-weighted distribution $\rho(\omega)$ (see appendix **??**). We plot $|t(\omega)|^2$ for $N = 150$ (graph a.) and for $N = 34$ (graph b.), together with the atomic frequency distribution $\rho(\omega)$ in the background. With $N = 150$, the spectrum exhibits the usual Rabi doublet, with two clear peaks separated by $2\Omega \approx 2\pi \times 1460$ MHz, corresponding to the coherent excitation of the polariton modes: this is the polaritonic regime. With $N = 34$, the spectrum exhibits many more peaks, corresponding to other eigenstates, because the collective coupling is sufficiently low for the protection effect to vanish: this is the disordered regime. The separation between the two ensemble of peaks (at higher and lower frequencies) is roughly $2\Omega \approx 2\pi \times 700$ MHz.

From observing other simulated spectra, we can see that these extra peaks appear only when the frequencies $\omega_\pm/2\pi = (\omega_c \pm \Omega)/2\pi$ (where one would expect the polaritons to be, in the polaritonic regime) lie within the frequency range of the distribution: $\approx [-1650 : -250]$ MHz. To make this observation quantitative, we compute the number of transmission peaks N_{peaks} above a threshold, for each spectrum. Graph c. of figure IV.1 shows N_{peaks} averaged over many spectra, for N ranging from 1 to 550: it shows the continuity between the disordered and the polaritonic regimes. For $N \leq 25 \pm 5$, N_{peaks} increases because the number of eigenstates $N + 1$ increases and all can couple to the cavity: thus they appear as extra peaks on the transmission spectrum. For larger N, collective coupling is strong enough for cavity protection to take place: the coupling to the cavity of these other eigenstates diminishes. Consequently, the amplitude of the corresponding spectral peaks diminishes and they end below the threshold, leading to a reduction N_{peaks}. Finally, for $N \geq 130 \pm 20$, $N_{peaks} = 2$ and only the two bright states couple to the cavity. This corresponds to Rabi

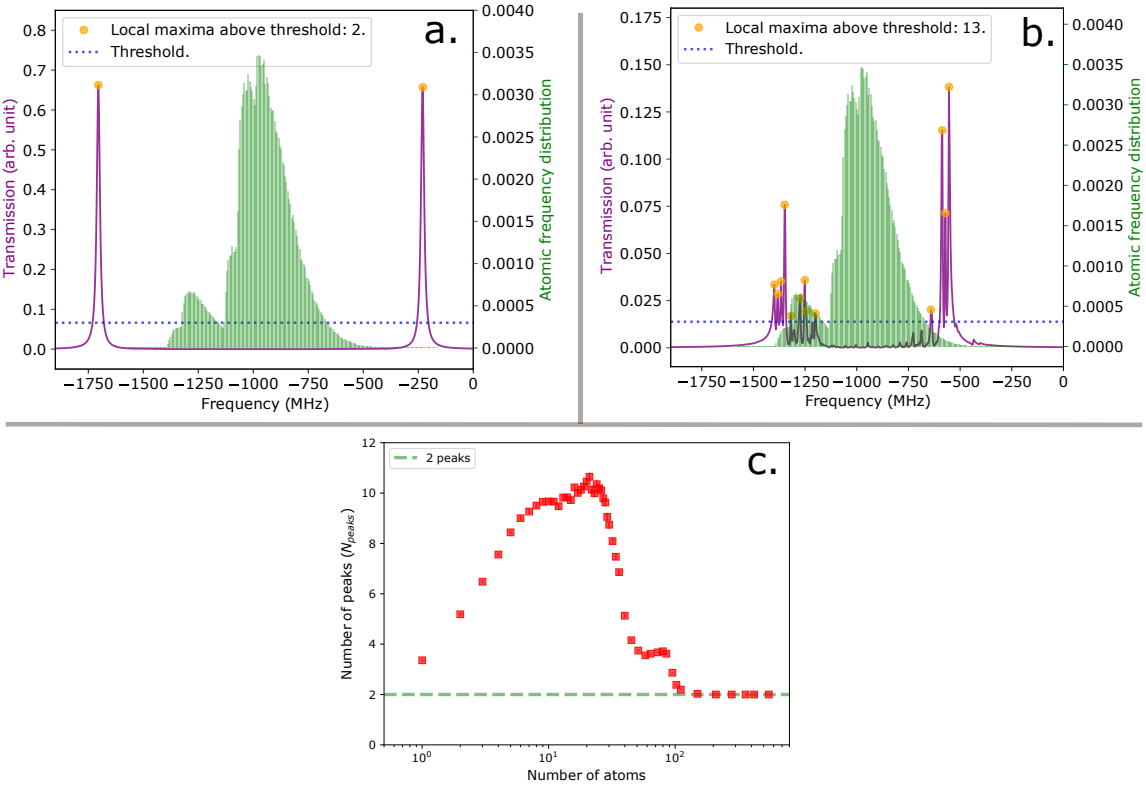

Fig. IV.1 *Illustration of the cavity protection effect with simulated transmission spectra. Picture a (respectively b) shows a transmission spectrum with* $N = 150$ *(respectively* $N = 34$*) atoms, in the polaritonic (respectively disordered) regime. To exhibit continuously the transition between the two regimes, we computed the number of peaks* N_{peaks} *of each spectrum, defined as* $1/10$ *of the maximal transmission of the spectrum. Graph c. shows the average value of* N_{peaks} *for atom number* N *ranging from* 1 *to* 550.

separation $\approx 2\Omega/2\pi \geq 1400 \pm 100$ MHz, which matches indeed roughly the size of the bounded frequency distribution.

IV.2 Photonic weight distribution to monitor the cavity protection effect

The study of the previous section shows that a transition occurs between an disordered regime and a polaritonic regime for atom numbers lower than 150. It is possible to see this evolution within such a small atom number range because we operate in the strong coupling regime at the single atom level. Such numbers of emitters are orders of magnitude below the numbers of previous solid-state experimental demonstrations of cavity protection ($\sim 10^{12}$ in ref [50], $\sim 7 \times 10^{14}$ in ref [52], and $\sim 10^{6\,to\,7}$ in ref [51]). So unlike these experiments, we cannot model our system with a continuous frequency distribution of emitters. We are sensitive to the finite size of the Hilbert space and to the discreteness of the spectrum of

the coupled emitters-cavity system. This leads to multipeak transmission spectra (see figure IV.1) rather than inhomogenously broadened polaritons as in [50–52] and to the ability to directly compute the eigenvalues and eigenvectors of the coupled system and extract their properties, such as their photonic weight PW.

The photonic weight is interesting because the cavity protection effect can directly be assessed by measuring the photonic weight distribution over the different eigenstates. For a cavity-protected inhomogenous system, or equivalently for an homogeneous system, the PW is distributed over the only two bright states. For an unprotected system the PW is distributed over more than two eigenstates. This leads us to introduce the sum S_{PW} of the PW of all the eigenstates except the two largest ones, to quantify the spreading of the PW and thus the coherence of the coupled system: S_{PW} is zero for the homogeneous case and tends to 1 when the PW is distributed over an infinite number of dark states.

Here is how we compute the PWs and S_{PW}. In the low excitation limit, we restrict the dynamics of the closed system to the one excitation manifold. For N two-level atoms, it is spanned by the $N+1$ basis states :

$$\{|1,G\rangle, |0,E_1\rangle, \ldots, |0,E_k\rangle, \ldots, |0,E_N\rangle\}\,, \tag{IV.1}$$

with $|G\rangle = |g_1 \ldots g_N\rangle$ and $|E_k\rangle = |g_1 \ldots e_k \ldots g_N\rangle$, where $|g_k\rangle$ (respectively $|e_k\rangle$) is the ground (respectively excited) state of the atom k. Due to the 1559 nm trapping light, a given atom k is excited to the subspace of the $5P_{3/2}$ manifold featuring 16 eigenvalues $\omega_{k,j}$ and eigenstates $|\psi_{k,j}\rangle$. The single excitation manifold is then spanned by the $16 \times N + 1$ basis states:

$$\{|1,G\rangle, |0,E_{1,1}\rangle, \ldots, |0,E_{k,j}\rangle \ldots |0,E_{N,16}\rangle\} \tag{IV.2}$$

where$|G\rangle = |G_1, \ldots, G_k, \ldots, G_N\rangle$, with $|G_k\rangle = |g_{k,1} \ldots g_{k,j} \ldots g_{k,16}\rangle$ and $|E_{k,j}\rangle = |G_1, \ldots, g_{k,1} \ldots \psi_{k,j} \ldots g_{k,16}, \ldots, G_N\rangle$. In this basis, the Tavis-Cummings Hamiltonian for mutilevels atoms is given by an arrowhead matrix, from which we can numerically extract the $D = 16\times N+1$ eigenstates Ψ_i^C and eigenvalues ε_i ($i = 1, \ldots, D$) of the atoms - cavity coupled system. We can then compute the photonic weight of the eigenstates Ψ_i^C defined as the weight of the $|1,G\rangle$ component: $PW_i = |\langle 1,G|\Psi_i^C\rangle|^2$. Finally, S_{PW} can be calculated as the sum of all photonic weights except the two largest ones: $S_{PW} = 1 - PW_{max1} - PW_{max2}$.

IV.3 Measuring the dark state contribution in experimental spectra

As we probe the spectrum in the low-excitation limit, the number of photons collected is low and the measured spectrum is strongly discretised as shown in Fig.IV.2. This prevents us from directly extracting the PW of eigenstates exhibiting a low transmission. So we find an experimental proxy for this theoretical quantity, that also characterises the degree of coherence of the system: we measure the fraction F_{out} of photon counts outside a frequency range $\Delta f/2\pi$, in which most of the counts of the polariton resonances lie in the polaritonic regime:

1) We define the typical frequency width $\Delta f/2\pi$ of the polariton peak in the polaritonic regime (for $\Omega/2\pi \geq 1000\,\text{MHz}$) as twice the standard deviation σ of the photon-count

weighted frequency distribution. In this regime, we measure $\Delta f/2\pi = 140\,\text{MHz}$ and $\approx 90\%$ of the counts are within Δf.

2) We separate the spectrum into two halves at the cavity frequency ω_c. For each half of the spectrum ($\pm$) we compute:

   a) $\omega_\pm$, the barycenter of the photon-count distribution

   b) the couplings $\Omega_\pm = |\omega_\pm - \omega_c|$ and $\Omega = (\omega_+ - \omega_-)/2$

   c) the total number of counts $N_{tot,\pm}$

   d) the number of counts $N_{out,\pm}$ that are outside the intervals $[\Omega_\pm - \Delta f/2; \Omega_\pm + \Delta f/2]$.

3) Finally, we compute the fractions of counts outside of these intervals, $F_{out,\pm}$ (respectively F_{out}), for the two halves of the spectrum (respectively the total spectrum).

All these steps are illustrated on figure IV.2. The definition of $\omega_\pm$ does not rely on a fit and allows computing Ω even for multi-peak spectra in the disordered regime. To each coupling value we can associate an effective atom number $N = (\Omega/g)^2$ to compare experimental and simulation results.

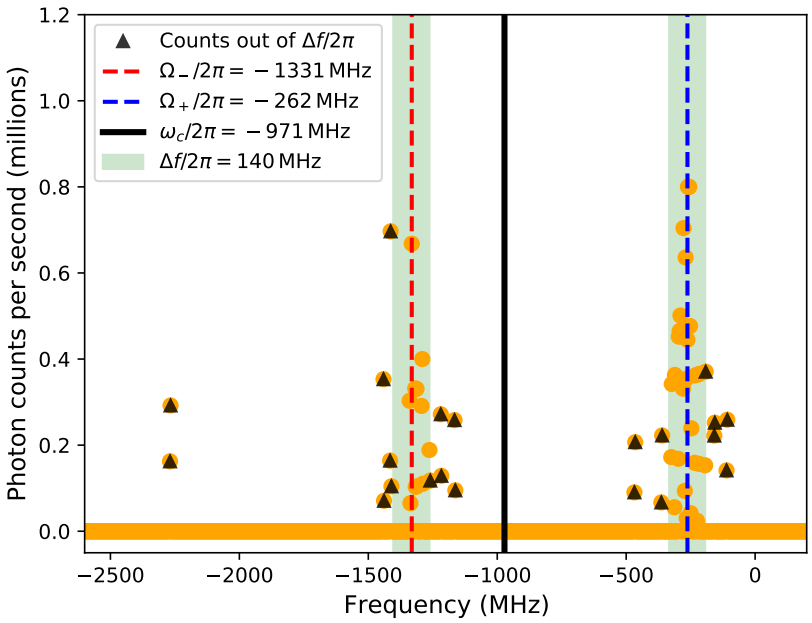

Fig. IV.2 *Single shot experimental spectrum. As we probe the coupled system in the low excitation regime, we collect few photons in transmission and the spectrum is discretised (orange dots). For each spectrum, we compute the fraction F_{out} of photons (identified with black triangles) that lies outside of a frequency window $\Delta f/2\pi$ (green colored area), centered on each peak distribution (red and blue dashed lines).*

IV.4 Across the transition from the disordered to the polaritonic regime

We have introduced two quantities (S_{PW} for the simulation, F_{out} for the experiment) that account for the degree of coherence and protection of the cavity-atoms coupled system. To explore experimentally the transition from the disordered to the polaritonic regime, we measure $\sim$ 2000 transmission spectra for an increasing number of atoms N (from $\sim$ 10 to 550). The trap depth is $U_0 = 1040 \pm 30\,\mu$K and the temperature is $T = 140 \pm 20\,\mu$K. The cavity frequency is set equal to the average frequency of the corresponding coupling distribution $\rho(\omega)$ (red distribution in figure III.1): $\omega_c = -970\,$MHz (this choice is justified in appendix **??**).

For each experimental spectrum, we compute Ω and F_{out} following the procedure described in IV.3. We get a cloud of points (Ω, F_{out}), which we average with 30 MHz-bins of Ω. We compare the resulting F_{out} values with the simulation of S_{PW}. For each value of the atom number N from 1 to 550 we draw N random atomic positions, deduce the associated values of frequencies and cavity couplings ($\omega_{k,j}$,$g_{k,j}$) and compute the PW of the different eigenstates as described in section IV.2. For each value of N, we average S_{PW} over 300 repetitions, and compute the corresponding coupling $\Omega = g\sqrt{N}$. Both F_{out} and S_{PW} are plotted on Fig. IV.3.

As expected, we find that the shape of F_{out} data closely traces the calculated S_{PW}. We interpret the common behavior of F_{out} and S_{PW} in terms of two competing effects. As N increases, the dimension $(N+1)$ of the Hilbert space of the system rises, and so does the number of states available to carry part of the photonic excitation outside Δf. The collective coupling Ω also increases (scaling as $\sqrt{N}$), and spreads the PWs to eigenstates close in frequency of Ω as long as the system stays in the disordered regime $\Omega \lesssim \Delta\omega$. Then, above a certain value of the collective coupling $\Omega_t/(2\pi) \simeq 300$ MHz corresponding to $N \simeq 25$ atoms, the cavity protection effect starts to reduce S_{PW} and F_{out}, which then decreases to an asymptotic value for higher Ω. In the large collective coupling limit, S_{PW} and F_{out} are low, because the photonic weight - and thus the photon counts - concentrate in the two polaritonic states. Even though S_{PW} and F_{out} account for the same features of the system, we insist that they cannot be strictly compared. Indeed, the exact values of F_{out} depend on the chosen value of Δf. However, after checking that the overall shape of F_{out} data is robust against such a choice (see Fig. IV.4), we can assert that S_{PW} and F_{out} are qualitatively similar. Their shape is close to that of N_{peaks} in figure IV.1 (section IV.1), because the number of resonances also relates to the overall coupling of dark states to the cavity.

To underline the role of cavity protection contribution, we simulate S_{PW} for a Lorentzian distribution with the same average frequency and HWHM width as the experimental one. In this case (see in Fig. IV.3), after the initial increase, S_{PW} stays on a plateau as no cavity protection occurs. In this case, the number of eigenstates coupled to the cavity mode does not depend on Ω but only on the width of the frequency distribution.

Finally, it is interesting to consider $F_{out,\pm}$ separately, because the atomic frequency distribution is asymetric. In the two plots of Fig. IV.5, we show both experimental values of $F_{out,\pm}$, as well as the simulated fractions $S_{PW,\pm}$ of the total photonic weight held by the dark states on the $\pm$ halves of the spectrum. All three curves agree qualitatively. We note that photonic weight fraction S_{PW} is sensitive to the fine details of the atomic frequency distribution. Indeed, on $S_{PW,-}$, the two peaks at $\Omega/2\pi = 300 \pm 10\,$MHz and $\Omega/2\pi = 510 \pm 15\,$MHz

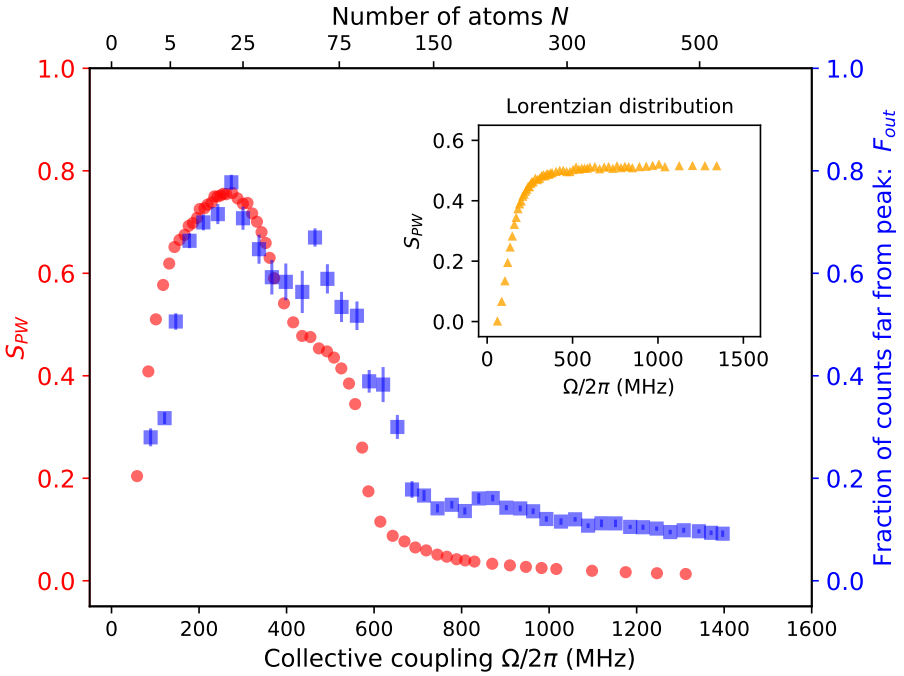

Fig. IV.3 *Transition from the disordered to the polaritonic regime. For a given atomic frequency distribution, we increase the number of atoms and thus the collective coupling. Blue squares: measured* F_{out}*. The vertical error bars are* $\pm\frac{\sigma}{\sqrt{N_p}}$*, where* σ *is the standard deviation of the* N_p *points gathered within bins of* $\Omega/2\pi = 30\,MHz$ *. Beyond a collective coupling* $\Omega_t/(2\pi) \simeq 300\,MHz$*, corresponding to* $N_t \simeq 25$ *atoms, the fraction of photon counts outside the two polariton peaks rapidly drops.* F_{out} *is closely traced by the simulated photonic weight* S_{PW} *(red circles): confirming that the off-peak transmission corresponds to dark states whose photonic weight drops as faster coupling wins over disorder-induced dephasing. For comparison, the inset shows* S_{PW} *in the case of a Lorentzian resonance frequency distribution. Since no cavity protection occurs in this case,* S_{PW} *remains high at large collective coupling.*

correspond to two lobes of the distribution (see the upper plot of Fig. IV.5).

As mentioned earlier, an interesting parallel can be made between our study of cavity protection and a complentary study with many analogies, performed simulatenously, and reported in [54]. The setup is shown in Figure 1 of reference [54]. In this CQED-cold-atom experiment ^{6}Li atoms interact with a near-concentric Fabry Perot cavity, in the strong coupling regime ($C_{max} = g^2/(2\kappa\gamma) = 3.2$). As in our experiment, atoms are trapped in an optical lattice commensurate with the probe lattice ($1342 = 2 \times 671$ nm) to ensure maximal and homogeneous coupling to the probe. Here, however, the distribution of frequency is generated from an extra dedicated *incommensurate* lattice, shown in blue Figure 1 of reference [54]. Due to its incommensurability, it induces a quasi-random distribution of lightshifted frequencies. As the resulting distribution is bounded, this system is eligible to

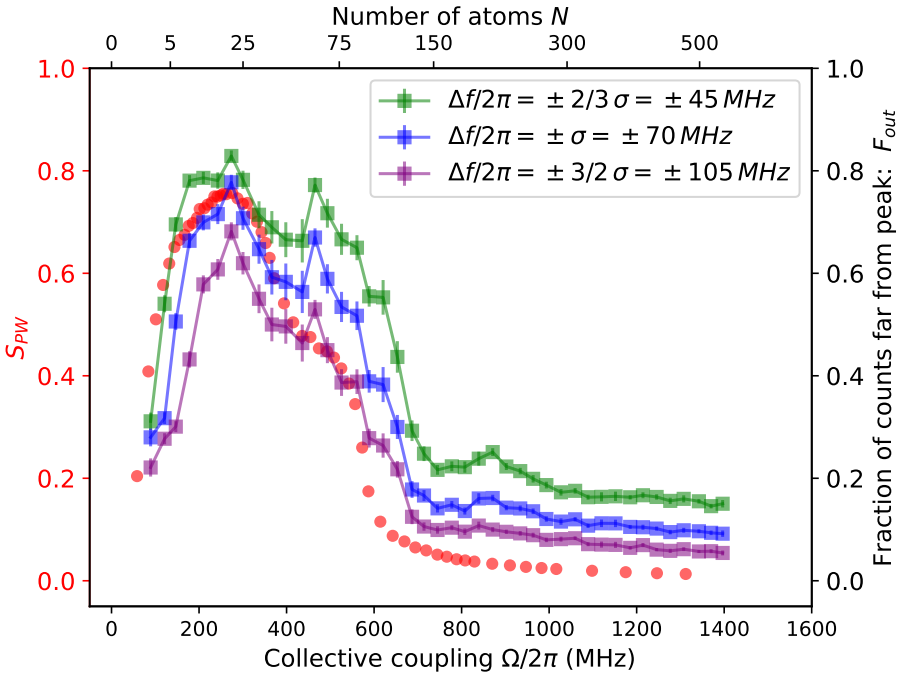

Fig. IV.4 *Robustness of F_{out} with respect to the size of the exclusion window Δf. Here we show F_{out} for several values of $\Delta f/2\pi$ chosen to define the exclusion window, together with the simulated photonic weight S_{PW}, as in Fig. 3 of the main text (red dots). The result is rather robust: when $\Delta f/2\pi$ decreases, the shape of F_{out} remains the same, and is shifted upwards as expected.*

cavity protection (see section I.3.2).

The ratio between the width of the frequency distribution W and the collective coupling $\Omega = g\sqrt{N}$ is varied by tuning W with the intensity of the lightshifting lattice. Upon driving the cavity mode, the cavity and the atomic responses are measured and expressed as photonic χ_p and atomic χ_a susceptibilities to the probe (see Figure 2.b of reference [54]). χ_p is proportional to the cavity transmission, which we measure as well. The authors extract supplementary information from the atomic excitation, and show that χ_a can be measured from the population of an auxiliary level, in which part of the atoms are depumped during the probing. Both the spectra of χ_p and χ_a (see Figure 2.c,d,e,f and k of reference [54]) exhibit two well separated polaritons for a small ratio W/Ω (polaritonic regime). In the disordered regime, for higher W/Ω, the polaritons tend to disappear, and a broad structure appears in between, corresponding to the dark/grey states.

The authors also derive the photonic weight (PW) from χ_p, for both the dark states and the polaritons. The results are shown in picture d, where the filled (respectively empty) markers are the PW of the polaritons (respectively dark states). When W/Ω increases, the polariton PW decreases and the dark state PW rises, as observed in our experiment (see figure IV.3). Several differencies should however be mentioned:

1) Both experiments cover complentary ranges of W/Ω: In [54] W is tuned down to 0,

while we explored $W > 2\Omega$, corresponding to "polaritonic" frequencies [1] entering the distribution.

2) In our experiment, the distribution is smooth at its edges (see figure IV.1), compared to that of [54]. Due to this shape difference, the PW held by the dark states - in the disordered regime - is quite differently spectrally distributed. In [54], dark states "show up" between the two "polaritonic" peaks . In our experiment, conversely the dark states show up close to the two "polaritonic" peaks rather than in the middle of the spectrum, which is clear on figure IV.1.b. This highlights that the precise shape of the distribution does matter, even for bounded distributions[2] which always exhibit cavity protection of sufficiently high Ω.

To finish with, we report here only the part of the study of [54] done for a cavity close to resonance with the atoms. The competition between interactions and disorder is also studied in the dispersive far-detuned regime, realising an effective Lipkin-Meshkov-Glick magnetic Hamiltonian. As the disorder increase, the authors observe a transition from a ferromagnetic to a paramagnetic phase.

IV.5 Conclusion

Cavity protection can be understood has a gapping mechanism that decouples from the cavity the dark $N-1$ middle eigenstates of the system, such that only the upper and lower frequency eigenstates are involved in the dynamics. In that sense, the system behaves as a frequency-homogeneous system, provided that the collective coupling is large enough compared to the width of the frequency distribution.

Cavity protection is a continuous effect: the coherence of the coupled system increases as $\Omega/\Delta\omega$ increases. The corresponding progressive narrowing of polaritonic resonances has been measured in all previous solid-state studies. Here we take advantage of our considerably smaller number of emitter to study the increasing coherence for a mesoscopic number of tens to hundreds of emitters. Such small numbers allow to fully diagonalise the frequency inhomogeneous Tavis Cummings Hamiltonian and compute the photonic weight distribution. The fraction of photonic weight held by the dark states accounts for the degree of *decoherence* of the system. In experimental spectra, the strong discretisation prevents from measuring the photonic weight distribution and we find a robust experimental proxy that accounts for the spreading of the spectral density far from the polaritonic resonances. Both simulated and experimental quantities agree qualitatively and map the degree of coherence of the system as the number of emitters increases: the coherence initially decreases due to spreading of the photonic weight among the dark states. For atom number higher than 25, cavity protection starts to act and limit this spreading, increasing the coherence. For atom numbers higher than 200, the photonic weight is shared by only the two polaritons and the system is in the fully protected, polaritonic regime.

[1] We use this term, abusively in the disordered regime, to refer to the frequencies $\pm\Omega$, where one would have two polariton peaks in the polaritonic regime

[2] A fact that theoretical studies have not pointed out, as far as we know.

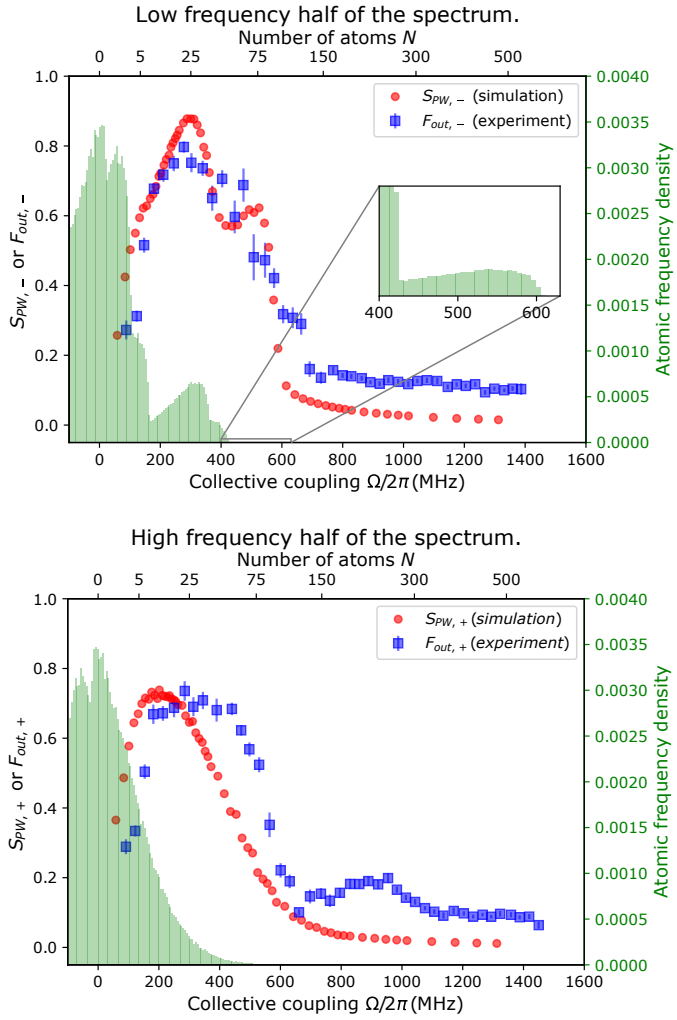

Fig. IV.5 *Sensitivity of the photonic weight distribution to local features of the frequency distribution.* $F_{out,\pm}$ *and* $S_{PW,\pm}$ *are shown for each* $\pm$ *half of the spectrum, together with the atomic frequency distribution (in green). Since this distribution is asymmetric, the curves are slightly different for the two halves. Most interestingly, for the low frequency half (upper graph),* $S_{PW,-}$ *is sensitive to small details of the frequency distribution, having a peak at the position of each of the peaks of the distribution, at* 300 *MHz and* 500 *MHz (see inset) respectively.*

Chapter V

Generation of multiple tweezers inside the fiber microcavity

An optical tweezers with a small waist is a convenient tool to trap a single atom probabilistically [55], when combined with resonant light. Once the tweezers is loaded with several atoms, shining resonant light on it induces light-assisted collisions, which expell pairs of atoms from the trap [112], with a rate $\propto 1/V \propto 1/(w_0^4)$ [113], where V and w_0 are the trap volume and waist of the tweezers. In a small trap volume, which we typically obtain by generating tweezers with waist close to diffraction limit: $w_0 \sim \lambda$, the "collisional blockade regime" [56] can be achieved, where the two-body losses are much faster than one-body losses, and atom pairs are lost until one or no atom is left in the trap. A single atom can thus be obtained with a probability of typically 50 % with conventional red-detuned optical molasses light. This probability can be increased up to ~ 90 % with tailored light-assisted collisions and blue detuned light, as shown in references [114, 115].

Several methods where introduced to generate and control multiple tweezers simulatenously. The two most powerful approaches are based on Spatial Light Modulators (SLM) and Acousto-Optic Deflectors (AOD). A SLM is a device able to imprint a phase mask to light passing through. Light can be tailored to almost arbitrary structure at a later position of interest along the optical path. And AOD is a acousto-optic crystal fed with a radiofrequency (RF) signal, turned to a soundwave in the crystal by a piezo. A laser beam passing through the crystal will be diffracted by the refractive index modulation induced by the sound wave, with an angle depending linearly on the frequency of the RF signal.

In the cold atoms community, SLM have been used to generate trapping potentials with arbitrary shapes (such as a flat potential) and the advantageous possibility to reconfigure the potential during the experiment [116–118]. The team of Antoine Browaeys at Institut d'Optique was the first to use a SLM to generate arrays of tweezers traps for individual atoms with an almost arbitrary geometry, first in 2D [119] and later in 3D [59]. In references [57, 59], the SLM-generated static tweezer array is combined with a single moving tweezers controlled by a 2D AOD and a tunable lens (to tune the tweezers focus along the 3^{rd} dimension) to rearrange single atoms within the SLM array of tweezers and generate almost 100 %-filling fraction in the aimed tweezer array, starting from a stochastically 50 %-filled larger array. At about the same time, the group of Mikhail Lukin at Harvard University developped a

method to rearrange $\approx$ 50 single atoms in an 1D array of tweezers generated by an 1D AOD [58]. A 1D AOD can generate multiple tweezers when driven by a multi-frequency RF signal. Destructive interferences prevent from generating such arrays, except if the relative phases and amplitudes of the frequency components are carefully optimised, as shown for the first time in reference [58]. Later, the Lukin group implemented a 2D tweezers architecture, similarly based on a SLM and a 2D AOD [60].

Without these rearrangement techniques, the probability to stochastically fully load an array of N tweezers with N single atoms is p^N, where p is the single tweezers loading probability, roughly equal to 50 % when the light-assisted collisions are produced by a standard red-detuned molasses. This exponential decay makes experiments with large N impracticable. Thanks to the rearrangement of single atoms in the arrays, both group pioneered the *deterministic* generation of almost perfectly filled single atoms arrays in 1D, 2D and 3D, opening the way to scalling up N. This was crucial for implementing quantum simulations with a few hundreds of Rydberg atoms (256 is [60], 196 in [62]), entering the regime where classical computation is intractable.

For our CQED experiment, we decided to implement tweezers in and close to our fiber cavity with AODs, since they are rather convenient to use and enable fast reconfiguration of tweezers arrays. As compared to the previously mentioned experiments, we need to align and focus the tweezers very precisely at the position of the micrometric cavity mode, which has been a major challenge. Already when mounting the aspherical lens producing the tweezers in the vacuum cell, the lens has been positioned with a lateral precision of a few tens of micrometers, as described in [89].

In this chapter, section V.1 describes the laser system and the optical layout that we have setup to generate tweezers in the microcavity, section V.2 presents how we generate multi-frequency RF signals, with optimised phases, for multi-tweezers operation of the AODs and section V.3 presents the results achieved with this tweezers setup.

V.1 Optical system

In this section, we will first present the optical performances of the high numerical aperture lens that we have set on top of our microcavity (V.1.1). Then we will describe our laser source (V.1.2), the full optical layout (V.1.3) and the alignement method we used (V.1.4) for focusing multiple tweezers inside the microcavity.

V.1.1 A high numerical aperture lens

We have set a high-resolution microscope to produce optical tweezers with submicron waists inside the fiber cavity, and furthermore address and image individually the intra-cavity trapping sites. The objective of this microscope is a single commercial molded aspherical lens (LightPath Technologies, Inc 352240), with numerical aperture NA = 0.5, focal length $f = 8$ mm and a working distance of 5.7 mm.

This objective, which has been characterized in [120] was chosen because:

1. it is diffraction limited for both ^{87}Rb D_2 line fluorescence imaging (780 nm) and our tweezers beam (808 nm) wavelengths.

2. for the imaging its resolution is small enough to resolve neighoor intra-cavity trapping sites, over a field of view corresponding to several tens of sites.

3. its working distance is large enough to be compatible with the mounting of the fiber cavity.

It has been rigidly mounted above the fiber cavity, inside the vacuum chamber [89]. A SNOM tip II.2 was used as a point-like source (1) to caracterize its optical performances at 780nm and (2) to align the lens with the cavity mode (see figure V.1):

1. The point spread function of the microscope was measured to check the diffraction-limit operation of the lens in our setup. Over a range of 60 µm perpendicularly to the optical axis its Full Width at Half Maximum (FWHM) is 0.80 $\pm$ 0.02 µm (see figure V.2). It corresponds to a Strehl ratio $S > 0.95$, which confirms the diffraction limited operation (conventionnally defined by $S > 0.8$). The FWHM is close to the lattice parameter $a = 780$ nm and should allow to resolve individually 75 trapping sites without any extra analysis. Indeed, our ratio FWHM/a ≈ 1.02 is quite comparable to that of the first quantum gas microscope [121] (FWHM/a ≈ 0.94). Using a deconvolution algorithm, we could resolve the 180 sites corresponding to the length of the cavity, $L = 145$ µm. Indeed, figure V.2 shows that over a range of 160 µm, FWHM < 1.0 µm $\Rightarrow$ FWHM/a ≈ 1.3 , a ratio similar that of the second pioneering quantum gas microscope experiment [122], where deconvolution has been implemented.

2. The FWHM increases as the SNOM tip is moved away from the optical axis. This was used to find the optical axis of the lens with a $\pm$10 µm uncertainty, and thus to set the transverse position of the lens with respect to the cavity. The same technique was used to optimise the distance between the lens and the cavity.

The mounting of the aspherical lens on top of the cavity, its alignement and the characterisation of its optical performances were all done by Francesco Ferri and are presented in more details in his thesis manuscript [89].

V.1.2 Tweezers beam generation

We have seen that the high NA lens that we have set in the vacuum chamber can serve as an objective for a high-resolution microscope. In the reverse propagation direction, it can also be used to generate sub-micrometer waist tweezers. The tweezers light is generated with a 808 nm single mode laser diode (Scheaumann M9-808-0150) mounted with a diffraction grating in a Littrow configuration. We send about 20 mW to seed a tapered amplifier (Toptica Eagleyard EYP-TPA-0808-02000-4006-CMT04-0000) that can deliver up to 1.4 W.

Each tweezers is a red detuned far-off resonant trap (FORT). The potential expression is given by equation II.3, with $P = 0$ as the tweezers' polarisation is linear.

Then, the power of a gaussian beam of waist w_0 and peak intensity I_{max} is $P = \pi w_0^2 I_{max}/2$: with $w_0 = 0.9$ µm (see section V.3), we need $P \approx 0.85$ mW to achieve a trap depth $U_0 = U_{dipole}(\vec{0}) = 1$ mK. Choosing our tweezers wavelength (808 nm) quite close to the D1 (795 nm) and D2 (780 nm) lines allows to work with more than 100 tweezers (1 mK deep) with a reasonable power (more details in section V.3).

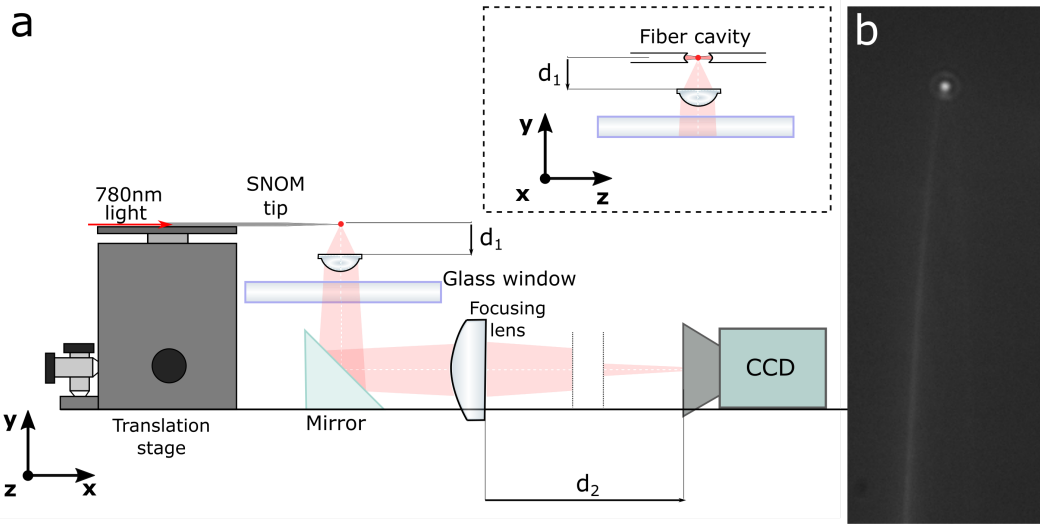

Fig. V.1 *a) Test setup used to align the objective aspherical lens with respect to the cavity mode, using a SNOM tip. b) SNOM tip used as a point-like source. The diffraction pattern is visible at the tip, which has a 100 nm aperture. Figure from [89].*

With such wavelength, one can be concerned about scattering of photons from the dipole trap, which induces heating: in the limit of a low saturation $I \ll I_{sat}$, the scattering rate Γ_{sc} is:

$$\Gamma_{sc} = \frac{I(\vec{r})\Gamma^3}{8I_{sat}}\left(\frac{1}{3(\omega_{dip}-\omega_{D_1})^2}+\frac{2}{3(\omega_{dip}-\omega_{D_2})^2}\right) \tag{V.1}$$

The average photon scattering heating power is $P_{heat} = 2E_{rec}\frac{\Gamma_{sc}}{2\pi}$, where $E_{rec} = \frac{\hbar^2k^2}{2m}$ is the recoil energy.

Thus the typical time t_{esc} for the atom to escape from the dipole trap is:

$$t_{esc} = \frac{U_0}{2E_{rec}\Gamma_{sc}/(2\pi)} \tag{V.2}$$

For a trap depth of $U_0 = 1$ mK, $t_{esc} \approx 150$ s, which is much larger than the time-scales of our experiments (tens to hundreds of ms). Also it means that trap photon scattering is not the main loss mechanism.

V.1.3 Acousto-optic deflector setup

The high NA lens can be used, together with acousto-optic deflectors, to generate multiple tweezers, well suited to produce 1D and 2D arrays of single atoms. For this purpose, the optical setup fulfils the following conditions:

1. The AOD is conjugated with the aspherical lens. Thus beams diffracted with different angles at the output of the AOD cross at the position of the aspherical lens.

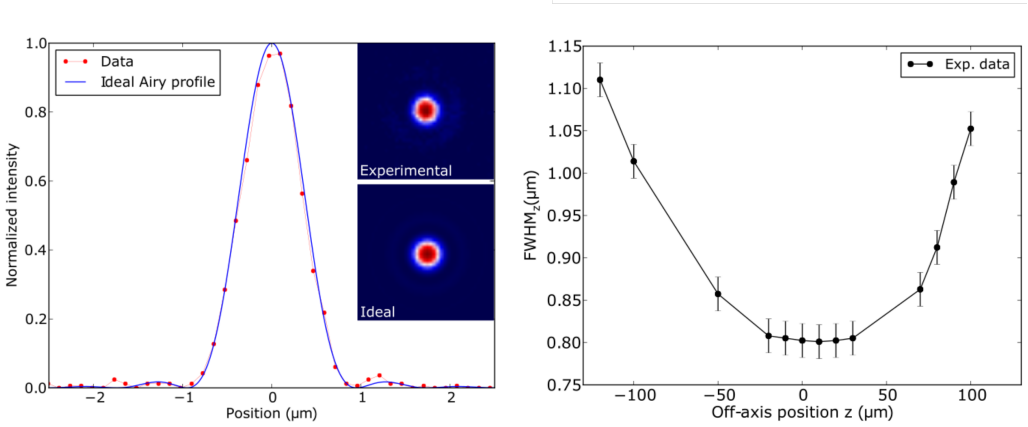

Fig. V.2 *a) Left: PSF measurement on the optical axis. Red data points correspond to a 1D cut, which is fitted with an Airy profile (blue line), provinding* $FWHM = 0.80 \pm 0.02 \mu m$*. Insets correspond to measured and ideal 2D PSF. Right: FWHM of the PSF VS z distance to the optical axis. Figure from [89]*

2. At the position of the aspherical lens, the tweezers beam waist is 4.5 mm, larger than the radius of the lens (4 mm), so as to be diffraction-limited by the lens and achieve the smallest possible waist. Such waist is larger than the AOD crystals. Thus we use collimated beams with a smaller waist $w = 1.7$ mm. After the crystals, we enlarge them to the desired size with a telescope of magnification M = 2.5.

3. The lens was designed for laser diode collimation and can be operated at the diffraction limit with a collimated outgoing beam only with a glass slab between its focal point (laser diode) and the lens. When used without such slab, it was shown in [120] that diffraction limit operation can be retrieved by using a slightly diverging beam going out of the aspherical lens, when the lens is used for imaging. We use it with reverse propagation, to focus a tweezers, so we need a slightly converging beam impinging on the lens to achieve diffraction-limited waist size for our tweezers. From a ray optics simulation of our layout using software OSLO, from Lambda Research Corporation, we compute that required gaussian beam angle is: $\theta = atan(\frac{\lambda}{\pi\omega_0}) = 0.4°$. This can be achieved by adding a positive lens (which we will call "convergence lens" from now on) at a point conjugated to the AOD Because of the non-negligeable size of the AOD casing, we have to use a M=1 telescope image of the AOD, where we put the convergence lens.

A specificity of our setting as compared to "free" space tweezers experiments is the requirement for the tweezers focus to be at the center of the cavity mode. As the tweezers propagation axis is perpendicular to the cavity axis, the precision of the tweezers focus positionning needs to be better than the cavity mode waist 5.7 μm. For this, we use a lens (Optotune ELC-10-30-TC) with a tunable focal distance, in the range $[50 - 120]$ mm, to tune the tweezers focus position over 70 micrometers, after the aspherical lens.

Figure V.4 shows the full optical setup. The fibers 1 and 2 are outcoupled with two different lenses to get beams of waist 1.7 mm and 0.7 mm respectively. The large beam (red on figure V.4) gives sub-micron tweezers, whereas the thin beam (light orange on figure

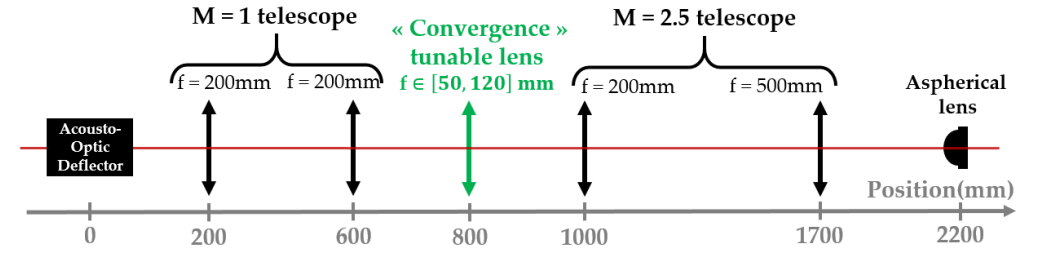

Fig. V.3 *Simplified optical layout. The $M = 1$ telescope consists of two $f = 200$ mm achromats (New Focus PAC32AR.16). The $M = 2.5$ is made of one similar $f = 200$ mm achromat, and a $f = 500$ mm achromat (New Focus PAC091AR.14).*

V.4) gives tweezers with larger waist (≈ 5.5 µm), with an extra $f = 500$ mm lens, located 500 mm before the AODs, that imprints a small convergence to have a smaller waist on the high NA lens. These larger tweezers can trap thousands of atoms, and have been used to check the alignement (see section V.3.4) and to perform preliminary measurements with the cavity (see section VI.4.1). Large and thin beams are combined with polarising beam splitter P_1 and carefully superposed over the entire optical path.

Together with the half-wave plates at the fiber outputs, P_1 splits the power between paths going through 1D and 2D AODs. Before each AOD, another half-wave plate allows to turn polarisation so as to tune the AOD diffraction efficiency. The beams going out of both AODs are recombined at P_2, after passing the first lens of the M=1 telescope. They then propagate with orthogonal polarisations, which prevents interferences between tweezers from different AODs, when they are superposed inside the cavity. For example, this is required for transferring atom(s) between 1D AOD tweezers and 2D AOD tweezers.

After the second lens, the beams is sent to the top breadboard located above the vacuum science chamber, using several 45° mirrors and an intermediate horizontal breadboard (see figure V.5 for a 3D representation of the setup). The tunable lens is set in one of the parts of the setup that have a vertical optical axis. This is recommanded by the manufacturer to limit the effect of gravity on the deformable polymer of which the lens is made, and thus prevents wavefront distorsion. The beam passes through the M=2.5 telescope and arrives in the region of combination.

Using the two identical dichroic mirrors D_1 and D_2 (Thorlabs DMSP805L), we combine and separate 3 different beams (see the table in figure V.4 for transmission values):

1) The 808 nm tweezers beam. Most of its power is reflected on dichroic mirror D_1 towards the vacuum science chamber below, where it converges in the fiber cavity. A few percent of its power (represented in lighter colors on figure V.4) is transmitted through D_1, passes through a high NA lens identical to the one in the vacuum chamber. The subsequent tweezers are imaged on a CMOS camera (C_1), with a M = 50 microscope made of a commercial objective (Mitutoyo Plan Apo x50) and a lower NA achromat. The field of view (130 x 110 µm) is almost as long as the cavity and the pixel size is 0.1 µm. This "parallel" tweezers imaging setup is used 1) to check that we achieve diffraction limit, thus validating most of the optical setup (which it has in common with the in-vacuum aspherical lens) and

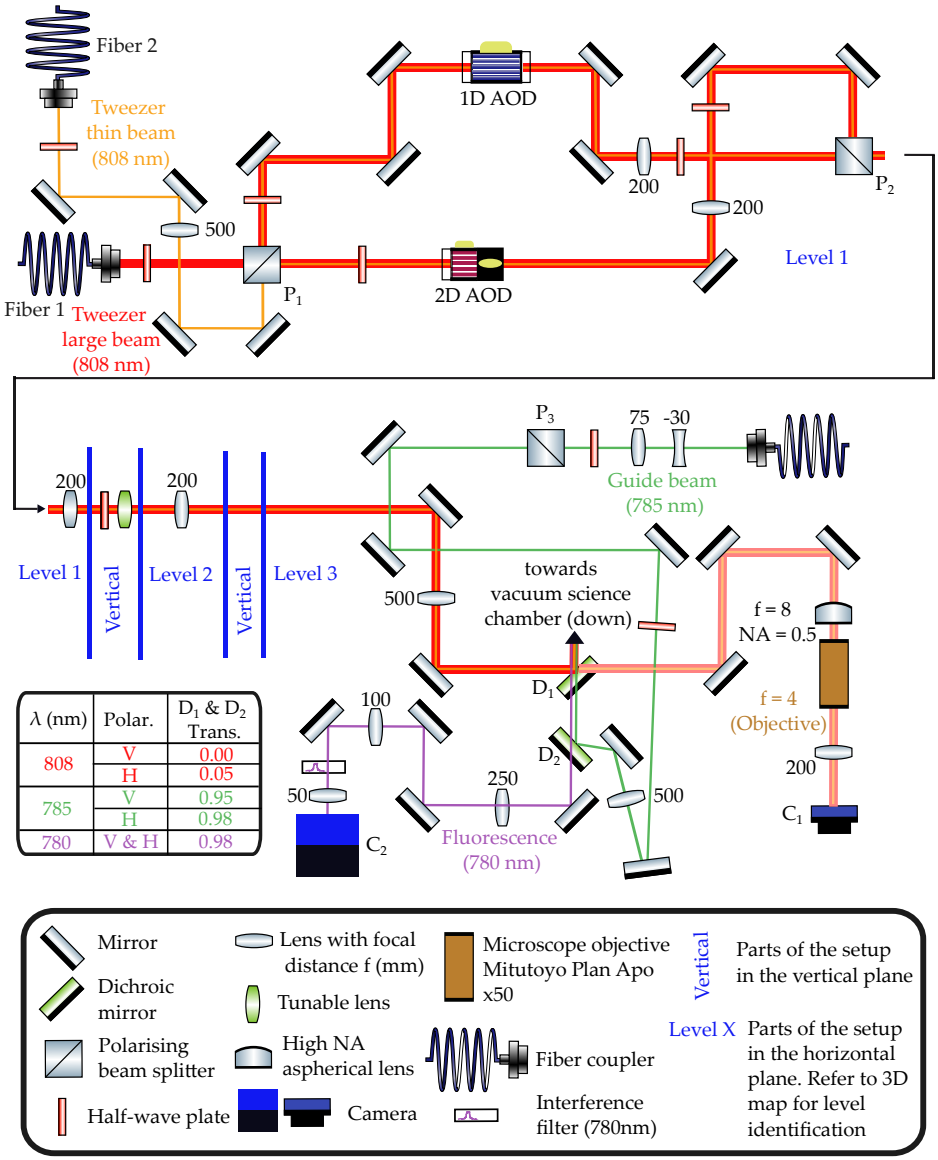

Fig. V.4 *Schematic of the full optical setup from optical fiber to vacuum science chamber. Levels 1, 2 and 3 are shown in the 3D CAD scheme of the setup (figure V.5)*

2) to measure and control the relative position of tweezers from both AODs. This setup is required because the geometry of our apparatus prevents us from collecting and imaging tweezers light going through the cavity.

2) The 785 nm guide beam (see section II.1.4) is collimated at the fiber outcoupler, enlarged with a M = 2.5 telescope and purified in polarisation with P_3. An extra 500 mm lens imprints a slight convergence on the beam such that the beam diameter is smaller on the aspherical lens, resulting in a waist of 50 µm inside the cavity, where it converges.

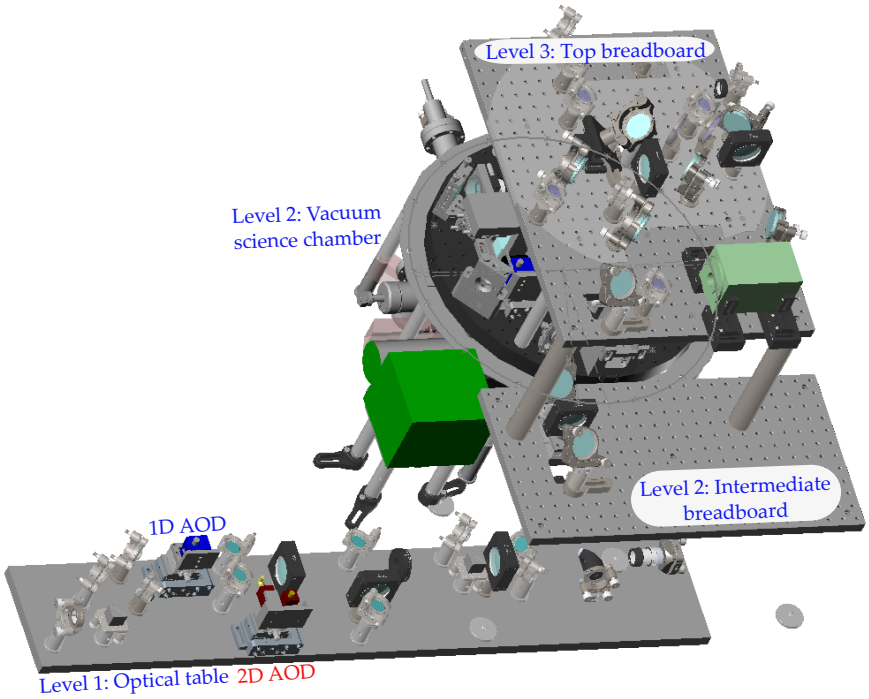

Fig. V.5 *3D CAD design of the tweezer optical setup.*

3) The 780 nm fluorescence photons emitted by the atoms and collected with the high NA lens. As explained in section V.1.1, this lens can indeed serve as the objective of a microscope to perform fluorescence imaging of the atoms. Figure V.6 shows the current microscope setup. The objective is associated with a few lower NA achromats to image the atoms on a low-noise sCMOS sensor (Andor Zyla 4.2 PLUS).

The overall magnification is M = 11. With this moderate value, each camera pixel corresponds to 0.6 μm in the intra-cavity plane. This value is well suited for tweezers single atoms imaging: we can set the distance between tweezers to a few micrometers, image each tweezers on few pixels (from 1 to 2x2 = 4 in our case, depending on atom temperature) to achieve a good signal-to-noise ratio and reduce fluorescence imaging duration. Until now, the imaging setup described here was not used for fluorescence detection but served as a means of aligning the tweezers beams with the cavity, which we will describe in the next section.

V.1.4 Alignement of the setup

The alignement of the AOD setup aims at:

- achieving good conjugation of the AOD with the aspherical lens, 2 meters away.
- overlapping beams going through 1D and 2D AODs.
- overlapping large and thin beams.
- aligning all tweezers beams with respect to the fiber cavity.

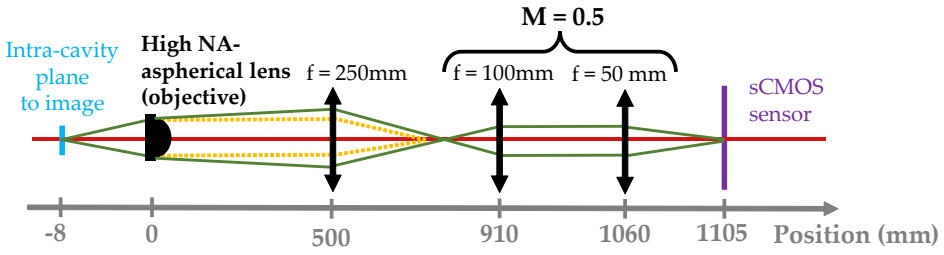

Fig. V.6 *a) Schematic of the intra-cavity microscope. The first f = 250 mm achromat produces an intermediate image of the atoms, which is then conjugated to the camera sensor with a M=0.5 telescope. The separation between the 250 and 100mm lenses (410mm) is more than the sum of their focal distances (350mm) to ensure that the beam conjugated to the sensor is slightly diverging out of the high NA lens, allowing for diffraction-limited resolution (as explained in section V.1.3). The overall magnification is 11.*

- setting the axes of diffraction of the AODs to match the axis of the cavity so that the array of tweezers is homogeneously coupled to the cavity.

Unlike the 1D AOD, the 2D AOD has two mirrors before the 1D/2D recombining cube P_2 and after the first 200 mm lens. Thus it is easier to align the 2D AOD with respect to the 1D AOD using these mirrors, since it does not spoil the alignement through the first 200 mm lens. Similarly, the thin beam can be aligned with respect to the large beam since it has four extra mirrors before combining cube P_1. Thus the large beam going through the 1D AOD will serve as a reference beam, with respect to which we align all other beams. Therefore its alignement with the fiber cavity is the critical step of the setup alignement. Since we cannot collect the tweezers light after it goes through the cavity, we use another method and repeat the two following steps until the procedure converges:

* we use the mirror closest to the cavity to align the beam with respect to the cavity mode, using the diffusion pattern of tweezers light on the fibers, observed with camera C_2 (see figure V.7).
    - Perpendicularly to the cavity axis: we voluntary shift an array of tweezers onto one of the fibers and tweak the mirror to center the tweezer array with respect to the long edges of the fibers (figure V.7: a and b)
    - Along the cavity axis: with an array of tweezers long enough we see part of the extremal tweezers light diffused on the cavity fibers. We tweak the mirror so as to equilibrate the amount of diffused light on both fibers. (figure V.7:c)
* we use the second closest mirror (excluding the dichroic) to center the tweezers beam with respect to the aspherical lens. The beam is slightly larger than the lens aperture, so we equilibrate the ring of diffused light around the lens.

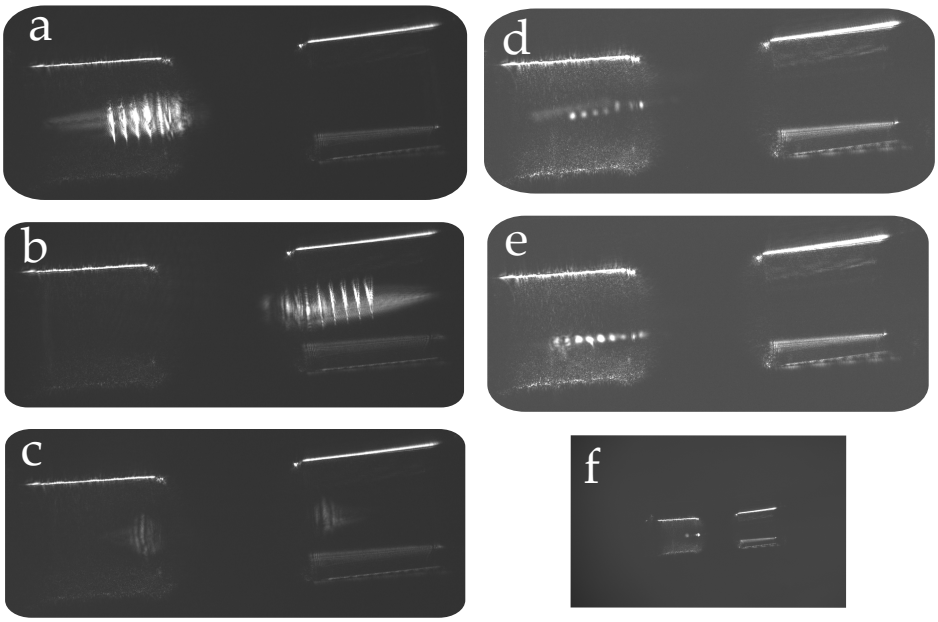

Fig. V.7 *Diffusion of tweezers beam(s) on the cavity fibers, which we use for alignement. An array of 9 tweezers extending over 130 μm (slighlty less than the cavity length) is generated with the large (a,b,c) / small (d, e) beam. With the last mirror of the setup, it can be translated left/right to cover one of the fibers (a/b) so as to check its centering with respect to the fiber, perpendicularly to the cavity axis. Then we translate it back to the center of the cavity and equilibrate the residual power diffused on the two fibers (c). We can also correct the misalignement of the array with respect to the fiber axis. Picture d: before / e: after (slight) angle correction. Picture f: Full field of view of the camera. These pictures were taken with a different camera (FLIR BFLY-PGE-23S6M-C) that we used before. Its pixel size is very similar but its field of view is slightly smaller: 1020x640 μm VS 1200x1200 μm currently (Andor Zyla 4.2 PLUS)*

V.2 Acousto-optic deflector radiofrequency signals

To control both the positions and the trap depths of multiple tweezers, we feed the AODs with a multi-frequency Radio Frequency (RF) waveform:

$$S = \sum_{k=1}^{N} A_k \cos(\omega_k t + \phi_k) \tag{V.3}$$

At the output of the AOD, each frequency component ω_k gives rise to a beam diffracted with a specific angle, depending linearly on ω_k, which converts to a tweezers at specific position in focal plane of the high NA lens. The trap depth of the tweezers is proportional to its peak intensity, thus to A_k^2. We generate multi-frequency RF waveforms with an arbitrary waveform generator (AWG): Spectrum Instrumentation M4i6622-x8. It synthesizes directly the waveform(s) for 1D AOD (respectively 2D AOD) in the frequency range 80 ± 25 MHz (respectively 100 ± 20 MHz), with sampling rate 600 MHz. We currently use the AWG in

the standard mode: waveforms are fully loaded in the card at once and then played at each experimental cycle, triggered by our sequencer. In this mode the maximal duration of the waveforms is set by the 4096 MBytes memory: with 2 bytes per sample, 4096 MBytes = 2048 MSamples. Then, with 4 channels and a 600 MHz sampling rate, the waveforms maximal duration is ≈ 0.85 s. It has been enough for all the experiments described in this manuscript. For longer experimental sequences, the card can be streamed continuously at high rates, thanks to its PCI Express interface. In that case, the card memory is no longer a limit.

At the output of the AWG, we get rid of the aliased frequency components by filtering signal outside of the frequency ranges $50-100$ MHz (respectively $50-150$ MHz) for the 1D AOD (respectively the 2D AOD). The filtered RF signals are then amplified up to 2 W of power and sent to the AODs. Power limitors prevent damaging the amplifiers with too high input powers.

As observed in [58], imperfections in the RF circuit and the AOD lead the optical output of the AOD to be non-linear with respect to the RF signal $S(t)$. To the lowest order of nonlinearity, new frequency components are generated at sum $(\omega_k+\omega_j)$ and difference $(\omega_k-\omega_j)$ frequencies. These components are far from the original frequencies ω_k. However, the next order of nonlinearity gives rise to frequencies such as $2\omega_k-\omega_j$, close to the originals (or sometimes equal to the originals, when S is a frequency comb to generate a tweezer array with regular spacing). They can then interfere with the initial frequency component ω_k. Such interferences change the relative intensities of the tweezers in the array, leading to inhomogeneity of the trap depths.

It is possible to reduce these undesirable interferences by tuning the phases ϕ_k. We follow the solution proposed in [58], except that we start with phases drawn randomly within $[0;2\pi]$, rather than all equal to 0. Then we compute the sum of all lowest order frequency difference terms:

$$J(t)=\sum_{i,l}\cos(\omega_i t+\phi_i-\omega_l t-\phi_l) \tag{V.4}$$

Finally we optimize each phase ϕ_k separately to minimize $\sqrt{\sum_t J(t)^2}$ and reduce these interferences.

Let us now consider an array of 40 tweezers with a distance of 3 µm between the tweezers (we will justify this choice in section V.3.1). We generate this array with a waveform with frequency separation $\delta\omega/2\pi\approx 600$ kHz between the 40 tones ω_k. The amplitudes are equal: $A_k=1$ and the phases are either 0 (a) or random (b) or optimised (c). Pictures a, b and c of figure V.8 correspond to these three choices of phases. For each picture, the top graph shows the multi-frequency waveform $S(t)$, in purple, and the bottom graph shows $J^2(t)$, which we want to minimize, in green. Between the two graphs, we display the power ratio $\langle S(t)^2\rangle_t/S^2_{peak}$, where $\langle S(t)^2\rangle_t$ is the time-averaged power, and $S^2_{peak}=\max[S^2]$ is the maximal instantaneous power. This ratio reflects the power contrasts of the waveform and has a maximal value of 50 %, for a single frequency waveform.

a) With phases equal to 0, $S(t)$ has a period $2\pi/\delta\omega$ and exhibits strong variations of power: the instantaenous power $\propto S^2(t)$ shoots up when all the frequency tones are

in phase. Thus the power ratio is low: 1.2 %. $J^2(t)$ has the same periodicity and a similarly strong power contrasts.

b) With random phases, the power contrasts are significantly reduced for both $S(t)$ and $J^2(t)$, because there are no such constructive interferences as with phases equal to zero. Thus the power ratio is improved by a factor ≈ 6.5.

c) After optimising the phases, the power contrasts are further reduced and the power ratio improves by a factor of ≈ 2.7.

By tuning the phases, power contrasts are signicantly reduced, which improves the AOD diffraction efficiency, and thus of the total power available for tweezers inside the cavity. Indeed, the Spectrum card rescales the waveform S so that the maximal instantaneous RF voltage $S_{peak} = \max |S|$ matches a user-defined limit S_{lim}, which can be set according to the RF amplifier specifications. So for a fixed value of S_{lim} the average RF power $\langle S(t)^2 \rangle_t$ scales as $1/S_{peak}^2$. Consequently, optimising the phases reduces S_{peak} and thus increases the average RF power and the AOD diffraction efficiency.

With the same 40-frequency RF signal, we measure the diffraction efficiency for the 3 configurations. The total power diffracted increases by a factor of ≈ 10 (from 2.5 % to 25 %) when going from phases equal to 0 to random phases, and further by a factor of ≈ 2 (from 25 % to 50 %) when going from random to optimised phases. The total improvement from the naive setting (phases equal to 0) to optimised phases is 20. These numbers match approximately the power factors computed from the purely numerical wavefunctions : 6.5, 2.7 and 17.6, which confirms experimentally that fine tuning the relative phases is crucial to achieve the power required to generate a reasonable number of tweezers, as we will see in section V.3.3.

V.3 Results

Now that we have described both the optical and RF setups with which we generate multiple tweezers, we will discuss their performances, in terms of:

- waist size (V.3.1).
- waist and trap depth homogeneity when generating multiple tweezers (V.3.2).
- the maximal number of tweezers that we can produce (V.3.3).

We will finally describe the extra capabilities offered the larger waist tweezers (V.3.4)

V.3.1 Tweezers waist

For the 2D AOD[1], in the high NA lens focal plane, the working optical field for the results shown in this manuscript is a rectangle of size $l \times d$, where:

[1] All the results of the section V.3 are for the 2D AOD. The 1D AOD gives very close results, with slighlty smaller waists, probably due to better conjugation of the aspherical lens to the sole crystal of the 1D AOD, as compared to the two crystals of the 2D AOD.

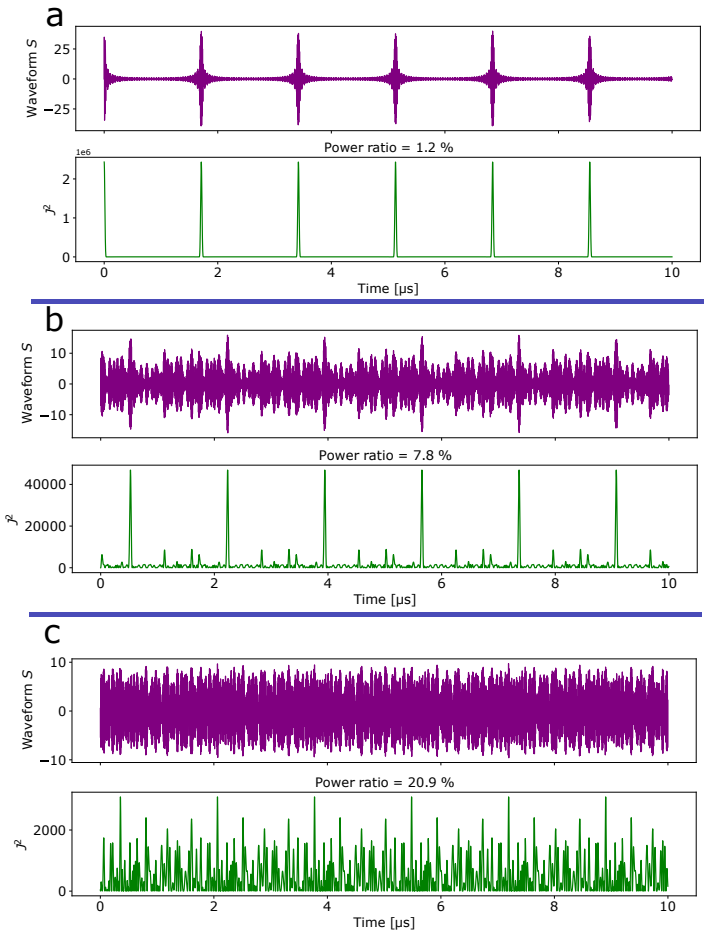

Fig. V.8 *Effect of phases ϕ_k on the waveform of a RF frequency comb $S(t)$, and on $J(t)^2$. $J(t)$ has a period of $2\pi/\delta\omega$ in the 3 cases. With phases equal to zero (a.) $J(t)^2$ exhibits strong peaks (please notice that the y axis values should be multiplied by 10^6) at times where the tones of $S(t)$ are in phase. With random phases (b.), these peak values are strongly reduced. After phase optimisation (c.), the strongest peaks are further reduced to a level where they are similar to other peaks in the signal. The great changes in $J^2(t)$ illustrate how much phase tuning can affect the non-linearities and subsequent interferences, within the simple model used here.*

* $l = 120$ µm is the length along the cavity axis. It is chosen smaller than the length of the cavity ($L = 145$ µm), with security margin to keep the tweezers away from the dielectric coatings of the fiber mirrors. It allows to fit an array of 40 tweezers with distance of 3 µm between tweezers.

* $d = 20$ µm is the distance between the cavity axis and the tweezers storage register axis. At such distance, the coupling g to the 780 nm probing field is reduced by a factor $\exp[-(d/w_0)^2] < 10^{-5}$. Thus the interaction between an atom in the register and the cavity is completely negligible.

With the parallel imaging setup (camera C_1 on figure V.4), we measure the radial intensity profiles of optical tweezers, focused in this plane, at all corners and at the center of the working optical field.

First, we notice that all profiles are quite spherical. Figure V.9 shows the most spherical (left picture) and the most elliptical (right picture) tweezers. To be more quantitative, we fit each profile with a 2D elliptical gaussian function, of the form $a(x-x_0)^2+2b(x-x_0)(y-y_0)+c(y-y_0)^2$, and get the waist sizes along the ellipse eigenaxes: w_a and w_b. The most circular tweezers has $w_a/w_b = 1.01$, whereas the most elliptical has $w_a/w_b = 1.24$. This residual ellipticity is due to optical aberrations and astigmatism of the gaussian beam.

Then, the waist values are quite uniform over the working field. For each image, we compute $w_0 = \frac{w_a+w_b}{2}$. Its mean value over all images is 0.81 µm and the standard deviation is 0.04 µm (5 % relative fluctuations). As we will see in section VI.3.1, 0.85 µm is an upper bound for the value of w_0 inside the fiber cavity, compatible with the values measured with the parallel imaging setup, and presented in this section. The corresponding Full Width at Half Maximum is FWHM $= \sqrt{2\ln(2)}w_0 \approx 1.00$ µm. This is 1.25 larger than the FWHM of the point spread function, 0.80 µm (quoted in section V.1.1) because of the residual optical aberrations (our setup being much more complex than the one used to caracterise the point spread function of the high NA lens, shown in figure V.1) and because of the gaussian intensity profile, which enlarges the focused beam spot as compared to a uniform intensity profile. A similar enlargement of 1.1 was observed in [120], using the same lens. Our waists values are comparable to that obtained in experimental setups with similar wavelengths and objective NA [58, 120]: they are satisfactorily close to the diffraction limit and small enough for collisionnal blockade.

V.3.2 Trap depth equalising

We consider here an array of 40 tweezers with separation of 3 µm between adjacent tweezers, covering a distance $l = 120$ µm. We start with the multi-frequency RF signal S with phases optimised with the purely numerical procedure explained in section V.3.2, and equal amplitudes A_k. Figure V.10, picture a. shows an image of the resulting tweezer array in the focusing plane. We fit each spot with a 2D gaussian profile to get the peak intensity I_k and the waist $w_{0,k}$ of each tweezers (Picture b). Graph c. shows the peak intensity I_k (normalised to the maximal value) and the waist $w_{0,k}$ of the 40 tweezers. The waists are rather homogenoeous, within the range $0.75-0.9$ µm. The peak intensity I_k varies of up to 40 %, with a clear position dependence, which may result from a combination of frequency-dependent AOD diffraction efficiency, tweezers-dependent transmission through the setup, and most probably non-linear effects and interferences as mentioned in section , which are probably not be fully compensated by the phase optimisation, which relies on a simple model.

And indeed, I_k variations are mainly *unrelated* to waist $w_{0,k}$ variations. The I_k distribution has a relative standard deviation $\sigma_I = 11\,\%$. Since $I_k \propto 1/(w_{0,k}^2)$, we compute $P_k = I_k \times w_{0,k}^2$, which is proportionnal to the tweezers power. The relative standard deviation of power, $\sigma_P = 9\,\%$, is non-zero and almost as large as σ_I. Thus, most of the inhomogeneity in intensity is not due to the waist inhomogeneity, but rather to power inhomogeneity because of the mechanisms we have just mentioned.

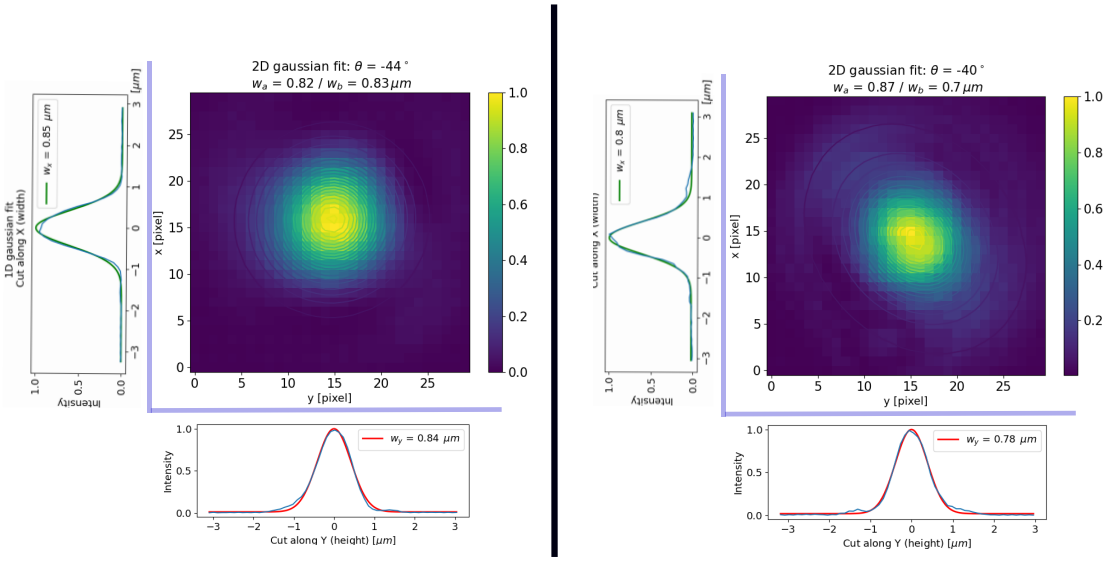

Fig. V.9 *2D Intensity profiles of optical tweezers at their focus, together with 1D cuts along the x and y camera axes. Both tweezers are generated by the 2D AOD, at two different corners of the working optical field. They are fitted with 2D (contour lines on the image) and 1D gaussian functions. The 2D fit contains information ellipticity, contrary to the 1D cut fits: for instance, for the bottom tweezers:* $w_a/w_b = 1.24$ *whereas* $w_x/w_y = 1.03$. *The small ellipticity is due to residual optical aberrations. The top tweezers shows a more spherical tweezer:* $w_a/w_b = 1.01$.

Since the tweezers trap depth U_0 is propotional to the peak intensity I_k, it is necessary to equalise the peak intensities so as to work with equal trap depths, which result in equal lightshifts, and thus homogeneous optical manipulation (cooling, pumping, ...) for the all tweezers in the array. Therefore we tune the RF amplitudes A_k to compensate the peak intensity I_k inhomogeneities. The procedure is repeated until σ_I saturates, which requires generally less than 10 repetitions. Figure V.11 shows I_k distribution before and after the tuning. The intensity inhomogeneity σ_I is reduced from 11 % to 2 %.

V.3.3 Power budget

Let us compute the maximum number of tweezers than we can work with. We start with 1 W of power after the T.A., of which half is available at the inputs of the AODs. Indeed, we loose 50% of the power in fiber coupling. Indeed, the mode at the output of the T.A. is highly elliptical and we correct part of it with several cylindral lenses. The resulting mode at the input of the fiber is not perfectly gaussian. We split this power equally between the 2 AODs. Then, in the multi-frequency regime the diffraction efficiency is $\approx 50\%$. Finally, the transmission from the AOD outputs to the glass cell is 70%. Thus we have $1000 \times 0.5^3 \times 0.7 \approx$ 90 mW available in the science chamber, for each AOD. This is enough to get more than 100 tweezers with a trap depth of 1 mK. We have seen that with 3 µm separation we can fit 40 tweezers inside the cavity so the power is not a limitation.

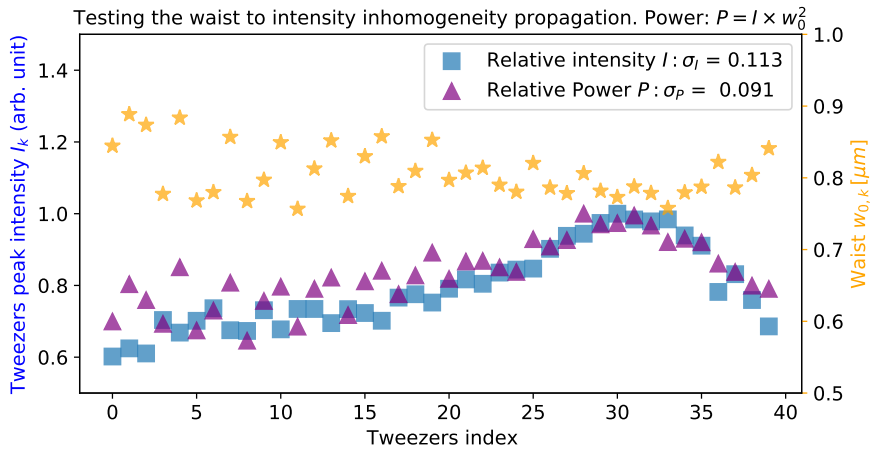

Fig. V.10 *Analysis of array of 40 tweezers, separated by* 3 µm. *The distribution of maximal intensities I_k is shown as blue squares, for equal amplitudes A_k. One can see that most of the intensity inhomogeneity among the tweezers is related to inhomogeneity of the tweezers power rather than the waist (see main text for details).*

V.3.4 Large tweezers images for alignement and preliminary tests

As we mentioned in section V.1.3, the thin beam of the AOD setup gives tweezers with a larger waist $w_0 \approx 5.5$ µm, that trap typically 1000 atoms with 1 mK depth. Such number of atoms can easily be detected with absorption imaging. Thus these tweezers provide a convenient way of testing the alignement of the tweezers with the cavity, the 3D steering of the tweezers position and the generation of multiple tweezers simultaneously (see figure V.12 for more details).

V.4 Conclusion

Our CQED setup has been designed with a high numerical aperture lens aligned with the micrometric cavity mode. It allows to focus sub-micrometer tweezers ($w_0 \approx 0.85$ µm), close to the diffraction limit, inside the cavity. Our tweezers are generated from a diode laser feeding a tapered amplifier, at 808 nm. The optical layout combines paths of two beams with different sizes (for submicron tweezers and larger 5.5 µm tweezers, used for calibration and preliminary tests) and two AOD systems (1D and 2D). All 4 beams are carefully aligned with the cavity mode. Multifrequency RF signals with optimised relative phases and amplitudes are generated by a AWG. They feed both AODs to generate multiple reconfigurable tweezers arrays in 1D and 2D. We are able to produce, simultaneously with *both* 1D and 2D AODs, up to 100 tweezers, with a conventional trap depth of 1 mK. This allows experiments with tens of single atoms inside and close to our strong coupling cavity.

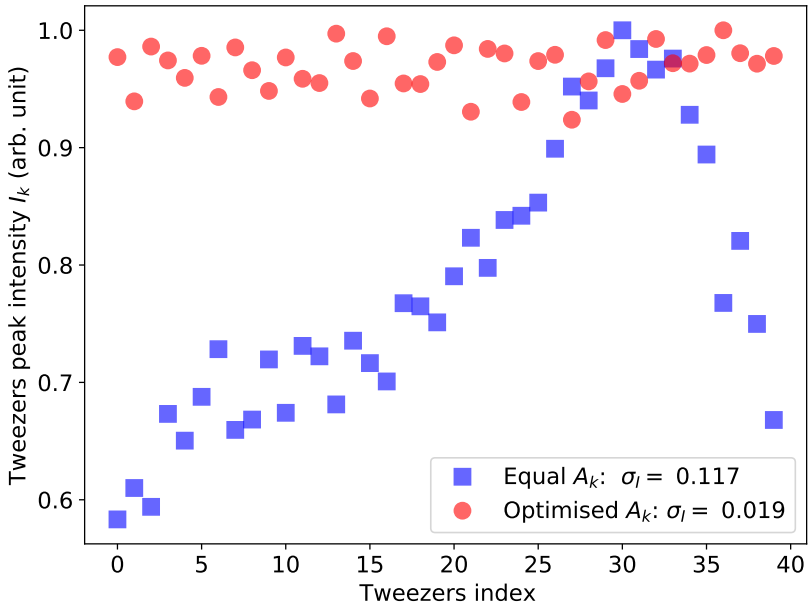

Fig. V.11 *Effect of amplitude optimisation on the homogeneity of the tweezers maximal intensity in an array of 40 tweezers separated by* 3 µm. *The tweezers peak intensity relative fluctuations are reduced from* 11 % *to* 2 %.

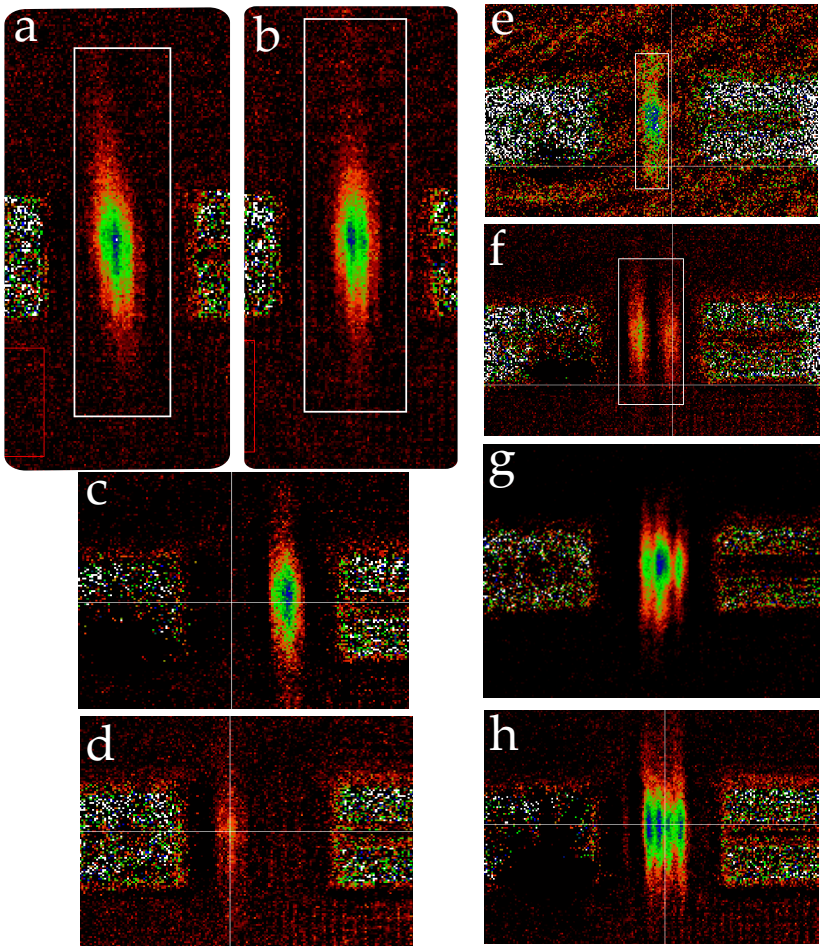

Fig. V.12 *Absorption imaging of clouds of atoms trapped in large tweezers. For a trap depth of* 1 mK*, we have 500 to 1500 atoms in each tweezers, depending on the position of the tweezers with respect to the cloud of atoms from which it is loaded. Absorption imaging allows to image such numbers of atoms. We use these images to 1) correct for misalignement of the tweezers propagation with respect to the cavity axis: in picture a, the tweezers is slightly tilted counter-clock wise. This is corrected on picture b. 2) tune of the tweezers position (e.g. along the cavity axis on pictures c and d). 3) test the generation of multiple tweezers (e,f,g and h). More details about multi-tweezers generation in section V.2*

Chapter VI

Strongly coupling a tweezer single atom and the microcavity

In this chapter, we first demonstrate the ability of our cavity to efficiently detect single atoms (VI.1), thanks to strong coupling. We then show how we reach the so-called "collisional blockade" regime, where a single atom is loaded in a single tweezer, produced by the 2D AOD (section VI.2). Then we characterise this single atom in the tweezer by measuring the trap frequency and the temperature (VI.3). An important requirement for our CQED platform is to maximise the coupling of the atom to the cavity. We present several methods for this optimisation (VI.4). We demonstrate the strong coupling of a single atom to the cavity, with a vacuum Rabi splitting measurement (VI.5). Finally, we demonstrate the collisional blockade in an array of a few tweezers (VI.7), which is the first step towards manipulating multiple single atoms within our dual-AOD cavity platform.

VI.1 A single atom hyperfine state detector

We saw in section I.1.4 that probing the cavity and measuring the transmission constitute a fast and quantum non-demolition measurement of the atomic hyperfine state. Together with reliable pumping in the hyperfine state coupled to the cavity, this ability turns to a measurement of the presence of an atom, which is used in this thesis to detect if there is an atom in the tweezer. In this first section, we verify the single atom hyperfine-detection ability of our micro-cavity for a single atom in the intra-cavity lattice trap, as a preliminary for single atom detection in the tweezer.

VI.1.1 Micro-wave single atom extraction

In this section we describe how the cavity is used as a single atom hyperfine state detector. We test this ability with a method used in earlier experiments in our group [73, 74]. It starts with the preparation, in the cavity trap lattice, of a small ensemble of N_a atoms in the Zeeman sublevel $F = 1, m_F = 1$, and no atom in $F = 2$, using the tools presented in section II.3.3. The cavity is resonant with the transition $F = 2 \rightarrow F' = 3$. We then apply a series of N_{trials} micro-waves pulses resonant with the transition $F = 1, m_F = 1 \rightarrow F = 2, m_F = 2$, with a probability p for each atom to be transferred to $F = 2, m_F = 2$. After each micro-wave pulse, we measure the cavity transmission with a probe beam on resonance with both

the cavity and the $F = 2, m_F = 2 \rightarrow F' = 3, m'_F = 3$ transition. A low value of transmission corresponds to having an atom in $F = 2$, a high value means no atom in $F = 2$ (all atoms in $F = 1$, or no atom at all - which can happen because the initial number of atom in $F = 1$ is random and has a small average value). This scheme benefits from the fact that atoms in $F = 1$ have a negligible effect on the cavity transmission. For instance, if we model N_a by a Poisson distribution of average $\overline{N_a} = 1.5$ (which is the value corresponding to the experimental results of section VI.1.2), the probability of having $N_a \geq 6$ or more is below 1 %. Then, for 5 atoms, the dispersive effect is 1 MHz typically, which, for a cavity resonance of HWHM $\kappa = 14.2$ MHz at 780 nm, leads to 0.5 % decrease in transmission, which is in the noise of our transmission measurement. The intracavity lattice trap is chopped (see II.3.3) during the entire series of micro-wave and probe pulses, to avoid the lighshift and level-mixing induced by the intra-cavity lattice (this effects are detailed in section III.1.1).

Now we will discuss how we choose the values of p, N_a and N_{trials}. Let us first assume that there are N_a atoms in $F = 1, m_F = 1$ and that $F = 2$ is empty. We then apply a single microwave pulse. Let N_2 be the number of atoms in $F = 2$ after the micro-wave pulse. Since transfers of different atoms from the $F = 1$ reservoir are independent, N_2 follows a binomial distribution of parameter p and N_a:

$$P(N_2 = k) = \binom{N_a}{k} p^k (1-p)^{N_a - k} \tag{VI.1}$$

Thus the probabilities to transfer 1 and 2 atoms to $F = 2$ (for a given N_a) are:

$$P(N_2 = 1) = N_a p (1-p)^{N_a - 1}, \text{ assuming } N_a \geq 1 \tag{VI.2}$$

and

$$P(N_2 = 2) = \frac{N_a(N_a - 1)}{2} p^2 (1-p)^{N_a - 2}, \text{ assuming } N_a \geq 2 \tag{VI.3}$$

Since we want to setup the detection for single atoms, we need the probability to transfer 2 atoms to be much smaller than the probability to transfer 1 atom:

$$\frac{P(N_2 = 2)}{P(N_2 = 1)} = \frac{N_a - 1}{2} \frac{p}{1-p} \ll 1 \tag{VI.4}$$

As $p \rightarrow \frac{p}{1-p}$ is an increasing bijection from $[0; 1[$ to $[0; +\infty[$, we can reach arbitrary small ratio $\frac{P(N_2=2)}{P(N_2=1)}$ for small p. However p should be high enough to have a non negligible average number of successful micro-waves transfers (out of N_{trials}). Thus we set $\overline{N_a} \approx 1.5$ and $p = 2.9\,\%$ so that $P(N_2 = 1)$ can be approximated by $N_a p$. Once averaged over many realisations of the Poisson random variable N_a, $P(N_2 = 1) \approx \overline{N_a} \times p = 4.3\,\%$.

With these values, *given* the detection of one (several) atom(s), the probabilities, with a Poisson-randomised N_a, that a single micro-wave pulse transfers one, two, three atom(s) in $F = 2$ are:

$$P(N_2 = 1 | N_2 \geq 1) = \frac{P(N_2 = 1)}{1 - P(N_2 = 0)} \approx 98.6\,\% \tag{VI.5}$$

$$P(N_2 = 2 | N_2 \geq 1) = \frac{P(N_2 = 2)}{1 - P(N_2 = 0)} \approx 1.3\,\% \tag{VI.6}$$

$$P(N_2 = 3|N_2 \geq 1) = \frac{P(N_2 = 3)}{1 - P(N_2 = 0)} \approx 0.015\,\% \tag{VI.7}$$

The probabilities to transfer more atoms are even smaller (scalling as p^{N_2}). So we can neglect the rare cases where more than one atom is transferred by a single micro-wave pulse.

Finally, if we denote N_{tot} the total number of atoms transferred to $F = 2, m_F = 2$ after N_{trials} micro-wave pulses, then N_{trials} is chosen such that, on average one atom is transferred: $\overline{N_{tot}} \approx 1$. We compute numerically the probability distribution of N_{tot}. Indeed, in case of a successful transfer to $F = 2$, the number of atoms in the reservoir N_a decreases. Thus the success probability of later micro-wave transfers decrease and the distribution of $P(N_{tot})$ is *not* binomial. From simulating 10^6 experiments with $N_{trials} = 40$, we find the following probabilities: $P(0) = 35.5\,\%$, $P(1) = 36.9\,\%$, $P(2) = 19.1\,\%$, $P(3) = 6.6\,\%$, $P(4) = 1.7\,\%$, and all other probabilities lower than $1\,\%$. The average is $\overline{N_{tot}} = 1.04$, significantly lower than the average of the binomial distribution where we would neglect reservoir depletion: $\overline{N_{tot,binom}} = p \times \overline{N_a} \times N_{trials} = 1.74$.

VI.1.2 Atom transmission extinction

We perform the sequence described in the previous sections and measure the transmission value of each probe pulse following a micro-wave attempt. The duration of the probe pulse is 300 µs and the intracavity average photon number is $n_{cav} = 2.0 \times 10^{-2}$. The sequence is repeated about 1000 times. The results are shown in figure VI.1.

Picture a. shows the histogram of the transmission measurement following the 1^{st} micro-wave attempt. With this histogram we can compute the transmission ratio and the probability to have an atom in $F = 2$. For this, we fit the two peaks with Poisson distributions and find averages of $T_0 = 40.0$ and $T_1 = 1.06$ counts for the empty cavity and the single atom respectively. The ratio in transmission, also called single atom extinction ratio, is $\frac{T_1}{T_0} = (2.7 \pm 0.4) \times 10^{-2}$. The expression for this ratio, in the low excitation limit, is given by equation I.15:

$$\frac{T_1}{T_0} = \frac{1}{\left(1 + \frac{g^2}{\kappa\gamma}\right)^2} = \frac{1}{\left(1 + 2C\right)^2} \tag{VI.8}$$

For an atom with the maximal coupling value $g_{max}/2\pi = 75$ MHz we expect a much lower transmission ratio: $\frac{T_1}{T_0}(g_{max}) = 5.5 \times 10^{-5}$. Here we obtain a higher extinction because of the thermal distribution of coupling strength values for the atom trapped in the lattice. In fact, the thermal-averaged extinction $\frac{T_1}{T_0}$ is predominantly determined by low coupling values of the distribution (for more detail about this point, please refer to section VI.4.2.4).

To differentiate the atom from the cavity, we define a threshold value of the transmission as the mean of the upper 10^{-3} quantile of the atomic distribution, denoted q_{atom}, and the lower 10^{-3} quantile of the cavity distribution[1], denoted q_{cav}. Transmission measurements below the threshold correspond to having an atom in $F = 2$. The corresponding probability is $p_{at} = 3.7\,\%$, comparable to the rough initial prediction of $4.3\,\%$.

[1]We abusively name "cavity" distribution the higher transmission values that can correspond to an empty cavity, or to a cavity with $F = 1$ atom(s)

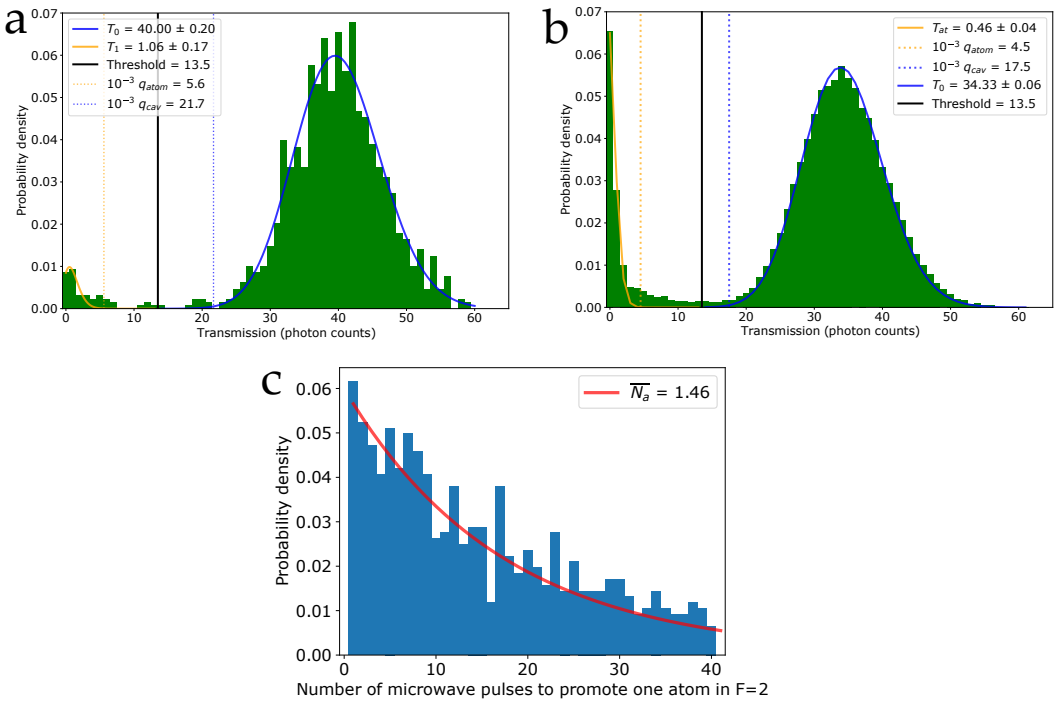

Fig. VI.1 *Pictures a. shows the histogram of the transmitted intensity after the* 1^{st} *microwave attempt. The* 10^{-3} *extreme quantiles of the fitted Poisson distribution (doted lines) are computed. The threshold to discriminate an atom in* $F = 2$ *from all other cases (empty cavity or cavity with* $F = 1$ *atom(s)) is defined as the mean of the two quantiles and displayed as a black solid line. Picture b. is the histogramm of the* $N_{trials} = 40$ *transmission measurements. Picture c: from the distribution in the number of micro-wave pulses required to transfer one atom to* $F = 2$*, one can fit equation VI.11, and extract the mean number of atoms* $\overline{N_a}$ *initially in* $F = 1$*.*

Picture b of figure VI.1 shows the histogram corresponding to all N_{trials} transmission measurements: this larger statistical set gives a smoother histogram. The probability to detect an atom in $F = 2$ is larger than in the 1^{st} attempt histogram (picture a.) because an atom can be detected in several successive measurements after being transferred to $F = 2$. Also, during the sequence, it is possible to have several atoms in $F = 2$, which induces a stronger coupling to the cavity than with a single atom, and thus reduces the transmission ratio: $T_{distri}/T_0 = (1.3 \pm 0.1) \times 10^{-2}$ (compared to $T_1/T_0 = (2.7 \pm 0.4) \times 10^{-2}$ for the 1^{st} attempt histogram). Indeed, starting with equation VI.8, for a strong coupling such that $2C \gg 1$, the transmission with N atoms in $F = 2$ is proportional to $1/(NC)^2$, where C is the single atom cooperativity. Thus for a statistical distribution of N, with a probability distribution $p(N)$, the mean transmission is:

$$T_{distri} \propto \sum_{N=1}^{N_{max}} \frac{p(N)}{(NC)^2} \tag{VI.9}$$

Thus the ratio of this transmission and the transmission of a single $F = 2$ atom $T_1 \propto 1/C^2$ is:

$$\frac{T_{distri}}{T_1} = \frac{\sum_{N=1}^{N_{max}} \frac{p(N)}{(NC)^2}}{1/C^2} = \sum_{N=1}^{N_{max}} \frac{p(N)}{N^2} \tag{VI.10}$$

Using the probabilities $p(N)$ from the simulation described in section VI.1.1, we find $T_{distri}/T_1 = 0.47$. This is compatible with the the ratio of transmission ratios extracted from the histogram: $(T_{distri}/T_{0,overall})/(T_1/T_{0,first}) = 0.48 \pm 0.08$, which confirms our estimation of statistics of $F = 2$ atoms. Please note that the empty cavity transmission T_0 is slightly different for the overall measurement and for the first probe pulse: $T_{0,first} \approx 40$ (picture a.) and $T_{0,overall} \approx 34$ (picture b). This could be due to a cavity lock imperfection in presence of the chopping of the locking light during the entire series of probe pulses, which could induce a systematic drift of the cavity frequency during the series, and thus a reduction of the intra-cavity power and of the transmission. Since both T_1 and T_0 are proportional to the intra-cavity power, we compensate this drift by computing and comparing to the simulation the power-independent quantity $(T_{distri}/T_{0,overall})/(T_1/T_{0,first})$ instead of the T_{distri}/T_1.

Picture c of figure VI.1 shows the histogram of the number of microwaves pulses required to transfer an atom to $F = 2$. Assuming that the reservoir of atoms in $F = 1, m_F = 1$ follows a Poisson law with an average value $\overline{N_a}$, the probability of detecting an atom in $F = 2$ after k micro-wave attempts is:

$$P_{promote}(k) = (1 - p\overline{N_{a,t}})^{k-1} \times p\overline{N_{a,t}} \tag{VI.11}$$

where:

$$\overline{N_{a,t}} = \frac{\overline{N_a}}{1 - e^{-\overline{N_a}}} \tag{VI.12}$$

The histogram is fitted with $P_{promote}(k)$ (red line on Picture c). From the fit we get $\overline{N_a} = 1.46$. Thus the probability to promote an atom, at each trial, is $p \times \overline{N_a} = 4.2\,\%$, compatible with previous estimations.

VI.1.3 Hyperfine-state lifetime

Once an atom is transferred to $F = 2$, it can be detected in several consecutive measurements. We observe experimentally that after a few couples of micro-wave / probe pulses, the atom leaves $F = 2$. Since the heating of the atom out of the trap with such small probe intensity is slow, we assume that the atom is not lost, but rather that it is back in cavity-uncoupled $F = 1$ state. This can be due to two mechanisms:

1) A micro-wave pulse transfers the atom back from $F = 2$ to $F = 1$.

2) The slight σ_- component of the probe photon (estimated to 2 % - see section II.3.4) can couple off resonantly $F = 2, m_F = 2$ to $F' = 2, m_{F'} = 1$, from which the atom can spontaneously decay to $F = 1$.

Picture d of figure VI.2 shows the histogram of the number of successive detections in $F = 2$, converted in the corresponding probe duration. We fit the histogram with an exponential decay, $t \to e^{(t-t_0)/\tau}$, from which we extract the lifetime $\tau \approx 0.94$ ms in $F = 2$.

We compare this lifetime to a simulation in which we model the experiment with reservoirs of atom(s) in $F = 1, m_F = 1$ and $F = 2, m_F = 2$ and a series of microwave pulses that have a small transfer probability $p = 2.9\,\%$ per atom. The hyperfine state transfers induced by the probe are neglected so as the exhibit the $F = 2/F = 1$ population dynamics related to the sole microwave pulses. The results are shown in picture e of figure VI.2, which is a histogram of the number of consecutives probe measurements where at least one atom is in $F = 2$. The histogram is fitted with a similar exponential decay, from which we extract a lifetime of $\tau_{sim} \approx 14.7$ micro-wave pulses (the simulation has no time unit), corresponding to $\tau_{MW} = \delta t_{probe}\tau_{sim} \approx 4.4$ ms in the experiment. As $\tau_{MW}/\tau \approx 4.7$, the experimental lifetime is predominantly defined by the probe-induced transfers and in the following we can neglect the lifetime-limiting effect of microwave pulses, transferring the atom back from $F = 2$ to $F = 1$. This is rather expected as the success probability of each microwave transfer is quite low.

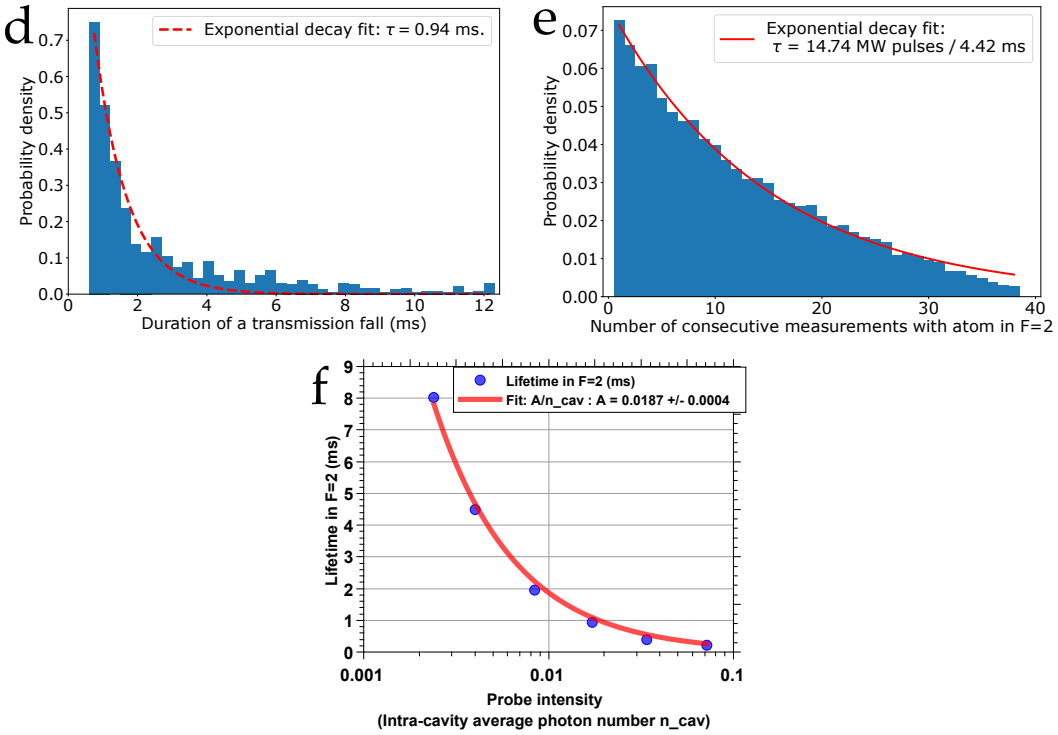

Fig. VI.2 *Picture d shows the distribution of the number of successive measurements of an atom in $F = 2$ ("transmission falls" as the transmission is low for this hyperfine state). It is converted to the duration the atom sees probe light before being depumped to $F = 1$. An exponential fit provides the lifetime of the single atom in presence of probe light. Picture e: Simulation. After being transfered to $F = 2$, an atom may be transfered back to $F = 1$ by a later microwave pulse. We make sure that the lifetime related to this process is much longer than probe-related lifetime fitted in picture d, and can thuse be neglected. Picture f: For variable probe intensity, we observe that the lifetime in $F = 2$ varies as 1/intensity.*

Within this approximation, we expect the probe hyperfine state transfer rate to be pro-

portional to the intracavity intensity n_{cav}, and thus the $F = 2$ lifetime τ to be inversely porportional to n_{cav}. To test this assumption, we vary n_{cav} geometrically over the range $[2.4 \times 10^{-3} - 7.2 \times 10^{-2}]$. To keep the average number of transmitted photons collected constant, we vary the duration of the probe pulse δt_{probe} as $1/n_{cav}$, over the range $[75 - 2400]$ µs. For each value of n_{cav}, we repeat the sequence 1000 to 1500 times. Picture f shows the $F = 2$ lifetime τ versus n_{cav}, where we observe a very nice fit $\tau = \frac{A}{n_{cav}}$.

To conclude section VI.1, we have demonstrated here that the cavity allows an efficient detection of the hyperfine state of a single atom in the intra-cavity lattice trap. As our qubit states are encoded in the these hyperfine states, this realises a qubit state detector. Together with the ability to prepare the atom in the strongly-coupled qubit state, the cavity can also be used to detect the *presence* of a single atom. Most of the following sections in this chapter involve single atom(s) in one (multiple) tweezer(s) and we will use the cavity transmission as a single atom detector.

VI.2 Trapping a single atom in a tweezer

VI.2.1 Intra-cavity molasses

To induce light-assisted collisions, we use beams in an optical molasses configuration to avoid heating atoms while expelling pairs of atoms from the tweezer. Our molasses consists of 3 pairs of contra-propagating beams with opposite circular polarisation. They are red-detuned by -30 MHz $\approx -5\ \Gamma$ with respect to the cycling transition $F = 2, m_F = 2 \leftrightarrow F' = 3, m_{F'} = 3$, and they have an intensity of typically 4 $\mathrm{I_{sat}}$ per beam. Apart from cooling light, each beam contains also $\approx 1.5\ \mathrm{I_{sat}}$ of repumper light ($F = 1 \rightarrow F' = 2$).

The geometrical configuration of the molasses beams is shown in figure VI.3. Initially, we tried using molasses beams focused at the position of the cavity, with small waist w_0 so as to limit the clipping of the beams by the cavity (as shown in picture c. of figure VI.3). We used beams with waist $w_0 \approx 80$ µm in the vertical xy plane, and a smaller waist of $w_0 \approx 40$ µm in the horizontal xz plane, where the beams are not perpendicular to the cavity axis, and given that we want to avoid coupling molasses photons in the cavity mode. Alignement of such small beams is difficult and we could not achieve the collisional blockade. Thus we changed the vertical beams to collimated beams of larger waist $w_0 \approx 1.5$ mm, and kept the smaller $w_0 \approx 40$ µm horizontal beams to avoid coupling photons inside the cavity mode.

Alignement of our molasses beams required simultaneously superposing the optical axes of contrapropagating beams and intersecting all beams at the position of the 145 µm-long micro-cavity, a supplementary constraint as compared to "free-space" tweezers experiments. We check that the beams intersect at the position of the cavity with images of the light scattered on the cavity fibers, such as pictures c and d of figure VI.3. Ultimately, the alignement was verified by looking at the effect of the molasses beams on the atoms trapped in a single optical tweezer, and reaching the collisional blockade regime, as explained in section VI.2.2. Apart from the cooling and repumping light, the molasses requires having a magnetic field close to 0 inside the fiber cavity. To achieve this, we apply a biais field, which we calibrate using ground-state micro-wave spectroscopy. From fitting the width of the spectrum with compensated fields, we estimate the total residual magnetic field to be on

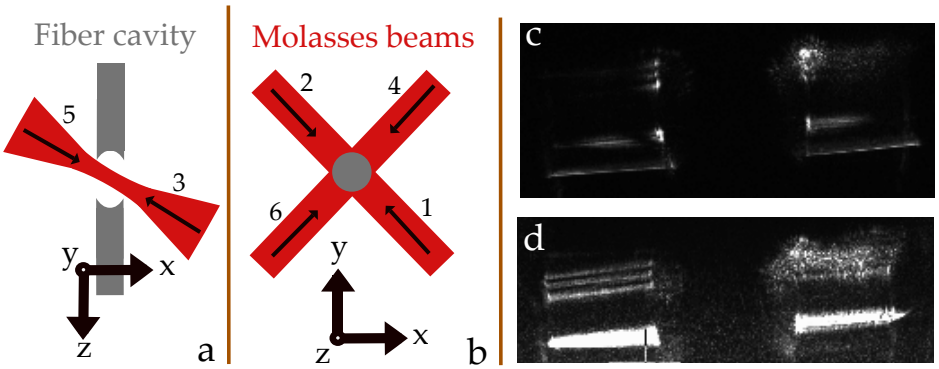

Fig. VI.3 *Picture a (respectively b) represents the geometry of the intra-cavity molasses beams that we use to obtain single atoms inside the fiber cavity, in the horizontal (respectively vertical) plane. The 3 axes of the pairs of beams 1/2, 4/6 and the cavity are perpendicular. The pair of beams 3/5 intersect with the cavity with a small angle (the axis perpendicular to the cavity is unavailable, being occupied by the transport dipole beam, described in section II.1.4). Pictures c and d are an image of the the fiber cavity - detection 4 / with camera C2 (see figure V.4 - where one can see the scattering pattern of beam #4. Picture c corresponds to the old configuration ($w_0 = 80$ µm) that led to minimal clipping of the molasses light on the fiber tips but much more critical alignement of beam pairs than with the new configuration ($w_0 = 1.5$ mm), shown in picture d.*

the order of 10 mG.

VI.2.2 Reaching the collisional blockade regime

In this section, we describe the loading of atoms in a single tweezer, and how we reach the collisional blockade regime, where there is at most one atom in the tweezer. Contrary to many tweezers experiments, we cannot load our tweezers from the MOT, because we cannot operate our MOT in the $L = 145$ µm long cavity. Instead we load the tweezers from the optical dipole trap used to transport the atoms to the micro-cavity (section II.1.4). This is similar to the experiment described in [65, 81], where the cavity is however much longer ($L = 9.4$ mm) and where a MOT could probably be operated, as this is the case for the other single-atom strong coupling tweezers-cavity experiment described in [67] ($L \approx 1.3$ mm).

The sequence is the following :

1. At the end of the transport, atoms are transferred (in 25 ms) from the crossed dipole trap (see section II.3.1) to a single tweezer, located at a distance $d = 18$ µm from the cavity axis, where the coupling to the cavity is negligible. The depth of the crossed dipole trap decreases from 80 to 0 µK while the depth of the tweezer increases from 0 to $U_{tweezer}$. In the early results shown in this paragraph, $U_{tweezer} = 2.5$ mK. All the later measurements shown in this manuscript were done at $U_{tweezer} = 800$ µK.

2. Molasses beams (cooling and repumper) are switched on for a duration δt_{mol}.

3. Starting from $\vec{B} \approx \vec{0}$ required for the molasses phase, a 3 G magnetic field along the cavity axis is switched on linearly in 2 ms. It stabilises during an extra 2 ms duration. It should be noted that the strong focusing of the tweezer light generates a fictitious magnetic field (see for instance reference [123]). Its direction is x, defined as the cross-product of the tweezer light propagation axis y and the tweezer polarisation axis z (for a reminder of axis definition, please refer to figure VI.14). The 3 G quantisation field is along z (so that the probe photons are σ_+ polarised) and it mitigates the perpendicular effective magnetic field.

4. The cavity is probed (see section VI.1) to check that there is no spurious atom left. Most of the times, there are none, because atoms not trapped in the tweezer are blasted by the molasses. We use this safety measurement to post-select and remove the rare cases where a spurious atom is left.

5. The tweezer is moved to the cavity in 1 ms.

6. The cavity is probed a second time to check if there is an atom in the tweezer.

Each probing of the cavity is preceeded by a 150 µs repumper pulse to make sure that atoms are in $F = 2$ and can be detected by the cavity, which is tuned, together with the probe laser, on resonance with the tweezer-ligthshifted transition $F = 2, m_F = 2 \rightarrow F' = 3, m_{F'} = 3$. We repeat this sequence about 100 times and compute the probability P_{at} of detecting atom(s) inside the tweezer as a function of δt_{mol}.

The results are shown in figure VI.4. The measurement shown in graph a. was done with a single vertical pair of molasses beams, with a -30 MHz detuning (with respect to the bare atom transition): P_{at} decreases continously as δt_{mol} increases. The cooling effect of the beam pair allows to keep the atoms inside the tweezer for much longer than with a single beam, which blasts the atoms away in a few ms. For instance, with a simple model where the temperature of the atom increases at a constant rate $R_{sc}T_{rec}$ (R_{sc} being the photon scattering rate, and T_{rec} the recoil temperature) we can compute that the typical time τ_{esc} for the atom to escape the tweezer trap: $\tau_{esc} = U/(R_{sc}T_{rec})$. For $I/I_{sat} = 4$ and a $-5\ \Gamma \approx -30$ MHz detuning, $\tau_{esc} \approx 3$ ms (respectively ≈ 9 ms) for $U = 800$ µK (respectively $U = 2.5$ mK). In spite of this cooling effect, P_{at} decreases monotonically because the cooling occurs only along one axis and so the atom can be heated out of the trap along the two other axes.

A radically different result is obtained when applying all 3 pairs simultaneously. As shown with the green circles dataset of graph b., after an initial decrease of P_{at} for $\delta t_{mol} \leq 10$ ms, P_{at} remains equal to $\approx 50\,\%$ for $\delta t_{mol} = [10 - 250]$ ms, which gives a first indication that we obtain a single atom in our tweezer with a 50 % probability in 10 ms, and that it stays trapped in the tweezer when applying a molasses for a longer duration (which contrasts with the single-pair results of graph a.). The shape of $\delta t_{mol} \rightarrow P_{at}(\delta t_{mol})$ and the $P_{at} = 50\,\%$ plateau are compatible with the collisional blockade mechanism. This contrasts with the other curve of picture b. (brown squares), where a 30 MHz blue detuning is used for the molasses beams, and for which we observe the blasting of all atoms out of the tweezer, in less than 1 ms.

We then measure $P_{at}(\delta t_{mol})$ for variable detuning of the molasses beams: $\delta/2\pi$ in the range $[-30, 50]$ MHz, with respect to the bare atom frequency, which converts to $\delta_{LS}/2\pi =$

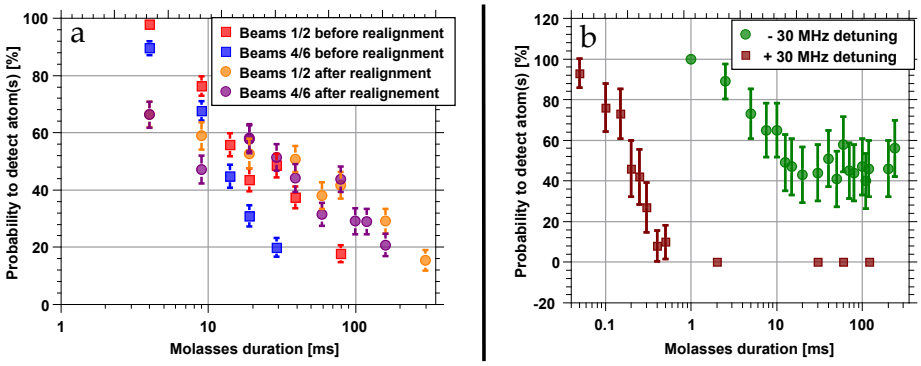

Fig. VI.4 *Effect of applying a molasses of variable duration δt_{mol} on one tweezer loaded with several atoms, for a single beam pair (graph a., left) and for all 3 pairs (graph b., right). Graph a: As mentioned in the previous section, this kind of measurement is used for ultimately checking the alignement of molasses beams: before the last step of alignement, the atomic losses is faster with the pair 4/6 (blue squares) than for pair 1/2 (red squares). This imbalance disappears after realignement (circle data points). All datapoints where taken with a* -30 MHz *detuning. Graph b: With all 6 beams, the response is different. After* 10 ms *of molasse, P_{at} is "locked" to* $\approx 50\,\%$ *(green circles), which suggests a single atom is obtained with a probability 1/2. A blue detuned molasses (brown squares) expells the atom from the tweezer in less than 1 ms.*

$[-82, -2]$ MHz with respect to the tweezer-lightshifted transition frequency at the bottom of the trap (the tweezer induces a blue lightshift on the transition): $LS_{min} \approx 52$ MHz for a trap depth of $U_{tweezer} = 2.5$ mK ($\delta_{LS}/2\pi = \delta/2\pi - LS_{min}$). The results are shown in figure VI.5. For $\delta_{LS}/2\pi \leq -60$ MHz, P_{at} decays to $50\,\%$, which signals the collisional blockade (see figure VI.5.a). For $\delta_{LS}/2\pi \geq -30$ MHz, P_{at} decays to 0 in a few milliseconds, because the molasses is close to resonance and thus the atoms are quickly blasted (see figure VI.5.c). For intermediate values of the $\delta_{LS}/2\pi$, P_{at} exhibits two decays, with an intermediate plateau at $50\,\%$, which suggests that after the initial decay, collisional blockade is achieved temporarly, and that later the single atom is blasted out of the tweezer (see figure VI.5.b). For all curves, we fit the decay with an empirical hyperbolic tangent function ($A\tanh[-\alpha(t-t_0)]+B$), from which we extract a decay rate α. For the intermediate detunings we fit only the first decay where we expect the two-body losses to occur.

Figure VI.5.d shows the decay rate α against $\delta_{LS}/2\pi$. We observe that α increases as the light comes to resonance with the lightshifted atoms. The maximal decay rate is achieved for a slightly red-detuning $\delta_{LS}/2\pi \approx -10$ MHz, which could be due the thermal averaging of the lightshift experienced by the trapped atoms. Very similar results were obtained in reference [124], with a very similar tweezer ($w_0 = 1.0$ µm; $\lambda = 850$ nm; $U_{tweezer} = 2.5$ mK), loaded with a few ^{87}Rb atoms, though we cannot compare quantitatively our decay rate α extracted from an empirical fit with their two-body losses rate β extracted from a Monte Carlo simulation of the data, and that has a different unit.

To conclude, we have seen in section VI.2 that when using our a red-detuning molasses, finely aligned with the micro-cavity, we observe a plateau at $P_{at} \approx 50\,\%$ that indicates a single atom is loaded probabilistically in the tweezer, thanks to collisional blockade. The

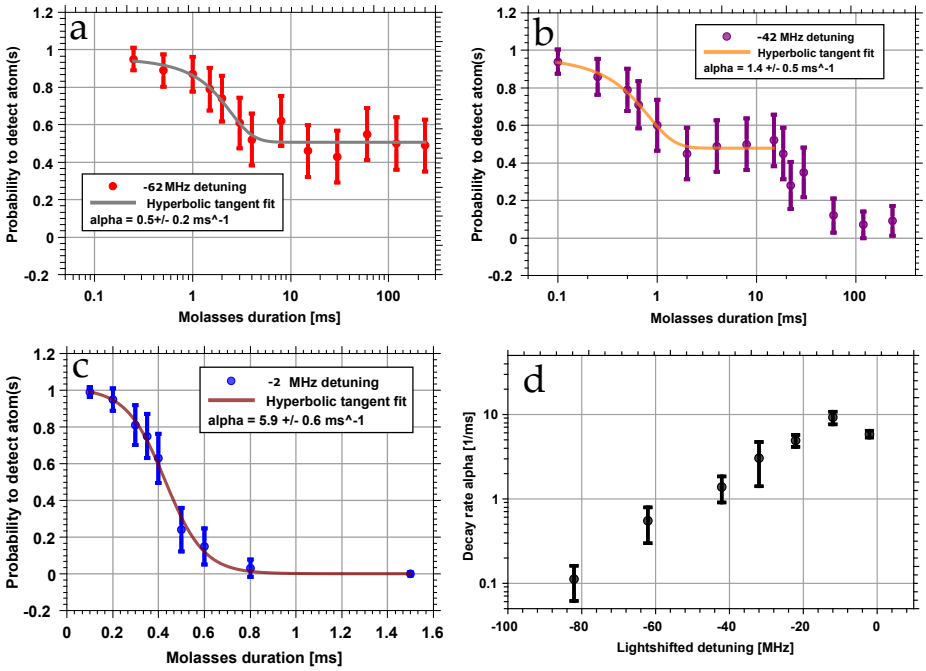

Fig. VI.5 *Effect of the detuning $\delta_{LS}/2\pi$ of the molasses. $\delta_{LS}/2\pi$ is the detuning with respect to the blue lightshift at the bottom of the $U_{tweezer}$ = 2.5 mK trap: +52 MHz. Graphs a, b and c correspond to a large, intermediate red-detunings and $\approx$ 0 detuning. The (initial) decay of each curve is fitted with the empirical function $A \times tanh[-\alpha(t - t_0)] + B$, from which we extract the loss rate α. Graph d. shows α agains the $\delta_{LS}/2\pi$, that exhibits a clear maximum when the molasses is on resonance with the lightshifted atoms.*

vacuum Rabi splitting measured in VI.5 will confirm that indeed at most one atom is loaded in the tweezer.

VI.3 Single tweezer atom characterisation

We present in this section the characterisation of the single atom in the tweezer trap, by measuring the trap frequencies in section VI.3.1 (that also provides an in-situ estimation of the waist) and the atom temperature, in section VI.3.2.

VI.3.1 Parametric measurement of the trap frequencies and waist verification

Since the temperature measurement discussed in section VI.3.2 requires knowing the trap frequencies $f_\perp$ (radial) and $f_\parallel$ (longitudinal), we start the characterisation of the single atom in the tweezer by measuring $f_\perp$ and $f_\parallel$ thanks to parametric heating modulation of the trap depth. We modulate the trap depth at frequency f_{mod}: when the f_{mod} is twice one of trap frequencies, a parametric excitation heats the atom out of the trap [125, 126].

The tweezer trap depth is U = 800 µK. The duration of the molasses is 15 ms, in order to be on the "collisional blockade plateau" $P_{at} \approx 50\,\%$. The experimental sequence starts as

the one described in section VI.2.2. It continues with:

7. Decrease of the trap depth from $U = 800$ µK to a lower value U_{low}, in 5 ms.
8. Modulation of the trap depth with a 30 % relative amplitude (peak to peak), for 100 ms.
9. Increase of the trap depth back to $U = 800$ µK.
10. The cavity is probed a third time to check if the atom is still trapped in the tweezer.

Both cavity probe measurements with the tweezer (steps 6 and 10) are done at 800 µK, so that the probing does not depends on U_{low}. Measurement 6 is used to post-select cases where an atom is successfully loaded in the tweezer. Upon these cases, measurement 10 serves to compute the survival probability S for a given modulation frequency f_{mod}.

Figure VI.6 shows S against the modulation frequency f_{mod}, for a trap depth $U_{low} = 540$ µK. One can see 3 peaks at 27 ± 2 kHz, 89 ± 5 kHz and 166 ± 2 kHz. We interpret the lowest and highest frequency peaks as the resonances corresponding to the axial ($f_{mod} = 2f_{\parallel}$) and radial ($f_{mod} = 2f_{\perp}$) trap frequencies. Indeed, as we will see in the following paragraph, the $f_{\perp}$ measured value is quantitativaly compatible with our expected values for tweezer power and waist.

Moreover, with this interpretation, we can compute $z_R = w_0/\sqrt{2} \times f_{\perp}/f_{\parallel} \approx 3.74$, which is higher than the gaussian beam value deduced from the waist: $z_{R,gauss} = \pi w_0^2/\lambda = 2.8$ µm, because we work close to the diffraction limit. Our ratio $z_R/z_{R,gauss} = 1.34$ is very close to that of experiments working with similar tweezers : in [127] $z_R/z_{R,gauss} = 1.14$ with $w_0 = 1.01$ μm and $\lambda = 850$ nm, and in [128], $z_R/z_{R,gauss} = 1.32$ with $w_0 = 0.9$ μm and $\lambda = 810$ nm. Because of this non-gaussian behavior, there is no easy analytical connection between $f_{\parallel} = \frac{1}{2\pi z_R}\sqrt{\frac{2U_0}{m}}$ and w_0. Thus we restricted our analysis to $f_{\perp} \to w_0$. For the intermediate peak, its frequency is not exactly half of the higher frequency peak ($f_{mod} = f_{\perp}$), where a parametric resonance can also happen [129, 130]. It could be related to anisotropy or anharmonicity of the tweezer trap, as the temperature is not negligible compared to the trap depth: $T/U \approx 1/8$ (see section VI.3.2).

From the measurement of the trapping frequencies, we can determine the waist w_0 of the tweezer inside the cavity. This is important in our setup, as we cannot collect and image the tweezer beam after it passes the science chamber. We have seen in section V.3.1 that the parallel imaging device garantees that our optical setup is suited for generating waists close to diffraction limit. It validates the wavefront quality of the beam up to dichroic mirror D_1 (see figure V.4), where the beam separates between the path towards the fiber-cavity and the path towards the parallel imaging device. From the measurement of $f_{\perp}$, we will now see that we can put an upper bound on the waist size inside the cavity, which is compatible with the waist size measured with images from the parallel device.

For this, let us express $f_{\perp}$ as a function of w_0. Starting with:

$$f_{\perp} = \frac{1}{2\pi w_0}\sqrt{\frac{4U_0}{m}}, \tag{VI.13}$$

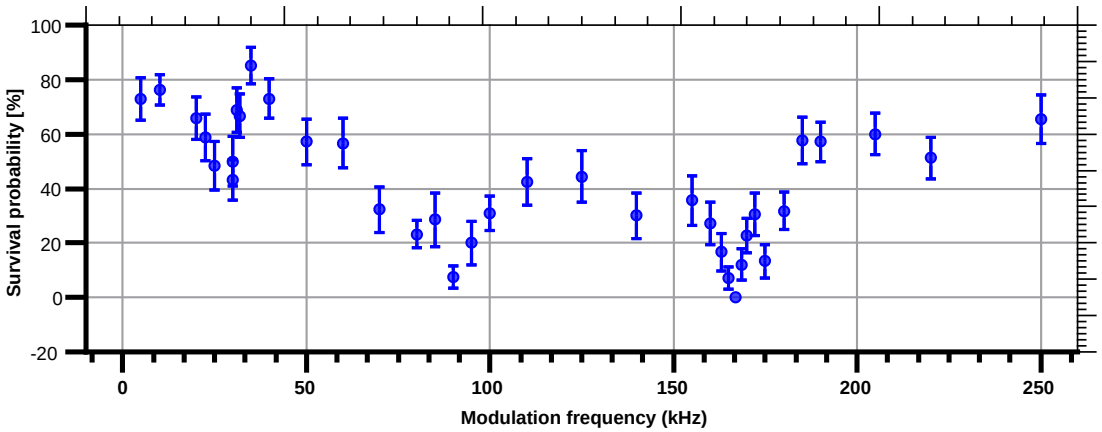

Fig. VI.6 *Parametric excitation spectrum in a tweezer of trap depth* $U_{low} = 540$ µK

where m is the mass of the atom. U_0, given by equation II.3, reduces to the following expression as the tweezer trap is linearly polarised:

$$U_0 = U_{dipole}(\vec{0}) = \frac{\hbar\Gamma^2}{24}\frac{I(\vec{0})}{I_{sat}}\left(\frac{1}{\omega_{dip}-\omega_{D_1}} + \frac{2}{\omega_{dip}-\omega_{D_2}}\right), \tag{VI.14}$$

with $I(\vec{0}) = 2P/(\pi w_0^2)$, where P is the power of the tweezer beam. Combining equations VI.13 and VI.14:

$$f_\perp = \frac{1}{2\pi w_0^2}\sqrt{P\frac{\hbar\Gamma^2}{3\pi}\left(\frac{1}{\omega_{dip}-\omega_{D_1}} + \frac{2}{\omega_{dip}-\omega_{D_2}}\right)} \tag{VI.15}$$

We see that we need to know the tweezer power P inside the vacuum cell. We cannot measure the power P after the cell, because we do not have optical access to the transmitted light. So we measure the power only before the aspherical lens and estimate the fraction transmitted $1 - e^{-2a^2/w^2} \approx 0.9$ [131], given the clipping of the beam (waist $w = 4.5$ mm) by the aspherical lens (radius $a = 10$ mm). Neglecting the non-ideal transmission through the dioptres, we obtain an upper bound to the intra-cavity tweezer power P, which provides, together with measurement of $f_\perp$, an a upper bound for the tweezer waist $w_0 \propto \sqrt[4]{P}/f_\perp$.

Then, for several values of P, from 120 to 390 µW (corresponding to U_{low} ranging from 150 to 490 µK, with the later-estimated waist $w_0 = 0.85$ µm), we measure the parametric excitation spectrum and extract $f_\perp$. The results are shown in figure VI.7, together with analytical expectations $P \to f_\perp(P|w_0)$, for $w_0 = 0.75, 0.80$ and 0.85 µm. The experimental values lie between $f_\perp(P|w_0 = 0.85\ \mu\text{m})$ and $f_\perp(P|w_0 = 0.80\ \mu\text{m})$, proving that 0.85 µm is an upper bound to the tweezer waist. This result is in very good agreement with the average waist measured with the parallel imaging device: 0.81 µm (see section V.3.1).

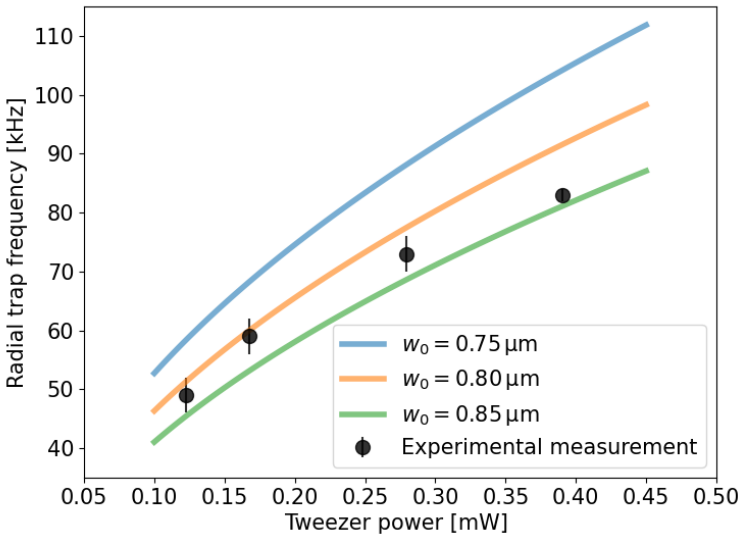

Fig. VI.7 *Estimation of the tweezer waist from the measured radial trap frequencies.*

VI.3.2 Release-recapture measurement of the temperature

Now that we have measured the trap frequencies, we can determine the temperature (more precisely, the statistical average energy of the atom, which we conveniently express as a temperature) of the single atom trapped in a single tweezer using a release-recapture measurement [132]. The sequence is similar as the one of section VI.3.1, except that the tweezer trap depth remains constant and equal to 800 µK and that the parametric excitation is replaced by a release-recapture of the tweezer atom:

7. The atom is released by switching off suddenly the tweezer.
8. After a duration of $\tau_{release}$, the tweezer is suddenly switched back to its initial trap depth.
9. After a delay of 5 ms, the cavity is probed for a third time, to check if the atom is still trapped in the tweezer.

We measure the survival probability S for various $\tau_{release}$. Following the method proposed in [132], we compare the experimental results with a Monte Carlo classical simulation of the free flight of the atom for a duration $\tau_{release}$, where the atom is considered recaptured if its kinetic energy is lower than the value of the trapping potential at the atom position, at the end of its free flight. The simulation is repeated for multiple values of the temperature and a least square calculation defines the best fit temperature. Figure VI.8 shows the experimental data together with the best fit simulation results, which yields $T = 102 \pm 5$ µK.

The ratio T/U dictats the size $\sigma_{x,y,z}$ of the gaussian thermal probability distribution of atomic position in the tweezer. As we will see in section VI.4 one main concern of our CQED

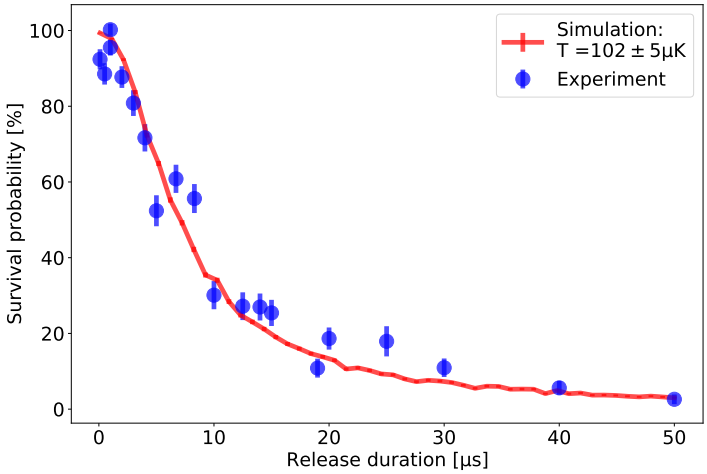

Fig. VI.8 *Release-recapture measurement of the temperature of a single atom in a tweezer together with the best fitting Monte Carlo simulation. For a short release* $\tau = 2$ µs*, the experimental survival probabilty is* $\approx 90\,\%$*, because of losses and imperfect measurement. Thus we rescale the experimental results to by a factor* $1/0.9$ *to match the simulations that do not include these imperfections. We find a best fit temperature of* $T = 102 \pm 5$ µK *for a trap depth of* $U = 800$ µK*.*

experiment is to optimise the coupling of the (thermal) single atom to the cavity mode. This requires a) aligning the tweezer with one antinode of the intra-cavity probe standing wave and b) having $\sigma_{x,y,z}$ sufficiently small so that the thermally distributed atom "explores" a region where the coupling is high enough. In section VI.4 we present different techniques for the alignement, to achieve a). We will also see that adding the intra-cavity lattice trap to the tweezer trap addresses a) and b) simultaneously, by pinning the bottom of the total trap potential close to a probe antinode, thus achieving a), and reducing the most critical size σ_z by more than a factor of 2, thus achieving b).

VI.4 Optimisation of the coupling to the cavity

As compared to free space tweezers experiments, an additional constraint of our setup is the precise positionning of the tweezers with respect to the cavity mode, which is necessary to achieve the strong coupling required for fast atomic hyperfine state detection (see section I.1.4) or entanglement of an array of single atoms (see section I.1.5). In this section, we present various methods to map the cavity mode with an ensemble of atoms or a single atom, from which one can choose the position of best coupling. We can map the square of the cavity coupling g^2 because it appears in several measurable quantities[2]:

[2]Indeed, the collective coupling Ω (section VI.4.1) and the single atom on resonance transmission ratio T_0/T_1 (equation VI.27) are functions of the effective coupling g_{eff}^2, which relates to g^2 as expressed in equation VI.17.

$$g(x,y,z)^2 \propto \frac{w_{cav}^2}{1+(\frac{z}{z_{R,cav}})^2} \exp\Big(\frac{-2(x^2+y^2)}{w_{cav}^2[1+(\frac{z}{z_{R,cav}})^2]}\Big) \times \cos(2\pi z/\lambda_1)^2, \tag{VI.16}$$

where x,y,z is the position of the atom with respect to a probe standing wave antinode at the center of the cavity, z is the cavity axis and y the vertical axis, along which the tweezer beam propagates (see figure VI.14).

The first term accounts for the gaussian structure, which is characterised by the waist size $w_{cav} = 5.7$ µm and the Rayleigh length $z_{R,cav} = \pi w_{cav}^2/\lambda = 126$ µm. In this entire chapter, the (single to few) tweezers are produced close to $z = 0$, where we can approximate $1+(z/z_{R,cav})^2 \approx 1$. As a first step, the simplified term $w_{cav}^2 \exp\Big(\frac{-2(x^2+y^2)}{w_{cav}^2}\Big)$ can be optimised with respect to x and y using the large tweezer ($w_0 \approx 5.5$ µm). Indeed, they can trap hundreds of atoms, for which the collective coupling can be measured at each repetition of the experiment (see section II.3.4) and thus conveniently mapped and optimised. This will be discussed in section VI.4.1. As a second step $w_{cav}^2 \exp\Big(\frac{-2(x^2+y^2)}{w_{cav}^2}\Big)$ can also be optimised using the single atom in the small tweezer ($w_0 = 0.85$ µm), by implementing a single-frequency measurement of the transmission ratio T_0/T_1, as explained in section VI.4.3.

The second term, $\cos(2\pi z/\lambda_1)^2$, accounts for the standing wave structure of the probing mode, with a periodicity $\lambda_1/2 = 395$ nm. It varies on a scale ≈ 15 times smaller than the first term. Thus a single atom in a small tweezer is the most suited, as it is a ≈ 7 times smaller probe than an ensemble of atoms in a large tweezer. Indeed, combining equations VI.19 and VI.13, we obtain that the typical size of the position probability distribution of atom along axes x and z is $\sigma_{x,z} = w_0/2\sqrt{k_B T/U_0}$. Thus, for an equivalent T/U_0 ratio, $\sigma_z \propto w_0$ is roughly 7 times smaller for the small tweezer than for the large tweezer.

Ultimately, the coupling can be improved by using the intra-cavity lattice trap, which has been specially engineered for this purpose (see section II.2.1). In section VI.4.2 we show how adding the lattice trap to the tweezer trap further improves the localisation of the single atom and thus its coupling.

VI.4.1 Collective coupling cavity mode mapping

With an ensemble of atoms trapped in the large tweezer, the collective coupling Ω can be measured at each repetition of the experiment. Let us now derive its expression as a function of the tweezer position x_t, y_t, z_t with respect to the cavity mode center (see figure VI.14 for a reminder of the tweezer and cavity geometry and the definition of the axes).

$\Omega^2(x_t, y_t, z_t) = N g_{eff}(x_t, y_t, z_t)^2$, where N is the number of atoms in the tweezer, and g_{eff} the effective coupling, defined by :

$$g_{eff}(x_t, y_t, z_t)^2 = \int_x \int_y \int_z g(x,y,z)^2 P(x-x_t, y-y_t, z-z_t)\, dx\, dy\, dz, \tag{VI.17}$$

with P the position probability distribution of the atomic ensemble. Assuming the atomic ensemble in the tweezer is at thermal equilibrium with temperature T:

$$P(x-x_t,y-y_t,z-z_t) \propto \exp\Big(\frac{-(x-x_t)^2}{2\sigma_x^2}\frac{-(y-y_t)^2}{2\sigma_y^2}\frac{-(z-z_t)^2}{2\sigma_z^2}\Big), \tag{VI.18}$$

with

$$\sigma_{x,y,z} = \frac{1}{\omega_{x,y,z}}\sqrt{\frac{k_B T}{m}}, \tag{VI.19}$$

where $\omega_{x,y,z}$ are the trapping frequencies of the tweezer ($\omega_{x,z} = 2\pi \times f_\perp$ and $\omega_y = 2\pi \times f_\parallel$). With the assumptions mentioned earlier, $g(x,y,z)^2$ simplifies to:

$$g(x,y,z)^2 \propto \exp\Big(\frac{-2(x^2+y^2)}{w_{cav}^2}\Big) \times \cos(2\pi z/\lambda_1)^2 \tag{VI.20}$$

Thus

$$g_{eff}(x_t,y_t,z_t)^2 \propto \int_x \exp(\frac{-(x-x_t)^2}{2\sigma_x^2}) \exp(\frac{-2x^2}{w_{cav}^2})\, dx \times \int_y \exp(\frac{-(y-y_t)^2}{2\sigma_y^2}) \exp(\frac{-2y^2}{w_{cav}^2})\, dy \times \int_z \exp(\frac{-(z-z_t)^2}{2\sigma_z^2}) \cos(2\pi z/\lambda_1)^2\, dz \tag{VI.21}$$

In this section we focus on scanning along x or y. So z_t and y_t (or x_t) are fixed, and we can integrate over z and y (or x), which gives a constant that we drop, as we derive a proportionality law. The remaining x (or y) integral is the convolution of two gaussians, which is an gaussian itself:

$$\Omega^2(x_t) \propto \exp\Big(\frac{-x_t^2}{2(\sigma_x^2+\sigma_{cav}^2)}\Big) \qquad \text{or} \qquad \Omega^2(y_t) \propto \exp\Big(\frac{-y_t^2}{2(\sigma_y^2+\sigma_{cav}^2)}\Big), \tag{VI.22}$$

where $\sigma_{cav} = w_{cav}/2$. One can see that the gaussian $\Omega^2(x_t)$ (respectively $\Omega^2(y_t)$) is centered at $x_t = 0$ (respectively $y_t = 0$), which corresponds to the desired optimal setting of a tweezer centered with respect to the probe antinode.

The experimental sequence is similar to that described in section VI.2.2, except that:

- The tweezers are produced inside the cavity rather than 18 µm away from its axis.
- To increase the number of atoms coupled to the cavity mode, 3 tweezers are generated, with a separation of 8 µm along the cavity axis z.
- The collective coupling is measured at each shot, with a frequency scan of the Rabi doublet (see section II.3.4).

The vertical (respectively horizontal) position y_t (respectively x_t) is scanned by the tunable lens (see figure V.4) (respectively the RF frequency of the corresponding axis of the 2D AOD (see section V.2). For each value of x_t or y_t, approximately 10 spectra are measured, and we extract the value of their vacuum Rabi splitting 2Ω. The average Rabi splitting is shown in figure VI.9. A gaussian function fits nicely both $\Omega^2(x_t)$ and $\Omega^2(y_t)$ scans and allows to point the tweezers position of optimal coupling to the cavity, along x_t and y_t respectively, with a precision of $\delta x \approx \pm 0.5$ µm and $\delta y \approx \pm 5$ µm. Given the 5.7 µm waist size of the cavity mode, the x_t optimisation is quite good, while the y_t optimisation is not very precise. This is due to the fact that the typical size of the atomic thermal ditribution in the large tweezer is set

by $w_0 \approx 5.5$ µm along x, comparable to the waist of the cavity mode $w_{cav} = 5.7$ µm, while the typical size along the y axis is set by $z_R \approx 120$ µm, much larger than $w_{cav} = 5.7$ µm.

If we extract a temperature from the $\sigma_{x,y}$-contribution to the widths of the fitted gaussian functions (equation VI.22), we obtain temperatures of ≈ 100 µK from the vertical y map and ≈ 240 µK from the horizontal x map. While the first value is reasonable, the second seems a bit high. This is partly due to the sensitivity of the temperature estimated with respect to the fitted width, because the latter is close to the cavity width, in the case of x. The measurements shown here should be mostly considered as a preliminary mapping of the cavity mode, which will be refined later directly with a single atom probe in a smaller-waist tweezer.

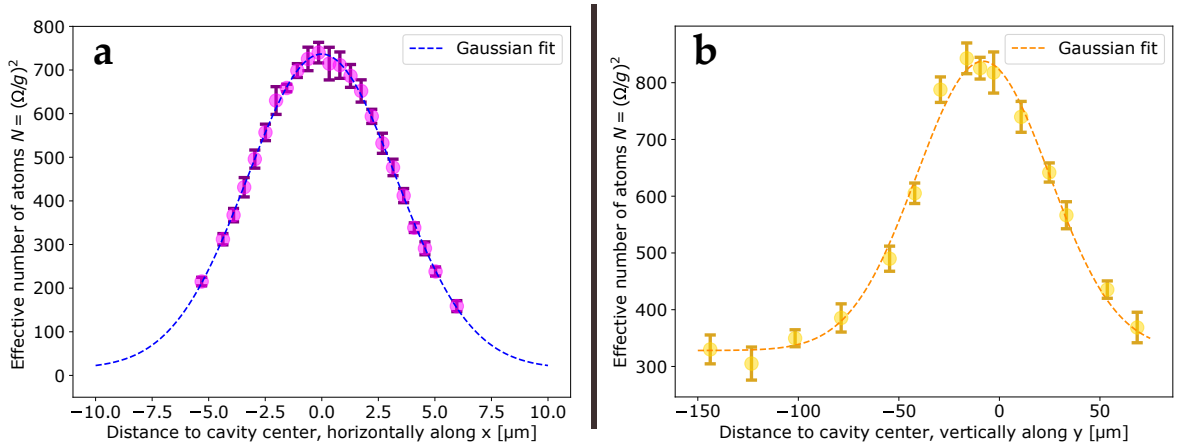

Fig. VI.9 *Mapping the relative position of (large) tweezers with respect to the cavity mode, along the x (picture a.) and y (picture b.) axes. From each spectrum, we extract the vacuum Rabi splitting 2Ω, which we convert to an effective number of atom $N = (\Omega/g_{eff})^2$, where $g_{eff} = 30$ MHz is a rough estimation of the effective coupling, defined as half the typical thermally averaged coupling: $g_{th} = 60$ MHz (see section **??**), to account for the spread of atoms over several nodes and antinodes of the probing field (along the z axis), which reduces the coupling by a factor 2 in average. The error bars correspond to ± 1 standard deviation. Figure VI.14 displays a schematics of the tweezer/cavity geometry and a reminder of the axes.*

VI.4.2 A hybrid trap with the intra-cavity lattice

VI.4.2.1 Coupling enhancement induced by the lattice

Here we show that the coupling to the 780 nm probing field of a single atom in a small tweezer can be improved by adding to the tweezer trap the intra-cavity lattice at 1559 nm, which is designed to trap atoms close to probe intensity maxima (see section II.2.1). Interestingly, in experiment of the group of Zhang (introduced in section I.2.1.3), an intracavity lattice trap is also used to help localising single atoms trapped in tweezers, especially along the cavity axis[67]. However, there are two major differences: 1) the lattice is blue detuned, and thus repelling, while ours is an attractive red-detuned lattice and 2) its *non commensurability* is such that only one every 26 lattice sites coincides with a probe antinode, instead of one

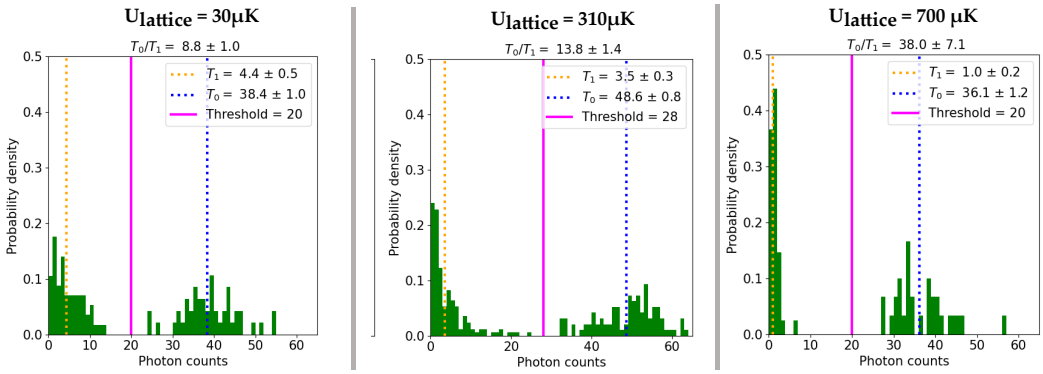

Fig. VI.10 *Effect of the the intra-cavity lattice (with variable trap depth $U_{lattice}$) on the coupling of a single tweezer atom. For each histogram, the threshold (pink line) is set so as to lie in the gap between the atomic lower transmission peak and the empty cavity upper transmission peak. Then, the average value of the single atom (respectively empty cavity) transmission T_1 (respectively T_0) is computed, and plotted as an orange (respectively blue) dashed line. Error on the average is a 68 % confidence interval $s/\sqrt{N}$, where s is the usual unbiased estimator for standard deviation. The value of T_0/T_1 is given above each historam. From left to right, $U_{lattice}$ increases and thus the coupling increases, which squeezes the atomic transmission distribution towards 0. Consequently T_0/T_1 increases.*

every two sites in our experiment. To demonstrate experimentally this improvement, we prefer not to measure the coupling of a single atom in a single frequency scan (as we do with atomic ensembles), because such scan would involve too many cycles that would depump the atom to $F = 1$ (as described in section VI.1.3), especially when scanning the Rabi peaks, where the intracavity probe power is maximal. And in fact as we will see in section VI.5, measuring the coupling of a single atom from its vacuum Rabi splitting requires measuring the transmission for each frequency of the spectrum separately. So here we implement a much lighter measurement, where we evaluate the coupling g from measuring the transmission of the tweezer single atom (T_1) and of the empty cavity (T_0), with a probe on resonance with both the atom and the cavity (see equation I.15):

$$\sqrt{\frac{T_0}{T_1}} = 1 + \frac{g^2}{\kappa\gamma}, \tag{VI.23}$$

The experimental sequence follows steps 1 to 5 described in VI.2.2. After step 5., a single atom in state $F = 2$ is loaded with a 50 % probability in a single tweezer, with trap depth $U_{tweezer} = 800$ μK, inside the cavity. Afterwards:

6. The trap depth of the intra-cavity lattice is increased from 15 μK to $U_{lattice}$, in 5 ms. The initial trap depth is non zero because the fiber cavity lock relies on the 1559 nm light (see caption of figure II.8). However, such small trap depth does barely affects the atoms, since their temperature is about 100 μK (see section VI.3.2)

7. The cavity is probed and the transmission is measured to detect if there is an atom. Similarly to the single atom detection in the trap lattice alone (section VI.1.1), the

lattice and the probe light are chopped at 2.8 MHz, with opposite phases to avoid their temporal overlap. So the atomic frequency is neither lightshifted nor broadened by the 1559 nm light (see section III.1.1) during the probing.

The measurement is repeated and the histogram of the transmission values is shown in figure VI.10, for $U_{lattice} = 30$, 310 and 700 μK. The transmission ratio T_0/T_1 increases very clearly when $U_{lattice}$ increases, as a consequence of the increasing coupling g to the probe field. The exact determination of g from the averaged transmission ratio T_0/T_1 requires knowing the thermal distribution of coupling values (as explained in section VI.4.2.4) as well as the relative position of the small tweezer with respect to the intra-cavity lattice, which will be discussed in sections VI.4.3 and VI.6. This was not the case for the dataset in figure VI.10, which is a preliminary demonstration of the coupling enhancement brought by adding the lattice trap to the tweezer trap. Further measurements exhibiting this enhancement, with more quantitative models, will be discussed in sections VI.4.3 and VI.6.1.

VI.4.2.2 Potential profile of the hybrid trap

Figure VI.11 shows the trapping potentials of the tweezer, the lattice, and the sum of the two, which we will call the "hybrid" trap. The tweezer trap depth is $U_{tweezer} = 800$ μK and the lattice trap depth $U_{lattice}$ is set to 30, 310 and 700 μK (picture a, b and c respectively), corresponding to the parameters of the measurements shown in figure VI.10. The tweezer center is displaced by $(\delta x, \delta y, \delta z) = (2.0, -3.0, 0.2)$ μm with respect to the center the closest antinode of the lattice. The precise value of this offset will be justified in section VI.5. For each value of $U_{lattice}$, we search for the position $(x_{min}, y_{min}, z_{min})$ of minimal depth of the hybrid trap and display the calculated values is the suptitle of each picture. As $U_{lattice}$ increases, the main effect is the strong decrease of z_{min} towards 0, meaning that the center of the hybrid trap gets closer to the center of the lattice antinode (located at $z = 0$), which is also an antinode of the probe lattice, where the coupling g is maximal. This is due to the much stronger confinement along z of the lattice, as compared to the tweezer. Indeed, for $U_{lattice} = 700$ μK, the value which we use systematically in the following sections, the trap frequency along z is $\omega_{l,z} = 234$ kHz for the lattice, larger than that of the tweezer: $\omega_{t,z} = 104$ kHz. Thus the lattice predominantly determines where the minimum z_{min} of the hybrid trap is located, along the z axis. This effect has a great benefit since the localisation of the single atom is the most critical along the z cavity axis, as the probing lattice varies on the scale of ~ 100 nm along z, compared to ~ 1 μm along x and y. Along the x, axis conversely, the tweezer determines entirely the localisation of the hybrid trap minimum, as its trap frequency dominates: $\omega_{t,x} = 104$ kHz $\gg \omega_{l,x} = 10$ kHz. Finally, along the y axis, the tweezer has a similar effect than the lattice ($\omega_{t,y} = 17$ kHz $\sim \omega_{l,y} = 10$ kHz).

Adding the intra-cavity lattice trap to the tweezer trap makes an essential difference for the localisation of the single atom, in terms of both the center and of the spread of the position probability distribution of the single atom. The additional trap is crucial to reach the strong coupling for the single atom (discussed in section VI.5), and provides a very beneficial robustness of this strong coupling with respect to imperfect centering of the tweezer relatively to the probe lattice, which is illustrated in section VI.5.4.

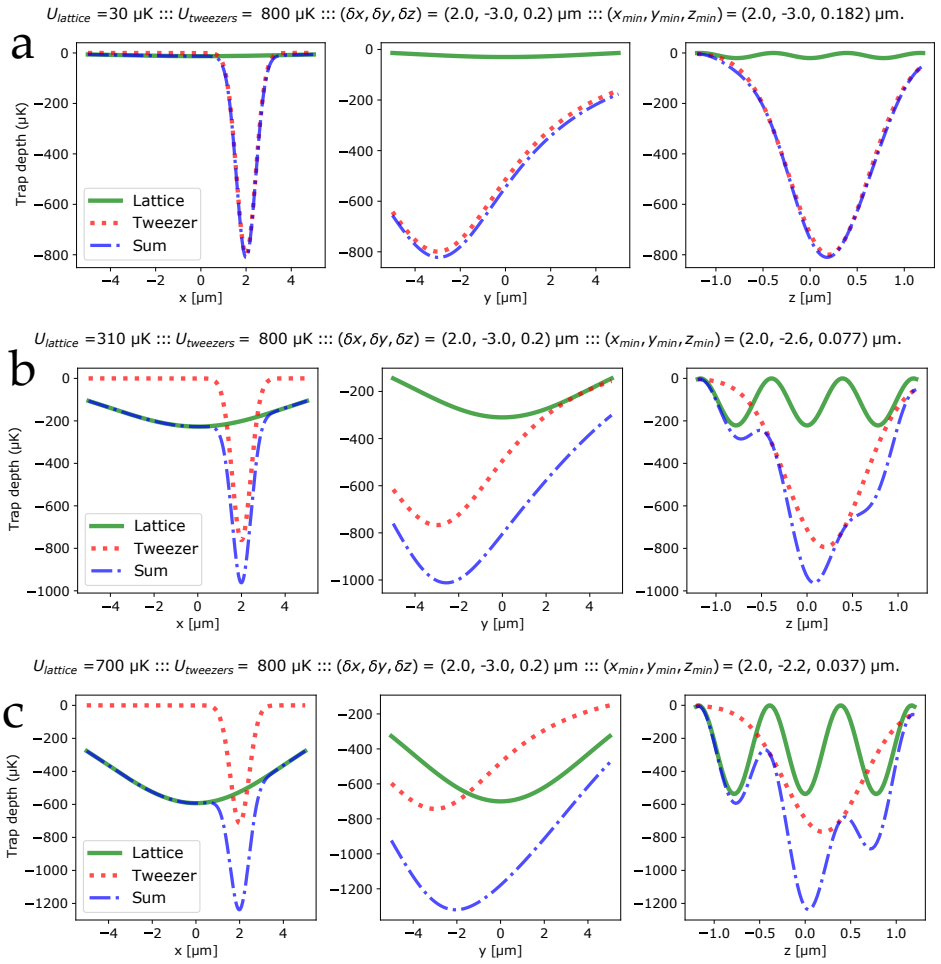

Fig. VI.11 *Lattice, tweezer and hybrid ("sum") trap potentials, for* $U_{lattice}$ = 30,310 *and* 700 μK *(picture a,b and c respectively), corresponding to the measurements of figure VI.10.* $U_{tweezer}$ *is fixed to* 800 μK. *For each picture, the left, middle and right plots correspond to* $x \rightarrow U(x, y = y_{min}, z = z_{min})$, $y \rightarrow U(x = x_{min}, y, z = z_{min})$ *and* $z \rightarrow U(x = x_{min}, y = y_{min}, z)$ *respectively.*

VI.4.2.3 Temperature in the hybrid trap

To determine the temperature in the hybrid trap, we perform a release-recapture measurement (see section VI.3.2), with a Monte Carlo simulation adapted to the hybrid trap. For the simulation, we need an harmonic approximation of the hybrid trap potential, from which we draw the atomic initial position and velocity, according to the corresponding gaussian distribution. We define $(x_{min}, y_{min}, z_{min})$ as the center of this gaussian distribution, and its standard deviations $\sigma_{x,y,z}$ (see equation VI.19) are computed from the trap frequencies defined from the second derivatives of the hybrid trap potential U_{sum}, at the position of the minimum:

$$\omega_{x,y,z} = \sqrt{1/m \frac{\partial^2 U_{sum}}{\partial x,y,z^2}(x_{min}, y_{min}, z_{min})}, \tag{VI.24}$$

The atom is release from the hybrid trap. If we use the hybrid trap for the recapture, as the lattice trap extends over $L = 145$ µm, the atom cannot escape along z and thus the measurement is insensitive to the atomic z velocity. To recover this sensitivity, the atom is released from the hybrid trap and recaptured by the tweezer only, and the Monte Carlo simulation is adapted consequently.

The experimental results and best fit simulation are shown in figure VI.12. They lead to a temperature of $T = 92 \pm 6$ µK, very close to the value obtained in the tweezer alone $T = 102 \pm 5$ µK (section VI.3.2). This result is surprising: we expect the temperature in the hybrid trap to be higher than the temperature in the tweezer, since the added lattice increases the confinement of the atom, especially along the cavity axis z. Maybe this intriguing result comes from our adapted scheme where the atom is recaptured by tweezer trap alone. This point would require further investigation.

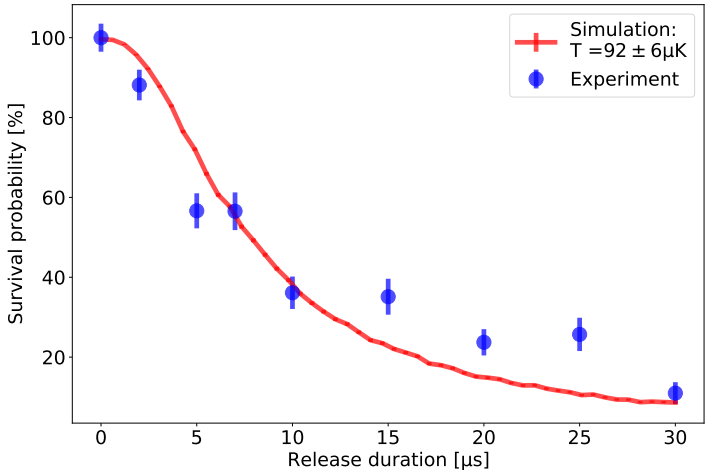

Fig. VI.12 *Release-recapture measurement of the temperature of a single atom in the hybrid trap. The trap depths are* $U_{tweezer} = 800$ µK, $U_{lattice} = 700$ µK. *In the simulation, the relative position of the tweezer with respect to the center of the closest antinode of the lattice is* $(\delta x, \delta y, \delta z) = (2.0, -3.0, 0.2)$ µm, *which corresponds to the simulations of (and will be justified in) section VI.5.*

VI.4.2.4 Single atom extinction in the hybrid trap

We present here a histogram of transmission in the hybrid trap ($U_{lattice} = 700$ µK and $U_{tweezer} = 800$ µK), for a probe on resonance with the atom and the cavity, with more statistics (1700 measurements) than required for the analyses presented in the previous sections (200 to 300 measurements), so as to compute precisely the single atom transmission exctinction

First, we compare this histogram to that obtained from micro-wave extraction of a single atom in the sole intra-cavity lattice (figure VI.2). For the two histograms, the probe duration and intensity are similar: 250 µs and $n_{cav} = 3.0 \times 10^{-2}$ for the tweezer, 300 µs and $n_{cav} = 2.0 \times 10^{-2}$ for the micro-wave extraction, leading to $T_0 \approx 51$ and ≈ 40 respectively.

In the micro-wave extraction scheme, the probability to detect an atom is $P_{at} = 4.2\,\%$ and is limited by the requirement to have a negligible probability to transfer two atoms to $F = 2$. In the tweezer, collisional blockade prevents from having two atoms in $F = 2$. Thus obtaining a single atom is much more efficient: here we achieve $P_{at} = 58\,\%$.

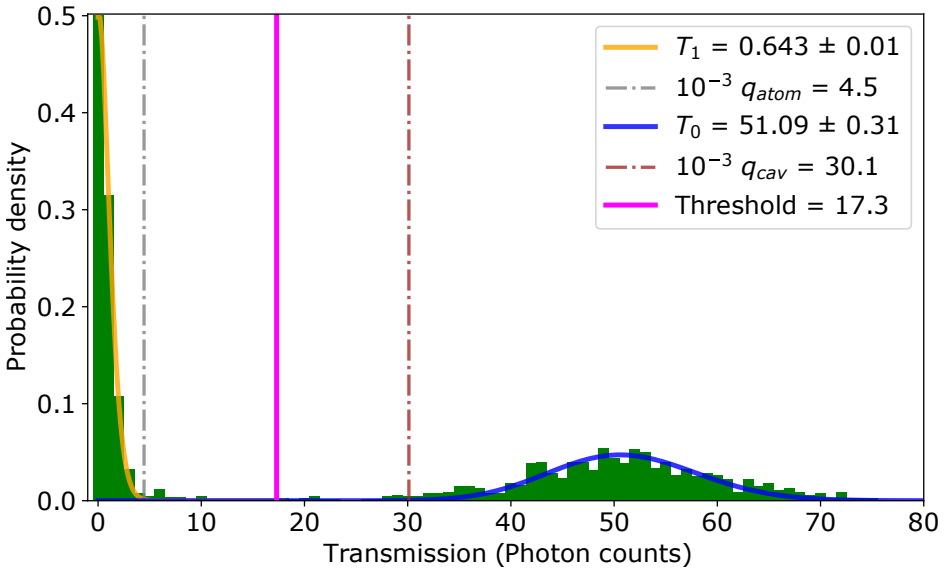

Fig. VI.13 *Transmission histogram of a single tweezer with a single atom ($P_{atom} = 58\,\%$) and higher statistics, to compute with higher resolution transmission values T_1 and T_0 of the single atom and empty cavity respectively. The threshold discriminating a single atom from the empty cavity is defined as the mean of the 10^{-3} lower quantile q_{cav} of the Poisson fit of the empty cavity distribution, and of the 10^{-3} upper quantile q_{atom} of the Poisson fit of the atomic distribution.*

Then, in the tweezer histogram, we fit both the low transmission atomic peak and the high transmission cavity peak with Poisson distributions. We obtain : $T_1 = 0.64 \pm 0.01$ and $T_0 = 51.1 \pm 0.3$, from which we can compute the single atom transmission extinction ratio $T_1/T_0 = (1.23 \pm 0.03) \times 10^{-2}$. The expression for this ratio, is given by equation I.15:

$$\frac{T_1}{T_0} = \frac{1}{\left(1 + \frac{g^2}{\kappa\gamma}\right)^2} = \frac{1}{\left(1 + 2C\right)^2} \tag{VI.25}$$

For an atom with coupling $g_{max}/2\pi = 75$ MHz and $g_{eff}/2\pi = 49$ MHz (this value is justified by a later simulation in section VI.5.3), the transmission ratios are $\frac{T_1}{T_0}(g_{max}) = 5.5 \times 10^{-5}$ and $\frac{T_1}{T_0}(g_{eff}) = 3.1 \times 10^{-4}$ respectively. The ratio for the histogram shown here is two orders of magnitude lower than $\frac{T_1}{T_0}(g_{eff})$ because of several effects:

1) The main effect is the thermal distribution of coupling strength g (computed later in section VI.5.3) and the strong non-linearity of $g \to \frac{T_1}{T_0}(g)$. In the experiment, we measure the transmission ratio averaged over many realisations of this distribution. Such average is predominantly determined the by low coupling tail of the coupling

distribution (see figure VI.17), because T_1/T_0 scales as $1/g^4$ (equation VI.25). Thus the thermal average will be much higher than the single-valued ratio computed from the thermal averaged coupling $\overline{g^2}$, which is the effective coupling g_{eff}^2 by definition (equation VI.17):

$$\left(\overline{\frac{T_1}{T_0}}\right) = \overline{\frac{1}{\left(1+\frac{g^2}{\kappa\gamma}\right)^2}} \gg \frac{1}{1+\frac{\overline{g^2}}{\kappa\gamma}} = \frac{1}{1+\frac{g_{eff}^2}{\kappa\gamma}} \tag{VI.26}$$

2) The second effect is a residual detuning between the cavity and the average lightshifted atomic frequency, explained in VI.5.3, that leads to a ratio twice higher.

3) Finally, the thermal distribution of the tweezer-lightshifted atomic frequencies (computed later in section VI.5.3) leads to further increasing the ratio by $\approx 20\,\%$.

The transmission ratio T_1/T_0 determines the performances of a tweezer occupation measurement, or the measurement of the hyperfine state of a tweezer single atom. Indeed, T_1/T_0 determines how well one can differentiate the two outputs of the measurement, and, given the photon shot-noise, how many transmitted photons one needs to collect to achieve this differentiation, given the user-defined acceptable error ϵ. Ultimately T_1/T_0 determines how fast one can measure for a given error ϵ.

We now discuss perspectives for improvement of T_1/T_0, based on a model for the thermal distributions of both the coupling and the lightshifted-atomic frequencies, which will be presented in section VI.4.3. In the near furture, we could easily reduce the single atom extinction ratio T_1/T_0 by a factor of ≈ 10 (from 1.2×10^{-2} to 1.3×10^{-3}) by:

1) optimising the centering of the tweezer with respect to the cavity mode, which results in an optimal coupling. This point will be discussed in the following sections, and a particularly precise method for this centering will be implemented in section VI.6.

2) tuning the cavity exactly on resonance with the thermal-averaged atomic frequency.

In the mid term, further reduction could be obtained by achieving a lower atomic temperature. For instance, by optimising our molasses phase, we could reach $T = 30$ µK, similarly to [128], where such temperature was obtained in a very similar tweezer ($\lambda_{tweezer} = 809$ nm, $w_0 \approx 0.9$ µm, $U_{tweezer} = 900$ µK) with conventional polarisation gradient cooling. With such temperature, T_1/T_0 drops to 7.1×10^{-5}, close to the minimal achievable value 5.5×10^{-5}. Reaching such a low temperature in our hybrid trap is probably a challenge. With a slightly higher temperature $T = 50$ µK, we would already improve the T_1/T_0 by an extra factor 10: 1.4×10^{-4}.

VI.4.3 Single atom cavity mode mapping

The collective coupling mapping described in section VI.4.1 permits to center the large tweezer with respect to the cavity mode, along the x and y axes, and provides a rough centering for the small tweezer. The z mapping cannot be done with the large tweezer, because the cloud of atoms extends over several periods of the cavity probe lattice. Here we refine the mapping with a single atom in a small tweezer, along all 3 axes. The intra-cavity lattice is on (we will use the hybrid trap from now on). To map the coupling to the cavity

mode, we vary the position x_t, y_t, z_t of the small tweezer, and measure the ratio T_0/T_1. A first naive idea consists in extending equation VI.23 to:

$$\sqrt{\frac{T_0}{T_1}} = 1 + \frac{g_{eff}(x_t,y_t,z_t)^2}{\kappa\gamma}, \tag{VI.27}$$

where g_{eff} is the convolution between the $g(x,y,z)^2$ and the P position probability distribution of the atom (equation VI.17), which depends on the position of the tweezer x_t, y_t, z_t. Then, as $x_t \to g_{eff}(x_t)^2$ and $y_t \to g_{eff}(y_t)^2$ have an expression similar to that of Ω^2 in equation VI.22 we *would* deduce from equation VI.27 that we *would* need to fit $\sqrt{T_0/T_1}$ with a gaussian function. Experimentally, we compute $\sqrt{\overline{T_0}/\overline{T_1}}$, where $\overline{T_0}$ (respectively $\overline{T_1}$) is the average transmission of the empty cavity (respectively single atom) peak in the histogram, expressed in units of number of photons detected[3].

The x and y maps of $\sqrt{\overline{T_0}/\overline{T_1}}$ are shown in figure VI.14. They are indeed well fitted by gaussian functions (the fits are *not* shown in the graph, which we explain in the following). However, the temperature deduced from the fitted $\sigma_{x,y}$ are completely incompatible with the release-recapture estimation of the temperature, and much higher than the trap depth. This stems from 3 effects:

1) From equation VI.17, $g_{eff}^2 = \overline{g^2}$ where the average is done upon sampling the P thermal distribution. Thus, the thermal-averaged version of equation VI.23 is: $\overline{\sqrt{T_0/T_1}} = 1 + \overline{g^2}/(\kappa\gamma) = 1 + g_{eff}^2/(\kappa\gamma)$. Ideally one would need to compute $\overline{\sqrt{T_0/T_1}}$ from our measurements. Unfortunately, there are many (integer) $T_1 = 0$ measurements, for which $\sqrt{T_0/T_1}$ cannot be computed. Thus experimentally we cannot estimated $\overline{\sqrt{T_0/T_1}}$ and we rather compute $\sqrt{\overline{T_0}/\overline{T_1}}$, for which the gaussian expression does not strictly hold.

2) Equation VI.23 assumes both cavity and probe are on resonance with the atomic frequency. Thus it has to be corrected in the case of a thermal distribution of atomic frequencies.

3) When changing the position of the tweezer during the map, the hybrid trap center and trap frequencies vary, and so does the thermal distributions of coupling strength and tweezer lightshifted frequency.

So instead of a gaussian fit, we use a Monte Carlo simulation of the transmission that takes into account the thermal distribution of positions of the atom in the hybrid trap, which converts to a distribution of coupling strengths g to the cavity, and to a distribution of tweezer-lightshifted atomic frequencies ω_a. It also includes how the hybrid trap is modified as a function of the tweezer position. For a probe on resonance with the cavity, tuned close to resonance with the average atomic frequency $\overline{\omega_a}$ (which we justify in section **??**), we compute the transmission ratio $T_{0,sim}/T_{1,sim}$ from equation I.11:

[3]Please note that in most parts of the manuscript, $\overline{T_0}$ and $\overline{T_1}$ are simply denoted T_0 and T_1, for simplicity. However, here, the difference does matter because of the non-linearity of the expressions, as explained in the next paragraph.

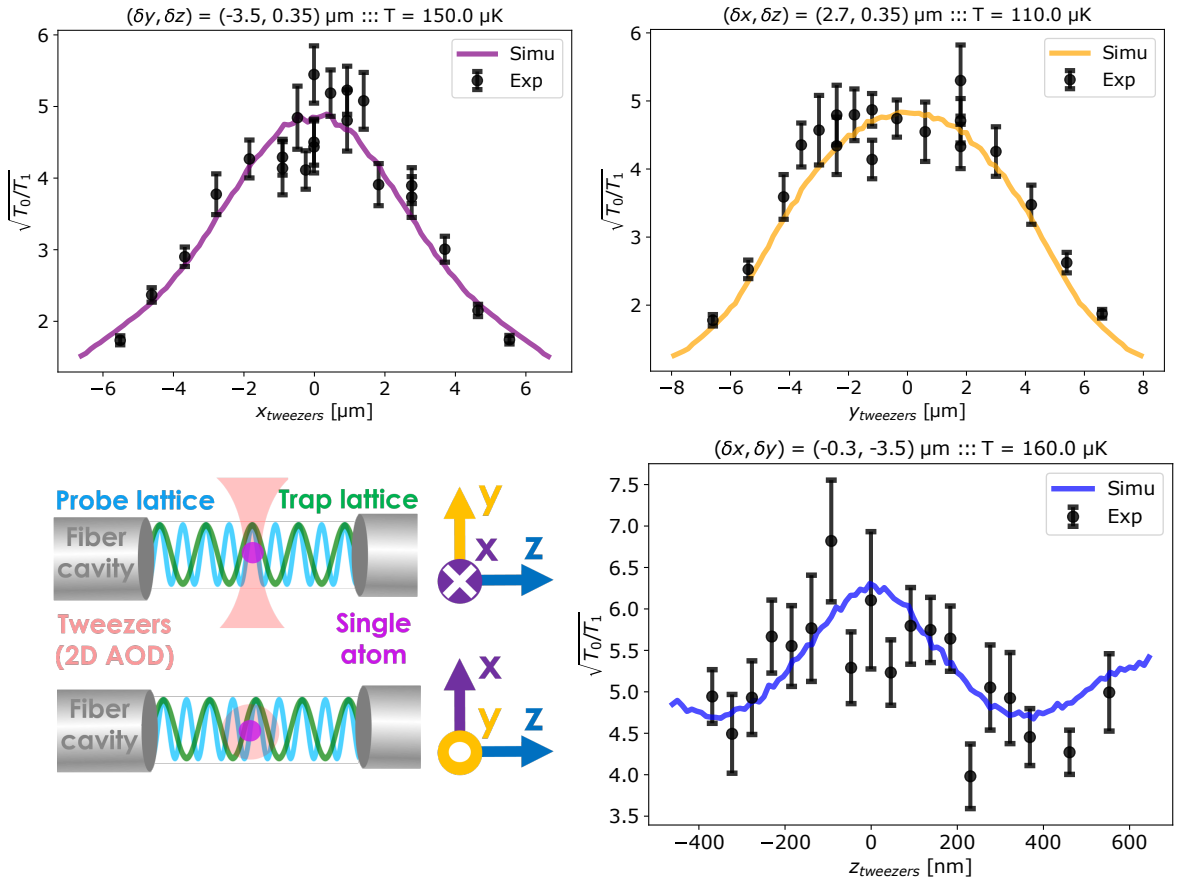

Fig. VI.14 *Mapping of the cavity mode based on measurement of the on-resonance transmission for a single atom in a single tweezer, displaced along x, y and z. The experimental data is compared to a Monte Carlo simulation that accounts for the thermal distributions of coupling strength and atomic frequency, as well as the tweezer off-centering. For each measurement, the off-centering $(\delta x, \delta y, \delta z)$ of the tweezer along the two axes complementary to that being scanned is plotted above the graph. The difference in δx between the $y/x_{tweezer}$ and the $z_{tweezer}$ scans is due to a correction of the x-tweezer position between the x-map and the z-map.*

$$\frac{T_{0,sim}}{T_{1,sim}} = \left(1 + \frac{g^2}{\kappa\gamma}\frac{1}{1+(\frac{\omega_c-\omega_a}{\gamma})^2}\right)^2 + \left(\frac{g^2}{\kappa\gamma}\frac{\omega_c-\omega_a}{\gamma(1+(\frac{\omega_c-\omega_a}{\gamma})^2)}\right)^2 \tag{VI.28}$$

In the simulation, we vary the position of the tweezer x_t, y_t, z_t accross the range of values explored in the measurement. For each position, we average the transmission ratio $\frac{T_{0,sim}}{T_{1,sim}}$ over $N_{real} = 100{,}000$ realisations of the thermal distribution. At each realisation, we draw the atomic position x,y,z in the thermal gaussian distribution with standard deviation given by equation VI.19, where the hybrid trap frequencies and the center of the harmonic approximating potential are calculated as in section VI.4.2. From the positions x,y,z, we compute

the coupling to the cavity mode $g(x,y,z)$ using equation VI.16, and the transition frequency $\omega_a(x,y,z)$, taking into account both the x,y,z-dependent lightshift induced by the π-polarised tweezer light and the Zeeman effect from the $3G$ quantisation magnetic field. Typical distributions of the couplings and the atomic frequencies are shown in figure VI.17.

Finally, from equation VI.28, we compute for the transmission ratio $T_{0,sim}/T_{1,sim}(g_k = g(x,y,z), \omega_k = \omega_a(x,y,z))$, which we average over the N_{real} realisations:

$$\sqrt{\overline{\left(\frac{T_{0,sim}}{T_{1,sim}}\right)}} = \sqrt{\frac{1}{N_{real}}\sum_{k=0}^{k=N_{real}}\left(1+\frac{g^2}{\kappa\gamma}\frac{1}{1+(\frac{\omega_c-\omega_a}{\gamma})^2}\right)^2+\left(\frac{g^2}{\kappa\gamma}\frac{\omega_c-\omega_a}{\gamma(1+(\frac{\omega_c-\omega_a}{\gamma})^2)}\right)^2} \quad \text{(VI.29)}$$

In the simulation $T_{0,sim}$ is not subjected to shot noise: it is a constant that depends on the probe power, fixed during the measurements. So $\sqrt{\overline{T_{0,sim}/T_{1,sim}}} = \sqrt{T_{0,sim}/\overline{T_{1,sim}}}$. From the experiment we measure $\sqrt{\overline{T_0}/\overline{T_1}}$. T_0 is subjected to shot noise and its average verifies $\overline{T_0} = T_{0,sim}$. Therefore experimental $\sqrt{\overline{T_0}/\overline{T_1}}$ and simulated $\sqrt{T_{0,sim}/\overline{T_{1,sim}}}$ can be compared. Both are plotted on figure VI.14.

We search manually for good fitting parameters:

1) $\delta x, \delta y, \delta z$ for the off-centering of the tweezer along the 2 axes not being mapped. Since all 3 measurements were done in a row, we take into account the correction brought to the off-centering from previous mappings. With this correction we find a set of off-centering values compatible with the experimental data.

2) the temperature T. Indeed, we observe that using the temperature $T = 92$ µK from the release-recapture measurement (figure VI.12) does not fit the data very well. For instance it gives simulated bell curves $x_t, y_t \to \sqrt{\overline{T_0}/\overline{T_1}}(x_t, y_t)$ thiner than the experimental curve. Higher temperatures ranging from 110 to 160 µK enlarge the simulated curve and are required to fit correctly the data (see the suptitles in figure VI.14). This could be due to underestimation of the temperature by the release-recapture measurement in the hybrid trap, which lead to a surprisingly low temperature (see section VI.4.2.3).

In spite of this effect, both the measurement and the simulation allow to point the cavity mode center with a precision of ±2 µm for x and ±3 µm for y. For y, the single atom map contrasts with the collective map: here the width $\sigma_{map,y}$ of a gaussian fit of the data is ≈ 8 times smaller ($\sigma_{map,y} = 3.8$ and 33 µm for the single atom and the collective maps respectively). Along the x axis, the width of the single atom map ($\sigma_{map,x} = 3.1$ µm) is only slightly smaller to that of the collective map ($\sigma_{map,x} = 3.3$ µm), because both widths are mainly determined by the size of the cavity mode $\sigma_{cav} = w_{cav}/2 \approx 2.8$ µm in the quadratic sum $\sigma^2_{map,x/y} = \sigma^2_{x/y} + \sigma^2_{cav}$ which appears in both the naive gaussian expression of the single atom map and in the similar expression for the collective map (equation VI.22).

For the z map, the SNR is significantly lower than for x and y. For instance, we can estimate the signal as the ratio between the maximal and minimal values of $\sqrt{\overline{T_0}/\overline{T_1}}$: it is

about 1.5 for z and rather 2.5 for x and y. This limited signal is due to the intra-cavity lattice, which attracts the atom to a probe antinode and ensures a good coupling g no matter the position of the tweezer $z_{tweezer}$. This prevents $\sqrt{\overline{T_0}/\overline{T_1}}$ from decreasing as much as in x and y maps. This is very good news for the robustness of strong coupling of our single atom with respect to imperfection in tweezer positionning along z, as we will see in multiple ways in the following sections. However, because of that the z map shown here can only be used for approximate estimations of:

1) the (local) maximum of $\sqrt{\overline{T_0}/\overline{T_1}}$, at the z position of optimal coupling. It can only be pointed with a precision of ± 0.15 µm.

2) the 780 nm periodicity, which corresponds to the distance between two neighboor intra-cavity lattice trapping sites.

We will see in VI.5 a last mapping method which has a much better SNR, and will allow for a more precise determination of the optimal coupling z position.

VI.5 Vacuum Rabi splitting of a tweezer single atom

In this section, we present the measurement of the vacuum Rabi splitting of a single atom trapped in a tweezer, which proves that strong coupling to the cavity is achieved at the single atom level and confirms that only one atom is loaded in our trap.

VI.5.1 Experimental methods for transmission spectrum measurement

We will now present the measurement of the transmission spectrum of the cavity, strongly coupled to a single atom in a tweezer. The cavity is close to resonance with the transition $F = 2, m_F = 2 \rightarrow F' = 3, m_{F'} = 3$, including the tweezer lighshift and the Zeeman shift from the $B = 3$ G quantification field. The experimental sequence is similar to that of section VI.4.2, for steps 1 to 6 (with trap depths $U_{tweezer} = 800$ µK and $U_{lattice} = 700$ µK). Then, the tweezer and cavity are probed twice and we measure the corresponding transmitted intensity $T_{\alpha,\beta}$. First (T_α) we probe at a variable detuning $\delta = \omega_p - \omega_c$, for which we want to measure the average transmission of a single atom $T_1(\delta)$ and of the cavity $T_0(\delta)$. Then (T_β) we probe on resonance ($\delta = 0$), which is the optimal detuning to determine if there is an atom in the tweezer. Before each measurement, a 150 µs repumper pulse ensures that the atom is in the strongly coupled $F = 2$ level. The duration of the probe pulse is 750 µs and its intensity corresponds to $n_{cav} = 7.9 \times 10^{-3}$ average intra-cavity photons.

For each value of the detuning δ, we repeat the sequence ≈ 200 times and measure $T_\alpha(\delta)$ and T_β at each repetition. We then plot the transmission histograms of a single atom and of the empty cavity, by post-selecting outcomes T_α depending on the values of T_β: if T_β is low (respectively high) it means there is an atom (respectively no atom) in the tweezer. This postselection is illustrated on figure VI.15. It is necessary for most values of δ, for which the distributions of transmission of the single atom and the empty cavity overlap (as in figure VI.15), forbiding from differentiating the single atom from the empty cavity with the transmission measurement at δ . Once the post-selection is done, for both histograms we

compute the mean transmission (which we simply denote $T_1(\delta)$ and $T_0(\delta)$ from now on) and the corresponding error bar. Please note that we perform the measurement of interest $T_\alpha(\delta)$ before the cavity/atom discriminating measurement $T_\beta(0)$, so that the atom has not yet been affected by the probe (for example by heating) when subjected to the most important measurement T_α.

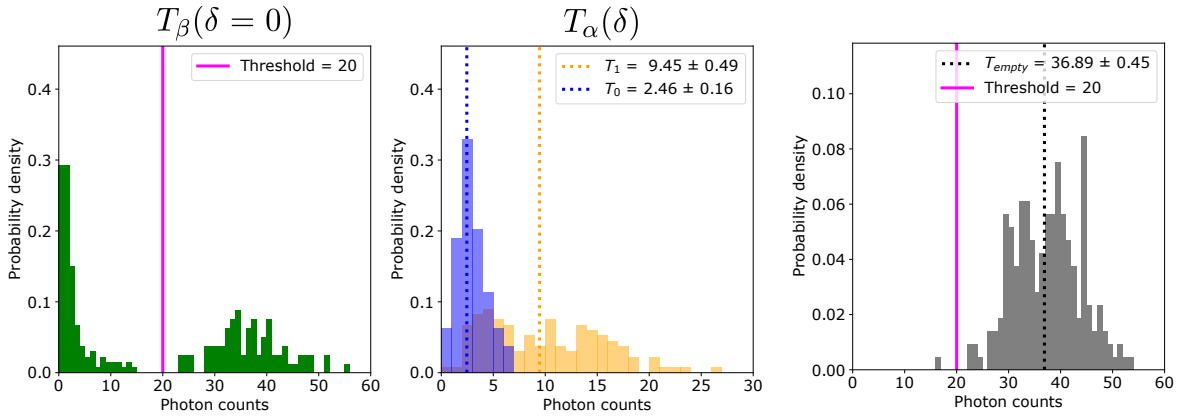

Fig. VI.15 *Measurement of the transmission of the single atom (and the empty cavity), for the detuning $\delta/2\pi = 70$ MHz. Since the single atom is loaded with a probability of 50 %, we post-select the transmission measurements T_α at the detuning of interest δ based on another measurement at $\delta = 0$ (measurements T_β). The left plot corresponds to the $T_\beta(\delta = 0)$ measurement, with which we post-select the results from the other measurement, $T_\alpha(\delta)$, shown in the middle plot. The blue/empty tweezer histogram gathers T_α measurements for which $T_\beta(\delta = 0) > T_{threshold}$. The yellow/single atom histogram corresponds to T_α measurements for which $T_\beta(\delta = 0) < T_{threshold}$. The average value of these histograms are plotted as dashed lines and displayed in the legend. The errors on the averages are the standard 68 % ($\pm\sigma$) confidence intervals: $= \pm\sigma/\sqrt{N_{sample}}$. Please notice that for this value of the detuning ($\delta/2\pi = 70$ MHz), $T_1 > T_0$ as we are close to the high frequency peak of the single atom vacuum Rabi splitting (see figure VI.16). The right gray histogram corresponds to the cavity measurement performed on resonance ($\delta = 0$), before moving the tweezer inside the cavity. It allows to check that the cavity is initially empty, which is the case, as there is only a high transmission peak.*

VI.5.2 Experimental spectrum

The resulting spectrum is shown in figure VI.16. The empty cavity transmission is fitted with a lorentzian, from which we extract a Half Width at Half Maximum (HWHM) of 16 MHz. This is close to the width measured in a single-shot frequency scan ($\kappa/2\pi = 14.2$ MHz) of the empty cavity. The slight enlargement is probably due to fluctuations of the cavity frequency during entire measurement, which lasts a few hours.

The single atom transmission exhibits a beautiful normal mode splitting. As a preliminary analysis, we can quite well fit the data by the empirical sum of two lorentzians (*not*

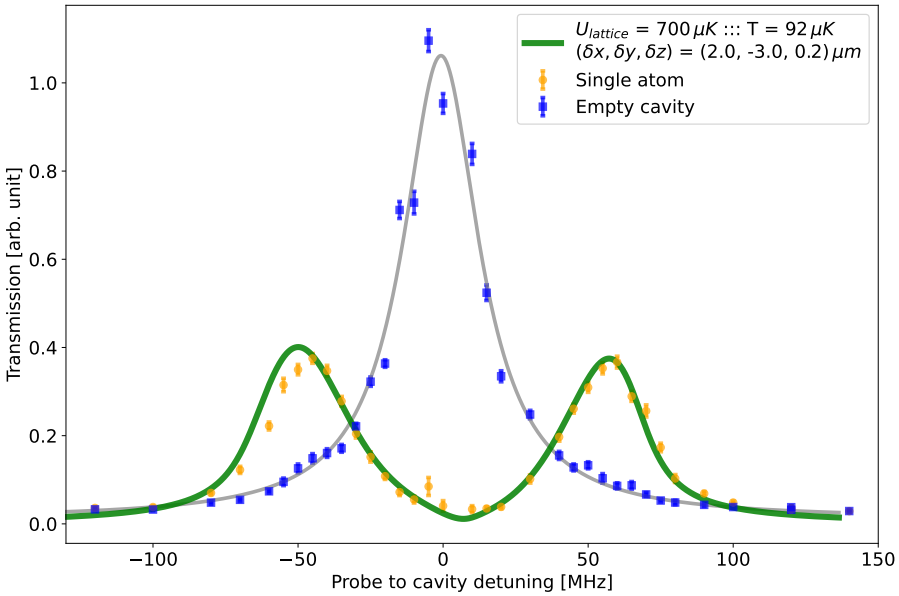

Fig. VI.16 *Transmission spectrum of a single atom (yellow points) in the hybrid trap, exhibiting a clear vacuum Rabi splitting* $2g$ *corresponding to a coupling* $g/2\pi \sim 50$ MHz. *The atomic transmission is fitted with a Monte Carlo calculation that accounts for inhomogeneity of the atomic transition frequency and the coupling strength that stems from the thermal distribution of position in the hybrid trap, and tweezer lighshift and coupling to the cavity, both of which are position-dependent. The calculation incorporates the offcentering* $(\delta x, \delta y; \delta z)$ *of the tweezer with respect to the intra-cavity lattice. The empty cavity transmission (blue points) is quite well fitted by a lorentzian.*

shown in the graph), to determine the distance between the peaks $2g_{lorentz}$, from which we deduce an effective single-atom coupling strength $g_{lorentz}/2\pi = 53 \pm 1$ MHz, and a HWHM of 16 ± 1 MHz. One can see that Rabi splitting is slightly offcentered with respect to the empty cavity: the center of the doublet is at $\omega_p - \omega_c \approx 6$ MHz. This is due to a slight detuning between the cavity and the mean atomic frequency, which is explained further in section VI.5.3. Such small detuning has a completely negligible effect on the estimation of the collective coupling from the Rabi separation.

The rather high value observed for g_{eff} indicates that the atom is polarised in $F = 2, m_F = 2$. Indeed, the coupling strenghs for other σ_+-driven transitions within in $F = 2 \rightarrow F' = 3$ are lower by a factor ranging from $\sqrt{2/3} \approx 0.82$ to $\sqrt{2/30} \approx 0.26$. In absence of any optical pumping in our experimental sequence, this result indicates that the σ_+ probe pulse polarises the atom, as observed in [66, 133].

The corresponding single-atom effective cooperativity is $C_{lorentz} = g^2_{lorentz}/(2\kappa\gamma) \approx 33$. We will see in section VI.5.3 that because of several effects, the lorentzian fits overestimates slightly the coupling, and that the actual effective coupling and cooperativity are $g_{eff}/2\pi =$

49 MHz and $C_{eff} \approx 28$, which is very satisfying. Indeed this value is close to the record cooperativity obtained with a single atom in a tweezer and an optical resonator, which to our knowledge is $C_{eff} \approx 36$, obtained in the nanophotonic experiment of the group of Lukin [63]. If we compare our results to that of Fabry-Perot cavity experiments, our tweezer single-atom cooperativity is much higher than the one achieved recently in experiments with tweezers in linear cavities with millimetric lengths: $C_{eff} \approx 1.15$ in [66] (Dan Stamper Kurn) and $C_{eff} \approx 1.1$ in [67] (Zhang). Here we fully benefit from the particularly small mode volume and waist possible with laser-machined fiber micro-cavities. For a presentation of the 3 experiments quoted here, please refer to section I.2.1.2.

As in references [66, 67], to achieve the best possible effective coupling, the tweezer needs to be centered with respect to an antinode of the probe standing-wave. In the data of figure VI.16, the effective coupling $g_{eff}/2\pi = 49$ MHz is smaller than the maximal value $g_{max}/2\pi = 75$ MHz mainly because of such residual off-centering and slightly because of the thermal distribution of positions of the atom in the tweezer which converts to a distribution of coupling values, which quadratically average to g_{eff} (see equation VI.17). Such thermal distribution also induces a distribution of tweezer-lightshifted atomic frequencies, which leads, together with the distribution of couplings, the HWHM $= 16 \pm 1$ MHz to be higher than the theoretical value of $(\kappa + \gamma)/2 \times 1/2\pi = 8.6$ MHz.

VI.5.3 Simulation

All the effects discussed in the previous section can be included in a Monte Carlo simulation of the transmission spectrum, that accounts for the statistical distribution of transition frequencies and coupling strenghts for a thermal ensemble in the hybrid trap, including the off-centering of the tweezer, caracterised by its position $\delta x, \delta y$ and δz with respect to the center of the closest probe antinode. This simulation is very similar to the one of section VI.4.3, except that here the probe frequency is varied. We use the transmission expression of equation I.11, which we normalize to 1 for the on-resonance empty cavity ($\omega_p = \omega_c$ and $g = 0$):

$$T_{norm}(\omega_p) = \frac{1}{\left(1 + \frac{g^2}{\kappa\gamma}\frac{1}{1+(\frac{\omega_p-\omega_a}{\gamma})^2}\right)^2 + \left(\frac{\omega_p-\omega_c}{\kappa} - \frac{g^2}{\kappa\gamma}\frac{\omega_p-\omega_a}{\gamma(1+(\frac{\omega_p-\omega_a}{\gamma})^2)}\right)^2} \tag{VI.30}$$

For each probe-to-cavity detuning $\delta = \omega_p - \omega_c$, we average the transmission $T_{norm}(\omega_p)$ over $N_{real} = 10{,}000$ realisations of the thermal distribution, the temperature being fixed to the value measured earlier, $T = 92$ µK (section VI.4.2.3). At each realisation we draw the atomic position x,y,z, in the thermal gaussian distribution from which we deduce the coupling $g(x,y,z)$ and the atomic transition frequency $\omega_a(x,y,z)$ (for more detail, see VI.4.3). The distributions obtained for the coupling and the atomic frequency are shown in figure VI.17. The frequency distribution (on the right) is asymmetric: the probability is higher that the atom is close to the center of the tweezer trap, and thus to have a frequency shift close to the maximal value 21 MHz. The low-frequency tail corresponds to the atom being away from the center of the trap. Ideally, the cavity should be tuned on resonance with mean atomic frequency (see section **??**), which is $\overline{\omega_a}/2\pi = 17.1$ MHz. On the day of the acquisition, the lightshift was slightly underestimated and so the cavity was tuned to ≈ 11.5 MHz. From that, the

Rabi doublet is expected to be centered at $(\overline{\omega_a}+\omega_c)/2\times 1/2\pi \approx 14.3$ MHz. We observe that the doublet is rather centered at 17.7 MHz (which corresponds to $(\omega_p-\omega_c)/2\pi = 5.6$ MHz on the frequency axis of figure VI.16). Such 3.4 MHz difference is reasonably low given the cavity frequency fluctuations ($\sigma \approx 3$ MHz). The coupling distribution exhibits a similar asymmetrical shape, which can be understood similarly from the hybrid trap confinement close to the probe antinode.

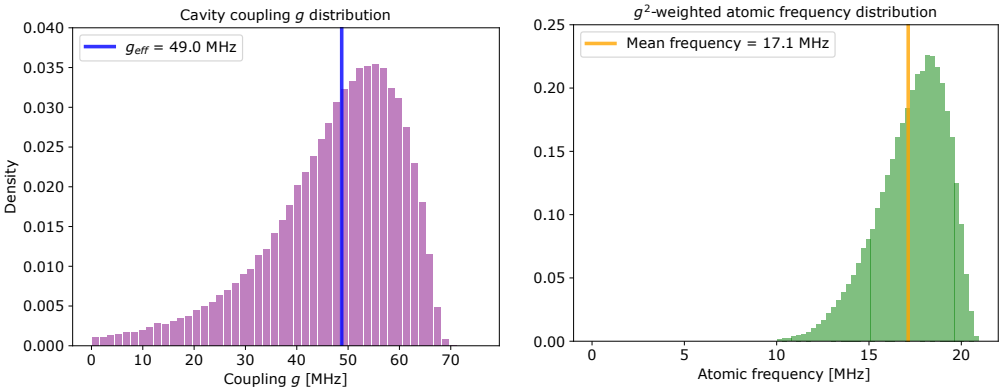

Fig. VI.17 *Distributions of coupling values g and atomic frequencies for* $U_{tweezer} = 800$ µK, $U_{lattice} = 700$ µK, $T = 92$ µK, *and tweezer off-centering* $(\delta x, \delta y, \delta z) = (2.0, -3.0, 0.2)$ µm *(fitting parameters for the spectrum). The atomic frequencies are referenced to the bare-atom frequency of the transition* $F = 2, m_F = 2 \rightarrow F' = 3, m_{F'} = 3$. *The differential lightshift induced by the π-polarised tweezer beam on the transition* $F = 2, m_F = 2 \rightarrow F' = 3, m_{F'} = 3$ *is positive and its maximal value at the bottom of the trap is* $\approx +16.8$ MHz. *We also take into account the* $\approx +4.2$ MHz *constant differential shift of the Zeeman effect.*

Finally we compute the transmission for this atom: $T_{norm}(\omega_p, g_k = g(x,y,z), \omega_k = \omega_a(x,y,z))$. The curve plotted on figure VI.16 is the average transmission : $\overline{T_{norm}(\omega_p)} = 1/N_{real}\sum_{k=0}^{k=N_{real}} T_{norm}(\omega_p, g_k, \omega_k)$. We search manually for good fitting parameters $\delta x, \delta y, \delta z$, which affect the effective coupling g_{eff} and thus the separation between the peaks. Indeed, on the day of the data acquisition, the tweezer centering was unfortunately not at the limit of sensitivity of the transmission ratio mappings decribed in section VI.4.3. We estimate that off-centering of up to $\delta x = \pm 2$ µm, $\delta y = \pm 5$ µm and $\delta z = \pm 0.25$ µm are possible. We find that $\delta x = (2.0 \pm 0.3)$ µm, $\delta y = (-3.0 \pm 0.5)$ µm, $\delta z = (0.2 \pm 0.1)$ µm fit nicely the data. Since the temperature estimation of the release-recapture measurement made in the hybrid trap (figure VI.12) depends as well on the tweezer off-centering, we repeat the simulations of both release-recapture and transmission spectrum several times until finding the values for $T, \delta x, \delta y, \delta z$ that fit both experimental curves. From their final fitted values, we compute from the simulation the effective coupling $g_{eff} = \sqrt{\frac{\sum_{k=1}^{N_{real}} g_k^2}{N_{real}}}$. We obtain $g_{eff}/2\pi \approx 49$ MHz and the corresponding cooperativity $C_{eff} \approx 28$.

We insist that this spectrum fitting is rather qualitative. For example, shifts in δx and δy can lead to the same variation of the effective coupling (though with different sensitivity,

because the tweezer is more confining along x than along y). However, such simulations are interesting as they provide an estimation for the typical tweezer off-centering more precise than the mappings discussed in section VI.4.3, which rely on a single-frequency transmission measurement, as well as the margin for improvement of the effective coupling. Indeed, for a perfectly centered tweezer ($\delta x = \delta y = \delta z = 0$), we estimate from a simulation that the effective coupling for $U_{lattice} = 700$ µK, $U_{tweezer} = 800$ µK and $T = 92$ µK is $g_{eff}/2\pi \approx 72$ MHz, corresponding to cooperativity $C_{eff} \approx 60$, much better than the previous value. To improve this alignement further and reach the highest coupling possible for these atom and trap parameters, we will introduce, in section VI.6, a new method that relies on the preliminary measurement of the single atom vacuum Rabi splitting.

VI.5.4 Robustness of the strong coupling with respect to tweezer position

Finally, for the tweezer off-centering $(\delta x, \delta y, \delta z)$ determined from fitting the vacuum Rabi splitting, we run several simulations of the transmission spectrum with a varying lattice trap depth, and a temperature $T = 92$ µK. The results are shown in figure VI.18. When the trap depth increases between $U_{lattice} = 15$ µK (the minimal value for locking the cavity - see caption of figure II.8) and 700 µK (the value commonly used), $g_{eff}/2\pi$ increases approximately from 35 MHz to 49 MHz, and C_{eff} increases from 14 to 28. As a result, the separation between the two polaritonic peaks increases. Meanwhile, the on-resonance transmission ratio T_1/T_0 decreases from 0.12 to 0.02, a 6-fold improvement. This illustrates the robustness enabled by the intra-cavity lattice, in terms of coupling strength, with respect to imperfect centering of the tweezer.

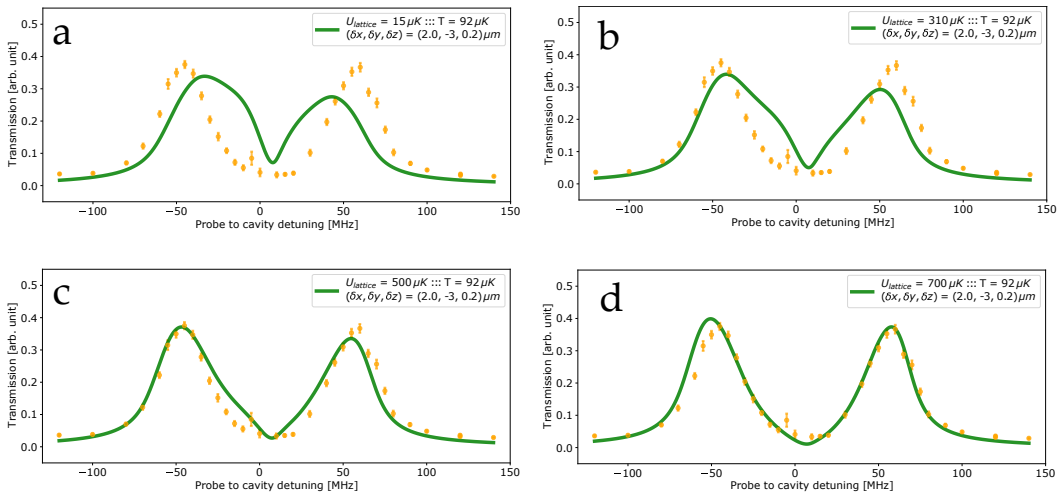

Fig. VI.18 *Simulation of the transmission spectrum for* $U_{lattice} = 15, 310, 500, 700$ µK *(pictures a,b,c and d respectively).* $U_{tweezer}$ *and* T *are fixed to* 800 *and* 92 µK *respectively, for a tweezer not perfectly centered with respect to the closest probe antinode* $(\delta x, \delta y, \delta z) = (2.0, -3.0, 0.2)$ µm. *On can see that the intra cavity lattice brings a significant improvement in terms of separation between the peaks and on-resonance transmission, which result from a stronger effective coupling.*

VI.6 Precision-enhanced cavity mode mapping on the slope of the polariton

In section VI.4.3, we have demonstrated the cavity mode mapping with a single atom in a tweezer, by measuring the on-resonance transmission ($\omega_p = \omega_c = \omega_a$). We have seen that the mapping along the cavity axis z has a poor SNR. Here we present another mapping technique, with improved SNR, which relies on a preliminary measurement of the vacuum Rabi splitting such as performed in section VI.5. It consists in measuring the single atom transmission on the slope of one of the polaritons, which is quite sensitive to the position of the polariton along the frequency axis, and thus to the effective coupling g_{eff}.

VI.6.1 Experimental results

Here the measurement is done on the positive slope of the high frequency polariton. The results are shown in figure VI.19, and they exhibit a periodic pattern. The distance between the two successive points of minimal transmission is 735 nm. From a previous calibration, we estimate the relative uncertainty in the distance between two tweezer positions to be 4 % and we get (735 ± 30) nm. The uncertainty due to sampling along $z_{tweezers}$ is actually higher. If we apply $\pm\Delta z/2$ uncertainties to the minima positions (where Δz is the distance between data points), we obtain (735 ± 60) nm, which includes the expected value of 780 nm. In the future, we would benefit from repeating the measurement with a smaller Δz.

However, it should be noticed that the SNR is much better than in the map performed with on-resonance transmission (bottom graph of figure VI.14). To interpret the shape of the results, let's first restrict the analysis to the range $z_{tweezer} = [400, 700]$ nm. Starting at the initial position of the tweezer, $z_i \approx 550$ nm, when $z_{tweezer}$ increases, the transmission increases, meaning that the positive polariton is shifting towards lower frequencies, and thus that g_{eff} decreases. For $z_{tweezer} < z_i$, the transmission decreases, which means, conversely, that g_{eff} increases. With this interpretation, prior to any fit, we can determine the position of optimal coupling as $z_0 = (370 \pm 45)$ nm, with a 3-fold enhanced precision as compared to the previous measurement (± 150 nm, see section VI.4.3).

VI.6.2 Fitting model

To fit the experimental results, we first model the single-atom transmission in the region of the positive frequency polariton by a lorentzian function, which is a good approximation:

$$T(\omega_p) = \frac{A}{1 + (\frac{\omega_p - \omega_+}{W})^2}\,, \tag{VI.31}$$

where ω_+ is the frequency of the polariton and W the experimental HWHM of the corresponding transmission peak. In this model, when the z_{trap} position of the atom is varied, $g_{lorentz}$ changes and so does the frequency of the polariton:

$$\omega_+(z_{trap}) = g_{lorentz}(z_{trap}) = g_{amp}\left|\cos\left\{2\pi/\lambda_1 \times (z_{trap} - z_0)\right\}\right|, \tag{VI.32}$$

with z_0 the position of the probe antinode, where the coupling is maximal. The probe frequency ω_p is fixed and set on the positive slope of the initial polariton, at a distance of

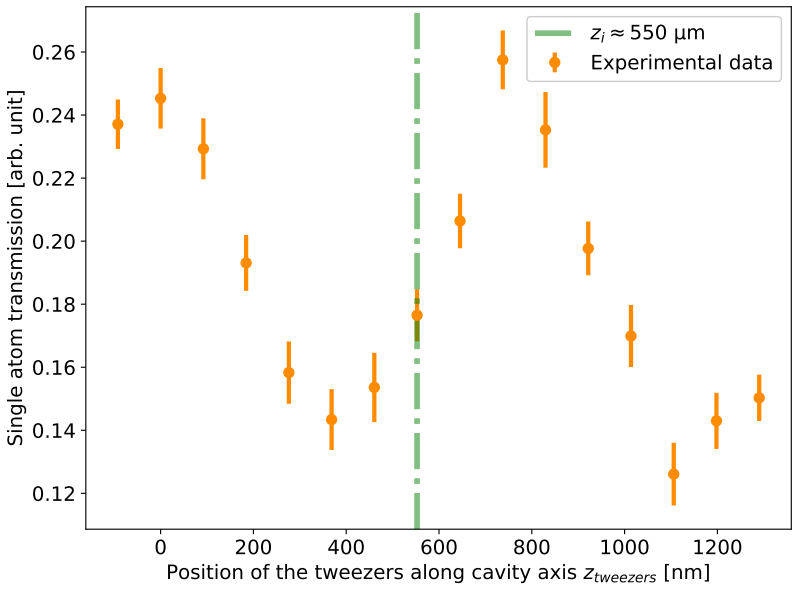

Fig. VI.19 *Map of the cavity mode along the z axis, for a probe on the side of the polariton. This method has a SNR much better than previous measurement with a probe on resonance (figure VI.14). Thus, the determination of the point of optimal coupling is about 3 times more precise. Please note that the 0 of the $z_{tweezers}$ axis is arbitrary. We estimate that it corresponds to the cavity center with a large uncertainty of* ±10 µm.

W from its central frequency. Thus, we rewrite the transmission as a function of z_{trap}:

$$T(z_{tweezer}) = \frac{A}{1 + \left(\omega_p - g_{amp}\left|\cos\left\{2\pi/\lambda_1 \times (z_{trap}[z_{tweezer}] - z_0)\right\}\right|\right)^2 / W^2}, \tag{VI.33}$$

Then we consider two different trapping configurations:

1) the atom is in the hybrid trap ($U_{tweezer} = 800$ µK, $U_{lattice} = 700$ µK), which corresponds to the experimental conditions for the data shown here

2) the atom is in the tweezer only. Though there is no measurement for this situation, we simulate it to highlight the effect of the lattice.

In the first case $z_{trap}[z_{tweezer}] = z_{hybrid}[z_{tweezer}]$, where the position z_{hybrid} of the hybrid trap is defined as the position of the minimal value of the sum of the tweezer and the lattice potentials (similarly to what is done in section VI.4.2). In the second case $z_{trap}[z_{tweezer}] = z_{tweezer}$. To simplify the analysis, we drop the variables x and y, and any residual off-centering of the tweezer along x and y will be accounted for as a reduction of the maximal coupling g_{amp} (in equation VI.33).

VI.6.3 Simulation results

Graph c of figure VI.20 shows that $z_{tweezer} \to z_{hybrid}$ is almost a step function (blue solid line). Each change of step corresponds to a jump of the minimal potential point from a trap

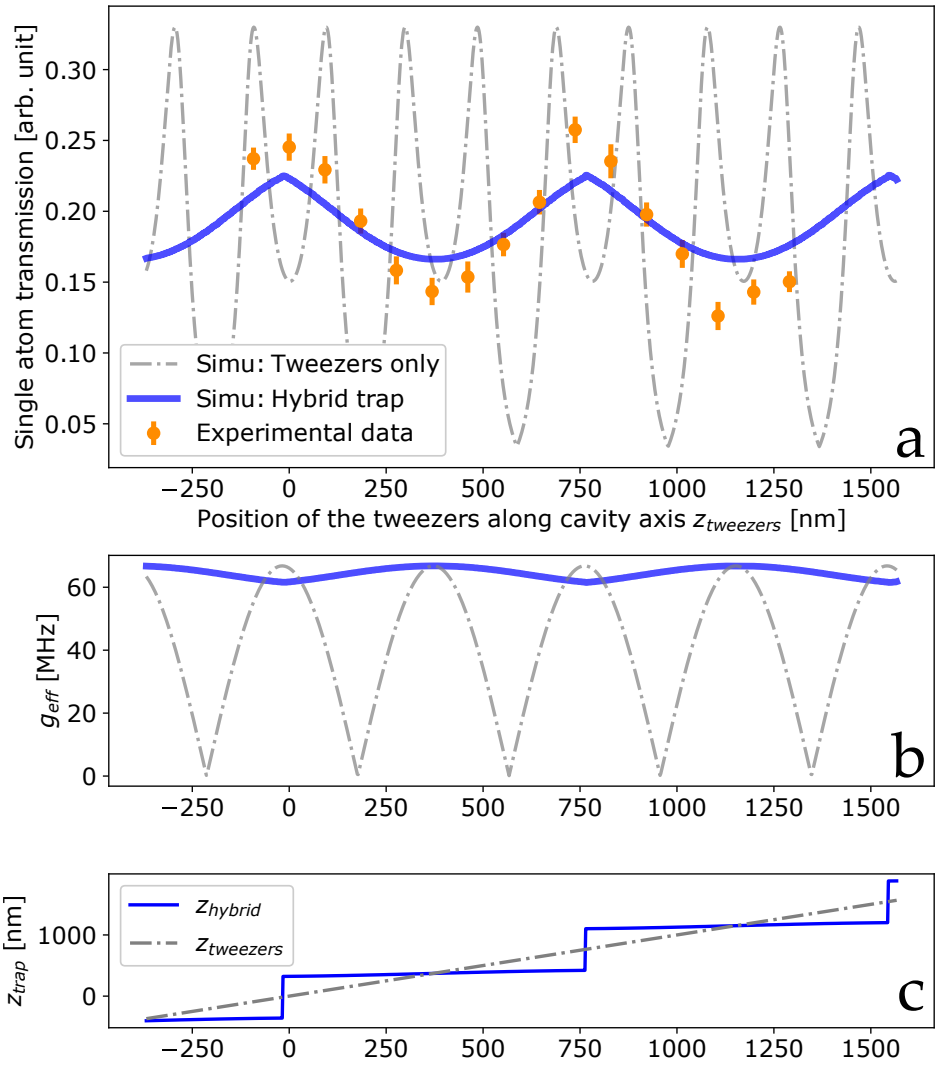

Fig. VI.20 *Simulation of the transmission on the slope of the polariton. For more details please refer to the main text.*

lattice site to its neighbor, 780 nm away. The jump corresponds to the tweezer passing by the the critical point equally distant to the two closest lattice antinodes. Between each jumps, $z_{tweezer} \rightarrow z_{hybrid}$ has a small slope, such that z_{hybrid} varies by only $\approx \pm 50$ nm around the lattice antinode, while $z_{tweezer}$ (gray dashed-dot line) varies by 780 nm ! This illustrate how strongly the intra-cavity lattice pins the atom along the z axis, which provides a coupling to the cavity very robust to imperfect centering of the tweezer with respect to the probe antinode.

This robustness is illustrated with graph b, where we compare the coupling $g_{lorentz}(z_{tweezer}) = g_{amp}|\cos[2\pi/\lambda_1 \times (z_{trap} - z_0)]|$ with the lattice (blue full line, $z_{trap}[z_{tweezer}] = z_{hybrid}[z_{tweezer}]$) and without (grey dashed-dotted line, $z_{trap}[z_{tweezer}] = z_{tweezer}$). Without the lattice, $g_{lorentz}$ varies from g_{amp} to 0 with the periodicity of probe lattice $780/2 = 395$ nm[4] With the lattice,

[4]The value of 0 might be surprising. For an atom with a thermal distribution of coupling g, the average

because the atom is pined close to a trap antinode, which is also a probe antinode, the coupling remains high ($g_{lorentz}(z_{tweezer}) \geq 0.9\, g_{amp}$) and varies with the periodicity of the trap lattice $1559/2 \approx 780$ nm due to the jumps that we have mentioned.

Graph a. shows the single atom transmission on the slope of the polariton. The blue line corresponds to a fit of the data with equation VI.33, where z_{trap} is replaced the "step" function $z_{hybrid}(z_{tweezer})$. A and W are fixed from the preliminary fit of the positive polariton in the full transmission spectrum, and only the best achievable coupling g_{amp} and the optimal position z_0 are free parameters. The best fit values are $g_{amp}/2\pi = 67 \pm 2$ MHz and $z_0 = 370 \pm 20$ nm. g_{amp} is higher than the $g_{lorentz}/2\pi \approx 53$ MHz value obtained in section VI.5.2 which indicates that the tweezer was not perfectly centered for the vacuum Rabi splitting, as the simulation of the transmission spectrum (see section VI.5.3) implies. By performing a full transmission spectrum measurement immediately after such z mapping of the coupling, and setting the tweezer position to the optimal value $z_0 = 370$ nm, we expect a vacuum Rabi splitting corresponding to an effective cooperativity of $C_{eff} = 45$[5], closer to the highest possible value for the temperature and trap parameters considered here: $C_{eff} = 60$ (see section VI.5.3). The remaining gap to $C_{eff} = 60$ could be closed by optimising as well the x,y position of the tweezer with the enhanced precision of such a polariton-slope transmission measurement.

The fit shown in graph a. is not perfect: its amplitude is smaller than that of the experimental data points, which suggests that we slightly overestimate the atom localisation induced by the lattice trap. There are several possible causes for that, which relate to imperfections of the lorentzian empirical model used here:

1) the cosine expression for the coupling (equation VI.32) is that of a 0 K-point-like atom. Indeed, with a thermal distribution of coupling, the g average value, which position of the polariton, cannot go down to 0. In our model here, only W (larger than the theoretical $(\kappa + \gamma)/2$ - see section VI.5.2) accounts for the thermal inhomogeneities in coupling and lightshifted atomic frequency.

2) the model of this section accounts for the change of position of the hybrid trap when $z_{tweezer}$ varies but not for the change of the hybrid trap z frequency (equation VI.24), which is reduced by up to 10 % when the tweezer is equidistant to two trapping sites.

3) the model assumes the width W of the lorentzian is constant, meaning that we neglect the variations of thermal distribution of couplings and of lightshifts when $z_{tweezer}$ varies.

A finer analysis of the results could be performed by implementing a Monte Carlo simulation of the average transmission including these effects, similarly to what is done in section VI.5.3.

Finally, we comment the fictitious single atom transmission in absence of the lattice (grey dashed-dotted line in graph a), obtained from equation VI.33, with $z_{trap}[z_{tweezer}] = z_{tweezer}$. The large variations of g_{eff} visible on graph b. result in much larger variations of $T(\omega_p)$

coupling of the distribution cannot be 0 except for $T = 0$ K. However, here, the expression of the coupling is that of a point-like atom, and only W accounts for the thermal distribution, as discussed below.

[5]To compute this cooperativity, we convert the lorentzian-approximation $g_{lorentz}$ into a effective coupling g_{eff} with the same ratio as observed in sections VI.5.3 and VI.5.3: $g_{eff} = 49/53 \times g_{amp} \approx 2\pi \times 62$ MHz

than with the hybrid trap. $T(\omega_p)$ has a periodicity of $780/2 = 390$ nm, equal to that of the probe lattice. The local maxima corresponds to the probe being on resonance with the polariton. There are two sets of local minima:

a) the upper minima correspond to antinodes of the probe, where the coupling is maximal and the probe is slightly red-detuned with respect to the (positive) polariton.

b) the lower minima correspond to nodes of the probe, where the coupling is minimal and thus the probe is signigicantly blue-detuned with respect to the polariton. The minimal transmission is not 0 since the lorentzian peak is not sufficiently far from the probe.

Such fictitious graph corresponds to a tweezer point-like atom, which experimentally would require a vanishing temperature. We plot it to emphasize the robustness brought by the hybrid trap, which is visible in transmission as well.

VI.7 Towards multiple strongly coupled tweezer single atoms

In the previous sections, we have showed that we are able to load a single atom in a single tweezer (generated by the 2D AOD). We characterise its temperature and trap frequency, demonstrate its strong coupling to the cavity and present several method to map the cavity mode and improve the coupling strength.

The next step towards the objective described in section I.2.2 is to generate multiple single atoms in multiple tweezers, which implies generating multiple tweezers, setting up the tweezers storage register outside of the cavity with the 1D AOD, transferring atoms from the storage register to the cavity for single tweezer detection.

VI.7.1 Preliminary alignements and angle measurements

We start by describing the few preliminary alignement and distance/angle measurements required to operate multiples tweezers with both AODs. First we align the 1D AOD beam, such as to generate an array at a distance of $d \approx 18$ µm from the cavity axis, where the coupling has a negligble value 20000 smaller than on the cavity axis. For this we use the cavity mode mappings described in sections VI.4 as a means to measure the relative position between the 2D AOD (with which all the tweezer measurements presented earlier were done) and the cavity mode. With this information, we generate an array of tweezers with the 2D AOD, at the aimed distance d of the cavity axis. Then we align the 1D AOD beam so as to superpose to the 2D AOD tweezer array the same array of tweezers, generated with the 1D AOD, using the parallel imaging device.

For an array of tweezers parallel to the cavity, one needs to know the angle between the array axis and the cavity axis, which is not required for the single-tweezer operation of earlier sections. In the horizontal plane (x,z) we measure this angle for the 2D AOD: $\theta_{xz} = 1.7 \pm 0.4°$ (see figure VI.21). This is very satisfying given that this tweezer array was aligned with the axis of the cavity optical fibers by eye, using images of tweezers light scattered on the fibers, such as pictures c. and d. on figure VI.3.

For a chain tweezers covering a significant part of the cavity length $\Delta z = 120$ µm, this angle converts to a shift of $\Delta x = 3.5$ µm, meaning that, if the cavity axis intersects the 2D

AOD array at the middle of the array, the extremal tweezer will be shifted by $\pm\Delta x/2 = \pm 1.7$ µm from the cavity axis. Due to this shift, the coupling strength g of extremal single atoms will be reduced by a factor $\exp[-(\Delta x/(2w_{cav})^2] \approx 0.91$. Given the 60 µm $z-$distance to the cavity center, the coupling strength also reduced by a factor $1/\sqrt{1+[\Delta z/(2z_R)]^2} \approx 0.90$ (this is independent of alignement). Assuming the central tweezer has been aligned with the cavity mode along all 3 axes, using the most precise method described in section VI.6, we expect its effective coupling to be $g_{eff}/2\pi = 62$ MHz (see section VI.6.3). Thus, the effective coupling of the extremal tweezers would be 18 % lower: $g_{eff}/2\pi = 51$ MHz, very close to the value from the vacuum Rabi splitting reported in section VI.5.2. So the coupling of the entire array of tweezers should be sufficiently high for most operations. For operations requiring a more homogeneous coupling strength within the array, one could further reduce the angle θ_{xz}, with the help of the goniometeres on which both AOD are mounted.

Using the parallel imaging device the angle between the 1D AOD and 2D AOD tweezers arrays was estimated to be $\approx 0.15 \pm 0.20°$, which converts, in the worst case, to a shift of ± 0.35 µm perpendicularly to the array, for the most extremal tweezers. This is not compltelty negligible as compared to the tweezers waist $w_0 = 0.85$ µm. However, we believe that it is still possible to transfer a single atom from one to the other AOD. In the short-term this should be sufficient. In the mid-term, such shift might induce some heating for a quick transfer of the atom between AODs. To avoid this, one would need to further align the 1D AOD storage register array of tweezers with respect to the 2D AOD array, using the goniometers mentioned above.

The results presented in the following were taken with tweezer array extending over at most 42 µm along the cavity axis. Thus the residual angle effects discussed here are not an issue.

VI.7.2 Demonstration of collisional blockade for up to 9 tweezers

We generate, with both the 1D and the 2D AODs, arrays of $N_{tweezers} = 5$ or 9 tweezers with a separation of $3 \times 1559 = 4677$ nm between neighbor tweezers, so that all tweezers are centered on trapping sites of the intra-cavity lattice, where the probe intensity is maximal. Phases and amplitudes of the AOD multi-frequency RF signals are optimised, as described in sections V.2 and V.3.2 respectively.

The 2D AOD tweezer array is loaded from the transport trap (see section VI.2.2). After applying a molasses of duration δt_{mol} and setting the $B = 3G$ quantification magnetic field along the cavity axis, the single atoms in the 2D AOD tweezer array are transferred in 3 ms to the 1D AOD tweezer array, overlapped to the 2D AOD array. The trap depth of each tweezer in both array is $U_{low} = 0.8$ mK, our standard value for the results of this manuscript. The 1D AOD array is our static atomic storage register.

Then, for each tweezer of the storage register:

1) the (probabilistic) atom is transferred to a single moving tweezer, generated by the 2D AOD. The storage register corresponding tweezer is kept on at U_{low}, and so we use a 10 times deeper moving tweezer (with trap depth $U_{high} = 8.0$ mK) to grab the atom.

2) the moving tweezer is displaced to the cavity in 0.6 ms

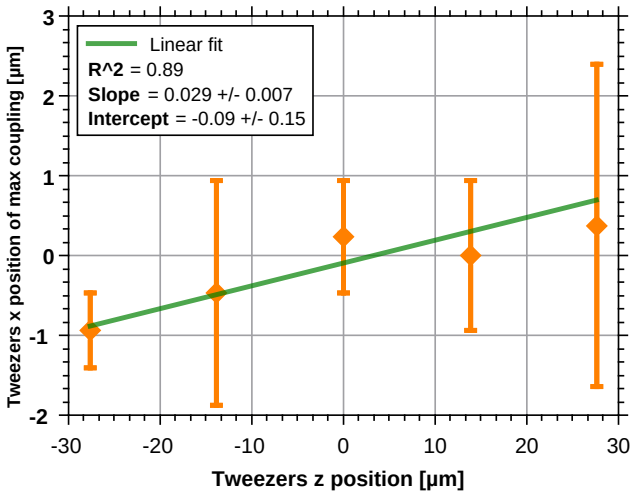

Fig. VI.21 *Single atom protractor ! The goal of the measurement is to evalutate the residual angle θ_{xz} between the cavity axis and the almost parallel axis of the 2D AOD tweezer array, in the horizontal (xz) plane. For several position z of the tweezers, we map the cavity mode along the x axis (see section VI.4.3) and point x center of the cavity mode. Both positions are defined in the reference of the 2D AOD axes. From a linear fit of the data we extract the slope, which is the angle $\theta_{xz} = 1.7 \pm 0.4°$.*

3) after a repumper pulse to ensure the atom would be in $F = 2$, we probe the moving tweezer on resonance to detect if there is a atom. The probing is done at a reduced trap depth, U_{low}, for which we have calibrated the detection and for which we expect much narrower thermal distributions of tweezers-lightshift than at U_{high}. After probing, the trap depth is increased back to U_{high}. Indeed, the intra-cavity lattice trap is constantly on at a trap depth $U_{lattice} = 700$ µK, rather than turned off and on and at each tweezer motion and probing respectively. This improves the frequency stability of the cavity, which is locked with the lattice light. Consequently, the moving tweezer has a trap depth U_{high} much higher than the lattice so that no is left in the lattice. Trap depth increase and decrease between U_{low} and U_{high} are done in 0.2 ms, and the probe duration is 0.5 ms.

4) the moving tweezer is displaced to its initial position in the atomic storage register, and its trap depth is lowered to 0 to leave the atom in the storage register.

Picture a. of figure VI.22 shows the probability P_{at} to detect atom(s) in the tweezers for various molasses duration δt_{mol}. P_{at} is averaged over all tweezers of the array. Similarly to the single-tweezer results (picture a in figure VI.4), one can see the decay of P_{at} for $\delta t_{mol} \leq 10$ ms due to two-body light-assisted losses, and, for $\delta t_{mol} \geq 15$ ms, the collisional blockade "plateau" at $P_{at} \approx 55\,\%$ (respectively $45\,\%$) for $N_{tweezers} = 5$ (respectively 9). Pictures b (respectively c) shows the probability to detect a single atom for each of the $N_{tweezers} = 5$ (respectively 9) tweezers, on the collisional blockade "plateau", after a molasses

of $\delta t_{mol} = 15$ ms . One can see that the probability is rather homogeneous among the different tweezers.

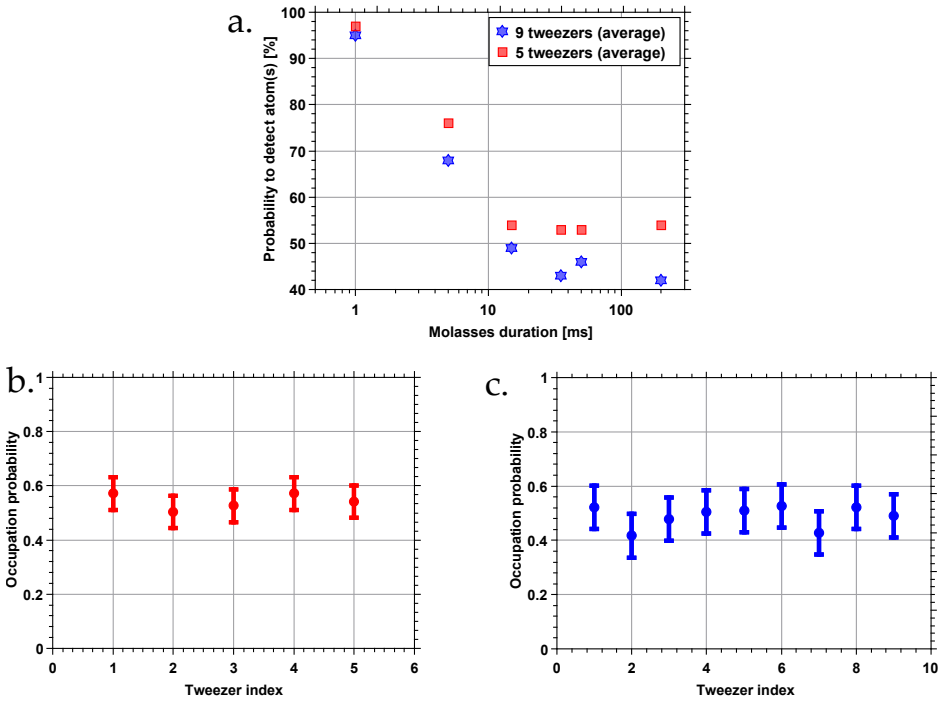

Fig. VI.22 *Picture a: Collisional blockade plateau for an array of 5 and 9 tweezers. The probability to detect an atom P_{at} is computed from averaging the results of all tweezers. Picture b. and c. show P_{at} for each tweezer separately, after a molasses of* 15 ms. *One can see that the probability is rather the same for all tweezers.*

VI.8 Conclusion

Our high cooperativity microcavity allows for a fast detection of the hyperfine state of an atom. After checking this ability with a single atom in the intra-cavity lattice, we have used this detection to measure the presence of single atom in a single tweezer. This measurement has been the basis of most of the results presented in this chapter. A standard red-detuned molasses is aligned on the cavity mode. Upon applying this light on the tweezers loaded with several atoms, the collisional blockade regime is reached, where a single atom is loaded probabilistically ($P_{at} \approx 50\,\%$) in each single tweezer.

As a first step, most of the work presented here has been performed with a single atom in a single tweezer, generated by the 2D AOD. In this configuration, we measure the atom temperature and the trap frequencies, which provide an in-situ verification of our tweezer waist. To achieve the optimal centering of our tweezer with an antinode of the intra-cavity probe standing-wave, and thus the best coupling possible to the cavity, we test various methods for mapping the effective coupling of the trapped atom(s). A first rough centering is based on measurements of the collective coupling with atomic ensembles in large tweezers. Going back to a single atom in a single tweezer, we then demonstrate that the effective

coupling is significantly improved if we add to the tweezer trap the intra-cavity lattice trap, which has been specially engineered to attract the atom to a probe antinode. This "hybrid" trap is very robust to imperfect centering of the tweezer with respect to the probe, for which it largely compensates. Nevertheless, the hybrid trap being on, we further optimise the coupling by mapping the cavity mode in all 3 directions with a single small tweezer, measuring the single atom transmission exctinction. An important step is then the demonstration of strong coupling of such tweezer single atom to the cavity, which we perform by measuring the single atom - single photon transmission spectrum. It exhibits a vacuum Rabi splitting with an effective cooperativity $C_{eff} \approx 30$. This is close to the record achieved for a tweezer single atom and a optical resonator. Once the Rabi splitting is measured, we use the transmission on the side of a polariton peak as a means to map the coupling when moving the tweezer along the cavity axis. This method is much more sensitive than the previous one. By mapping the cavity mode along all 3 axes with this new method, we expect to reach effective cooperativities in the range $50 - 60$, close to the maximal value, $C_{max} = 65$.

Finally, we start operating multiple tweezers simultaneously with our dual-AOD architecture. The 1D AOD tweezer array is positionned 18 µm away from the cavity axis, where it forms our 1D AOD qubit storage register. In the horizontal plane, we measure the residual angles between a) the 1D and 2D AOD axes and b) the 2D AOD and the cavity axes. These angles are sufficiently small to operate a chain of 40 tweezers covering almost all the cavity length, where all trapped atoms would experience a strong and rather homogeneous coupling. We then demonstrate the (probabilistic) single atom loading of up to 9 tweezers. This constistutes the first steps towards manipulating individually tens of single atoms strongly coupled to the cavity.

Chapter VII

Conclusion

VII.1 Summary of the results

This manuscript describes the work done on a platform that aims at combining strong coupling Cavity Quantum ElectroDynamics (CQED) with tweezer array.

The strong interaction of a single atom and the cavity field can be used to a) perform quantum non demolition and fast detection of the atomic qubit state and b) generate entangled states such as quantum-metrology relevant squeezed states or the symmetric W states and c) to mediate infinite-range interactions between atoms through the cavity mode. Single atom tweezer array, that can be conviniently generated by AODs, allow for fast reconfiguration of the tweezers positions. We implement a dual-AOD architecture, where the one-dimensional AOD is used to generating an array for storage of single atoms uncoupled to the cavity mode (the "qubit storage register"), and the two-dimensional AOD (the qubit "bus") is used to transfer one or multiple atoms from and to the cavity, for the cavity-operations we have mentioned. This combination should allow collective and single-atom resolved detection and addressing.

In our experiment, cold ^{87}Rb atoms are transported from a 3D-MOT to our fiber-cavity with a transport trap that achieves the submicrometric precision required to operate with cavity modes waists of a few micrometers. Our microcavity is a high finesse fiber Fabry Perot resonator engineered in our group, designed to achieve strong and homogeneous single-atom coupling over the entire length ($L = 145$ µm) of the cavity. It sustains two standing waves: one at 780 nm, to probe the D_2 line of ^{87}Rb and the second at 1559 nm, a far-off resonant trap lattice, commensurate with the probe. Thus atoms trapped in all the lattice sites are maximally and equally coupled to the probe. With atomic ensembles loaded in this trap, we observe a collective strong coupling to the cavity.

The lattice light at 1559 nm induces a strong differential lightshift. Combined with the finite temperature of the atoms, this generates a significant distribution of atomic transition frequencies. In spite of this inhomogeneity, we measure polaritonic resonances much narrower than the frequency distribution. This signals coherent interaction of our atomic ensemble with the cavity mode, an effect called cavity protection, that requires the collective coupling Ω to be large compared to the width of the frequency distribution, $\Delta\omega$. As the coupling of each atom is so strong, this condition is fulfilled for as few as two hundred atoms, a

number much lower than in previous solid-state demonstrations of this cavity protection effect. Thanks to the high degree of control of our cold-atom setup, we vary the ratio $\Omega/\Delta\omega$ and observe the evolution of coherence when the system transits from a cavity-unprotected regime to a cavity-protected regime. We exhibit the role of the dark states in this transition, both in simulations and in experiments: in the unprotected regime they hold a significant fraction of the total photonic weight, such that the probability for the single excitation to decay in the dark states manifold is high.

In the cavity-protected regime, we apply a temporal modulation of the intracavity lattice power. This induces an efficient and tunable frequency modulation of the atomic transition, which transfers to a frequency modulation of the polaritons. We develop a model that accounts very well for our measurement of the corresponding frequency-modulated Rabi splitting. Finally we verify the linear transfer of the frequency modulation predicted in this model.

The lattice light induces a strong and tunable distribution of frequency which allows to study cavity protection with fully controlled parameters, as in the other cold-atom recent study of similar mechanisms, in reference [54]. When we do not want these inhomogeneities, we can simply chop the lattice (at a rate much higher than all trapping frequencies) alternatively with the resonant light we apply on the atoms: optical pumping, cavity probing or blasting light. This is done especially for all the cavity probe measurements with tweezers, in the second part of the thesis.

Indeed, we use the high numerical aperture lens aligned with our microcavity mode to focus sub-micrometer tweezers inside the cavity. The optical layout combines two sizes of beams (for submicron and for larger tweezers), and the two AOD systems (one-dimensional and two-dimensional). The corresponding four beams are carefully aligned with the cavity mode. Multifrequency RF signals with optimised relative phases and amplitudes feed both AODs. We are able to generate simultaneously up to one hundred tweezers per AOD, in reconfigurable arrays.

As a preliminary to detecting a single atom in a single tweezer, we check the ability of our high-cooperativity microcavity to detect efficiently the qubit state of a single atom, in the intracavity lattice. We then reach the collisional blockade regime, in which we obtain probabilistically a single atom in the tweezer. The single atom is characterised with temperature and trap frequencies measurements. The later provide an in-situ verification of the tweezer waist, compatible with a previous estimate. Significant effort is made to optimise the coupling of the single atom in the tweezer to the cavity mode and benefit from the full potential of our CQED setup. By adding the trapping potential of the intracavity lattice to the tweezer potential, we obtain a "hybrid" trap that very efficiently confines the atom close to a probe antinode, where the coupling is maximal. The hybrid trap provides coupling robust to imperfect centering of the tweezer. Still, the coupling can be optimised by minimising the single atom transmission as a function of the position of the tweezer.

We demonstrate strong coupling of the single atom in the hybrid trap, with an effective cooperativity of $C_{eff} \approx 30$, similar to the best values obtained with a single atom in a tweezer and an optical resonator. We find a method to more precisely center the tweezer along the cavity axis, by measuring the transmission on the slope of the polariton peak, which is very sensitive to changes of the coupling.

We finally turn to operating multiple tweezers with both AODs. We setup our one-

dimensional AOD qubit storage register far from the cavity mode and demonstrate the (probabilistic) single atom loading of up to nine tweezers. This constitutes the first step towards manipulating individually tens of single atoms strongly coupled to the cavity.

VII.2 Outlook

VII.2.1 Strong coupling of a deterministic number of qubits

Our experiment has just entered the phase where we operate multiple single atoms in multiple tweezers. In the near term, we would like to strongly couple a *determined* number of atoms N_a in the cavity. This involves loading $N_t > N_a$ tweezers with single atoms, determining the atom-occupation in the chain of tweezers with individual tweezer cavity detection, rearranging the qubit storage register in a defect free array (as in reference [58]) and finally coupling in the cavity N_a single atoms. We could then measure the Rabi splitting of this determined number of atoms. This has been achieved recently in reference [67]. However, a major difference in our proposed scheme is that N_a would be *predetermined*, thus requiring no such N_a-post-selection as in the work of [67].

VII.2.2 Fast and high-fidelity mid-circuit measurement

Then, we intend to demonstrate arbitrary "mid-circuit" measurements, for which our dual-AOD-cavity platform is well suited. "Mid-circuit" refers to a measurement of a subsystem that does not affect other parts of the system. It is crucial to many applications such as quantum error correction [134, 135] or measurement-based quantum computing [136]. An ideal "mid-circuit" measurement needs to be 1) sufficiently local so as not perturb the unmeasured parts, 2) high-fidelity, and 3) much shorter than the decoherence time of the system. These requirements are not well satisfied by fluorescence detection of single atom arrays in tweezers or optical lattices. Indeed, because of the rather small collection solid angle, fluorescence involves many scattered photons and thus is quite long (typically 10 and 100 ms for tweezers and lattices respectively). Also, scattered photons can be destructive when absorbed by nearby atoms. Conversely, a strong coupling cavity with a tweezer array is very well suited for mid-circuit measurements. Indeed:

1) Strong coupling cavities allow for high fidelity and fast state measurement. For instance, infidelity below 10^{-3} for 100 µs has been achieved by measuring both reflection and transmission of the cavity probe light [73]. Simultaneously, another experiment reached $\approx 5 \times 10^{-2}$ in 85 µs, with cavity-enhanced fluorescence detection [137]. Similar performances with the same detection scheme were obtained recently in the tweezers-cavity experiment of Dan Stamper-Kurn [66], precisely in the context of mid-circuit measurement.

2) A tweezer array allows for coupling one or several atoms to the cavity while keeping others out of the mode, and thus unaffected. In [66], with their one-dimensional tweezer array perpendicular to the cavity axis, a minimal mid-circuit measurement is performed with two atoms: it is shown that the measurement of the first atom does not perturb the hyperfine qubit coherence of the second atom. With our dual-AOD architecture, we intend to extend this mid-circuit measurement to simultaneous detection of an *arbitrary* subset of our single atom array.

3) Finally, in a tweezers-cavity setup, the cavity limits strongly the effect of the measurement on the *unmeasured* qubits. In cavity-enhanced fluorescence, the cavity reduces the number of scattered photons required for the measurement (only one hundred photons in [66]). When probing the cavity mode as we do, the number of scattered photons can be much lower, thanks to the coupling strength of fiber cavities: an earlier experiment in our group achieved around one photon scattered for an infidelity 10^{-2} [14].

VII.2.3 Quantum simulation of an all-to-all coupling disordered spin chain

In the field of material science, the inhomogeneity in frequency that we have discussed (chapters III and IV) is very common and can be a limitation. For instance, in organic semiconductors, the mobility of charge carriers is reduced by such inhomogeneities, which limits their technological applications. However, strong coupling to a resonator can be very beneficial, as in our case with cavity-protected coherence (see III). Indeed, it has been experimentally demonstrated that coupling such devices to a cavity can significantly enhance their conductivity through hybridisation of electronic transitions [138]. This leads to delocalised polaritons which enhance the charge transport. Later, a theoretical work showed that *exciton*-transport could also be enhanced by similar phenomena [139].

We have seen in chapter IV that, in presence of disorder, the "dark" states may couple to the cavity. It was shown theoretically that these dark states are distributed on a few emitters [140], which can be arbitrarily distant. Due to this "semi-localisation" (and the corresponding semi-delocalisation), the coherent energy transport is more efficient with the dark states than with the polaritons. In another theoretical work [141], it was shown that, when increasing the ratio $\Delta\omega/\Omega$ (where $\Delta\omega$ is the disorder strength and Ω the collective coupling), at first the transport efficiency decreases exponentially (which is reminiscent of Anderson localisation 's physics [142]). However, surprisingly, for stronger disorder, the transport efficiency increases with $\Delta\omega/\Omega$ ("disorder-enhanced transport" regime). For even stronger disorder, there exists a range of $\Delta\omega/\Omega$ where transport efficiency is flat ("disorder-independent transport" regime).

With our experimental setup, we could simulate such transport properties. We would prepare a chain of single atoms in the cavity with a tunable disorder strength, insert an excitation on a chosen atom, switch on and off the infinite-range atom interactions, with two-photon Raman transitions assisted by the cavity, and finally measure the (distribution in) final position of this excitation. It would be very exciting to demonstrate experimentally the different regimes of transport efficiency predicted in [141], and, following the study of chapter IV, to contribute to deepen experimental understanding of the role of dark states in the dynamics of the disordered coupled system.

VII.2.4 Quantum metrology with spatially distributed entanglement

In the context of quantum metrology, a system with quantum correlations is used to perform measurements with a precision surpassing the limits of classical physics. Spin-squeezed states [41] are the most common type of entangled states used to that purpose. In an interferometric measurement with spin ensembles, using squeezed states rather than the uncorrelated "coherent spin states" improves the sensitivity in detecting the relative phase between the two arms, and thus reduces the uncertainty of the quantity inferred from this phase [40].

Such entanglement-enhancement has mainly been applied to measuring a single quantity, and correspondingly a single phase. Multiparameter quantum metrology [143–146] extends these methods to the simultaneous measurement of several quantities, or a combination of several quantities. For instance, a non-local entangled state involving distant "subsystems" at points A and B could be used to measure the difference in an external field Ξ (for instance the magnetic field) at A and B (*i.e.* estimating the gradient $\Xi(A) - \Xi(B)$) with a *higher* quantum enhancement than if entanglement is produced locally and separately at A and B [147]. We intend to apply such schemes, with our ability to 1) generate squeezing from cavity-feedback [42], 2) measure "subsystems" separately with the cavity, and 3) perform local rotations by selectively tuning a "subsystem" to resonance with a micro-wave field, thanks to controllable tweezers-lightshift.

With these tools, our setup is very well suited for such measurements where locally-addressable nonlocal entanglement enhances the sensitivity, which can apply to measuring gradients and certainly other interesting quantities that depend on more than two parameters. More generally, our experiment could implement schemes where *spatially distributed* entanglement is a ressource, may it be for quantum metrology or for other purposes.

VII.2.5 Conclusion

Our platform is part of this new generation of CQED experiments where the capabilities of strong coupling are combined with the exquisite degree of control of tweezer single atoms [63–67]. Our experiment opens the way to interesting quantum simulations of all-to-all coupled spin ensembles, with single-atom resolution and the availability of controlled disorder. Moreover, thanks to the ability of our dual-AOD architecture to couple to the cavity any subset of the single atom array, we intend to demonstrate arbitrary mid-circuit measurements and to use *spatially distributed* entanglement for quantum metrology and beyond.

Appendices

Bibliography

[1] "Minutes of the 1948 Annual Meeting at New York, January 26-29, 1949"; Phys. Rev. **75**, pp. 1279–1336 (1949). Cited page 5

[2] H. Tanji-Suzuki, I. D. Leroux, M. H. Schleier-Smith, M. Cetina, A. T. Grier, J. Simon and V. Vuletić; "Chapter 4 - Interaction between Atomic Ensembles and Optical Resonators: Classical Description"; in "Advances in Atomic, Molecular, and Optical Physics", , volume 60, edited by E. Arimondo, P. Berman and C. Lin; (pp. 201–237) (Academic Press, 2011). Cited page 5

[3] P. Goy, J. M. Raimond, M. Gross and S. Haroche; "Observation of Cavity-Enhanced Single-Atom Spontaneous Emission"; Phys. Rev. Lett. **50**, pp. 1903–1906 (1983). Cited page 6

[4] Y. Kaluzny, P. Goy, M. Gross, J. M. Raimond and S. Haroche; "Observation of Self-Induced Rabi Oscillations in Two-Level Atoms Excited Inside a Resonant Cavity: The Ringing Regime of Superradiance"; Phys. Rev. Lett. **51**, pp. 1175–1178 (1983). Not cited.

[5] D. Meschede, H. Walther and G. Müller; "One-Atom Maser"; Phys. Rev. Lett. **54**, pp. 551–554 (1985). Not cited.

[6] G. Rempe, H. Walther and N. Klein; "Observation of quantum collapse and revival in a one-atom maser"; Phys. Rev. Lett. **58**, pp. 353–356 (1987). Cited page 6

[7] G. Rempe, R. J. Thompson, R. J. Brecha, W. D. Lee and H. J. Kimble; "Optical bistability and photon statistics in cavity quantum electrodynamics"; Phys. Rev. Lett. **67**, pp. 1727–1730 (1991). Cited page 6

[8] R. J. Thompson, G. Rempe and H. J. Kimble; "Observation of normal-mode splitting for an atom in an optical cavity"; Phys. Rev. Lett. **68**, pp. 1132–1135 (1992). Cited page 6

[9] A. B. Mundt, A. Kreuter, C. Becher, D. Leibfried, J. Eschner, F. Schmidt-Kaler and R. Blatt; "Coupling a Single Atomic Quantum Bit to a High Finesse Optical Cavity"; Phys. Rev. Lett. **89**, p. 103001 (2002). Cited page 6

[10] A. Wallraff, D. I. Schuster, A. Blais, L. Frunzio, R.-. S. Huang, J. Majer, S. Kumar, S. M. Girvin and R. J. Schoelkopf; "Strong coupling of a single photon to a superconducting qubit using circuit quantum electrodynamics"; Nature **431**(7005), pp. 162–167 (2004). Cited page 6

[11] J. P. Reithmaier, G. Sęk, A. Löffler, C. Hofmann, S. Kuhn, S. Reitzenstein, L. V. Keldysh, V. D. Kulakovskii, T. L. Reinecke and A. Forchel; "Strong coupling in a single quantum dot–semiconductor microcavity system"; Nature **432**(7014), pp. 197–200 (2004). Cited page 6

[12] T. Yoshie, A. Scherer, J. Hendrickson, G. Khitrova, H. M. Gibbs, G. Rupper, C. Ell, O. B. Shchekin and D. G. Deppe; "Vacuum Rabi splitting with a single quantum dot in a photonic crystal nanocavity"; Nature **432**(7014), pp. 200–203 (2004). Cited page 6

[13] C. Guerlin, J. Bernu, S. Deléglise, C. Sayrin, S. Gleyzes, S. Kuhr, M. Brune, J.-M. Raimond and S. Haroche; "Progressive field-state collapse and quantum non-demolition photon counting"; Nature **448**(7156), pp. 889–893 (2007). Cited page 6

[14] J. Volz, R. Gehr, G. Dubois, J. Estève and J. Reichel; "Measurement of the internal state of a single atom without energy exchange"; Nature **475**(7355), pp. 210–213 (2011). Cited pages 6, 15, 16, 17, and 136

[15] S. Deléglise, I. Dotsenko, C. Sayrin, J. Bernu, M. Brune, J.-M. Raimond and S. Haroche; "Reconstruction of non-classical cavity field states with snapshots of their decoherence"; Nature **455**(7212), pp. 510–514 (2008). Cited page 6

[16] J. McKeever, A. Boca, A. D. Boozer, R. Miller, J. R. Buck, A. Kuzmich and H. J. Kimble; "Deterministic Generation of Single Photons from One Atom Trapped in a Cavity"; Science **303**(5666), pp. 1992–1994 (2004). Cited page 6

[17] M. Keller, B. Lange, K. Hayasaka, W. Lange and H. Walther; "Continuous generation of single photons with controlled waveform in an ion-trap cavity system"; Nature **431**(7012), pp. 1075–1078 (2004). Cited page 6

[18] H. J. Kimble; "The quantum internet"; Nature **453**(7198), pp. 1023–1030 (2008). Cited page 6

[19] A. Reiserer and G. Rempe; "Cavity-based quantum networks with single atoms and optical photons"; Rev. Mod. Phys. **87**, pp. 1379–1418 (2015). Cited page 6

[20] T. Wilk, S. C. Webster, A. Kuhn and G. Rempe; "Single-Atom Single-Photon Quantum Interface"; Science **317**(5837), pp. 488–490 (2007). Cited page 6

[21] S. Ritter, C. Nölleke, C. Hahn, A. Reiserer, A. Neuzner, M. Uphoff, M. Mücke, E. Figueroa, J. Bochmann and G. Rempe; "An elementary quantum network of single atoms in optical cavities"; Nature **484**(7393), pp. 195–200 (2012). Cited page 6

[22] L.-M. Duan, B. Wang and H. J. Kimble; "Robust quantum gates on neutral atoms with cavity-assisted photon scattering"; Phys. Rev. A **72**, p. 032333 (2005). Cited page 6

[23] X.-M. Lin, Z.-W. Zhou, M.-Y. Ye, Y.-F. Xiao and G.-C. Guo; "One-step implementation of a multiqubit controlled-phase-flip gate"; Phys. Rev. A **73**, p. 012323 (2006). Cited page 6

[24] A. Reiserer, N. Kalb, G. Rempe and S. Ritter; "A quantum gate between a flying optical photon and a single trapped atom"; Nature **508**(7495), pp. 237–240 (2014). Cited page 6

[25] S. Welte, P. Thomas, L. Hartung, S. Daiss, S. Langenfeld, O. Morin, G. Rempe and E. Distante; "A nondestructive Bell-state measurement on two distant atomic qubits"; Nature Photonics **15**(7), pp. 504–509 (2021). Cited page 6

[26] D. J. Wineland, R. E. Drullinger and F. L. Walls; "Radiation-Pressure Cooling of Bound Resonant Absorbers"; Phys. Rev. Lett. **40**, pp. 1639–1642 (1978). Cited page 6

[27] W. D. Phillips and H. Metcalf; "Laser Deceleration of an Atomic Beam"; Phys. Rev. Lett. **48**, pp. 596–599 (1982). Not cited.

[28] S. Chu, L. Hollberg, J. E. Bjorkholm, A. Cable and A. Ashkin; "Three-dimensional viscous confinement and cooling of atoms by resonance radiation pressure"; Phys. Rev. Lett. **55**, pp. 48–51 (1985). Not cited.

[29] E. L. Raab, M. Prentiss, A. Cable, S. Chu and D. E. Pritchard; "Trapping of Neutral Sodium Atoms with Radiation Pressure"; Phys. Rev. Lett. **59**, pp. 2631–2634 (1987). Cited page 6

[30] S. Nussmann, K. Murr, M. Hijlkema, B. Weber, A. Kuhn and G. Rempe; "Vacuum-stimulated cooling of single atoms in three dimensions"; Nature Physics **1**(2), pp. 122–125 (2005). Cited page 6

[31] S. Reick, K. Mølmer, W. Alt, M. Eckstein, T. Kampschulte, L. Kong, R. Reimann, A. Thobe, A. Widera and D. Meschede; "Analyzing quantum jumps of one and two atoms strongly coupled to an optical cavity"; Journal of the Optical Society of America B **27**(6), p. A152 (2010). Cited pages 6 and 18

[32] S. Welte, B. Hacker, S. Daiss, S. Ritter and G. Rempe; "Cavity Carving of Atomic Bell States"; Phys. Rev. Lett. **118**(21), p. 210503 (2017). Cited pages 6, 7, and 18

[33] S. Welte, B. Hacker, S. Daiss, S. Ritter and G. Rempe; "Photon-Mediated Quantum Gate between Two Neutral Atoms in an Optical Cavity"; Phys. Rev. X **8**, p. 011018 (2018). Cited pages 7 and 18

[34] F. Brennecke, T. Donner, S. Ritter, T. Bourdel, M. Köhl and T. Esslinger; "Cavity QED with a Bose–Einstein condensate"; Nature **450**(7167), pp. 268–271 (2007). Cited page 7

[35] F. Brennecke, S. Ritter, T. Donner and T. Esslinger; "Cavity Optomechanics with a Bose-Einstein Condensate"; Science **322**(5899), pp. 235–238 (2008). Cited page 7

[36] K. Baumann, C. Guerlin, F. Brennecke and T. Esslinger; "Dicke quantum phase transition with a superfluid gas in an optical cavity"; Nature **464**(7293), pp. 1301–1306 (2010). Cited page 7

[37] R. Landig, L. Hruby, N. Dogra, M. Landini, R. Mottl, T. Donner and T. Esslinger; "Quantum phases from competing short- and long-range interactions in an optical lattice"; Nature **532**(7600), pp. 476–479 (2016). Cited page 7

[38] Z. Chen, J. G. Bohnet, S. R. Sankar, J. Dai and J. K. Thompson; "Conditional Spin Squeezing of a Large Ensemble via the Vacuum Rabi Splitting"; Phys. Rev. Lett. **106**, p. 133601 (2011). Cited pages 7 and 18

[39] J. G. Bohnet, K. C. Cox, M. A. Norcia, J. M. Weiner, Z. Chen and J. K. Thompson; "Reduced spin measurement back-action for a phase sensitivity ten times beyond the standard quantum limit"; Nature Photonics **8**(9), pp. 731–736 (2014). Cited pages 7 and 18

[40] D. J. Wineland, J. J. Bollinger, W. M. Itano, F. L. Moore and D. J. Heinzen; "Spin squeezing and reduced quantum noise in spectroscopy"; Phys. Rev. A **46**, pp. R6797–R6800 (1992). Cited pages 7 and 136

[41] M. Kitagawa and M. Ueda; "Squeezed spin states"; Phys. Rev. A **47**, pp. 5138–5143 (1993). Cited pages 7, 18, and 136

[42] M. H. Schleier-Smith, I. D. Leroux and V. Vuletić; "Squeezing the collective spin of a dilute atomic ensemble by cavity feedback"; Phys. Rev. A **81**, p. 021804 (2010). Cited pages 7, 18, and 137

[43] I. D. Leroux, M. H. Schleier-Smith and V. Vuletić; "Implementation of Cavity Squeezing of a Collective Atomic Spin"; Phys. Rev. Lett. **104**(7), p. 073602 (2010). Cited pages 7 and 18

[44] O. Hosten, N. J. Engelsen, R. Krishnakumar and M. A. Kasevich; "Measurement Noise 100 Times Lower than the Quantum-Projection Limit Using Entangled Atoms"; Nature **529**(7587), pp. 505–508 (2016). Cited pages 7 and 18

[45] F. Haas, J. Volz, R. Gehr, J. Reichel and J. Esteve; "Entangled States of More Than 40 Atoms in an Optical Fiber Cavity"; Science **344**(6180), pp. 180–183 (2014). Cited pages 7 and 17

[46] G. Barontini, L. Hohmann, F. Haas, J. Estève and J. Reichel; "Deterministic generation of multiparticle entanglement by quantum Zeno dynamics"; Science **349**(6254), pp. 1317–1321 (2015). Cited pages 7 and 17

[47] R. Houdré, R. P. Stanley and M. Ilegems; "Vacuum-Field Rabi Splitting in the Presence of Inhomogeneous Broadening: Resolution of a Homogeneous Linewidth in

an Inhomogeneously Broadened System"; Phys. Rev. A **53**(4), pp. 2711–2715 (1996). Cited pages 7, 22, 24, 25, and 57

[48] Z. Kurucz, J. H. Wesenberg and K. Mølmer; "Spectroscopic Properties of Inhomogeneously Broadened Spin Ensembles in a Cavity"; Phys. Rev. A **83**(5), p. 053852 (2011). Cited page 24

[49] I. Diniz, S. Portolan, R. Ferreira, J. M. Gérard, P. Bertet and A. Auffèves; "Strongly Coupling a Cavity to Inhomogeneous Ensembles of Emitters: Potential for Long-Lived Solid-State Quantum Memories"; Phys. Rev. A **84**(6), p. 063810 (2011). Cited pages 7, 22, 24, 25, 55, and 57

[50] S. Putz, D. O. Krimer, R. Amsüss, A. Valookaran, T. Nöbauer, J. Schmiedmayer, S. Rotter and J. Majer; "Protecting a Spin Ensemble against Decoherence in the Strong-Coupling Regime of Cavity QED"; Nature Phys **10**(10), pp. 720–724 (2014). Cited pages 7, 25, 26, 27, 28, 63, 65, and 66

[51] T. Zhong, J. M. Kindem, J. Rochman and A. Faraon; "Interfacing Broadband Photonic Qubits to On-Chip Cavity-Protected Rare-Earth Ensembles"; Nat Commun **8**(1), p. 14107 (2017). Cited pages 26, 27, 28, and 65

[52] J. D. Breeze, E. Salvadori, J. Sathian, N. M. Alford and C. W. M. Kay; "Room-Temperature Cavity Quantum Electrodynamics with Strongly Coupled Dicke States"; npj Quantum Inf **3**(1), p. 40 (2017). Cited pages 7, 25, 26, 27, 28, 63, 65, and 66

[53] M. Baghdad, P.-A. Bourdel, S. Schwartz, F. Ferri, J. Reichel and R. Long; "Spectral Engineering of Cavity-Protected Polaritons in an Atomic Ensemble with Controlled Disorder"; arXiv (2022). Cited pages 7, 49, and 63

[54] N. Sauerwein, F. Orsi, P. Uhrich, S. Bandyopadhyay, F. Mattiotti, T. Cantat-Moltrecht, G. Pupillo, P. Hauke and J.-P. Brantut; "Engineering random spin models with atoms in a high-finesse cavity"; arXiv (2022). Cited pages 7, 28, 64, 69, 70, 71, and 134

[55] N. Schlosser, G. Reymond, I. Protsenko and P. Grangier; "Sub-poissonian loading of single atoms in a microscopic dipole trap"; Nature **411**(6841), pp. 1024–1027 (2001). Cited pages 7 and 73

[56] N. Schlosser, G. Reymond and P. Grangier; "Collisional Blockade in Microscopic Optical Dipole Traps"; Phys. Rev. Lett. **89**, p. 023005 (2002). Cited pages 7 and 73

[57] D. Barredo, S. de Léséleuc, V. Lienhard, T. Lahaye and A. Browaeys; "An Atom-by-Atom Assembler of Defect-Free Arbitrary Two-Dimensional Atomic Arrays"; Science **354**(6315), pp. 1021–1023 (2016). Cited pages 7 and 73

[58] M. Endres, H. Bernien, A. Keesling, H. Levine, E. R. Anschuetz, A. Krajenbrink, C. Senko, V. Vuletic, M. Greiner and M. D. Lukin; "Atom-by-Atom Assembly of Defect-Free One-Dimensional Cold Atom Arrays"; Science **354**(6315), pp. 1024–1027 (2016). Cited pages 19, 74, 83, 86, and 135

[59] D. Barredo, V. Lienhard, S. de Léséleuc, T. Lahaye and A. Browaeys; "Synthetic three-dimensional atomic structures assembled atom by atom"; Nature **561**(7721), pp. 79–82 (2018). Cited page 73

[60] S. Ebadi, T. T. Wang, H. Levine, A. Keesling, G. Semeghini, A. Omran, D. Bluvstein, R. Samajdar, H. Pichler, W. W. Ho, S. Choi, S. Sachdev, M. Greiner, V. Vuletić and M. D. Lukin; "Quantum phases of matter on a 256-atom programmable quantum simulator"; Nature **595**(7866), pp. 227–232 (2021). Cited pages 7 and 74

[61] A. Browaeys and T. Lahaye; "Many-body physics with individually controlled Rydberg atoms"; Nature Physics **16**(2), pp. 132–142 (2020). Cited page 7

[62] P. Scholl, M. Schuler, H. J. Williams, A. A. Eberharter, D. Barredo, K.-N. Schymik, V. Lienhard, L.-P. Henry, T. C. Lang, T. Lahaye, A. M. Läuchli and A. Browaeys; "Quantum simulation of 2D antiferromagnets with hundreds of Rydberg atoms"; Nature **595**(7866), pp. 233–238 (2021). Cited pages 7 and 74

[63] P. Samutpraphoot, T. Đorđević, P. L. Ocola, H. Bernien, C. Senko, V. Vuletić and M. D. Lukin; "Strong Coupling of Two Individually Controlled Atoms via a Nanophotonic Cavity"; Phys. Rev. Lett. **124**, p. 063602 (2020). Cited pages 8, 19, 121, and 137

[64] T. Đorđević, P. Samutpraphoot, P. L. Ocola, H. Bernien, B. Grinkemeyer, I. Dimitrova, V. Vuletić and M. D. Lukin; "Entanglement transport and a nanophotonic interface for atoms in optical tweezers"; Science **373**(6562), pp. 1511–1514 (2021). Cited pages 8 and 19

[65] E. Deist, J. A. Gerber, Y.-H. Lu, J. Zeiher and D. M. Stamper-Kurn; "Superresolution Microscopy of Optical Fields Using Tweezer-Trapped Single Atoms"; Phys. Rev. Lett. **128**(8), p. 083201 (2022). Cited pages 8, 19, 21, and 98

[66] E. Deist, Y.-H. Lu, J. Ho, M. K. Pasha, J. Zeiher, Z. Yan and D. M. Stamper-Kurn; "Mid-circuit cavity measurement in a neutral atom array"; arXiv (2022). Cited pages 8, 20, 120, 121, 135, and 136

[67] Y. Liu, Z. Wang, P. Yang, Q. Wang, Q. Fan, G. Li, P. Zhang and T. Zhang; "Realization of strong coupling between deterministic single-atom arrays and a high-finesse miniature optical cavity"; arXiv (2022). Cited pages 8, 20, 21, 98, 108, 121, 135, and 137

[68] E. T. Jaynes and F. W. Cummings; "Comparisons of Quantum and Semiclassical Radiation Theories with Application to the Beam Maser"; Proceedings of the IEEE **51**, pp. 89–109 (1963). Cited page 11

[69] J. J. Sanchez-Mondragon, N. B. Narozhny and J. H. Eberly; "Theory of Spontaneous-Emission Line Shape in an Ideal Cavity"; Phys. Rev. Lett. **51**, pp. 550–553 (1983). Cited page 12

[70] G. Hechenblaikner, M. Gangl, P. Horak and H. Ritsch; "Cooling an atom in a weakly driven high-Q cavity"; Phys. Rev. A **58**, pp. 3030–3042 (1998). Cited page 13

[71] R. H. Dicke; "Coherence in Spontaneous Radiation Processes"; Phys. Rev. **93**, pp. 99–110 (1954). Cited page 15

[72] M. Tavis and F. W. Cummings; "Exact Solution for an N-Molecule—Radiation-Field Hamiltonian"; Phys. Rev. **170**, pp. 379–384 (1968). Cited page 15

[73] R. Gehr, J. Volz, G. Dubois, T. Steinmetz, Y. Colombe, B. L. Lev, R. Long, J. Estève and J. Reichel; "Cavity-Based Single Atom Preparation and High-Fidelity Hyperfine State Readout"; Phys. Rev. Lett. **104**, p. 203602 (2010). Cited pages 15, 91, and 135

[74] R. Gehr; *Cavity based high-fidelity and non-destructive single atom detection on an atom chip*; Ph.D. thesis; Université Pierre et Marie Curie - Paris VI (2011). Cited pages 16 and 91

[75] M. H. Schleier-Smith, I. D. Leroux and V. Vuletić; "States of an Ensemble of Two-Level Atoms with Reduced Quantum Uncertainty"; Phys. Rev. Lett. **104**, p. 073604 (2010). Cited page 18

[76] S. Kuhr, W. Alt, D. Schrader, M. Müller, V. Gomer and D. Meschede; "Deterministic Delivery of a Single Atom"; Science **293**(5528), pp. 278–280 (2001). Cited page 18

[77] M. Khudaverdyan, W. Alt, I. Dotsenko, T. Kampschulte, K. Lenhard, A. Rauschenbeutel, S. Reick, K. Schörner, A. Widera and D. Meschede; "Controlled insertion and retrieval of atoms coupled to a high-finesse optical resonator"; New Journal of Physics **10**(7), p. 073023 (2008). Cited page 18

[78] S. Brakhane, W. Alt, T. Kampschulte, M. Martinez-Dorantes, R. Reimann, S. Yoon, A. Widera and D. Meschede; "Bayesian Feedback Control of a Two-Atom Spin-State in an Atom-Cavity System"; Physical Review Letters **109**(17) (2012). Cited page 18

[79] Y. Miroshnychenko, W. Alt, I. Dotsenko, L. Förster, M. Khudaverdyan, D. Meschede, D. Schrader and A. Rauschenbeutel; "An atom-sorting machine"; Nature **442**(7099), pp. 151–151 (2006). Cited page 19

[80] P. Samutpraphoot; *A quantum network node based on a nanophotonic interface for atoms in optical tweezers*; Ph.D. thesis; Harvard University (2021). Cited page 19

[81] J. A. Gerber; *Cavity Quantum Electrodynamics with a Locally Addressable Quantum Gas*; Ph.D. thesis; University of California, Berkeley (2021). Cited pages 19 and 98

[82] J. Lee, G. Vrijsen, I. Teper, O. Hosten and M. A. Kasevich; "Many-atom–cavity QED system with homogeneous atom–cavity coupling"; Opt. Lett. **39**(13), pp. 4005–4008 (2014). Cited page 21

[83] Z. Zhang, C. H. Lee, R. Kumar, K. J. Arnold, S. J. Masson, A. L. Grimsmo, A. S. Parkins and M. D. Barrett; "Dicke-model simulation via cavity-assisted Raman transitions"; Phys. Rev. A **97**, p. 043858 (2018). Not cited.

[84] E. J. Davis, G. Bentsen, L. Homeier, T. Li and M. H. Schleier-Smith; "Photon-Mediated Spin-Exchange Dynamics of Spin-1 Atoms"; Phys. Rev. Lett. **122**(1), p. 010405 (2019). Cited page 21

[85] S. Haroche and J.-M. Raimond; *Exploring the Quantum: Atoms, Cavities, and Photons* (Oxford University Press, 2006); ISBN:978-0-19-170862-6. Cited page 23

[86] J. Dubail, T. Botzung, J. Schachenmayer, G. Pupillo and D. Hagenmüller; "Large Random Arrowhead Matrices: Multifractality, Semilocalization, and Protected Transport in Disordered Quantum Spins Coupled to a Cavity"; Phys. Rev. A **105**(2), p. 023714 (2022). Cited page 24

[87] S. Garcia; *Interfaces fibrées entre atomes uniques et photons uniques*; Ph.D. thesis; Ecole Normale Supérieure (2015). Cited pages 31 and 38

[88] C. Lebouteiller; *Dispositif pour le chargement rapide d'une cavité miniaturisée : vers un registre de qubits atomiques*; Ph.D. thesis; Université Pierre et Marie Curie - Paris VI (2016). Not cited.

[89] F. Ferri; *Strong coupling between a fiber-cavity mode and a commensurate atomic lattice*; Ph.D. thesis; PSL Research University, Ecole Normale Supérieure (2018). Cited pages 32, 34, 35, 38, 39, 41, 43, 74, 75, 76, and 77

[90] M. Baghdad; *Ensemble atomique inhomogène protégé de la décohérence par son couplage fort à la cavité*; Ph.D. thesis; PSL Research University, Ecole Normale Supérieure (2020). Cited pages 31, 40, 42, 44, and 49

[91] J. H. Shirley; "Modulation transfer processes in optical heterodyne saturation spectroscopy"; Opt. Lett. **7**(11), pp. 537–539 (1982). Cited page 33

[92] D. J. McCarron, S. A. King and S. L. Cornish; "Modulation transfer spectroscopy in atomic rubidium"; Measurement Science and Technology **19**(10), p. 105601 (2008). Cited page 33

[93] F. Ferri, A. L. Rooij, C. Lebouteiller, P.-A. Bourdel, M. Baghdad, S. Schwartz, S. Garcia, J. Reichel and R. Long; "An Optical Elevator for Precise Delivery of Cold Atoms Using an Acousto-Optical Deflector"; New J. Phys. **24**(4), p. 043013 (2022). Cited pages 36 and 37

[94] D. Hunger, T. Steinmetz, Y. Colombe, C. Deutsch, T. W. Hänsch and J. Reichel; "A Fiber Fabry–Perot Cavity with High Finesse"; New J. Phys. **12**(6), p. 065038 (2010). Cited page 38

[95] K. Ott; *Towards a squeezing-enhanced atomic clock on a chip*; Ph.D. thesis; Université Pierre et Marie Curie - Paris VI (2016). Cited page 38

[96] K. Ott, S. Garcia, R. Kohlhaas, K. Schüppert, P. Rosenbusch, R. Long and J. Reichel; "Millimeter-long fiber Fabry-Perot cavities"; Opt. Express **24**(9), pp. 9839–9853 (2016). Not cited.

[97] S. Garcia, F. Ferri, K. Ott, J. Reichel and R. Long; "Dual-Wavelength Fiber Fabry-Perot Cavities with Engineered Birefringence"; Opt. Express **26**(17), p. 22249 (2018). Cited page 38

[98] H. Mabuchi, J. Ye and H. Kimble; "Full observation of single-atom dynamics in cavity QED"; Applied Physics B: Lasers and Optics **68**(6), pp. 1095–1108 (1999). Cited page 39

[99] R. W. P. Drever, J. L. Hall, F. V. Kowalski, J. Hough, G. M. Ford, A. J. Munley and H. Ward; "Laser phase and frequency stabilization using an optical resonator"; Applied Physics B: Lasers and Optics **31**(2), pp. 97–105 (1983). Cited page 40

[100] E. D. Black; "An introduction to Pound–Drever–Hall laser frequency stabilization"; American Journal of Physics **69**(1), pp. 79–87 (2001). Cited page 40

[101] K. L. Corwin, S. J. M. Kuppens, D. Cho and C. E. Wieman; "Spin-Polarized Atoms in a Circularly Polarized Optical Dipole Trap"; Phys. Rev. Lett. **83**, pp. 1311–1314 (1999). Cited page 41

[102] C. Cohen-Tannoudji and J. Dupont-Roc; "Experimental Study of Zeeman Light Shifts in Weak Magnetic Fields"; Phys. Rev. A **5**, pp. 968–984 (1972). Cited page 41

[103] N. Vansteenkiste, P. Vignolo and A. Aspect; "Optical reversibility theorems for polarization: application to remote control of polarization"; J. Opt. Soc. Am. A **10**(10), pp. 2240–2245 (1993). Cited page 42

[104] Kastler, Alfred; "Quelques suggestions concernant la production optique et la détection optique d'une inégalité de population des niveaux de quantifigation spatiale des atomes. Application à l'expérience de Stern et Gerlach et à la résonance magnétique"; J. Phys. Radium **11**(6), pp. 255–265 (1950). Cited page 42

[105] J. Dalibard, S. Reynaud and C. Cohen-Tannoudji; "Proposals of stable optical traps for neutral atoms"; Optics Communications **47**(6), pp. 395–399 (1983). Cited page 44

[106] S. Chu, J. E. Bjorkholm, A. Ashkin and A. Cable; "Experimental Observation of Optically Trapped Atoms"; Phys. Rev. Lett. **57**, pp. 314–317 (1986). Cited page 44

[107] J. P. Brantut, J. F. Clément, M. R. de Saint Vincent, G. Varoquaux, R. A. Nyman, A. Aspect, T. Bourdel and P. Bouyer; "Light-Shift Tomography in an Optical-Dipole Trap for Neutral Atoms"; Phys. Rev. A **78**(3), p. 031401 (2008). Cited page 50

[108] B. Arora, M. S. Safronova and C. W. Clark; "Magic Wavelengths for the $np\text{\ensuremath{-}}ns$ Transitions in Alkali-Metal Atoms"; Phys. Rev. A **76**(5), p. 052509 (2007). Cited page 50

[109] F. Le Kien, P. Schneeweiss and A. Rauschenbeutel; "Dynamical Polarizability of Atoms in Arbitrary Light Fields: General Theory and Application to Cesium"; Eur. Phys. J. D **67**(5), p. 92 (2013). Cited page 50

[110] L. W. Clark, N. Jia, N. Schine, C. Baum, A. Georgakopoulos and J. Simon; "Interacting Floquet Polaritons"; Nature **571**(7766), pp. 532–536 (2019). Cited pages 57 and 58

[111] J. R. Johansson, P. D. Nation and F. Nori; "QuTiP 2: A Python Framework for the Dynamics of Open Quantum Systems"; Computer Physics Communications **184**(4), pp. 1234–1240 (2013). Cited page 60

[112] K.-A. Suominen; "Theories for cold atomic collisions in light fields"; Journal of Physics B: Atomic, Molecular and Optical Physics **29**(24), pp. 5981–6007 (1996). Cited page 73

[113] S. J. M. Kuppens, K. L. Corwin, K. W. Miller, T. E. Chupp and C. E. Wieman; "Loading an optical dipole trap"; Phys. Rev. A **62**, p. 013406 (2000). Cited page 73

[114] T. Grünzweig, A. Hilliard, M. McGovern and M. Andersen; "Near-deterministic preparation of a single atom in an optical micro-trap"; Nat. Phys. **6**, pp. 951–954 (2010). Cited page 73

[115] B. J. Lester, N. Luick, A. M. Kaufman, C. M. Reynolds and C. A. Regal; "Rapid Production of Uniformly Filled Arrays of Neutral Atoms"; Phys. Rev. Lett. **115**, p. 073003 (2015). Cited page 73

[116] A. L. Gaunt and Z. Hadzibabic; "Robust Digital Holography For Ultracold Atom Trapping"; Scientific Reports **2**(1) (2012). Cited page 73

[117] A. L. Gaunt, T. F. Schmidutz, I. Gotlibovych, R. P. Smith and Z. Hadzibabic; "Bose-Einstein Condensation of Atoms in a Uniform Potential"; Phys. Rev. Lett. **110**, p. 200406 (2013). Not cited.

[118] V. Boyer, C. M. Chandrashekar, C. J. Foot and Z. J. Laczik; "Dynamic optical trap generation using FLC SLMs for the manipulation of cold atoms"; Journal of Modern Optics **51**(14), pp. 2235–2240 (2004). Cited page 73

[119] F. Nogrette, H. Labuhn, S. Ravets, D. Barredo, L. Béguin, A. Vernier, T. Lahaye and A. Browaeys; "Single-Atom Trapping in Holographic 2D Arrays of Microtraps with Arbitrary Geometries"; Phys. Rev. X **4**, p. 021034 (2014). Cited page 73

[120] Y. R. P. Sortais, H. Marion, C. Tuchendler, A. M. Lance, M. Lamare, P. Fournet, C. Armellin, R. Mercier, G. Messin, A. Browaeys and

P. Grangier; "Diffraction-limited optics for single-atom manipulation"; Physical Review A **75**(1) (2007). Cited pages 74, 77, and 86

[121] W. S. Bakr, J. I. Gillen, A. Peng, S. Fölling and M. Greiner; "A quantum gas microscope for detecting single atoms in a Hubbard-regime optical lattice"; Nature **462**(7269), pp. 74–77 (2009). Cited page 75

[122] J. F. Sherson, C. Weitenberg, M. Endres, M. Cheneau, I. Bloch and S. Kuhr; "Single-atom-resolved fluorescence imaging of an atomic Mott insulator"; Nature **467**(7311), pp. 68–72 (2010). Cited page 75

[123] A. M. Kaufman, B. J. Lester and C. A. Regal; "Cooling a Single Atom in an Optical Tweezer to Its Quantum Ground State"; Phys. Rev. X **2**, p. 041014 (2012). Cited page 99

[124] A. Fuhrmanek, R. Bourgain, Y. R. P. Sortais and A. Browaeys; "Light-assisted collisions between a few cold atoms in a microscopic dipole trap"; Phys. Rev. A **85**, p. 062708 (2012). Cited page 100

[125] T. A. Savard, K. M. O'Hara and J. E. Thomas; "Laser-noise-induced heating in far-off resonance optical traps"; Phys. Rev. A **56**, pp. R1095–R1098 (1997). Cited page 101

[126] M. E. Gehm, K. M. O'Hara, T. A. Savard and J. E. Thomas; "Dynamics of noise-induced heating in atom traps"; Phys. Rev. A **58**, pp. 3914–3921 (1998). Cited page 101

[127] S. de Léséleuc; *Quantum simulation of spin models with assembled arrays of Rydberg atoms*; Ph.D. thesis; Université Paris-Saclay (2018). Cited page 102

[128] H. J. Levine; *Quantum Information Processing and Quantum Simulation with Programmable Rydberg Atom Arrays*; Ph.D. thesis; Harward University, Cambridge (2021). Cited pages 102 and 114

[129] S. Friebel, C. D'Andrea, J. Walz, M. Weitz and T. W. Hänsch; "CO_2-laser optical lattice with cold rubidium atoms"; Phys. Rev. A **57**, pp. R20–R23 (1998). Cited page 102

[130] J. Wu, R. Newell, M. Hausmann, D. J. Vieira and X. Zhao; "Loading dynamics of optical trap and parametric excitation resonances of trapped atoms"; Journal of Applied Physics **100**(5), p. 054903 (2006). Cited page 102

[131] A. E. Siegman; *Lasers* (University Science Books, 1986); ISBN:0-935702-11-5. Cited page 103

[132] C. Tuchendler, A. M. Lance, A. Browaeys, Y. R. P. Sortais and P. Grangier; "Energy distribution and cooling of a single atom in an optical tweezer"; Phys. Rev. A **78**, p. 033425 (2008). Cited page 104

[133] S. Welte; *Photon-mediated quantum information processing with neutral atoms in an optical cavity*; Ph.D. thesis; Max-Planck-Institut für Quantenoptik, Garching (2019). Cited page 120

[134] P. W. Shor; "Scheme for reducing decoherence in quantum computer memory"; Phys. Rev. A **52**, pp. R2493–R2496 (1995). Cited page 135

[135] A. M. Steane; "Error Correcting Codes in Quantum Theory"; Phys. Rev. Lett. **77**, pp. 793–797 (1996). Cited page 135

[136] R. Raussendorf and H. J. Briegel; "A One-Way Quantum Computer"; Phys. Rev. Lett. **86**, pp. 5188–5191 (2001). Cited page 135

[137] J. Bochmann, M. Mücke, C. Guhl, S. Ritter, G. Rempe and D. L. Moehring; "Lossless State Detection of Single Neutral Atoms"; Phys. Rev. Lett. **104**, p. 203601 (2010). Cited page 135

[138] E. Orgiu, J. George, J. A. Hutchison, E. Devaux, J. F. Dayen, B. Doudin, F. Stellacci, C. Genet, J. Schachenmayer, C. Genes, G. Pupillo, P. Samorì and T. W. Ebbesen; "Conductivity in Organic Semiconductors Hybridized with the Vacuum Field"; Nature Mater **14**(11), pp. 1123–1129 (2015). Cited page 136

[139] J. Schachenmayer, C. Genes, E. Tignone and G. Pupillo; "Cavity-Enhanced Transport of Excitons"; Phys. Rev. Lett. **114**(19), p. 196403 (2015). Cited page 136

[140] T. Botzung, D. Hagenmüller, S. Schütz, J. Dubail, G. Pupillo and J. Schachenmayer; "Dark State Semilocalization of Quantum Emitters in a Cavity"; Phys. Rev. B **102**(14), p. 144202 (2020). Cited page 136

[141] N. C. Chávez, F. Mattiotti, J. A. Méndez-Bermúdez, F. Borgonovi and G. L. Celardo; "Disorder-Enhanced and Disorder-Independent Transport with Long-Range Hopping: Application to Molecular Chains in Optical Cavities"; Phys. Rev. Lett. **126**(15), p. 153201 (2021). Cited page 136

[142] F. Evers and A. D. Mirlin; "Anderson transitions"; Rev. Mod. Phys. **80**, pp. 1355–1417 (2008). Cited page 136

[143] P. C. Humphreys, M. Barbieri, A. Datta and I. A. Walmsley; "Quantum Enhanced Multiple Phase Estimation"; Phys. Rev. Lett. **111**, p. 070403 (2013). Cited page 137

[144] T. J. Proctor, P. A. Knott and J. A. Dunningham; "Multiparameter Estimation in Networked Quantum Sensors"; Phys. Rev. Lett. **120**, p. 080501 (2018). Not cited.

[145] W. Ge, K. Jacobs, Z. Eldredge, A. V. Gorshkov and M. Foss-Feig; "Distributed Quantum Metrology with Linear Networks and Separable Inputs"; Phys. Rev. Lett. **121**, p. 043604 (2018). Not cited.

[146] M. Gessner, L. Pezzè and A. Smerzi; "Sensitivity Bounds for Multiparameter Quantum Metrology"; Phys. Rev. Lett. **121**, p. 130503 (2018). Cited page 137

[147] M. Gessner, A. Smerzi and L. Pezzè; "Multiparameter squeezing for optimal quantum enhancements in sensor networks"; Nature Communications **11**(1), p. 3817 (2020). Cited page 137

Pierre-Antoine BOURDEL **5 décembre 2022**

Sujet : Ensembles atomiques en microcavité: de la protection par la cavité au contrôle d'atomes uniques.

Résumé : Générer et manipuler des états quantiques intriqués multiparticules est un des défis excitants de la physique expérimentale moderne. À cette fin, nous avons construit une plateforme où des atomes froids sont fortement couplés à une microcavité optique fibrée, sous un microscope de gaz quantique. Piégés dans un réseau à 1560nm, les atomes ont un couplage fort et homogène à la sonde à 780nm. Celui-ci permet leur interaction cohérente avec la cavité, malgré la forte hétérogénéité en fréquence induite par le piège. C'est la première observation d'un effet de protection par la cavité avec moins de 200 émetteurs. Nous mesurons le couplage croissant des états noirs à la cavité à mesure que le désordre l'emporte sur l'interaction collective. Dans le régime protégé nous démontrons la modulation en fréquence des polaritons, via la fréquence atomique. Ensuite, nous mettons en place des pinces optiques dans la microcavité, pour générer et manipuler plusieurs atomes uniques. La cavité permet la détection rapide et non destructive d'un atome unique dans une pince. Par une mesure du doublet de Rabi, nous démontrons son couplage fort à la cavité, avec une coopérativité effective de 30. Pour finir, nous obtenons des atomes uniques dans une chaine de 9 pinces. Ce travail conduira à la manipulation de plusieurs atomes individuels, fortement couplés à la cavité, avec des applications en métrologie quantique multiparamètre, mettant à profit des états intriqués spatialement étendus et localement mesurables, et la simulation quantique d'une chaine de spins adressables, avec des interactions de portée infinie via la cavité.

Mots clés : Intrication multiparticules, Électrodynamique quantique en cavité, Atomes uniques, Pinces optiques, Métrologie quantique, Simulation quantique

Subject : Atomic ensembles in a microcavity: from cavity protection to single atom control

Abstract: Generating and manipulating multiparticle quantum entangled states is an exciting challenge of modern physics. Along this line, we have built a platform where cold rubidium atoms are strongly coupled to a fiber-based microcavity, under a quantum gas microscope. The atoms are trapped in a lattice at 1560 nm, which allows strong and homogeneous coupling to the commensurate probe lattice at 780 nm. First, we observe a coherent interaction between the cavity and the atoms, in the strong coupling regime, in spite of a large frequency inhomogeneity induced by the trap. It is the first report of such cavity protection effect with less than 200 emitters. We measure the growing coupling of the dark states to the cavity as the disorder takes over the collective coupling. In the protected regime we engineer frequency-modulated polaritons through a modulation of the atomic frequency. Then, we setup optical tweezers in the microcavity to obtain and manipulate several single atoms. The cavity enables fast and non demolition detection of a single atom in a tweezer. We measure the vacuum Rabi splitting of this atom, demonstrating its strong coupling with an effective cooperativity of 30. Finally, we obtain single atoms in a chain of 9 tweezers. This work opens to way to manipulating many individual atoms strongly coupled to the cavity, with applications in multiparameter quantum metrology, using spatially distributed and locally measurable entanglement as a resource, and quantum simulation of a chain of addressable spins with cavity-mediated infinite range interactions.

Keywords : Multiparticle entanglement, Cavity quantum electrodynamics, Single atoms, Optical tweezers, Quantum metrology, Quantum simulation